Adaptive Model Predictive Control for Microstructure Control in Laser Material Processing

by

Richard Hendrik van Blitterswijk

A thesis
presented to the University of Waterloo
in fulfillment of the
thesis requirement for the degree of
Doctor of Philosophy
in
Mechanical and Mechatronics Engineering

Waterloo, Ontario, Canada, 2024

© Richard Hendrik van Blitterswijk 2024

Examining Committee Membership

The following served on the Examining Committee for this thesis. The decision of the Examining Committee is by majority vote.

External Examiner:	**Daulun Chen**, Professor Dept. of Mechanical, Industrial, and Mechatronics Engineering, Toronto Metropolitan University
Supervisor:	**Amir Khajepour**, Professor Dept. of Mechanical and Mechatronics Engineering, University of Waterloo
Internal Member:	**Adrian Gerlich**, Associate Professor Dept. of Mechanical and Mechatronics Engineering, University of Waterloo
Internal Member:	**Mihaela Vlasea**, Associate Professor Dept. of Mechanical and Mechatronics Engineering, University of Waterloo
Internal-External Member:	**Nasser Lashgarian Azad**, Associate Professor Dept. of Systems Design Engineering, University of Waterloo

Author's Declaration

This thesis consists of material all of which I authored or co-authored: see Statement of Contributions included in the thesis. This is a true copy of the thesis, including any required final revisions, as accepted by my examiners.

I understand that my thesis may be made electronically available to the public.

Statement of Contributions

I would like to acknowledge the names of my co-authors who contributed to the research described in this thesis. These include:

Prof. Amir Khajepour: Supervising the research, generating novel concepts for this thesis, facilitating access to laboratory resources, and reviewing and proofreading papers.

Prof. Pascal Etman: Supervising the research, and reviewing and proofreading papers.

Dr. Mohammad Farshidianfar: Providing expertise in laser-directed energy deposition, providing technical support in the design of and conducting experiments, and reviewing and proofreading papers.

Dr. Lucas Botelho: Brainstorming early concepts in adaptive model predictive control for temperature and cooling rate control, providing technical support in the design of and conducting experiments, and reviewing, proofreading, and editing papers.

Abstract

Laser material processing (LMP) has revolutionized traditional fabrication methods across industries, evolving from laser cutting to encompassing advanced techniques like laser heat treatment (LHT), laser welding, and laser additive manufacturing, enabling precise alteration of material properties and unprecedented design freedom across industries. However, achieving consistent material characteristics remains a significant challenge, particularly in advanced additive manufacturing processes such as laser-directed energy deposition (LDED), where the complex interplay between process parameters and material properties hinders uniform product quality, emphasizing the need for advanced process control strategies.

Conventional control methods like proportional-integral-derivative controllers struggle to anticipate the intricate interactions inherent in LMP processes, making it difficult to control multiple parameters simultaneously. Model-based control strategies, leveraging numerical models, offer promise in providing a comprehensive understanding of process dynamics. However, their practical implementation in real-time control applications is impeded by the computational challenges of numerical models. Overcoming these obstacles is crucial to harnessing the full potential of numerical models for enhanced process control and ensuring consistent, reproducible material characteristics.

In this research, a novel adaptive model predictive control (AMPC) algorithm was developed to address the challenges of ensuring consistent material characteristics in LMP processes. Initially, a two-dimensional (2D) adaptive thermal model was designed for real-time prediction of thermal dynamics during the LHT process, focusing on parameters like peak temperature and spatial cooling rate. Subsequently, a one-dimensional (1D) adaptive thermal model was developed with improvements on efficiency, accuracy, and suitability for control applications compared to the 2D counterpart, focusing on real-time prediction of the temperature distribution and spatial cooling rate. Additionally, an model predictive control (MPC) algorithm utilizing a 2D thermal model was developed for single-input single-output (SISO) peak temperature control during LHT to improve the consistency of hardness and hardening depth. Finally, an AMPC algorithm was

designed using the 1D adaptive thermal model for multi-input multi-output (MIMO) temperature and spatial cooling rate control during LDED to achieve consistent material characteristics throughout the process.

A series of LHT and LDED experiments were designed to assess the real-time thermal dynamic prediction capabilities of the models and the real-time control capabilities of the MPC algorithms in LMP. These experiments encompass open-loop LHT and LDED scenarios, targeting the validation of adaptive 1D and 2D thermal models, respectively. Additionally, closed-loop LHT and LDED experiments were designed to investigate the efficacy of the MPC algorithms in controlling one or multiple process parameters to achieve consistent hardness values. The 2D adaptive thermal model effectively adjusted to the thermal dynamic changes in real-time, yielding precise predictions of peak temperature and spatial cooling rates during LHT. Similarly, validations of the 1D adaptive thermal model showcased near-perfect temperature and cooling rate predictions during LDED, along with impressive computational efficiency. Utilizing the SISO MPC algorithm ensured consistent hardness and hardening depth through closed-loop peak temperature control during LHT. Meanwhile, deploying the MIMO AMPC algorithm enabled consistent hardness across the entire deposition process. This was achieved by simultaneously controlling the temperature and spatial cooling rates during the LDED experiments.

In conclusion, this research marks significant advancements in real-time process control within LMP applications. Through the integration of adaptive thermal models and MPC algorithms, the study achieves the crucial objective of ensuring consistent material characteristics in LMP manufactured parts. The developed AMPC algorithm demonstrates unprecedented levels of control, stability, and reliability. Moreover, its versatility and simplicity extend its applicability beyond LMP processes, enabling adoption in various advanced manufacturing processes utilizing concentrated energy sources. Thus, the AMPC methodology holds the potential to address the crucial need in advanced manufacturing by ensuring consistent and reproducible material characteristics in manufactured parts across the entire industry.

Acknowledgements

I am immensely grateful to Prof. Amir Khajepour for offering me the invaluable opportunity to pursue this research project and for his constant guidance and support throughout my doctoral studies. His mentorship has been pivotal in shaping my academic journey. Furthermore, I extend my sincere appreciation to Prof. Adrian Gerlich for his significant contributions to material science, which greatly enriched this endeavor. Additionally, I thank Prof. Pascal Etman for his insightful guidance during the initial stages of my research in Canada, empowering me to make informed decisions and chart the course of my work.

Special gratitude is due to Mohammad Farshidianfar, whose prior research and laboratory expertise provided the foundation for this project, and to Lucas Botelho, with whom I collaborated extensively in conducting experiments. Their continuous assistance significantly enhanced the quality of this research. Furthermore, I am thankful to all the technicians in the Mechatronics Vehicle Systems Lab for their technical expertise, particularly during troubleshooting moments, which were crucial in overcoming challenges and ensuring the success of my endeavors.

Beyond my academic mentors and colleagues, I extend heartfelt thanks to my partner, Parnika, for her enduring encouragement and love, which have been a constant source of strength. I am deeply thankful to my lifelong friends, whose steadfast confidence in me has been a cornerstone of my perseverance, propelling me forward even in the face of adversity. Immense gratitude goes to my parents, Henk and Lea, and my sister, Jannette, for their boundless love, sacrifices, and unwavering support, which have significantly contributed to my success and guided my life's trajectory. Special recognition is reserved for Gerard Janssen, my special education teacher, whose dedication and faith in my abilities have been a lasting source of inspiration on my educational journey.

Lastly, warm thanks to my entire family and all those who stood by me, providing persistent encouragement, serving as an enduring source of motivation.

Dedication

To my beloved parents,

Who believed in me when others doubted, who inspired me to follow my dreams, and who taught me the power of perseverance.

This thesis is a testament to your unwavering support, guiding me from special education to the culmination of my academic journey with a Ph.D. earned in a foreign country.

Your encouragement and belief in me have been instrumental every step of the way.

Table of Contents

Examining Committee ii

Author's Declaration iii

Statement of Contributions iv

Abstract v

Acknowledgements vii

Dedication viii

List of Figures xv

List of Tables xxii

List of Abbreviations xxv

List of Symbols xxvii

1 Introduction **1**

1.1 Motivation . . . 1

1.2 Laser Material Processing . . . 3

1.2.1 Laser Heat Treatment . . . 3

1.2.2 Laser-Directed Energy Deposition . . . 4

1.3 Statement of Objectives and Scope . . . 6

1.4 Thesis Overview . . . 7

2 Literature Review and Background **9**

2.1 Effect of Process Parameters on Material Characteristics . . . 11

2.1.1 Porosity . . . 11

2.1.2 Hardness . . . 12

2.1.3 Surface Roughness . . . 13

2.1.4 Residual Stress . . . 14

2.1.5 Microstructure . . . 15

2.1.6 Tensile Strength . . . 16

2.1.7 Fatigue Behavior . . . 17

2.1.8 Wear Resistance . . . 18

2.1.9 Dimensional Accuracy . . . 19

2.1.10 Summary . . . 21

2.2 Process Modeling in Laser Material Processing . . . 22

2.2.1 Analytical Modeling . . . 22

2.2.2 Numerical Modeling . . . 24

2.2.3 Empirical Modeling . . . 27

2.2.4 Machine Learning 29
2.2.5 Summary 30
2.3 Process Monitoring in Laser Material Processing 32
2.3.1 Thermal Monitoring 32
2.3.2 Vision Monitoring 33
2.3.3 Acoustic Monitoring 34
2.3.4 Spectral Monitoring 35
2.3.5 Summary 36
2.4 Process Control in Laser Material Processing 37
2.4.1 Classical Process Control Techniques 37
2.4.2 Modern Process Control Techniques 39
2.4.3 Summary 44
2.5 Chapter Summary 45

3 Experimental Setup and Thermal Monitoring 47
3.1 Experimental Setup for Research on Laser Material Processing 48
3.2 Thermal Dynamics Monitoring 51

4 Thermal Dynamic Modeling for Laser Material Processing 56
4.1 Two-Dimensional Adaptive Thermal Model 57
4.1.1 2D Dynamic Model 57
4.1.2 2D Finite Difference Model 60
4.1.3 2D Adaptive Thermal Model 65
4.1.4 Summary 68

4.2 One-Dimensional Adaptive Thermal Model 69
4.2.1 1D Dynamic Model 69
4.2.2 1D Finite Difference Model 71
4.2.3 1D Adaptive Thermal Model 77
4.2.4 Advantages of the 1D Adaptive Thermal Model 81
4.2.5 Summary 84
4.3 Chapter Summary 85

5 Model Predictive Control for Laser Material Processing 86
5.1 SISO Model Predictive Control for LHT 88
5.1.1 SISO State-Space Model Formulation 89
5.1.2 SISO Optimization Problem Formulation 91
5.1.3 SISO MPC Implementation 95
5.2 MIMO Adaptive Model Predictive Control for LDED 96
5.2.1 MIMO State-Space Model Formulation 96
5.2.2 MIMO Optimization Problem Formulation 102
5.2.3 MIMO AMPC Implementation 105
5.3 Chapter Summary 107

6 Experiments 108
6.1 Real-Time Thermal Dynamic Prediction Experiments 109
6.1.1 2D Adaptive Thermal Model Predictions in LHT 109
6.1.2 1D Adaptive Thermal Model Predictions in LDED 112
6.1.3 Model Performance Evaluation 114

6.2 Real-Time Microstructure Control Experiments . . . 115
6.2.1 Closed-Loop LHT Process with MPC . . . 115
6.2.2 Closed-Loop LDED Process with AMPC . . . 118
6.2.3 Controller Performance Evaluation . . . 121
6.3 Chapter Summary . . . 122

7 Results and Discussions **123**
7.1 Real-Time Thermal Dynamic Prediction Experiments Results . . . 124
7.1.1 2D Adaptive Thermal Model Predictions in LHT . . . 124
7.1.2 1D Adaptive Thermal Model Predictions in LDED . . . 137
7.2 Real-Time Microstructure Control Experiments Results . . . 142
7.2.1 Closed-Loop LHT Process with MPC . . . 142
7.2.2 Closed-Loop LDED Process with AMPC . . . 154
7.3 Chapter Summary . . . 177

8 Conclusions and Future Work **179**
8.1 Conclusions . . . 179
8.2 Future Work . . . 183

Letter of Copyright Permission **185**

References **188**

APPENDICES **217**

A Laser Heat Treatment Process Parameters **218**
A.1 Thermal Dynamic Predictions in LHT with a 2D Adaptive Thermal Model 218

B Laser Heat Treatment Experiments Results **220**

B.1 Real-Time Thermal Dynamic Prediction Experiments Results with a CS Substrate 220

B.2 Real-Time Thermal Dynamic Prediction Experiments Results with an SS Substrate 225

C Directed Energy Deposition Experiments Results **230**

C.1 Real-Time Thermal Dynamic Prediction Experiments Results 230

C.2 Vickers Hardness Measurements of the LDED Wall Experiments 234

List of Figures

1.1 Schematic of the laser heat treatment process. 4

1.2 Schematic of the laser-directed energy deposition process. 5

3.1 Experimental setup at the ALFa laboratory of the UW for conducting LHT and LDED experiments. 48

3.2 Experimental setup at the ALFa laboratory of the UW used for conducting LHT experiments (on the right) and LDED experiments (on the left). . . 49

3.3 Typical temperature distribution for LHT (on the left) and LDED (on the right). 52

3.4 Temperature measurement visualization, including pixel tracking relative to a specific point on the workpiece surface. 53

3.5 Spatial cooling rate using two temperature points within the HAZ from a single image. 54

4.1 IPG-1000-IC laser beam, captured using IPG's laser diagnostics software. 60

4.2 Schematic representation of the nodal network for the 2D FD model of the LHT process. 61

4.3 Visualization of the HAZ during a typical LDED process. The right border (in green) indicates the region of the melt pool, and the left border (in yellow) indicates the solidified region. The white center line denotes the direction of movement during the process. 70

4.4 Schematic representation of the nodal network for the 1D FD conduction model of the L-DED process. 72

4.5 Illustration of the LDED process highlighting the melt pool and the nodal network projected onto the solidified region, along with a temperature graph corresponding to the model's temperature predictions. 73

5.1 MPC block diagram used to control the peak temperature during LHT. . 95

5.2 AMPC block diagram used to control the process inputs during LDED. . 106

6.1 Single-track LHT experimental case and substrate dimensions. 109

6.2 Single-track LDED experimental case. 112

6.3 The LDED process inputs used for the adaptive 1D thermal model validation. The solid red line represents laser power, and the dashed blue line represents traveling speed. 113

6.4 Multi-track LHT experimental case with adjacent tracks, top view (left), side view (right). 116

6.5 Single-track LHT experimental case on a substrate with variable thickness, top view (top), front view (bottom). 116

6.6 Five-layer LDED wall experimental case. 119

7.1 Carbon steel substrate featuring all five single LHT tracks. 124

7.2 Stainless steel substrate featuring all five single LHT tracks. 125

7.3 Real-time peak temperature and spatial cooling rate comparison between the 2D non-adaptive thermal model predictions and the LHT process measurements of the v_{ramp} experiment with a carbon steel substrate. 126

7.4 Real-time peak temperature and spatial cooling rate comparison between the 2D non-adaptive thermal model predictions and the LHT process measurements of the P_{step} experiment with a stainless steel substrate. 128

7.5 Real-time peak temperature and spatial cooling rate comparison between the 2D adaptive thermal model predictions and the LHT process measurements of the v_{ramp} experiment with a carbon steel substrate. 131

7.6 Real-time parameter estimation of the v_{ramp} experiment with a carbon steel substrate. 131

7.7 Real-time peak temperature and spatial cooling rate comparison between the 2D adaptive thermal model predictions and the LHT process measurements of the P_{step} experiment with a stainless steel substrate. 133

7.8 Real-time parameter estimation of the P_{step} experiment with a stainless steel substrate. 133

7.9 Carbon steel substrate showing the four LDED experiments, each depositing a single track with a different deposited material. 138

7.10 Real-time temperature and spatial cooling rate comparison between the adaptive 1D thermal model predictions and the LDED process measurements of the experiment with Stellite® 6 powder. 139

7.11 Real-time parameter estimation of the experiment with Stellite® 6 powder. 139

7.12 Carbon steel substrate featuring a single LHT track, processed with a closed-loop controlled temperature using a step setpoint. 143

7.13 Peak temperature and traveling speed results of the closed-loop single-track experiment with a step setpoint temperature and a constant laser power of 300 W. 143

7.14 Carbon steel substrate featuring six adjacent LHT tracks, processed with closed-loop controlled peak temperature. 145

7.15 Carbon steel substrate featuring six adjacent LHT tracks, processed in open-loop. 145

7.16 Peak temperature and traveling speed results of the open-loop multi-track experiment with constant laser power of 300 W and a constant traveling speed of 3.33 mm/sec 146

7.17 Peak temperature and traveling speed results of the closed-loop multi-track experiment with constant laser power of 300 W. 147

7.18 Carbon steel substrate featuring two single LHT tracks: one processed in open-loop and the other with closed-loop controlled temperature. 149

7.19 Peak temperature and traveling speed results of the open-loop single-track experiment with a variable substrate thickness, a constant laser power of 300 W, and a constant traveling speed of 3.33 mm/sec. 150

7.20 Peak temperature and traveling speed results of the closed-loop single-track experiment with a variable substrate thickness and a constant laser power of 300 W. 150

7.21 Carbon steel substrate with two five-layer LDED wall experiments: one in open-loop and the other with closed-loop temperature control. 154

7.22 Carbon steel substrate with two five-layer LDED wall experiments: one with closed-loop controlled spatial cooling rate and the other with simultaneous closed-loop controlled temperature and spatial cooling rate. . . . 154

7.23 Temperature and spatial cooling rate results of the five-layer LDED wall experiment in open-loop. 155

7.24 Melt pool edge position at 1200 °C during the five-layer LDED wall experiment in open-loop. 156

7.25 Hardness measurements from the three cross sections of the five-layer LDED wall experiment in open-loop. 157

7.26 Temperature and spatial cooling rate results of the five-layer LDED wall experiment with closed-loop controlled temperature. 158

7.27 Real-time parameter estimation of the five-layer LDED wall experiment with closed-loop controlled temperature. 160

7.28 Melt pool edge position at 1200 °C during the five-layer LDED wall experiment with closed-loop controlled temperature. 161

7.29 Hardness measurements from the three cross sections of the five-layer LDED wall experiment with closed-loop controlled temperature. 162

7.30 Temperature and spatial cooling rate results of the five-layer LDED wall experiment with closed-loop controlled spatial cooling rate. 163

7.31 Melt pool edge position at 1200 °C during the five-layer LDED wall experiment with closed-loop controlled spatial cooling rate. 164

7.32 Hardness measurements from the three cross sections of the five-layer LDED wall experiment with closed-loop controlled spatial cooling rate. . 165

7.33 Temperature and spatial cooling rate results of the five-layer LDED wall experiment with closed-loop controlled temperature and spatial cooling rate. 167

7.34 Real-time parameter estimation of the five-layer LDED wall experiment with simultaneous closed-loop controlled temperature and spatial cooling rate. 168

7.35 Melt pool edge position at 1200 °C during the five-layer LDED wall experiment with simultaneous closed-loop controlled temperature and spatial cooling rate. 168

7.36 Hardness measurements from the three cross sections of the five-layer LDED wall experiment with closed-loop controlled temperature and spatial cooling rate. 169

7.37 DIC deposition height measurements across deposition length for of all four five-layer LDED wall experiments. 173

7.38 Mean hardness measurements from the three cross sections of all four five-layer LDED wall experiments. 174

B.1 Real-time peak temperature and cooling rate comparison between the 2D adaptive thermal model predictions and the LHT process measurements during the *Const* experiment with a carbon steel substrate. 221

B.2 Real-time parameter estimation during the *Const* experiment with a carbon steel substrate. 221

B.3 Real-time peak temperature and cooling rate comparison between the 2D adaptive thermal model predictions and the LHT process measurements during the P_{ramp} experiment with a carbon steel substrate. 222

B.4 Real-time parameter estimation during the P_{ramp} experiment with a carbon steel substrate. 222

B.5 Real-time peak temperature and cooling rate comparison between the 2D adaptive thermal model predictions and the LHT process measurements during the P_{step} experiment with a carbon steel substrate. 223

B.6 Real-time parameter estimation during the P_{step} experiment with a carbon steel substrate. 223

B.7 Real-time peak temperature and cooling rate comparison between the 2D adaptive thermal model predictions and the LHT process measurements during the v_{step} experiment with a carbon steel substrate. 224

B.8 Real-time parameter estimation during the v_{step} experiment with a carbon steel substrate. 224

B.9 Real-time peak temperature and cooling rate comparison between the 2D adaptive thermal model predictions and the LHT process measurements during the *Const* experiment with a stainless steel substrate. 225

B.10 Real-time parameter estimation during the *Const* experiment with a stainless steel substrate. 226

B.11 Real-time peak temperature and cooling rate comparison between the 2D adaptive thermal model predictions and the LHT process measurements during the P_{ramp} experiment with a stainless steel substrate. 226

B.12 Real-time parameter estimation during the P_{ramp} experiment with a stainless steel substrate. 227

B.13 Real-time peak temperature and cooling rate comparison between the 2D adaptive thermal model predictions and the LHT process measurements during the v_{ramp} experiment with a stainless steel substrate. 227

B.14 Real-time parameter estimation during the v_{ramp} experiment with a stainless steel substrate. 228

B.15 Real-time peak temperature and cooling rate comparison between the 2D adaptive thermal model predictions and the LHT process measurements during the v_{step} experiment with a stainless steel substrate. 228

B.16 Real-time parameter estimation during the v_{step} experiment with a stainless steel substrate. 229

C.1 Real-time temperature and spatial cooling rate comparison between the 1D adaptive thermal model predictions and the L-DED process measurements during the experiment with Inconel 625 powder. 231

C.2 Real-time parameter estimation during the experiment with Inconel 625 powder. 231

C.3 Real-time temperature and spatial cooling rate comparison between the 1D adaptive thermal model predictions and the L-DED process measurements during the experiment with H13 Tool Steel powder. 232

C.4 Real-time parameter estimation during the experiment with H13 Tool Steel powder. 232

C.5 Real-time temperature and spatial cooling rate comparison between the 1D adaptive thermal model predictions and the L-DED process measurements during the experiment with Stainless Steel 431 powder. 233

C.6 Real-time parameter estimation during the experiment with Stainless Steel 431 powder. 233

C.7 Boxplot with the Hardness measurements across deposition heights from the three cross sections of the five-layer L-DED wall experiment in open-loop. 234

C.8 Boxplot with the Hardness measurements across deposition heights from the three cross sections of the five-layer L-DED wall experiment with closed-loop controlled temperature. 234

C.9 Boxplot with the Hardness measurements across deposition heights from the three cross sections of the five-layer L-DED wall experiment with closed-loop controlled spatial cooling rate. 235

C.10 Boxplot with the Hardness measurements across deposition heights from the three cross sections of the five-layer L-DED wall experiment with closed-loop controlled temperature and spatial cooling rate. 235

List of Tables

6.1 LHT substrate material specifications. 110

6.2 The five distinct LHT experiment cases conducted for both substrate materials, each with a track length (L_{track}) of 135 mm. 111

6.3 LDED substrate material specifications. 112

6.4 LDED deposition powder specifications. 114

6.5 Substrate specifications of the three experiment cases. 117

6.6 Controller setpoints for the three LHT experiment cases with constant laser power. 117

6.7 Controller setpoints and open-loop process inputs for the four LDED wall experiment cases. 120

6.8 LDED substrate material specifications. 120

6.9 LDED deposition powder specifications. 120

7.1 MAPE of the 2D non-adaptive thermal model with respect to the LHT process after the experiments with a carbon steel substrate. 127

7.2 MAPE of the 2D non-adaptive thermal model with respect to the LHT process after the experiments with a stainless steel substrate. 129

7.3 MAPE of the 2D adaptive thermal model with respect to the LHT process after the experiments with a carbon steel substrate. 132

7.4 MAPE of the 2D adaptive thermal model with respect to the LHT process after the experiments with a stainless steel substrate. 134

7.5 MAPE of the adaptive 1D thermal model with respect to the LDED process after the LDED experiments with all four powders. 140

7.6 Microscopic images at cross section 2 and 5 of the closed-loop single-track experiment with a step setpoint temperature. 144

7.7 Hardness measurements of the closed-loop single-track experiment with a step setpoint temperature. 144

7.8 Microscopic images at cross section 2 of all six tracks from the open-loop and closed-loop multi-track experiment. 148

7.9 Hardness measurements of both LHT multi-track experiments. 148

7.10 Microscopic images at cross section 2 and 5 of the open-loop and closed-loop single-track experiment with a variable substrate thickness. 151

7.11 Hardness measurements of the single-track open-loop and closed-loop experiment with a variable substrate thickness. 152

7.12 Comparison of melt pool evolution across deposition layers for all four LDED Experiments. 171

A.1 The process parameters of the five different LHT experiment cases conducted with the carbon steel substrate. 218

A.2 The process parameters of the five different LHT experiment cases conducted with the stainless steel substrate. 219

List of Abbreviations

1D	one-dimensional v, 7, 56, 87, 112, 124, 180
2D	two-dimensional v, 7, 56, 87, 109, 124, 179
3D	three-dimensional 4
AE	acoustic emission 35
AM	additive manufacturing 4
AMPC	adaptive model predictive control v, 3, 10, 87, 118, 154, 179
ANN	artificial neural network 25
CCD	charge-coupled devices 33
CMOS	complementary metal-oxide-semiconductor 34
CNC	computer numerical control 48
CNN	convolutional neural network 29
CT	computer tomography 12
DIC	digital image correlation 173
EMPC	explicit model predictive control 88
FD	finite difference 57
FDM	finite difference model 26, 82
FEM	finite element model 24, 82
HAZ	heat-affected zone 3, 26, 48, 57
HIP	hot isostatic pressing 11
HT	heat treatment 14

IR	infrared 26, 50, 60, 129
LAM	laser additive manufacturing 1, 9
LDED	laser-directed energy deposition v, 1, 9, 48, 56, 97, 109, 124, 180
LHT	laser heat treatment v, 1, 9, 48, 56, 87, 109, 124, 179
LMP	laser material processing v, 1, 9, 47, 56, 86, 108, 137, 179
LPBF	laser powder bed fusion 23
LQT	linear quadratic tracking 26
LW	laser welding 1, 9
MAPE	mean absolute percentage error 114, 126
MIMO	multi-input multi-output vi, 40, 87, 118, 142
ML	machine learning 22
MPC	model predictive control v, 3, 42, 76, 86, 108, 123, 179
NMPC	nonlinear model predictive control 88
NN	neural network 29
OES	optical emission spectroscopy 35
PDE	partial differential equation 57
PID	proportional-integral-derivative 10
QP	quadratic programming 95
$\mathbf{R_a}$	surface roughness 13
RMPC	robust model predictive control 42, 88
SISO	single-input single-output v, 37, 87, 119, 166
SLM	selected laser melting 11
TT	tribological testing 18
UTS	ultimate tensile strength 16
VIR	vision and infrared 50

List of Symbols

$\mathbf{A}$	State space state matrix 89
$\mathbf{B}$	State space input matrix 89
$\mathbf{C}$	State space output matrix 89
c_p	Specific heat capacity 57, 58, 71
c_v	Volumetric heat capacity 58, 64–66
$\mathbf{d}$	Constraint vector representing the quadratic constraints 94, 105
$\mathbf{E}$	Error vector between model predictions and process measurements 78
$\mathbf{F}$	Quadratic term matrix used in the quadratic objective function 93, 104
Fo	Finite-difference form of the Fourier number 63, 67, 75
$\mathbf{G}$	Prediction matrix representing the relationship between the state vector and the predicted output 93, 104
$h_\mathrm{c,r}$	Convection and radiation constant 59, 64–66
J	Objective function to be minimized in an optimization problem 91, 102
k	Thermal conductivity 57, 64–66, 71
M	Number of model nodes in the m-direction 61, 76

m	Horizontal nodal coordinate axis 61, 72
N	Number of model nodes in the n-direction 61
n	Vertical nodal coordinate axis 61
N_{c}	Control horizon 91, 92, 102
N_{p}	Prediction horizon 91, 92, 97, 99, 102
$\mathbf{P}$	Terminal weighting matrix penalizing deviations from desired states or objectives 91, 101
p	Single time frame 52, 55, 62, 63, 66, 67, 74, 76, 78, 79, 89, 91–94, 97–100, 103, 104
P	Laser power 60, 71, 75, 90
$\mathbf{Q}$	Weighting matrix penalizing deviations from desired states or objectives 66, 78, 92
$Q_{\mathrm{conv/rad}}$	Combined heat transfer by convection and radiation 58
Q_L	Total energy input from the laser 57, 59, 63
$\mathbf{R}$	Weighting matrix penalizing rate of change of the optimization variables 67, 79, 93
T	Temperature 52, 54, 57–59, 61–66, 72, 74–76
t	Time 52, 57, 62, 71
$\mathbf{T}$	Vector with all model states 78
ΔT	Change in temperature 52, 54
Δt	Change in time 52–54, 62, 64, 76
$\Delta\dot{T}$	Cooling rate 52
∇T	Spatial cooling rate 55, 65, 76
$\Delta\mathbf{U}$	Changer in process inputs vector over the control horizon 92–94, 102–104
$\mathbf{u}$	Process inputs vector 89, 90, 100–102, 104
$\Delta\mathbf{u}$	Changer in process inputs vector 91, 104
v	Traveling speed 53, 55, 57, 59, 75, 76, 90, 97, 101

$\mathbf{W}$	Coefficient matrix representing the quadratic constraints 94, 105
x	Horizontal coordinate axis 55, 57, 58, 61–64, 67, 71, 72, 76, 77
Δx	Change in the x-direction 54, 61, 64, 65, 72, 76
$\mathbf{x}$	State vector 89
y	Vertical coordinate axis 61–64, 67, 77, 102
Δy	Change in the y-direction 61, 64, 65
$\mathbf{Y}$	Predicted output vector over the prediction horizon 92, 93, 102, 103
$\mathbf{y}$	Predicted output vector 89–91, 102
$\mathbf{y}_{\text{ref}}$	Reference output vector 91
$\mathbf{Y}_{\text{ref}}$	Reference output vector over the prediction horizon 92, 102
α	Thermal diffusivity 75–78
β	Model output boundary tuning parameter 75, 77, 78
η	Order of the Gaussian profile 60
$\mathbf{\Gamma}$	Control matrix governing the influence of process inputs on the predicted outputs 93, 103
γ	Model input boundary tuning parameter 75, 77, 78
μ	Laser absorption coefficient 60
$\mathbf{\Phi}$	Prediction matrix representing the relationship between the state vector and the predicted output 93, 103
ρ	Material density 57, 58, 71
θ	Vector with the material constants/model parameters 66, 78, 80
$\Delta\theta$	Vector with the change in material constants/model parameters 67, 79, 80
ζ	Heat input location correction factor 71

"All our dreams can come true if we have the courage to pursue them, for there is nothing impossible to him who will try."

— Walt Disney; Alexander the Great

Chapter 1

Introduction

1.1 Motivation

Laser material processing (LMP) leads advanced manufacturing, transforming traditional methods across industries. Originating with laser cutting, known for its exceptional accuracy and efficiency in cutting materials, LMP has evolved into a multifaceted domain encompassing numerous advanced processes. Among these is laser heat treatment (LHT), a method that revolutionizes heat treatment by enabling precise tailoring of material properties through controlled heating and rapid cooling in specific regions. This approach enhances surface hardness and wear resistance while preserving the bulk material's integrity. Following LHT, laser welding (LW) has emerged as a cornerstone technique in LMP, offering unparalleled precision in joining materials with minimal distortion. By harnessing the focused energy of lasers, LW ensures high-quality welds, making it indispensable across industries where structural integrity is paramount. At the pinnacle of LMP stands laser additive manufacturing (LAM), such as laser-directed energy deposition (LDED). This advanced technique allows for layer-by-layer manufacturing of complex components with exceptional design freedom and geometrical intricacy. By enabling additive buildup, LAM overcomes the limitations of traditional subtractive methods, advancing manufacturing capabilities and product innovation.

Despite the remarkable advantages and capabilities of LMP processes, achieving consistent and reproducible material characteristics remains one of the most significant challenges. These challenges are especially evident in advanced processes such as LHT, LW, and LDED. In these methods, the intricate interplay between process parameters and material characteristics presents a formidable barrier to achieving uniform product quality. Furthermore, the vast array of process parameters, each with its own complex interactions and influences on material properties, exacerbates these challenges. Even slight deviations in process conditions can result in significant variations in material properties, hampering the scalability, reliability, and widespread adoption of LMP processes. These challenges emphasize the urgent need for advanced process control strategies capable of real-time prediction and control of the thermal dynamics during LMP.

While conventional control methods, such as proportional-integral-derivative controllers, have been instrumental in certain aspects of process control, they offer limited predictive capabilities and struggle to anticipate the complex interactions inherent in LMP processes. In addition, the vast array of LMP process parameters and their intricate interactions often overwhelm conventional methods, making it practically impossible to effectively control the numerous process parameters simultaneously. As a result, these methods struggle to anticipate the nuanced influences of each parameter on material properties. In contrast, model-based control strategies, particularly those leveraging numerical models, hold immense promise in addressing these limitations by providing a more comprehensive understanding of the complex process dynamics.

Numerical models can accurately predict various aspects of LMP processes, including peak temperatures, cooling rates, melt pool dimensions, microstructural evolution, residual stresses, and distortion in the manufactured parts. These factors are crucial for achieving consistent material characteristics and ensuring reproducibility. However, the practical implementation of numerical models in real-time control applications has been hindered by computational challenges. Many existing numerical models, while theoretically robust, face practical limitations due to their demanding computational requirements. Despite their potential to accurately correlate process parameters with material properties, these models often fall short when it comes to real-time control applications.

To address this challenge, this research aims to develop a novel adaptive model predictive control (AMPC) algorithm specifically designed for real-time microstructure control in LMP. This involves combining existing model predictive control (MPC) techniques with efficient numerical models capable of accurately predicting crucial thermal dynamics, specifically the temperatures and cooling rates within the heat-affected zone (HAZ) of LMP processes. The ultimate goal is to effectively leverage these predictive models with MPC techniques, enabling real-time model-based control of thermal dynamics to achieve consistent and reproducible material characteristics.

1.2 Laser Material Processing

LMP processes represent an advanced field in manufacturing, utilizing concentrated energy sources to modify material properties or fuse materials. This section examines two distinct LMP processes, namely LHT and LDED, which are the focal points of this research. LHT involves using a laser to modify the properties of metal substrates, while LDED employs a laser for layer-by-layer fabrication using melted and fused metal powder.

1.2.1 Laser Heat Treatment

LHT is an advanced surface modification process that enhances the performance of metallic components through the precise rapid heating and cooling of localized areas [1]. This process significantly improves surface properties, including hardness, strength, wear resistance, and fatigue life. LHT uses a focused laser beam directed at the workpiece's outer surface, as illustrated in Figure 1.1. The laser induces controlled heating to create a HAZ at a specific temperature. Shielding gas from the nozzle prevents oxidation by protecting the HAZ from reacting with oxygen at high temperatures [2]. The adjacent material acts as a heat sink, rapidly cooling the area and forming a heat-treated track as the workpiece moves. Importantly, this method selectively alters only the material properties at the HAZ, leaving the base material unchanged. As a result, locally altered surface properties can be achieved. For example, in the tool and die manufacturing industry, LHT is

applied for the heat treatment of molds, dies, and cutting tools. The localized heating can be tailored to specific areas, enhancing hardness and wear resistance where needed, resulting in tools with an extended lifespan and improved performance.

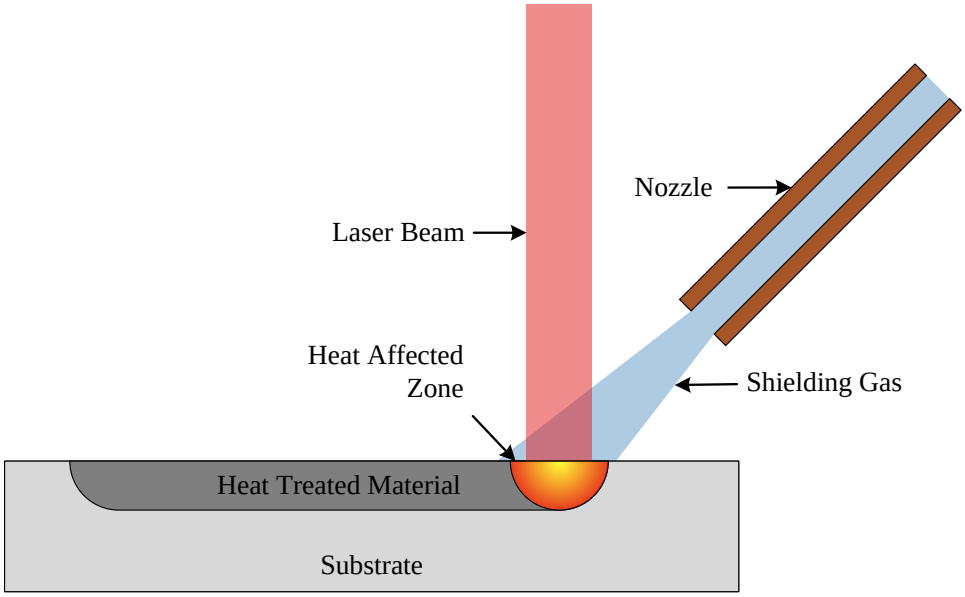


Figure 1.1: Schematic of the laser heat treatment process.

1.2.2 Laser-Directed Energy Deposition

LDED is a subset of additive manufacturing (AM), which is a process to create three-dimensional (3D) objects from digital 3D models by depositing material layer by layer [3]. AM is a rapidly growing industry due to its distinctive advantage in manufacturing complex parts that were unable to be manufactured efficiently or at all using traditional manufacturing methods [4]. LDED is an AM process in which a focused laser beam is directed onto a substrate surface, as illustrated in Figure 1.2. At the substrate surface, the laser simultaneously melts and fuses both the substrate material and the added feedstock material. Afterwards, the melt pool rapidly solidifies and cools down near the HAZ, resulting in a deposition with very high bonding strength [5]. Also, shielding gas is applied with the powder to prevent oxidation of the deposited material.

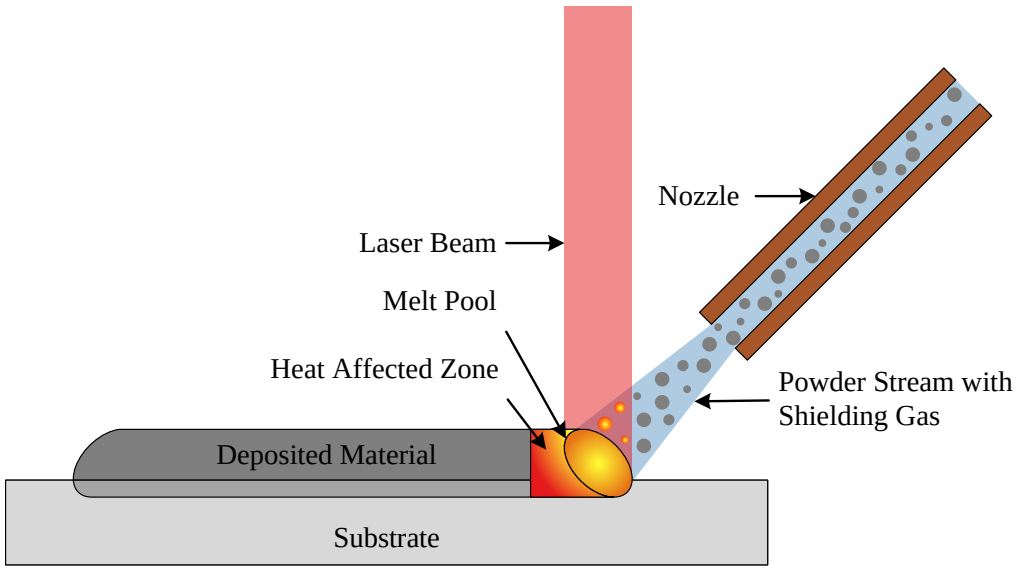


Figure 1.2: Schematic of the laser-directed energy deposition process.

LDED stands out as a versatile additive manufacturing method due to its wide range of capabilities. LDED deposits material locally layer-by-layer and can achieve very high position rates. This allows for the rapid buildup of material, which enables the manufacturing of very large parts. For instance, in the aerospace industry, LDED is utilized to manufacture large components like rocket nozzles, where intricate designs and material strength are crucial. LDED allows for precise control over the deposition process. This precision enables the precise deposition of material in specific areas, making it ideal for repairing localized damage or wear on existing components. For example, in the automotive industry, LDED is utilized for repairing critical components such as gears and molds. LDED can work with a large range of materials, including metals, alloys, and some composites. This versatility allows for the application of coatings tailored to meet specific requirements, such as wear resistance, corrosion resistance, or thermal properties. To illustrate, in the oil and gas industry, LDED is used for coating surfaces on parts that are exposed to harsh environments. This includes coatings for pipelines, valves, and drilling equipment to enhance their resistance to corrosion and wear.

1.3 Statement of Objectives and Scope

The main objective of this research is to:

"Develop an AMPC algorithm suitable for real-time control of thermal dynamics in LMP processes, with the goal of indirectly controlling the microstructure through real-time monitoring, prediction, and control of thermal dynamics."

To achieve this goal, it is necessary to understand the thermal dynamics during the LMP processes and how the process inputs, such as the traveling speed and the laser power, affect the thermal dynamic features, such as temperatures and cooling rates within the HAZ. This understanding is crucial because the thermal dynamics directly influence the material's microstructure. A real-time monitoring system using an infrared camera is employed to observe the process and gather essential data on the thermal dynamics. Thermal dynamic models are developed to establish the relationship between process inputs and thermal dynamics while also considering how these dynamics impact microstructure evolution. Furthermore, adaptive model optimization algorithms are developed to enhance the prediction accuracy of the models in real-time. In addition, MPC strategies are devised to use these thermal dynamic models to optimize process control inputs in real-time. Subsequently, the monitoring system, prediction model, model optimization algorithm, and control algorithm are integrated into an AMPC algorithm, which provides real-time control of both the thermal dynamics and the resulting microstructure in LMP.

This controller will enable fully automated LMP, leading to a substantial improvement in the consistency and quality of the final product's microstructure. Additionally, this controller will minimize, if not completely eliminate, the reliance on post-processing steps such as heat treatment, stress relief, and homogenization treatment to achieve the desired microstructure. Moreover, the controller serves as an effective manufacturing tool, enabling the simultaneous control of multiple process inputs to achieve the desired material characteristics, which significantly reduces the reliance on excessive trial-and-error experimentation.

1.4 Thesis Overview

This thesis is divided into the following seven chapters:

Chapter 2 offers a comprehensive review of the literature on microstructure control in LMP. It explores key topics including material characteristics, process monitoring, process modeling, and process control. These areas are essential for the development of AMPC algorithms in LMP.

Chapter 3 provides detailed insights into the experimental setup utilized in this research, which is located at the Automated Laser Fabrication laboratory of the University of Waterloo, including the configuration and components of the setup. Furthermore, this chapter explains the details of the thermal monitoring system and how the thermal dynamics are monitored in real-time.

Chapter 4 delves into the development of multiple adaptive thermal models designed to predict thermal dynamics in LMP. These models, including both one-dimensional (1D) and two-dimensional (2D) variants, are constructed using partial differential equations describing heat transfer in the process. The finite difference method is then applied to solve these equations. Additionally, nonlinear optimization algorithms, coupled with thermal imaging, are utilized to enable real-time optimization of model parameters, thereby improving the prediction accuracy and adaptability of the developed thermal models.

Chapter 5 introduces multiple MPC algorithms designed for real-time control of thermal dynamics during LMP to indirectly optimize the material's microstructure. The first algorithm is based on the non-adaptive 2D model developed in Chapter 4, resulting in a linear MPC algorithm. The second algorithm utilizes the 1D adaptive model developed in Chapter 4, resulting in an adaptive MPC algorithm. These controllers are developed by transforming the two thermal dynamic models into state-space models. Using these models, quadratic optimization problems are formulated to reduce the error between the actual and reference states. This enables precise control of the thermal dynamics during LMP processes, ultimately yielding a consistent microstructure.

Chapter 6 outlines the validation experiments that are designed to validate the models developed in Chapter 4 and the MPC algorithm developed in Chapter 5. This chapter details the experimental procedure, including the process conditions, materials, model parameters, and sample preparation utilized in these experiments.

Chapter 7 presents a thorough analysis of the results obtained from the validation experiments outlined in Chapter 6. This chapter provides insights into the performance of the developed models and MPC algorithms in experimental settings representative of industrial LMP applications. Additionally, this chapter explores the implications of the findings and their significance in advancing the understanding and application of thermal dynamics control in laser material processing.

Chapter 8 concludes the thesis with a comprehensive examination of the research findings and their implications. Furthermore, potential directions for future research and improvements to the methodologies outlined in earlier chapters are proposed. This chapter provides a reflective analysis of the study's accomplishments and lays the groundwork for continued advancements in the field of LMP.

Chapter 2

Literature Review and Background

Laser material processing (LMP) has emerged as a transformative technology in modern manufacturing, reshaping traditional fabrication methods across diverse industries. Originating with laser cutting, which demonstrated the capability to precisely cut through various materials with exceptional accuracy and efficiency [6, 7], LMP has evolved into a multifaceted domain encompassing numerous advanced processes. Among these is laser cleaning, which uses a laser instead of a stream of abrasive material for the cleaning process, resulting in a clean surface without affecting the underlying material [8]. Laser heat treatment (LHT) enables precise alteration of material characteristics at localized regions, enhancing surface hardness and wear resistance while preserving the material properties of the bulk material [9, 1]. Laser welding (LW) has emerged as a cornerstone technique in LMP, offering unparalleled precision in joining materials with minimal distortion [10]. At the pinnacle of LMP stands laser additive manufacturing (LAM), such as laser-directed energy deposition (LDED), enabling the layer-by-layer manufacturing of complex components with unprecedented design freedom and geometrical intricacy [11].

Despite the remarkable advantages and capabilities of LMP processes, achieving consistent and reproducible material characteristics remains one of the most significant challenges [12]. These challenges are especially evident in advanced processes such as LHT, LW, and LAM, where the sheer number of process parameters and their intricate inter-

play on the material characteristics pose a formidable obstacle to achieving consistent product quality [13, 14, 15]. Even slight deviations in process conditions can result in significant variations in material properties [16], undermining the scalability, reliability, and widespread adoption of LMP processes.

To address these challenges and ensure consistent material characteristics in LMP processes, the implementation of automatic or in-situ process control is imperative. While conventional control methods, such as proportional-integral-derivative (PID) controllers, have been instrumental in certain aspects of process control [17, 18], they offer limited predictive capabilities and struggle to anticipate the complex interactions inherent in LMP processes. In contrast, model-based control strategies, particularly those leveraging numerical models, hold immense promise in addressing these limitations by providing a more comprehensive understanding of the complex process dynamics [19].

With these challenges in mind, this literature study aims to explore key aspects of microstructure control within LMP, leveraging real-time monitoring of the thermal dynamics. By investigating material characteristics, process monitoring techniques, process control strategies, and process modeling approaches, this study seeks to establish a foundation for implementing advanced control algorithms, particularly adaptive model predictive control (AMPC) for LMP, to achieve consistent material characteristics, such as consistent hardness. The insights gained from this literature study will offer valuable guidance for the development and application of the AMPC algorithm developed in this work.

2.1 Effect of Process Parameters on Material Characteristics

Understanding how process parameters affect material characteristics is crucial for addressing the challenges associated with LMP. This section investigates the intricate interplay between various process parameters and their impact on material properties and behaviors. Through a comprehensive review of relevant literature, the aim is to uncover key insights into the fundamental aspects of how process parameters influence the material characteristics in LMP, laying the groundwork for a deeper understanding of microstructure control and optimization strategies.

2.1.1 Porosity

Porosity, characterized by the presence of voids within solid substances, significantly impacts the quality and mechanical properties of components produced through LMP [20], such as LW and LAM. In LAM processes like selected laser melting (SLM) and LDED, porosity poses a significant concern, potentially compromising the integrity of fabricated components [21]. Common manifestations of porosity include shrinkage pores, gas pores, and lack of fusion. Shrinkage pores result from inadequate liquid metal supply during solidification, while gas pores occur due to trapped gas between powder particles. Lack of fusion defects stems from the incomplete remelting of solidified layers, leading to incomplete metallurgical bonds.

Mitigating porosity is crucial for enhancing component quality in LMP. Adjusting process parameters such as laser power, scanning or traveling speed, and powder feed rate can effectively reduce porosity-related defects [22]. Moreover, preheating the substrate and employing post-processing techniques like hot isostatic pressing (HIP) have proven effective in alleviating porosity-related issues [23]. HIP involves subjecting fabricated parts to high temperature and pressure in an inert gas environment, consolidating the material, and eliminating porosity, which ultimately improves mechanical properties [24].

Various measurement techniques, including the Archimedes method and X-ray computer tomography (CT), are commonly utilized to quantify porosity and evaluate component quality [25]. The Archimedes method measures fluid displacement upon immersing the component to determine its volume and calculate porosity. Conversely, X-ray CT provides detailed cross-sectional images for precise porosity quantification and assessment of internal features, ensuring the integrity of manufactured parts.

In summary, optimizing process parameters is crucial in LMP to mitigate porosity issues and enhance component quality. By maintaining ideal process parameters throughout the fabrication process, efficient solidification is achieved, gas entrapment is minimized, and complete metallurgical bonds are promoted, ultimately leading to improved mechanical properties of the manufactured part.

2.1.2 Hardness

The hardness of a part is crucial as it determines its resistance to plastic deformation, penetration, indentation, and scratching, thereby influencing its quality and durability. Higher hardness values enhance the resistance to wear from friction or erosion. Indentation tests, including Brinell, Rockwell, and Vickers, are commonly used to assess hardness, with the shape of the indenter being a key differentiator among these tests.

The hardness of parts manufactured via LMP is influenced by various factors, including laser power, scanning or traveling speed, material composition, layer thickness, powder feed rate, and the thermal history during processing. Optimal parameter selection leads to improved hardness, with microstructure refinement being crucial for enhancing mechanical properties [26, 27, 28]. Furthermore, material density, impacted by parameters such as volumetric energy density, also contributes to hardness values [1].

Moreover, the presence of porosity and the relative density of the material significantly influence hardness. Higher porosity levels can lead to decreased hardness, highlighting the importance of controlling process parameters to minimize porosity and achieve desired hardness levels [29]. Additionally, hardness is essential for assessing a material's working

life and durability, particularly in near-surface layers. Despite strict processing conditions in LAM, trace elements such as nitrogen and oxygen can impact hardness, necessitating precise control over processing environments [30].

Overall, hardness testing and process control are integral parts of ensuring the quality and performance of components manufactured through LMP. By understanding the intricate relationship between process parameters and material characteristics, manufacturers can optimize fabrication processes to achieve consistent and desired hardness levels, thereby enhancing the overall quality of fabricated parts.

2.1.3 Surface Roughness

Surface roughness (R_a) represents the average roughness of a surface profile and is a critical parameter in LMP. It is calculated as the arithmetic average of the absolute deviations from the mean line of a surface profile over a specified evaluation length. The equation for calculating R_a is given by:

$$R_a = \frac{1}{L} \int_0^L |y(x)| \, dx$$

where L is the evaluation length, and y(x) represents the surface height as a function of position along the surface.

In LMP, R_a is influenced by a multitude of factors, including material characteristics, process parameters, and post-processing techniques [31]. Achieving R_a values below 1 µm is crucial for high-end applications, necessitating optimization of factors like build angle, layer thickness, and process parameters [32]. Process parameters such as laser power, powder feed rate, and scanning or traveling speed significantly affect surface roughness, with lower R_a associated with higher laser power and scanning or traveling speed [33]. Layer thickness plays a critical role in dimensional accuracy and surface smoothness, with thinner layers enhancing surface quality [34]. Moreover, various factors like particle size, layer thickness, part geometry, and build direction orientation further shape surface roughness in LMP components [35].

In general, R_a values serve as crucial indicators for evaluating fatigue performance, wear resistance, and the overall accuracy of fabricated parts. Techniques such as optimizing process parameters and adjusting building orientations can mitigate surface irregularities caused by improper melting, thereby enhancing the overall quality of fabricated parts.

2.1.4 Residual Stress

Residual stress in LMP presents a significant challenge due to the intricate interplay of localized temperatures and rapid thermal cycles. Predicting and mitigating residual stress necessitates a sophisticated approach involving fine-tuning process parameters and employing stress-alleviating post-processing methods [36]. Thermal and structural stresses arise during LMP, predominantly due to uneven laser heating and subsequent volume changes during solidification [21]. Furthermore, the residual stress is mainly determined by the thermal dynamics of the process, such as the peak temperature and cooling rate [37, 38, 39, 40]. High residual stress levels can significantly alter material properties and lead to defects like warping and cracking, underscoring the critical importance of managing residual stress for ensuring component quality [41]. Mitigating residual stress is essential, particularly for components subjected to high cycle fatigue conditions, where stress-relieving post-processing procedures become crucial. Techniques such as heat treatment (HT) and mechanical treatments offer effective means to alleviate residual stress and enhance component durability [42].

The complexity of residual stress mitigation in LMP underscores the importance of tailored approaches for specific materials and applications. By refining process parameters, integrating process control techniques to control the thermal dynamics, and implementing appropriate post-processing techniques, manufacturers can effectively mitigate RS-related issues, ensuring the production of high-quality components with enhanced mechanical properties.

2.1.5 Microstructure

The microstructure of materials refers to the arrangement and characteristics of their microscopic constituents, such as grains, phases, and defects [43]. It encompasses features at the atomic, molecular, and crystalline levels, influencing the material's overall properties and behavior. In LMP processes, the microstructure plays a crucial role in determining the mechanical properties and performance of the fabricated parts. The intricate interplay of process parameters, including laser power, scanning or traveling speed, and powder characteristics, profoundly influences the resulting microstructure [12]. Fine-tuning these parameters is critical to achieving the microstructural features that meet specific requirements, such as ensuring minimum required strength, fatigue performance, hardness, and other essential properties [44].

Thermal dynamics of the LMP process play the most significant role in shaping the microstructure and properties of fabricated parts [32, 45, 46, 47]. The rapid heating and cooling cycles inherent in LMP contribute to the formation of unique microstructural features, such as cellular dendritic structures and columnar grains [48]. By controlling the thermal dynamics during the fabrication process, engineers can manipulate the microstructure to achieve the desired material properties. For example, by controlling the peak temperature during manufacturing, consistent hardness and hardening depth can be achieved, ensuring uniform mechanical properties throughout the material, particularly for steels [49]. Furthermore, by controlling the cooling rate during fabrication, engineers can induce the formation of specific microstructures within the part, such as martensite in steels, resulting in components with high strength and fatigue performance [17, 18]. Moreover, controlling the cooling rate directly dictates the phase transformation process, thereby allowing for fine adjustments of the hardness and other mechanical properties of the final parts [50].

Post-processing techniques further complement the LMP processes by refining and optimizing the microstructure of fabricated parts. Heat treatments, surface finishing, and mechanical treatments are commonly used to improve material properties, dimensional accuracy, and surface quality. These techniques allow for the removal of residual

stresses, enhancement of mechanical properties, and attainment of specific surface characteristics, contributing to the overall performance and functionality of the manufactured components.

The intricate interplay among process parameters and thermal dynamics significantly shapes the microstructure and properties of parts produced via LMP. By comprehensively understanding the relationship between process parameters and thermal dynamics, engineers can craft tailored microstructural features that precisely meet the performance demands of various applications. This approach guarantees the production of high-quality, functional components with precisely controlled microstructural characteristics.

2.1.6 Tensile Strength

Tensile strength is a fundamental mechanical property crucial for assessing the performance and reliability of materials, particularly in applications where stretching forces are acting on the material. In LMP, understanding the tensile behavior of fabricated components is paramount for ensuring their structural integrity and suitability for diverse operational environments. The evaluation of tensile strength involves measuring the maximum stress a material can withstand before fracturing under tension, providing valuable insights into its structural robustness and load-bearing capacity [51].

In recent studies focusing on LMP-fabricated materials like 316L stainless steel, researchers have conducted comprehensive analyses of tensile properties to decipher the effects of processing parameters and post-processing techniques on material performance [52]. For instance, investigations into the influence of HT temperature on the tensile behavior of 316L stainless steel revealed a notable decrease in yield strength alongside minimal changes in ultimate tensile strength (UTS) [53]. Additionally, the examination of gas-atomized samples highlighted exceptional mechanical qualities characterized by high UTS values, attributed to the presence of fine grains resulting from rapid cooling during fabrication [54].

The intricate relationship between material properties, LMP processing parameters, and post-processing techniques plays a crucial role in determining the tensile strength of components manufactured via LMP. Therefore, optimal parameter selection is essential for ensuring the production of high-quality and high-performance components. By carefully considering and adjusting these factors, engineers can tailor the microstructure and mechanical properties of parts, thereby enhancing their tensile strength and overall performance across various applications.

2.1.7 Fatigue Behavior

Fatigue behavior, the gradual deterioration of materials under cyclic loading, is a critical aspect in evaluating the reliability of engineering components. In LAM manufactured parts, fatigue performance varies depending on orientation, with horizontally built components typically demonstrating superior fatigue life. This variation arises from factors such as component density, residual stress, and microstructure, which are influenced by parameters like volumetric energy density and building direction. Additionally, changes in build direction lead to anisotropy in the microstructure, significantly impacting fatigue performance. Moreover, increased scanning or traveling speed and porosity further reduce fatigue resistance.

LMP processes, such as LAM, involve rapid melting and solidification, creating unique microstructures compared to conventional manufacturing methods. Studies have shown that the cooling rates and thermal gradients present during these processes affect grain size, phase distribution, and the presence of defects such as porosity and microcracks [50, 12]. These microstructural features play a crucial role in determining the fatigue life of LAM manufactured parts. Key process parameters in LAM, such as laser power, scanning or traveling speed, layer thickness, and cooling rate, significantly impact the resulting fatigue properties. For instance, higher laser power and slower traveling speeds generally lead to better fusion between layers but can also increase residual stresses, which negatively affect fatigue performance [55]. Conversely, optimizing these parameters to reduce residual stresses and control microstructure can enhance fatigue life [56, 57].

Residual stresses, inherent in LMP due to localized heating and rapid cooling cycles, can be either tensile or compressive and profoundly affect fatigue behavior. Tensile residual stresses are particularly detrimental, accelerating crack initiation and propagation under cyclic loading [58]. Various post-processing techniques, such as thermal annealing and mechanical peening, have been explored to mitigate these stresses and improve fatigue performance [59]. Surface finish also significantly influences fatigue life. LAM parts often exhibit high roughness due to the layer-by-layer deposition process, with surface irregularities serving as stress concentrators and crack initiation points [60]. Additionally, increased surface roughness and porosity exacerbate fatigue failure [61]. Multiple studies confirm these findings, highlighting the importance of surface quality and defect mitigation in LMP-manufactured components [62, 63, 64]. Therefore, machining, polishing, and other surface treatment methods are essential for enhancing fatigue resistance.

Research indicates that, with proper process optimization and post-processing, LAM components can achieve fatigue lives comparable to those produced by traditional methods [65]. Moreover, several case studies have demonstrated the effectiveness of LAM in producing components for aerospace and automotive applications subjected to cyclic loads [66]. Therefore, understanding the intricate relationship between material properties, manufacturing parameters, and post-processing techniques is crucial for enhancing fatigue behavior in LAM manufactured parts. By meticulously adjusting parameters, engineers can tailor microstructure and mechanical properties to enhance fatigue resistance, ensuring the reliability and longevity of components across various applications.

2.1.8 Wear Resistance

Wear resistance is a critical property in determining the longevity and performance of manufactured parts subjected to frictional and abrasive forces. Understanding how various process parameters and material features influence wear resistance is essential for optimizing the design and manufacturing of these components. Tribological testing (TT), which involves assessing the friction, wear, and lubrication characteristics of materials, provides valuable insights into their performance under different operating conditions.

Using TT, research has concluded that multiple process parameters, such as laser power, scanning or traveling speed, layer thickness, and powder feed rate, dictate the wear resistance of the manufactured part [27, 67, 68]. For example, increasing laser power and scanning speed may lead to improvements in wear resistance by promoting denser microstructures and reducing defects such as porosity. On the other hand, certain adjustments, such as higher layer thickness or powder feed rate, may result in decreased wear resistance due to potential surface irregularities or inadequate fusion between layers.

Research studies have found that post-treatments and alloying significantly affect wear resistance in LAM manufactured components. For example, wear tests conducted on samples fabricated using SLM revealed that post-processing techniques like hot-pressing can significantly reduce wear resistance and friction coefficients compared to other methods [69]. Similarly, the addition of strengthening elements like Inconel 625 can enhance material hardness and wear resistance, while HT at high temperatures may decrease wear resistance due to grain coarsening and other microstructural changes [70].

Achieving optimal wear resistance in LMP-manufactured components requires a comprehensive understanding of the interplay between process parameters, material composition, and post-processing techniques. Using TT, coupled with detailed analysis of wear mechanisms and surface characteristics, provides invaluable insights for enhancing the performance and durability of manufactured parts. Moreover, implementing process control measures ensures consistent and repeatable production, thereby enhancing wear resistance in LMP-manufactured components. By leveraging these insights with effective process control strategies, engineers can tailor approaches to improve wear resistance and extend the service life of LMP-manufactured parts across diverse applications.

2.1.9 Dimensional Accuracy

The dimensional accuracy of components in LMP significantly influences feedstock utilization, post-processing costs, and overall process efficiency. Precise fabrication, aligned with intended geometrical specifications, minimizes material waste and reduces the requirement for extensive post-processing steps. Achieving such precision is highly depen-

dent on effectively controlling process parameters, as they directly impact the geometry accuracy of the fabricated parts. Thus, optimizing process parameters becomes crucial to ensuring that the manufactured components meet the desired dimensional specifications efficiently.

Challenges such as surface balling, uneven material deposition, and thermal accumulation are prevalent in LMP processes, significantly impacting surface quality and dimensional accuracy. Thermal accumulation, a critical concern in LMP, arises from the rapid temperature changes induced by the laser, leading to the buildup of residual heat within the material. This accumulated thermal energy can result in distortions, warping, and dimensional inaccuracies in the fabricated components [71, 72]. Surface quality in LMP is mainly influenced by the formation of plasma plumes during the interaction between the molten pool and the laser beam, which can introduce defects and imperfections on the fabricated surface [73, 14].

Furthermore, surface balling remains a persistent challenge, particularly with powder feedstock, and is attributed to factors such as excessive surface tension and poor wettability of molten particles [74, 75, 76]. In deposition processes such as LDED, unique structures like corners and crosses often exhibit uneven material deposition and thermal accumulation, exacerbating dimension deviation and complicating automation during deposition. Factors such as unreasonable feedstock feed speed or feed angle can further exacerbate issues such as the formation of weak link liquid bridges and collisions with abnormal humps, ultimately resulting in process termination [77, 78].

The dimensional accuracy of components in LMP is influenced by various factors, including process parameters and material characteristics. Despite challenges such as surface balling and thermal accumulation, advancements in process optimization and control strategies offer opportunities for improving surface quality and dimensional accuracy in LMP. By implementing advanced monitoring and process control techniques, dimensional accuracy can be significantly improved, resulting in enhanced product quality, reduced waste, reduced post-processing, and greater overall efficiency.

2.1.10 Summary

Optimizing process parameters is essential in LMP to achieve desired material characteristics and ensure consistent product quality. Process parameters such as laser power, scanning or traveling speed, powder feed rate, and material composition profoundly influence the final quality of LMP-fabricated components, including factors like porosity, hardness, surface roughness, residual stress, microstructure, tensile strength, fatigue behavior, and wear resistance.

While significant advancements have been made in understanding and optimizing these factors, challenges remain in achieving consistent material characteristics. To address these challenges effectively, it is critical to advance the fields of real-time monitoring, process control, and the utilization of predictive models. These advancements will enable manufacturers to dynamically adjust process parameters in real-time, ensuring precise control over material characteristics and product quality.

2.2 Process Modeling in Laser Material Processing

Modeling of LMP processes offers valuable insights into the complex dynamics and intricate laser-material interactions in LMP. This section explores the wide range of modeling approaches utilized in LMP, including analytical, numerical, empirical, and machine learning (ML) methods. By examining existing literature on process modeling in LMP, the aim is to analyze the strengths and limitations of different modeling techniques and their applications in predicting process outcomes and optimizing process parameters. Through a critical analysis of existing models and methodologies, areas for future research and development in process modeling for LMP applications can be identified.

2.2.1 Analytical Modeling

Analytical modeling in LMP involves the application of mathematical formulations and theoretical principles to understand the fundamental physics underlying laser-material interactions. These models offer valuable insights into temperature distribution, phase changes, and material behavior, providing researchers with a structured framework for predicting process outcomes based on fundamental principles and assumptions. By leveraging mathematical analysis, analytical models serve as a foundation for optimizing LMP processes and developing control strategies.

Numerous articles in the literature highlight the utilization of analytical models to improve the understanding of the complex dynamics in LMP and to optimize the process parameters. For example, a comprehensive analytical-computational model integrates laser-powder interaction formulations with finite element models, enabling precise control over deposition geometry and residual stresses [79]. A physics-based analytical model predicts temperature distribution and solidification microstructure variations under different scanning strategies in multi-track LDED [80]. An explicit analytical description of heat accumulation effects during LAM aids in the optimization of process parameters to minimize temperature increase and enhance productivity [81]. A simplified analytical model analyzes energy absorption in LDED, shedding light on powder stream character-

istics and process conditions [82]. A specific energy density model describes deposited clad geometry, facilitating comparison and standardization of process parameters across different LDED machines [83]. A pixel-based analytical model predicts and compensates for overfill in LDED, enhancing geometric quality and facilitating first-time-right production [84].

Among the developed analytical models, the Rosenthal analytical solution is one of the most widely used analytical and foundational models in the study of heat conduction in LMP, welding, and cutting processes [85]. This solution provides a mathematical description of the temperature distribution in a semi-infinite solid subjected to a moving heat source, offering valuable insights into the thermal behavior during processes such as LAM. The primary advantage of the Rosenthal solution lies in its simplicity and efficiency, allowing for quick predictions of temperature fields without the need for extensive computational resources. It has been widely used to understand the relationship between process parameters and thermal profiles, which is critical for optimizing process outcomes such as melt pool dimensions and cooling rates. For instance, it has been used to predict temperature distribution in laser powder bed fusion (LPBF) [86], where in situ measurements were compared to model predictions to understand layer roughness during the process. Additionally, it has been utilized to understand thermal dynamics in SLM [87], aiding in the analysis of complex melt flow, pore formation, spatter, and denudation zones, which are critical for optimizing the process parameters and improving the final product quality. In addition, a theoretical framework is introduced utilizing the Rosenthal solution for analyzing and optimizing melting processes, such as welding and LAM, showcasing its potential in identifying productivity constraints and guiding process optimization across various materials and applications [88]. Another study integrates residual heat and melt pool bead spreading into a physics-based process model that utilizes the Rosenthal model to predict temperature fields and final clad geometries [89]. Experimental validation in single-track and multi-track deposition demonstrates strong agreement across varying specific energy levels and powder feed rates. However, there are discrepancies between experimental and model-predicted results due to model simplifications and process changes.

Despite their utility and widespread use, analytical models, such as the Rosenthal solution, exhibit significant limitations. These models rely on simplifying assumptions, including uniform material properties, a constant heat source, and an infinite medium, which fail to accurately reflect the complexities of real-world LMP processes. Consequently, they often overlook important phenomena such as varying material properties at high temperatures, phase changes, and complex part geometries. Additionally, analytical models neglect the dynamic nature of laser-material interactions, making them impractical for real-time process control applications, where adaptive and flexible modeling approaches are crucial. This lack of adaptability and understanding of the physical interaction significantly reduces their effectiveness in scenarios requiring high precision and reliability [32, 15]. Therefore, while analytical models are an invaluable tool for advancing our understanding of the complexities within LMP processes, their limitations underscore the pressing need for more advanced models capable of addressing the variability of LMP processes, adapting to real-world changes, and supporting closed-loop control applications.

2.2.2 Numerical Modeling

Numerical modeling plays a crucial role in studying LMP by using computational algorithms and simulation techniques to analyze complex physical processes that occur during LMP. This approach involves discretizing the governing equations that describe phenomena such as heat transfer, fluid flow, and phase transformation and then solving them iteratively across spatial and temporal domains. This approach provides researchers with a detailed understanding of the underlying dynamics of LMP processes, enabling them to optimize the process parameters to achieve higher-quality manufactured parts.

The most common and widely used numerical modeling method in the literature is finite element model (FEM) due to its versatility and ability to model the laser-material interactions in LMP, including thermal effects, phase changes, and material deformation. For example, an FEM has been developed for LHT to predict the temperature during rotational LHT, which resulted in close approximations between the model and the real

process [90, 91]. A three-dimensional FEM of the SLM process has been developed to simulate the conduction, transition, and keyhole modes of the process [92]. This model enabled accurate predictions of the mode in which the current process is taking place. Another FEM of the SLM process has been developed to simulate and understand the relationship between powder layer thickness and shrinkage ratio [93]. Results indicated that the shrinkage ratio decreased almost linearly as the layer thickness increased.

An FEM of the LDED process has been developed that includes surface heat losses as a volumetric heat sink term [94]. Results showed that this model was able to accurately predict the experimental melt-pool dimensions of single-track and multi-layer depositions over a range of process parameters [94]. Another FEM has been developed for the thermal behavior and microstructure evolution during LDED [95]. Experimental results highlighted that the heat buildup during manufacturing reduced the cooling rate, which in turn reduced the residual stress. These examples represent just a fraction of the extensive literature available on FEM models, showcasing their versatility and understanding the complex LMP processes. However, using FEM effectively requires careful attention to detail and a significant amount of computational power, which makes it impractical and too computationally demanding to be used for real-time control applications [96, 97, 98, 99].

Researchers have also tried to combine FEM with ML algorithms to reduce the computational complexity of numerical models or to improve the generalization and robustness of the ML algorithms. For example, an FEM is combined with an artificial neural network (ANN) to predict the residual stress in LDED [100, 101]. The ANN is trained using thermal data from the FEM, and the ANN residual stress predictions are compared to the FEM residual stress predictions. Results show that the combined FEM-ANN model has comparable prediction accuracy compared to the FEM. In addition, the ANN predictions show a time improvement between 4x and 9x compared to the FEM predictions.

Another study added physics-informed features of the LDED process to the inputs of an ML algorithm [102]. The physics-informed features were extracted from an FEM and include features such as the melt pool geometry and temperature. By adding these physics-informed features, the generalization and robustness of the ML model were signif-

icantly improved. Nonetheless, while combining FEM with ML algorithms offers promising avenues for reducing the computational complexity and improving the generalization of FEM, there are still notable limitations. The computational efficiency gains observed in these hybrid approaches are not significant enough to enable real-time prediction and control applications due to the inherent computational demands of the models.

In contrast to the FEM, the finite difference model (FDM) offers a less complex and more computationally efficient alternative, making it much simpler to implement and requiring fewer computational resources compared to the FEM and ML methods. For example, an efficient FDM has been developed to predict the temperature of a cylinder during LHT [103, 104]. The simulation results showed a close correlation to the experiment tests. In addition, another study developed an FDM for fast prediction and process optimization of part-scale temperature evolution in LPBF [105], highlighting the FDMs potential for efficient and accurate real-time applications.

In addition to their effectiveness in real-time applications, FDMs can also be an effective tool for real-time process control. The ability to not only predict but also dynamically adjust process parameters in response to real-time data underscores their value in maintaining optimal process conditions. For instance, the integration of an FDM into a linear quadratic tracking (LQT) controller has shown promising results in maintaining a consistent melt pool temperature during LHT by controlling the traveling speed [50]. This study achieved consistent microstructure throughout the heat-treated area. The computational efficiency of the FDMs is achieved by restricting the FDMs to the area around the heat-affected zone (HAZ) and updating the boundary states with real-time thermal data from an infrared (IR) camera. This research further highlights the efficiency and versatility of FDMs in accurately and efficiently predicting thermal dynamics in real-time, showcasing their potential for real-time control applications in LMP.

In summary, numerical modeling has proven to be a powerful tool for understanding and simulating the complex physical processes that occur during LMP. While FEMs excels at capturing intricate interactions, it is too computationally demanding for real-time control applications. Integrating FEM with ML aims to mitigate this, but the same com-

putational challenge persists. In contrast, FDM offers a more computationally efficient option, showing promise for real-time prediction and control in LMP. By focusing on specific areas and utilizing real-time data, FDM has proven to be efficient and adaptable, making it ideal for model-based control applications. Further advancements in computationally efficient numerical modeling techniques, coupled with real-time monitoring and advanced model-based control strategies, have the potential to achieve consistent and repeatable material characteristics in LMP.

2.2.3 Empirical Modeling

Unlike analytical and numerical modeling in LMP, which depend on theoretical formulations, empirical modeling in LMP utilizes the direct observation and analysis of real-world process data to establish relationships and insights between process parameters and outcomes, such as material properties, surface roughness, or defect formation. Empirical modeling is particularly useful when the underlying physics of the process are complex or not fully understood, allowing researchers and engineers to predict process outcomes based on experimental data.

Numerous studies have explored various aspects of LMP processes using direct observation and analysis of real-world data. One study investigates the influence of post-HT on the microstructure and fracture toughness of Inconel 718 fabricated via LDED [106]. Various HT methods are applied to evaluate their effects on the microstructural evolution and room-temperature fracture toughness. The results highlighted significant changes in microstructural characteristics and fracture toughness due to post-HT. In addition, these results underscore the importance of tailored HT processes for enhancing the quality of LDED-produced Inconel 718 parts. Another study analyzes the effects of traveling speed and laser power on the properties of gradient walls fabricated via LDED [107]. Results indicate that variations in these process inputs result in significant variations in wall dimensions, surface roughness, and microhardness. In addition, it is observed that higher traveling speeds resulted in decreased surface roughness but increased microhardness due to the higher cooling rates.

Furthermore, a bidirectional powder deposition strategy is utilized to deposit Ti–15Mo alloy with LDED [108]. Microstructural characterization before and after HT reveals changes in grain morphology and distribution of precipitates, impacting the material's mechanical properties significantly. Despite marginal improvements in UTS post-HT, there was a decrease in elastic modulus and a small decrease in total elongation, indicating subtle alterations in mechanical properties due to HT. Moreover, the influence of oxidation on the surface and material properties during LDED of stainless steel 316 L is investigated [109]. Results indicate that surface oxidation can enhance laser energy utilization and deposition efficiency by lowering laser reflectance.

Additionally, hot-wire-based LDED is used for LAM of Inconel 625 thin-walled parts [110]. The microstructural analysis revealed significant enhancements in mechanical properties compared to wire arc additive manufacturing. Another study examined the microstructural characteristics and mechanical properties of deposited Stellite® 6 alloy under varied LDED processing conditions [111]. This research established optimized process parameters for the deposition of Stellite® 6, resulting in enhanced mechanical properties and wear resistance, showcasing the potential for streamlined manufacturing of advanced alloys without additional post-processing. Lastly, a comparative analysis of the microstructural evolution and strengthening behavior of Al-Mg-Sc-Zr alloys processed with LDED and LPBF is conducted [112]. This study indicates that LPBF exhibits fewer primary Al3(Sc,Zr) phases during solidification and enhanced precipitation strengthening due to the higher cooling rates.

Although empirical studies play a crucial role in improving material characteristics, they may not guarantee consistent and repeatable outcomes. This underscores the necessity for closed-loop control to ensure process stability and consistent material properties. However, empirical studies alone may not suffice for closed-loop control due to their limitations in capturing the complex dynamics of the process. Therefore, integrating numerical models for closed-loop control is essential for achieving consistent and reliable material characteristics in LMP processes.

2.2.4 Machine Learning

In both empirical modeling and ML in LMP, a variety of data sources, including process parameters, monitored process data, and material properties, are utilized to gain insights and make predictions. However, there are fundamental differences in how these approaches leverage the data. Empirical modeling relies on data to create mathematical models, while ML models are trained on this data to uncover complex patterns and relationships. By training models on this data, ML algorithms can identify complex patterns and relationships that may not be apparent through traditional analytical or numerical methods. These models can then be used for various tasks in LMP, such as process optimization, defect detection, and material characterization [113, 114].

Of all the ML algorithms, neural network (NN) are the most used due to their sophisticated architecture and computational power, making them highly suitable for real-time prediction and control applications in LMP. One such application is correlating process parameters to deposition geometry characteristics, achieved using an ANN with genetic algorithm [115]. This network predicts deposition width, height, and angle from laser power, scanning speed, and powder thickness. Another study used ANN with particle swarm optimization-ANN [116], predicting deposition width, height, and capture efficiency from laser power, scanning speed, and powder flow rate. Furthermore, the complete deposition geometry during LDED was predicted using ANN, including width, heights, and shape. This was achieved by using the process inputs, deposition material, and deposition location as inputs to the ANN. Another study predicted the deposition height during LDED by training an ANN with seven features [117].

Extending the correlation between process parameters and deposition geometry characteristics involves incorporating process images into the network. A study correlated process parameters with molten pool images to weld waist and back width [118], utilizing morphological features from processed images. To utilize real-time images directly, convolutional neural networks (CNNs) are used. In one study, a CNN predicted laser power and traveling speed from real-time infrared images [119]. In another study, a CNN predicted deposition dimensions from real-time vision images [120]. Recently, a

CNN has been trained on a combination of vision images, IR images, process inputs, and layer numbers [121], enabling accurate predictions of the deposition width and height during multi-layer deposition. These ML algorithms generally achieve geometry or thermal dynamics prediction accuracy between 95-98%, showing great potential for real-time geometry prediction in LMP.

Another application involves correlating process parameters with thermal dynamics. However, only a few studies exist. In one research paper, two machine learning algorithms, extreme gradient boosting and long short-term memory, were developed [122], correlating process parameters with infrared images and melt-pool temperature. A physics-informed NN was developed to predict temperature and melt pool fluid dynamics during LAM [123], showing promising potential for physics-informed deep learning in LMP.

ML algorithms demonstrate significant progress in real-time prediction of material characteristics during LMP. However, these advancements are limited to specific experimental cases and require further experimentation. Moreover, none of these algorithms have been tested for real-time control purposes. While ML algorithms show great potential, there is still a substantial amount of development to do before ML algorithms are capable of both predicting and controlling material characteristics during LMP processes.

2.2.5 Summary

Process modeling, including analytical modeling, numerical modeling, empirical modeling, and machine learning, is essential in LMP as it provides invaluable insights into the complex dynamics within LMP, enabling process optimization and control. Analytical modeling utilizes mathematical formulations to understand the fundamental physics underlying laser-material interactions, offering predictive capabilities based on theoretical principles. Numerical modeling, on the other hand, employs computational algorithms to simulate complex physical processes like heat transfer and phase transformation, enabling a detailed understanding of LMP dynamics and parameter optimization. Empirical modeling relies on real-world data to establish relationships between process parameters and

outcomes, which is particularly beneficial when the underlying physics are complex or not fully understood. Meanwhile, ML algorithms harness diverse data sources to uncover intricate patterns and relationships, aiding in process optimization, defect detection, and material characterization.

Despite advancements in process modeling techniques, most developed models are either theoretical, with little or no validation against real-life results, or semi-empirical, limiting the results to specific experimental cases and requiring further experimentation. Moreover, the majority of models are either too computationally intensive or lack adaptability to real-world variability, thereby preventing their use for real-time control applications. Therefore, there is a strong interest in the development of models like the restricted FDM model [50], which are accurate and can adapt to real-world changes while also being computationally efficient for real-time control applications. By combining these models with process monitoring and model-based process control, manufacturers can achieve complete control over material characteristics and product quality throughout the manufacturing process.

2.3 Process Monitoring in Laser Material Processing

As LMP processes, such as LDED and LPBF, continue to advance, there is a growing need for real-time monitoring to optimize process parameters and mitigate defects. This section focuses on the various techniques and methodologies used for real-time monitoring of LMP processes. By examining existing literature on process monitoring in LMP, the aim is to identify state-of-the-art monitoring technologies and their applications in different LMP processes. Additionally, the section explores the challenges and opportunities associated with process monitoring, paving the way for the development of advanced monitoring strategies for enhanced process control.

2.3.1 Thermal Monitoring

Thermal monitoring methods are crucial in LMP for understanding the thermal evolution during melting and solidification as well as the thermal dynamics of the heat-affected zone. By capturing key features like peak temperature, cooling rate, and heating rate, thermal monitoring facilitates a comprehensive understanding of the thermal dynamic processes in LMP, enabling precise control and process optimization.

With LAM, thermal monitoring provide valuable insights into the formation mechanisms of internal defects and geometric distortions in components. For instance, utilizing an IR camera coaxial with the laser beam allows for the real-time monitoring of molten pool temperature in LPBF, enabling the measurement of molten pool width and the extraction of temperature gradient profiles [124]. Additionally, another study used a coaxial IR camera during LDED to extract geometric features of the melt pool, such as area, length, width, and orientation [125]. Furthermore, the integration of IR cameras for monitoring and controlling the cooling rate during the LDED process in real-time has shown promising results, leading to increased consistency in material properties [126, 127]. In parallel, a novel method utilizing tandem pyrometers has been developed to monitor cooling rates in real-time during LDED, showcasing effectiveness even at high operational speeds, achieving a remarkable frequency of 1 kHz [128].

Thermography systems have been widely applied to characterize the molten pool size and diagnose process stability [129]. A multi-sensor monitoring system, including a near-infrared wavelength camera and a visible wavelength camera, has been constructed to monitor porosities in fabricated parts by analyzing laser absorption rate characteristics and temperature field evolution in LPBF [130]. A two-color pyrometer has been utilized to monitor instantaneous anomalies in the molten pool during LPBF and used ML algorithms for data fusion analysis of macro-computed tomography data to recognize internal pores of components [131]. A hyperspectral line camera has been used to capture spectra of closely spaced points on the molten pool surface and achieve high-precision temperature measurement with a spatial resolution of 12 µm/pixel via a nonlinear least-square algorithm, fulfilling the requirement of high-precision temperature measurement in LDED [132]. These findings underscore the critical importance of thermal monitoring methods in LMP, offering invaluable insights into material behavior and enabling enhanced process control and optimization.

Thermal monitoring methods provide invaluable insights into the intricate thermal behavior of materials throughout LMP processes, enabling real-time monitoring of critical parameters such as molten pool temperature distribution and cooling rate. This enables enhanced process control and optimization, allowing for precise adjustments during fabrication. Additionally, by enabling the timely detection of defects and process anomalies, thermal monitoring ensures the high quality and reliability of manufactured components, contributing to overall product quality and process stability in LMP.

2.3.2 Vision Monitoring

In LMP, vision monitoring emerges as a pivotal method for extracting crucial local structural features and component layer shapes. This method enables the identification of parameters such as height, width, and distortion, while also facilitating the recognition of internal defects within components. With the advent of advanced ML techniques such as CNN, internal features can now be efficiently extracted from captured images. Commonly utilized visual monitoring systems, such as charge-coupled devices (CCD) and

complementary metal-oxide-semiconductor (CMOS) cameras, equipped with appropriate waveband filters, play a significant role in enhancing accuracy, especially concerning dimension feedback in LMP processes [133, 134].

The literature showcases significant advancements in vision monitoring technologies for LMP. For instance, a trinocular optical detector consisting of three CCD cameras was developed, along with image processing algorithms utilizing a recurrent neural network, enabling real-time detection of deposition height in LDED [135]. Additionally, a monitoring system for the molten pool in LDED was established, leveraging a laser coaxial CMOS camera and combining molten pool images with process parameter data to predict layer geometry [136]. Visual data analysis proves effective for monitoring and diagnosing process states, as demonstrated by the development of a fusion algorithm for image processing to detect laser-material interaction regions in LDED [137]. Similarly, a method was proposed to monitor molten pool evolution and predict crystal growth behavior based on molten pool contour data in LDED [138]. A CCD camera was used to capture a sequence of molten pool images in LDED, and an intelligent particle swarm optimization algorithm was utilized to predict the molten pool geometry [139]. These findings underscore the importance of integrating advanced vision monitoring techniques to enhance the understanding and control of LMP processes.

The integration of advanced vision monitoring technologies in LMP has significantly enhanced real-time process monitoring, defect detection, and prediction of geometric features. By leveraging ML methods and intelligent algorithms, researchers and engineers can extract valuable insights from captured visual data, leading to improved accuracy and efficiency in LMP processes. This advancement not only enhances the manufacturing process but also contributes to improved manufactured part quality, ensuring the production of high-quality components across various industries.

2.3.3 Acoustic Monitoring

LMP relies on advanced monitoring technologies to supervise fabrication processes, aiming to ensure product quality and process efficiency. While traditional methods like vision

and thermal monitoring offer insights into external characteristics and thermal behaviors, they may overlook internal defects crucial for component integrity. In contrast, acoustic emission (AE) monitoring, which captures acoustic waves generated during laser-material interaction, presents a promising solution by providing valuable insights into internal defects [140, 141]. The integration of AE monitoring into LMP processes represents a significant advancement in defect detection and process monitoring capabilities.

The acoustic waves from the molten pool during LMP processes carry essential information about internal defects such as pores and cracks, offering rapid processing and cost-effective defect detection [142]. Structural-borne AE sensors have been effectively utilized to monitor crack and pore formation in powder-based LDED processes, with sophisticated data analysis techniques like principal component analysis and CNNs facilitating defect recognition [143]. Moreover, the integration of AE sensors into LPBF systems has further enhanced defect detection capabilities, enabling real-time detection of micro-cracks and pores and facilitating improved process monitoring and quality control [144]. Additionally, the utilization of air-borne AE monitoring techniques has minimized structural noises and allowed for flexible installation, contributing to the versatility of defect detection methods in LAM [145].

AE monitoring presents significant potential for enhancing defect detection and process monitoring in LMP. By harnessing the valuable information transmitted by acoustic waves, AE sensors enable real-time detection and characterization of defects such as pores and cracks. Therefore, incorporating AE monitoring technology into LMP processes can further enhance quality control and production efficiency of manufactured components.

2.3.4 Spectral Monitoring

optical emission spectroscopy (OES) is recognized as a valuable tool for compositional analysis in LMP, leveraging characteristic spectral lines emitted from the HAZ [146, 147]. Studies utilizing OES have investigated various aspects of LMP processes. For example, one study utilized OES to analyze the chemistry and relative intensities of excited species in LPBF, correlating spectral characteristics with process parameters [148]. Similarly,

another study explored the relationship between deposition stability and spectral characteristics in resistance hot-wire LDED, observing significant productivity improvements under specific voltage conditions [149]. Furthermore, OES has been demonstrated as an effective in-situ technique for characterizing internal defects in LPBF, achieving high prediction accuracy for pores through Fourier transform analysis and ML [150].

While OES has significantly contributed to compositional analysis, process conditions, and defect prediction in LMP, its application has limitations. These include challenges in interpreting complex spectral data and the inability to directly measure certain internal defects. Nonetheless, OES continues to hold promise for advancing monitoring and quality control in LMP.

2.3.5 Summary

In LMP, utilizing monitoring methods is essential to understanding and controlling the intricate thermal and structural dynamics during manufacturing. Methods such as thermal, vision, acoustic, and spectral monitoring play pivotal roles in capturing key process features and detecting defects, ultimately ensuring the quality and reliability of manufactured components. While thermal monitoring provides insights into the thermal dynamics of the HAZ, vision monitoring enables precise dimensional feedback and defect recognition. Acoustic monitoring offers rapid defect detection through the analysis of acoustic waves generated during processing, while spectral monitoring contributes to compositional analysis and defect prediction.

Despite advancements in monitoring technologies, challenges persist in interpreting complex data and effectively integrating monitoring systems with control strategies to achieve consistent material characteristics. Therefore, continuous innovation and integration of advanced monitoring techniques with predictive models and process control strategies are critical to overcome these challenges and enhance the overall quality and performance of LMP-fabricated components. By combining process monitoring, process control, and predictive models, manufacturers can achieve complete control over material characteristics and product quality throughout the manufacturing process.

2.4 Process Control in Laser Material Processing

In the early stages of LMP, open-loop process control strategies were predominantly used, requiring manual adjustments of process parameters based on periodic quality assessments. These assessments involve analyzing dimensional accuracy, surface finish, mechanical properties, and overall product quality to ensure that the parts are manufactured to the desired standards and specifications. However, finding the optimal process parameters manually is exceedingly costly, often leading to increased production expenses, time-consuming interventions, and production delays. Moreover, the extensive range of process parameters, each with its own intricate interactions and impacts on material properties, exacerbates these challenges. Even minor deviations in process conditions can result in significant variations in material properties, undermining the scalability, reliability, and widespread adoption of LMP processes.

Subsequently, closed-loop process control techniques have received wide attention for their capacity to automatically correct errors during the process, thereby increasing manufacturing efficiency and product quality and improving the reproducibility and consistency of the manufactured parts [151]. Despite the significant advancements in closed-loop control, substantial challenges persist due to the complexity of LMP processes. Therefore, a comprehensive study of process control techniques in LMP has been undertaken. This study delves into both conventional and modern control techniques, aiming to explore their respective strengths, limitations, applications, and challenges in the context of LMP. By combining existing knowledge in this field, valuable insights can be gained for the development of advanced process control strategies.

2.4.1 Classical Process Control Techniques

Classical closed-loop control strategies in LMP primarily consist of error-based single-input single-output (SISO) control strategies which aim to regulate various process parameters to achieve desired material characteristics. These methods commonly utilize controllers such as PID controllers, which adjust the input parameters based on the dif-

ference between the desired output and the actual output of the system. In LMP, process parameters such as laser power, scanning or traveling speed, powder feed rate, and laser beam focus may be controlled to ensure precise material deposition and part quality. These control strategies often rely on monitoring techniques that provide real-time feedback on the state of the process. In addition, these methods may also incorporate SISO transfer functions derived from system identification processes using either real-world data or complex computer simulations. These transfer functions serve as mathematical representations of the relationship between input parameters and output responses, facilitating the design of control algorithms for LMP.

Controlling the thermal dynamics in LMP processes is critical due to its direct influence on material properties and microstructural consistency [77]. As a result, process control predominantly focuses on controlling the process thermal dynamics in real time. This focus has led to the development of various control strategies in the literature to achieve more consistent material characteristics. For instance, in LHT, a PID controller has been developed to maintain a consistent temperature of the HAZ, thereby ensuring uniform microstructure [152]. Similarly, the hardness and hardening depth can be controlled by maintaining a consistent peak temperature in LHT [153]. In LDED, maintaining a consistent cooling rate through real-time monitoring of traveling speed with feedback from an infrared camera resulted in a homogeneous microstructure in the deposited layers [17, 18]. Furthermore, achieving a consistent melt pool size through real-time adjustment of the laser power, monitored by an infrared camera, has proven effective in enhancing wear resistance in deposited layers [154]. Also, a PID control algorithm utilizing an infrared camera managed to ensure consistent layer dimensions by maintaining uniform layer width during the process [155]. In LPBF, real-time monitoring of melt pool geometry with an infrared camera resulted in consistent geometry by controlling the laser power using a PID controller [156]. In addition, controlling the laser power to obtain a stable molten pool temperature in LPBF resulted in more uniform microstructures and higher mechanical properties of deposited parts [157]. Beyond the common PID control, rule-based controllers have been developed for LDED to maintain a consistent melt pool temperature, resulting in reduced variation in porosity and micro-hardness [158].

Besides controlling the thermal dynamics, other features such as melt pool geometry and layer height have been controlled during the process. These methods mainly use visual-sensing methods. For example, a CMOS camera has been used to maintain a consistent melt pool width during LDED by controlling the laser power. This method resolved issues such as overmelting, balling, and high surface roughness [159]. In LPBF, real-time monitoring of melt pool geometry with an infrared camera resulted in consistent geometry by controlling the laser power using a PID controller [156]. Additionally, an inline coherent imaging method has been utilized to extract the area features of protrusions and depressions in each layer, achieving in-situ correction and decreasing the surface roughness of the samples by 54% [160]. Furthermore, achieving uniform layer height in LDED has been realized through the utilization of CCD cameras to measure molten pool height, coupled with adaptive sliding mode control algorithms for real-time speed control [161]. These varied control strategies underscore the importance of closed-loop control mechanisms in LMP processes.

Classical closed-loop process control techniques represent a significant advancement; however, they are not without their limitations. Challenges such as the complexity of LMP processes with numerous interrelated parameters and their influence on material characteristics persist. Therefore, the comprehensive relationships between process parameters and material characteristics need to be established [45, 162]. This is what modern process control is aiming at by combining control algorithms with advanced methodologies, such as computer simulations, real-time models, and ML, that elucidate these relationships.

2.4.2 Modern Process Control Techniques

Modern closed-loop process control strategies in LMP have evolved to encompass a diverse array of advanced techniques aimed at achieving consistent and repeatable material characteristics. These strategies separate themselves from the classical error-based SISO control methods and incorporate model-based approaches, leveraging mathematical models of the LMP process to predict the optimal process inputs offline or in real-time.

In addition, ML algorithms have emerged as powerful tools in process control, capable of learning complex relationships between input parameters and output responses from large datasets, enabling adaptive and data-driven control strategies [163]. Moreover, the emerging field of multi-input multi-output (MIMO) control is revolutionizing LMP by enabling the optimization and control of multiple process variables simultaneously, thereby significantly improving the reproducibility and consistency of the manufactured parts.

Mathematical models have been used in conjunction with PID controllers to improve the quality of manufactured parts. One possible method is by using the calculation results of complex FEM as the input data of the control system to improve the qualities of the manufactured parts in LMP. For example, a closed-loop control framework in LPBF based on an FEM has been established [164]. With this framework, the output signals collected from the FEM were used to update the control signals of the controller that controls the process. As a result, the calculated molten pool width from the model was fed into the proportional-integral controller to adjust the laser power of the process, which resulted in a significant reduction in the melt pool width variations.

While an FEM is highly accurate, each manufactured part requires its own developed and simulated FEM, which require a lot of computational resources and time. The use of analytical models, however, requires much less resources and time and can be used in real-time. For example, an analytical, control-oriented model was developed to calculate the molten pool dynamics during LPBF [165]. The calculated cross-sectional area of the molten pool was used as a feed-forward signal for the nonlinear inverse dynamic controller to control the laser power and keep the melt-pool cross-sectional area at a constant set point during the build process.

Similarly, an analytical control-oriented model of the SLM process was developed [166]. This model describes the melt pool evolution, consisting of a thermal model using the energy balance of lumped melt pool volume and a disturbance model that uses the disturbing heat from neighboring tracks as the initial temperature of the melt pool. A PID controller was used in this research to control the laser power, minimizing the effect of inter-track disturbance on the melt pool area. Simulation results revealed that the proposed controller reduces the chance of pore formation, which improves the quality

of manufactured parts. While analytical models are efficient enough to be used in real-time, they lack prediction accuracy compared to numerical models. Additionally, current methods primarily utilize SISO control approaches, neglecting the need for MIMO control to ensure consistent and repeatable material characteristics.

The most basic and common MIMO control system consists of an inner and outer control loop, where the inner loop controls a system parameter at each time step of the process while the other loop controls a system parameter after each layer. For example, a dual-loop PID control was designed to achieve MIMO control [167]. This controller enabled simultaneous control of the overlap rate and the height deviation. A two-channel pyrometric camera is used to monitor the melt pool size, and a constant melt pool size is achieved by laser power control with a PID controller. In addition, laser triangulation sensors are used to observe the layer shape and overlap, and a consistent overlap is achieved by controlling the lateral movement of the processing head with a PID controller. Similarly, a dual-loop control system has been proposed, integrating an inner-loop temperature controller and an outer-loop height controller [168]. With this controller, a laser-line triangulation sensor and a thermal camera have been utilized to monitor the layer height and the molten pool temperature, respectively. Simulation-based results demonstrated significantly improved dimensional accuracy and maintained desired thermal behavior during the LDED process.

Instead of having an inner and outer control loop, it is also possible to have a more complex control system consisting of two separate PID control loops, controlling multiple process parameters simultaneously in real-time. Such a system has been proposed to achieve consistent microstructure and geometry in LDED [50] simultaneously. The first controller controls the laser power to maintain a consistent layer height with height measurements from a CCD camera, while the second controller controls the traveling speed to maintain a consistent cooling rate with temperature measurements from an IR camera. Results showed that this MIMO control system is capable of achieving consistent layer heights and microstructure during single layer depositions in LDED. While these error-based MIMO control systems show great results, these methods are limited to specific experimental conditions and require further testing. Moreover, these approaches

are unable to accurately understand the intricate relationship between thermal dynamics and material characteristics. Therefore, more advanced model-based control strategies and ML control strategies are needed for MIMO control.

A more advanced method of model-based control algorithms is using mathematical models for real-time prediction within model predictive control (MPC) algorithms. For example, a robust model predictive control (RMPC) algorithm has been developed to achieve consistent layer height and temperature during LDED simultaneously [169]. The RMPC algorithm utilizes an analytical lumped parameter model as the prediction model, with layer height and melt pool temperature monitored using a CCD camera and pyrometer, respectively. The results show that this controller can effectively achieve MIMO control and deal with uncertainties and disturbances. However, it is important to note that these results have been obtained from simulations and have not yet been validated on a real LDED system. This limitation is significant because simulation results do not fully capture the complexities and unforeseen challenges of real-world applications, affecting the reliability and effectiveness of the proposed algorithm in practical scenarios.

Besides using an analytical model, a numerical model has also been utilized with an advanced prediction control algorithm. An LQT algorithm has been developed to achieve a consistent hardness during LHT by controlling the traveling speed [50]. The LQT algorithm utilizes a FDM as the prediction model, and the melt pool temperatures are monitored using an IR camera. By maintaining a constant melt pool temperature, consistent hardness and hardening depth have been achieved. While the results show great capabilities, the algorithm has only been validated for a very limited number of experiments and requires further validation. Nonetheless, using a numerical model with real-time monitoring and an advanced prediction control algorithm shows the most promise.

Along with advanced model-based control algorithms, ML algorithms are capable of understanding the manufacturing state from the preceding step and executing decision-making in the subsequent step. For instance, a deep reinforcement learning framework has been proposed to intuitively learn the influence of process parameters on heat accumulation. This framework can identify the area of heat accumulation and maintain a consistent depth of molten pool by adjusting either the laser power or the scanning speed

[170]. Furthermore, a multi-input NN has been introduced to formulate a control model for analyzing the intricate thermal history in LPBF. The overall sintering condition was assessed based on process characteristics and thermal histories, and the laser power for the next layer was adjusted using a PID controller to achieve real-time compensation for differences in heat accumulation [171]. Additionally, an adaptive neuro-fuzzy inference system control algorithm, utilizing CCD camera data, has been used to regulate travel speed and ensure consistent layer heights [172]. While the proposed ML algorithms offer significant potential in optimizing LMP processes, they also come with numerous downsides, particularly when dealing with the complexity inherent in LMP. Large, complex datasets are required due to the intricate relationship between process parameters and material characteristics in LMP, making it essential to capture a wide range of operating conditions and material variations. Additionally, the high computational requirements of certain advanced ML algorithms can pose challenges in real-time applications, where rapid decision-making is crucial. The nonlinear nature of LMP further complicates modeling efforts, as traditional linear methods may struggle to capture the complex interactions between process variables accurately. Moreover, ML algorithms may face difficulties in dealing with uncertainties inherent in LMP, such as material inconsistencies, machine variability, and environmental factors, potentially leading to unreliable predictions or control decisions.

Modern closed-loop process control strategies in LMP have evolved significantly, adopting a variety of advanced techniques to ensure consistent and reliable material characteristics. These strategies have moved beyond traditional error-based SISO control methods, incorporating both mathematical and ML models and enabling MIMO control. However, most of these advanced approaches use PID controllers for the control action, and PID controllers are unable to leverage the predictive information from these models directly. Therefore, utilizing advanced model-based control methods like MPC is required. MPC offers crucial advantages over PID control in LMP applications, including the ability to optimize control actions over a future horizon, handle constraints explicitly, and adapt to changing process conditions [173]. Furthermore, MPC excels in integrating MIMO control, optimizing control actions across multiple process variables

simultaneously, which is a necessity in LMP due to the intricate relationship between process parameters and material characteristics. Therefore, utilizing MPC in LMP processes holds immense potential to improve process stability and achieve consistent and repeatable material characteristics of the manufactured part.

2.4.3 Summary

The evolution of closed-loop process control strategies in LMP reflects a significant shift towards achieving consistent and repeatable material characteristics. Moving beyond traditional error-based SISO control methods, these strategies integrate model-based approaches, leveraging mathematical models of the LMP process with PID control to control the process in real-time. In addition, ML algorithms have empowered control strategies, further enhancing process control capabilities. Moreover, MIMO control is revolutionizing LMP, enabling simultaneous optimization and control of multiple process variables, substantially improving reproducibility and consistency in manufactured parts.

Despite advancements in process control techniques, the predominant reliance on PID controllers poses limitations in effectively utilizing the predictive information derived from the mathematical models, underscoring the need for advanced model-based control methods such as MPC in LMP processes. Therefore, continuous innovation and integration of advanced MPC techniques that utilize the predictive capabilities of computationally efficient mathematical models are critical to achieving consistent and repeatable material characteristics. By implementing advanced MPC algorithms, manufacturers can achieve complete control over material characteristics and product quality throughout the manufacturing process.

2.5 Chapter Summary

LMP has emerged as a transformative technology with diverse applications spanning from laser cutting to LAM. Despite its remarkable advantages, achieving consistent and reproducible material characteristics remains a significant challenge, especially in advanced processes such as LAM. These challenges originate from the intricate interplay of numerous process parameters on the material characteristics. Even slight deviations in process conditions can lead to variations in material properties, which undermine scalability, reliability, and widespread adoption of LMP processes.

To address these challenges, this literature study explored key aspects of microstructure control within LMP, focusing on the effect of process parameters on material characteristics, process modeling, process monitoring, and process control. Optimizing process parameters such as laser power, traveling speed, and powder feed rate are essential for achieving desired material properties and ensuring consistent product quality in LMP processes. These parameters exert significant influence on various material characteristics, such as porosity, hardness, surface roughness, residual stress, microstructure, tensile strength, fatigue behavior, wear resistance, and dimensional accuracy.

Process modeling techniques, including analytical, numerical, empirical, and machine learning models, offer valuable insights into the complex dynamics of LMP. Analytical modeling provides insights into fundamental physics, while numerical modeling simulates complex processes like heat transfer and phase transformation. Empirical modeling uses real-world data to establish relationships between parameters and outcomes, while machine learning uncovers patterns aiding in optimization and defect detection. However, most models lack validation against real-life results or are too computationally intensive for real-time control. Therefore, there is a need for accurate, adaptable, and computationally efficient models for real-time control applications.

Process monitoring methods, such as thermal, vision, acoustic, and spectral monitoring, play a crucial role in capturing key process features and detecting defects in real-time. Thermal monitoring provides insights into the thermal dynamics of the HAZ, vision monitoring enables precise dimensional feedback, acoustic monitoring offers rapid

defect detection, and spectral monitoring contributes to compositional analysis. However, challenges persist in interpreting complex data and integrating monitoring systems with control strategies effectively. Therefore, continuous innovation and integration of advanced monitoring techniques with predictive models and process control strategies are essential.

Process control strategies have progressed towards closed-loop methods, integrating model-based approaches and machine learning algorithms to achieve consistent material characteristics. Moving beyond traditional error-based control methods, such as PID controllers, MPCs, and MIMO techniques, enables simultaneous optimization and control of multiple process variables. While significant progress has been made, the prevalent reliance on PID controllers presents constraints in leveraging predictive data from mathematical models effectively. Additionally, the computational demands of advanced model-based algorithms and the complexities of integrating machine learning present practical challenges. Therefore, the integration of advanced MPC techniques that utilize the predictive capabilities of computationally efficient mathematical models is critical to achieving consistent and repeatable material characteristics.

Insights gained from these areas underscore the significance of MIMO control, which integrates real-time monitoring with model-based process control, leveraging accurate and computationally efficient mathematical models. This approach enables precise control over material characteristics, ensuring consistent and repeatable product quality throughout the manufacturing process. Therefore, this research focuses on the development of an AMPC algorithm suitable for real-time microstructure control in LMP, integrating real-time monitoring, prediction, and control of the thermal dynamics.

Chapter 3

Experimental Setup and Thermal Monitoring

In previous studies [174, 153, 50], a closed-loop automated laser material processing (LMP) system was developed at the Automated Laser Fabrication laboratory of the University of Waterloo. This system aimed to enhance production consistency and achieve desired engineering properties in LMP processes. Additionally, prior research [121] introduced a novel monitoring system for real-time monitoring of thermal dynamics and geometric features in LMP. This chapter provides a comprehensive examination of the experimental setup, including its configuration and components. Furthermore, it delves into the details and methods used for real-time monitoring of thermal dynamics.

3.1 Experimental Setup for Research on Laser Material Processing

The setup of the LMP system used in this research is depicted in Figure 3.1. This setup is capable of conducting both laser heat treatment (LHT) and laser-directed energy deposition (LDED) experiments and can be used for a variety of applications, such as hardening, cladding, coating, welding, rapid prototyping, and thermal post-processing.

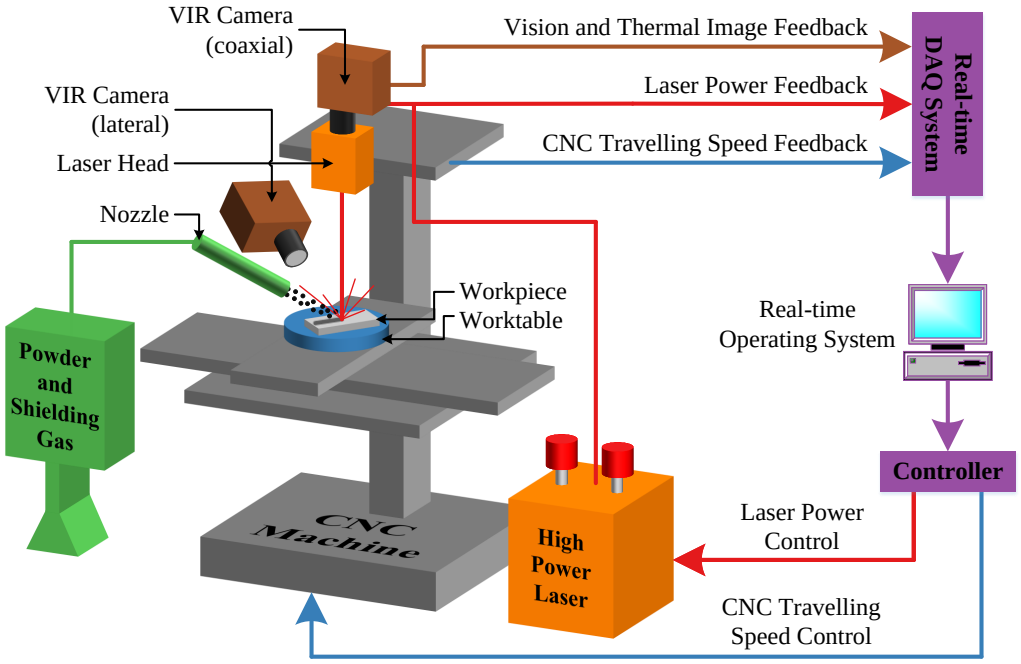


Figure 3.1: Experimental setup at the ALFa laboratory of the UW for conducting LHT and LDED experiments.

As shown in Figure 3.1, the laser beam is transferred to the laser head, which is installed on a computer numerical control (CNC) machine. The laser head directs the laser beam onto the workpiece, producing a heat-affected zone (HAZ) (without transforming solid into liquid) in the LHT process mode and a melt pool (transforming solid into liquid) in the LDED process mode. Argon shielding gas is supplied onto the HAZ

during the LHT process to prevent oxidation. Shielding gas with additional metal powder is supplied onto the melt pool during the LDED process. In the latter case, as the metal powder and a thin layer of the workpiece surface are melted, a thin layer (clad) is deposited on the workpiece. Due to rapid heating and cooling, unstable phases such as martensite may be formed in the workpiece during LHT, and a strong bond is formed between the deposited layer and the workpiece during LDED. The laser and the movement of the worktable are controlled by the real-time operating system to produce the required track profile on the workpiece.

The thermal camera used in this setup captures images of the thermal process in real-time, and these images are used to find the peak temperature and cooling rate. An image of the LMP setup with a clear image of the camera unit is shown in Figure 3.2.

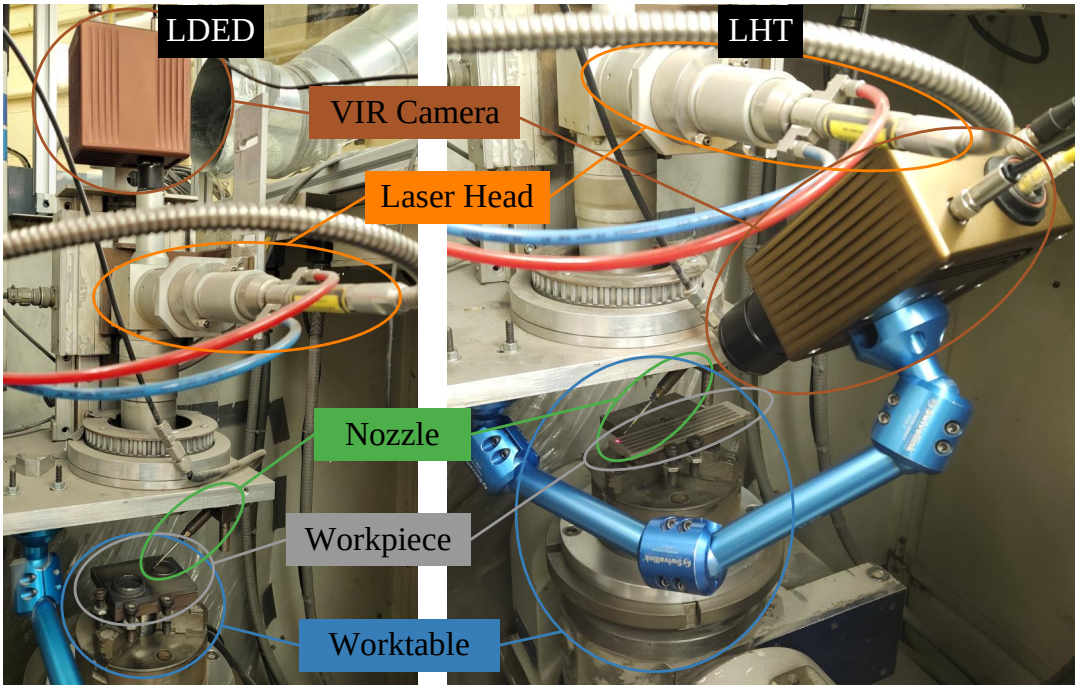


Figure 3.2: Experimental setup at the ALFa laboratory of the UW used for conducting LHT experiments (on the right) and LDED experiments (on the left).

As illustrated in Figure 3.2, the positioning of the camera unit varies depending on the process being conducted. During LDED, the camera unit is positioned coaxially with the laser beam to capture the whole melt pool. In contrast, during LHT, the camera is laterally oriented at a 45° angle and perpendicular to the movement direction of the worktable. This lateral positioning is necessary due to the lower intensity of light at lower temperatures and due to the internal optics of the laser head blocking some of the light, ensuring optimal thermal monitoring of lower temperatures during the LHT process.

The LMP setup shown in Figure 3.1 and Figure 3.2 consists of the following equipment:

- An IPG fiber laser YLR-1000-IC with a higher-order Gaussian beam profile is used as the heat source.
- The Sulzer Metco TWIN 10-C powder feeder is used to supply argon-shielding gas with or without powder.
- The lateral nozzle feeds the argon-shielding gas, with or without powder, onto the substrate. The nozzle has an inside diameter of 1.6 mm and an outside diameter of 3.1mm.
- A 3-axis Fadal VMC 3016 CNC machine is used to position and move the worktable with the workpiece during the process.
- Retinex vision and infrared (VIR) camera containing the Optris PI 08M infrared (IR) camera [175], which is used to capture thermal data during the process. This camera is specifically calibrated for laser applications and is capable of measuring temperatures between 575 °C and 1900 °C, with an accuracy of ±1% for readings below 1500 °C and ±1.5% for readings above 1500 °C.
- A real-time operating system within NI LabVIEW controls the process inputs, including CNC traveling speed and laser power. It sends control commands to the system through an NI PCI-7342 motion controller device. The operating system also acquires feedback data from the LMP system via a DAQ card, enabling precise control and dynamic adjustments during the process.

3.2 Thermal Dynamics Monitoring

In this research, the Optris PI 08M IR camera [175] is utilized to capture thermal data during the LMP process. This camera features a narrow spectral response at 800 nm and is specifically calibrated for LMP processes, ensuring accurate temperature measurements ranging from 575 °C to 1900 °C. The accuracy of the temperature measurements is specified as ±1% for temperatures below 1500 °C and ±1.5% for temperatures above 1500 °C. These calibration standards enable reliable real-time monitoring of thermal dynamics during LHT and LDED processes, covering the typical temperature ranges for most metals and almost all steel alloys encountered in LMP processes.

It is important to note that these temperature measurements are relative rather than absolute, as they are influenced by factors such as emissivity. Emissivity, a material property that affects the amount of infrared radiation emitted by a surface, can vary depending on the surface conditions and the state of the material. In many cases, the emissivity of the solid phase differs considerably from that of the liquid phase, posing challenges for accurate temperature measurement. However, the solid phase emissivity values tend to exhibit relatively consistent behavior. While there may be variations between different materials, within a given material, the emissivity values remain relatively stable across the solid temperature ranges, which is particularly notable in steel alloys. This uniformity in emissivity within the solid phase helps maintain measurement accuracy. Consequently, all algorithms developed in this research focus on the solid phase to ensure the accuracy and reliability of the results. Furthermore, for each material processed during LMP, the emissivity value in the camera's accompanying software is optimized such that the measured maximum temperature of the solid region matches the melting point of the material being processed. In addition, adjustments are made to the transmissivity based on the VIR camera housing, positioning, and laser optics configuration of the LMP setup. Transmissivity refers to the material's capacity to allow infrared radiation to pass through it. This calibration process ensures precise temperature measurements tailored to the specific materials and experimental setup.

Figure 3.3 illustrates the typical temperature distribution observed during LHT and LDED processes. At each time frame p, a thermal image is taken, capturing the thermal distribution of the HAZ. Each pixel of this image measures the temperature T^p of a specific point of the HAZ. For example, there is a point on the trailing edge of the melt pool where the melt pool solidifies, as shown on the left in Figure 3.4. The higher the intensity of the pixel (the brighter the pixel), the higher the temperature will be, and the pixel with the highest intensity corresponds to the peak temperature T^p_{peak}.

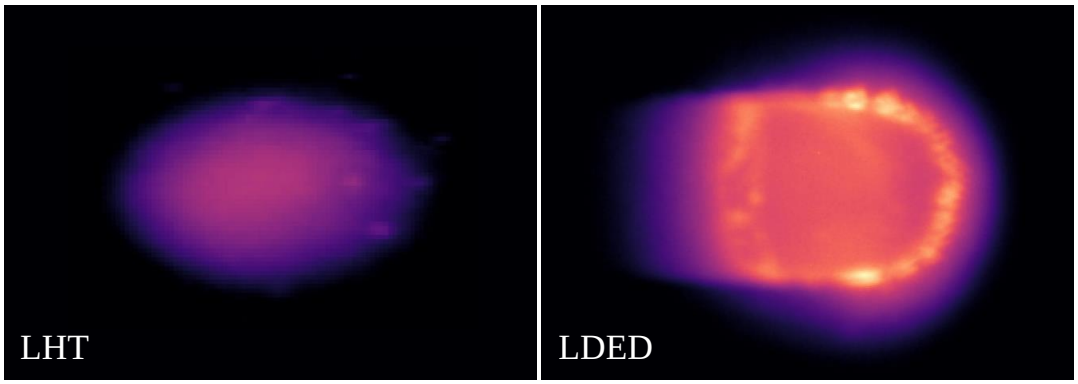


Figure 3.3: Typical temperature distribution for LHT (on the left) and LDED (on the right).

To calculate the cooling rate $\Delta\dot{T}$ of a specific point in the HAZ, consecutive thermal images captured at different time intervals are analyzed as shown in Figure 3.4. In this figure, the left frame displays a thermal image at time t^p. At this time, a temperature T^p is measured at the edge of the melt pool. This point is then tracked until it reaches a certain temperature T^{p+i} at time t^{p+i}, as depicted in the thermal image on the right frame. After tracking the specific point from T^p to T^{p+i}, the temperature gradient can be calculated by determining the change in temperature $\Delta T^{p+i} = T^p - T^{p+i}$. The cooling rate can then be determined using the formula:

$$\Delta\dot{T}^{p+i} = \frac{\Delta T^{p+i}}{\Delta t^{p+i}} \tag{3.1}$$

where Δt^{p+i} is the time difference between the two frames $\Delta t^{p+i} = t^{p+i} - t^p$

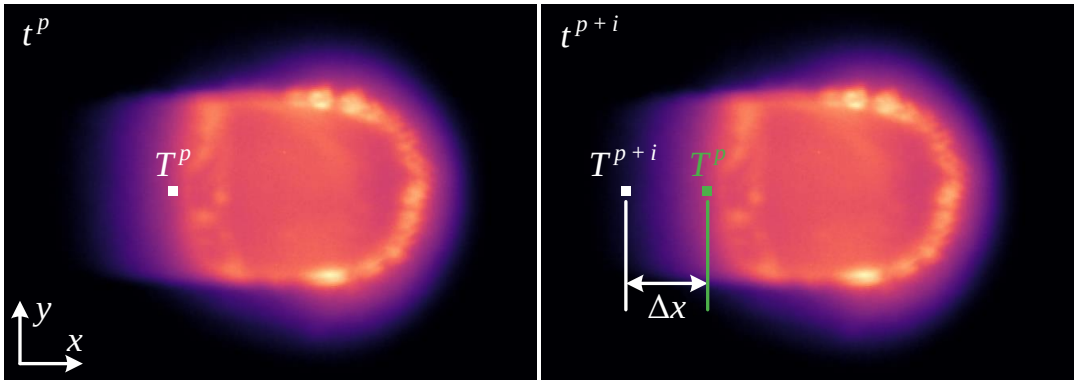


Figure 3.4: Temperature measurement visualization, including pixel tracking relative to a specific point on the workpiece surface.

While directly calculating the time difference between frames can be a valid approach, it may not fully capture the dynamic nature of processes such as laser material processing. In such processes, the speed of the tracked point might not remain constant due to fluctuations in laser power, variations in material properties, or changes in process conditions. Consequently, relying solely on the time difference between frames for predicting the cooling rate may not be sufficient. The cooling rate depends not only on the time interval but also on the actual movement of the tracked point during that time. By computing the time interval Δt^{p+i} using the displacement of the tracked point Δx^{p+i} and the speed of the process v^{p+i} through the formula $\Delta t^{p+i} = \frac{\Delta x^{p+i}}{v^{p+i}}$, this approach accounts for the actual movement of the point while adjusting for any fluctuations in speed. This enables a more accurate estimation of the time interval between frames, leading to a more precise calculation of the cooling rate. The following equation illustrates the expected relationship between the cooling rate and the calculated time interval, incorporating both the displacement of the tracked point and the speed of the process.

$$\dot{\Delta T}^{p+i} = \frac{T^p - T^{p+i}}{\frac{\Delta x^{p+i}}{v^{p+i}}} = \Delta T^{p+i} \frac{v^{p+i}}{\Delta x^{p+i}} \tag{3.2}$$

Throughout the LMP process, the traveling speed and the process thermal dynamics of the HAZ typically change very slowly. Consequently, the cooling rate of the material only changes slowly. As a result, an alternative method for determining the cooling rate, known as the spatial cooling rate, becomes possible. Unlike the traditional approach involving consecutive thermal images, the spatial cooling rate relies on analyzing temperature data from a single snapshot of the HAZ, as depicted in Figure 3.5. This method offers valuable insights into how temperature gradients evolve with respect to the spatial coordinates of the material. Moreover, in numerical models and state-space representations, spatially distributed data is often preferred over discrete time series data like consecutive thermal images. In this context, the spatial cooling rate, which accounts for temperature gradients across the material surface, becomes more relevant. It offers insights into how temperature varies with position in the material, aligning well with the requirements of spatially distributed numerical calculations and state-space representations.

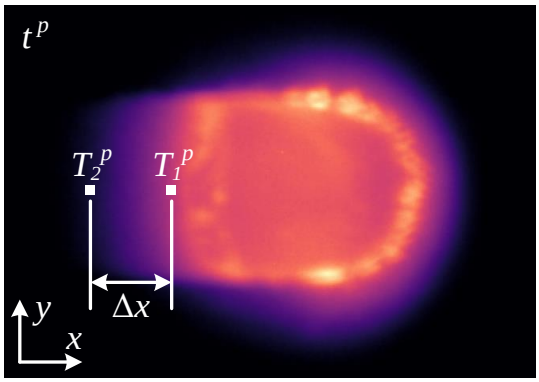


Figure 3.5: Spatial cooling rate using two temperature points within the HAZ from a single image.

With the spatial cooling rate, two temperature points within the HAZ are selected from the same image, as illustrated in Figure 3.5. These points are denoted as T_1^p and T_2^p. The temperature difference between these two points, denoted as ΔT^p, is directly determined from the single image, allowing for an immediate assessment of the temperature gradient. To compute the corresponding time interval Δt^p, the displacement Δx^p

between the selected points is divided by the speed v^p in the x-direction of the LMP process at time p. With this information, the spatial cooling rate, denoted as ∇T^p, is calculated as follows:

$$\nabla T^p = \Delta T^p \frac{v^p}{\Delta x^p} \tag{3.3}$$

Based on the rationale outlined earlier, this research will exclusively utilize the spatial cooling rate equation, as denoted by Equation (3.3), for all subsequent cooling rate measurements, calculations, and predictions, rather than relying on the conventional cooling rate equation represented by Equation (3.2).

Chapter 4

Thermal Dynamic Modeling for Laser Material Processing

Thermal dynamic modeling involves the mathematical representation of heat transfer within a given system. In the context of laser material processing (LMP), these models play a crucial role in predicting temperature distributions, peak temperatures, and cooling rates during the process. This chapter delves into the development of two adaptive thermal models for the prediction and control of thermal dynamics in LMP. These models aim to accurately predict the heat transfer, especially the heat conduction, within the process. The chapter begins with the development of a two-dimensional (2D) adaptive thermal model, specifically designed for the prediction and control of the thermal dynamics during laser heat treatment (LHT). Subsequently, the chapter delves into the development of a novel one-dimensional (1D) adaptive thermal model, specifically designed for the prediction and control of the thermal dynamics during laser-directed energy deposition (LDED). This model is a significant step forward from the previous 2D version, improving the computational efficiency, increasing the prediction accuracy, and expanding the suitability and versatility for control applications.

4.1 Two-Dimensional Adaptive Thermal Model

In order to benefit from the accuracy of numerical modeling while remaining computationally fast for real-time prediction and control applications, a simplified 2D finite difference (FD) model for the LHT process is developed. First, a 2D thermal dynamic model is developed using the partial differential equations (PDEs) of conduction, convection, and radiation. Subsequently, the FD method is used to solve these equations. Finally, a computationally efficient optimization algorithm is constructed to tune the material constants of the model in real-time.

4.1.1 2D Dynamic Model

The heat transfer during LHT can be divided into two main components: heat transfer by conduction, which involves heat transfer within the workpiece, and heat transfer by convection and radiation, which includes the exchange of heat between the workpiece, its surroundings, and the heat source. For the first component of heat transfer, the classical 2D nonlinear equation of conduction with a moving heat source in the x-direction is defined as follows [176]:

$$\frac{\partial}{\partial x}\left(k(T)\frac{\partial T}{\partial x}\right)+\frac{\partial}{\partial y}\left(k(T)\frac{\partial T}{\partial y}\right)+Q_L(x,y,t)=\frac{\partial \rho(T)c_{\mathrm{p}}(T)T}{\partial t}+v(t)\frac{\partial \rho(T)c_{\mathrm{p}}(T)T}{\partial x} \tag{4.1}$$

where $T=T(x,y,t)$ is the 2D transient temperature [K]; $k(T)$ is the temperature-dependent thermal conductivity [W/(mK)]; $c_{\mathrm{p}}(T)$ is the temperature-dependent specific heat capacity [J/(kgK)]; $\rho(T)$ is the temperature-dependent density [kg/m^3]; $Q_L(x,y,t)$ is the amount of energy added in two dimensions to the heat-affected zone (HAZ) during LHT [W/m^3]; $v(t)$ is the traveling speed [m/s]; and t the time [s].

This conduction equation is highly nonlinear, which makes the model computationally demanding. To improve the computational efficiency of the model, the temperature dependency of the material constants (k, ρ, and c_{p}) is removed from the conduction equa-

tion. Additionally, the equation is simplified by combining the material constants ρ and c_p into the volumetric heat capacity c_v [J/(m^{3}K)]. Finally, the equation is restructured, which results in the following simplified 2D heat conduction equation with a moving heat source in the x-direction:

$$k\left(\frac{\partial^2 T}{\partial x^2}+\frac{\partial^2 T}{\partial y^2}\right)+Q_L(x,y,t)=c_\mathrm{v}\left(\frac{\partial T}{\partial t}+v\frac{\partial T}{\partial x}\right) \tag{4.2}$$

Removing the temperature dependency of material constants, while beneficial for computational efficiency, can introduce inaccuracies as material properties often vary with temperature. This simplification assumes constant material properties, which might not capture the dynamic behavior of the heat conduction process accurately. To mitigate these potential issues, a model optimization algorithm will be introduced in Section 4.1. This algorithm will continuously adjust and optimize the model parameters at high frequency, compensating for the approximations made by removing temperature dependency. By integrating this optimization process, the model will better account for variations in material properties, maintaining accuracy and effectiveness in real-time applications.

The second component of heat transfer, encompassing both convection and radiation ($Q_\mathrm{conv/rad}$), is defined by [177] as follows:

$$Q_\mathrm{conv/rad}(x,y,t)=-h_\mathrm{c}\left(T-T_0\right)-\epsilon(T)\sigma\left(T^4-T_0^4\right) \tag{4.3}$$

where h_c is the convective heat transfer coefficient [W/(m^{2}K)]; T_0 is the ambient temperature [K]; $\epsilon(T)$ is the temperature-dependent emissivity coefficient; and σ is the Stefan-Boltzmann constant [$5.67\cdot10^{-8}$ W/(m^{2}K^4)].

The inclusion of the temperature-dependent radiation term in Equation (4.3) introduces significant nonlinearity to the heat transfer by convection and radiation. This nonlinearity increases the computational demands of the model. To minimize the computational complexity and reduce the processing time, a combined heat transfer coefficient proposed by Goldak [178] and used in the literature [177, 179, 180] is selected:

$$Q_{\text{conv/rad}}(x, y, t) = -24.1 \cdot 10^{-4} \epsilon T^{1.61} \left(T - T_0\right) \tag{4.4}$$

Despite the simplicity of this coefficient, it remains highly nonlinear due to the multiplication of $T^{1.61}\left(T - T_0\right)$. Moreover, the emissivity ϵ is both material- and temperature-dependent and must be measured for every experiment [178]. To further simplify this equation, the nonlinear term $24.1 \cdot 10^{-4} \epsilon T^{1.61}$ is consolidated into a single coefficient, denoted as $h_{\text{c,r}}$, which can be manually tuned or optimized in real-time. This simplification results in the following equation for heat transfer by convection and radiation:

$$Q_{\text{conv/rad}}(x, y, t) = -h_{\text{c,r}} \left(T - T_0\right) \tag{4.5}$$

Combining the two simplified heat transfer components from Equations (4.2) and (4.5) results in a 2D heat transfer equation, which includes conduction, convection, radiation, and a moving heat source. The 2D heat transfer equation with a moving heat source is given by:

$$k \left(\frac{\partial^2 T}{\partial x^2} + \frac{\partial^2 T}{\partial y^2} \right) + Q_L(x, y, t) = c_{\text{v}} \left(\frac{\partial T}{\partial t} + v(t) \frac{\partial T}{\partial x} \right) + h_{\text{c,r}} \left(T - T_0\right) \tag{4.6}$$

The simplified 2D heat transfer equation includes two essential processing input variables: $v(t)$, representing the heat source traveling speed, and $Q_L(x, y, t)$, representing the laser heat source generated by the (IPG-1000-IC) laser. According to laser diagnostics software provided by IPG, the laser beam profile may exhibits a higher-order Gaussian curve, as illustrated in Figure 4.1. The specific shape and order of the Gaussian curve depend on the laser's focusing distance.

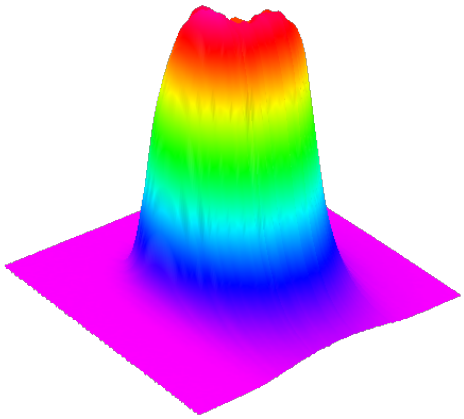


Figure 4.1: IPG-1000-IC laser beam, captured using IPG's laser diagnostics software.

As depicted in Figure 4.1, the laser integrated in the LMP setup, illustrated in Figure 3.1, may exhibit a higher-order Gaussian curve. Consequently, the laser heat source is characterized by a higher-order Gaussian distribution [177, 181], represented as follows:

$$Q_L(x,y,t) = \frac{2\mu P(t)}{\pi r_\mathrm{b}^2 \Delta z} \exp -2\left(\frac{x^2+y^2}{r_\mathrm{b}^2}\right)^\eta \tag{4.7}$$

In Equation (4.7), η is the order of the Gaussian profile and r_b is the laser beam radius [m], both depending on the focusing distance of the laser beam. Additionally, μ is the absorption coefficient; P is the effective laser power [W]; and $\Delta z = 1$ mm accounts for the transformation of a volumetric heat distribution into a surface heat flux.

4.1.2 2D Finite Difference Model

After developing the 2D model describing the heat transfer dynamics in the LHT process, the next crucial step is to implement numerical methods for solving the PDEs describing the heat transfer efficiently. This subsection utilizes the FD method to discretize the heat transfer equation and obtain numerical solutions. The FD method is chosen for its capability to transform continuous differential equations into discrete algebraic equations, aligning well with the pixelated structure of infrared (IR) images used for real-time

temperature monitoring during the LHT process. With the FD method, the temperatures of the heat transfer equation are calculated at discrete points known as nodes, collectively forming a nodal network. The nodal network used to solve the dynamic model (4.6) is shown in Figure 4.2. In this figure, each node represents a certain region defined by Δx and Δy. Additionally, the temperature $T_{m,n}$ of each node m,n is determined by the average temperature of the corresponding region.

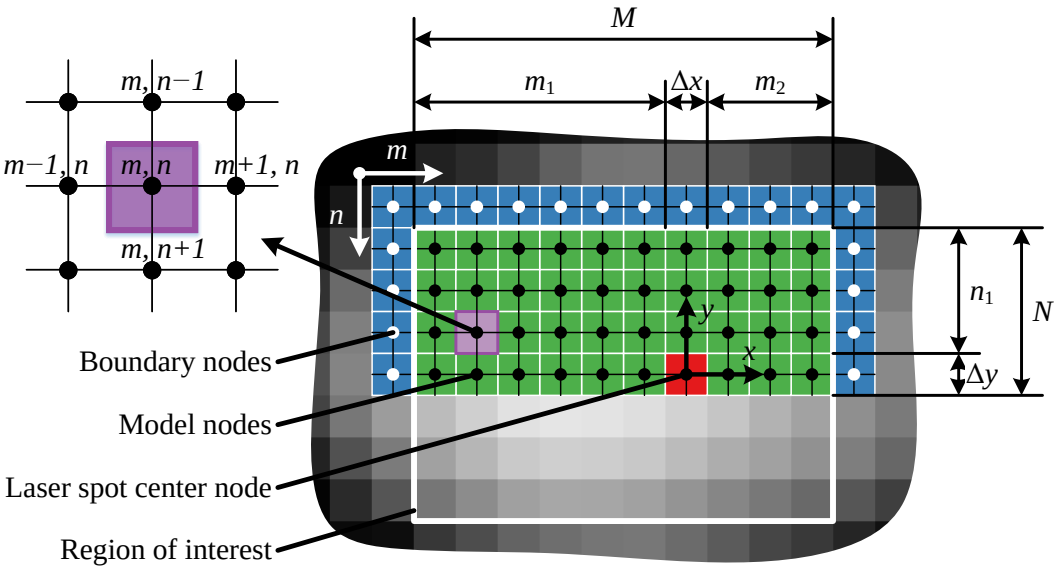


Figure 4.2: Schematic representation of the nodal network for the 2D FD model of the LHT process.

To enable the discretization of the 2D model, the coordinate system is transformed from x,y to m,n, as depicted in Figure 4.2. To improve the computational efficiency, the region of interest in the nodal network is restricted to the HAZ. Additionally, the LHT process is considered symmetric with respect to the laser spot centerline in the x-direction. Consequently, aligning the region of interest with the x-axis allows for the calculation of only half of the nodes within this region, resulting in a $M \times N$ area that further enhances computational efficiency. The temperatures of the nodes in this area, labeled "Model nodes", are predicted in real-time. Conversely, the temperatures of the nodes positioned

at the boundary of the region of interest, labeled "Boundary nodes", are obtained in real-time from thermal images captured by the IR camera during the LHT process. These boundary nodes are assigned fixed temperature values based on the measured data, which corresponds to Dirichlet boundary conditions [182]. This approach provides accurate and consistent boundary temperatures but may limit flexibility in adapting to rapid changing conditions.

After defining the nodal network, the FD method is used to solve the PDEs governing the heat transfer dynamics of the HAZ. This method involves replacing the continuous PDEs with discrete approximations, allowing for numerical solutions to be obtained [183]. One common approach is to use central-difference approximations for the spatial derivatives. For example, using the central-difference approximation for the first derivative with respect to x yields:

$$\left.\frac{\partial T}{\partial x}\right|_{m,n}^{p} \approx \frac{T_{m+1,n}^{p} - T_{m-1,n}^{p}}{2\Delta x} \tag{4.8}$$

Moreover, using the central-difference approximations for the second derivative with respect to x and y yields:

$$\left.\frac{\partial^2 T}{\partial x^2}\right|_{m,n}^{p} \approx \frac{T_{m+1,n}^{p} + T_{m-1,n}^{p} - 2T_{m,n}^{p}}{(\Delta x)^2} \qquad \left.\frac{\partial^2 T}{\partial y^2}\right|_{m,n}^{p} \approx \frac{T_{m,n+1}^{p} + T_{m,n-1}^{p} - 2T_{m,n}^{p}}{(\Delta y)^2} \tag{4.9}$$

To discretize the model in time [183], an integer p is introduced to indicate the time dependency of T, where $t_p = p\Delta t$, with Δt representing the time interval between two successive time frames and p indicating the current time frame. Using the forward-difference approximation, the time derivative can be expressed as:

$$\left.\frac{\partial T}{\partial t}\right|_{m,n}^{p} \approx \frac{T_{m,n}^{p+1} - T_{m,n}^{p}}{\Delta t} \tag{4.10}$$

where the time derivative is expressed in terms of the difference in temperature associated with the future time frame $p{+}1$ and the current time frame p. Consequently, the calculations are carried out at successive time frames separated by Δt.

The FD form ${Q_L}^p_{m,n}$ of the laser heat source (4.7) is determined by integrating the higher-order Gaussian beam profile over the shaded region of each node, which is mathematically expressed as:

$$ {Q_L}^p_{m,n} = \frac{2\mu P^p}{\pi r_\mathrm{b}^2 \Delta x \Delta y \Delta z} \int_{(n-\frac{1}{2})\Delta y}^{(n+\frac{1}{2})\Delta y} \int_{(m-\frac{1}{2})\Delta x}^{(m+\frac{1}{2})\Delta x} \exp -2\left(\frac{x^2+y^2}{r_\mathrm{b}^2}\right)^\eta dxdy \tag{4.11} $$

The complete FD formulation of the 2D model is obtained by substituting Equations (4.8), (4.9), (4.10), and (4.11) into Equation (4.6). This transformation results in a FD model that restricts temperature calculations to discrete points in both space and time. Rearranging the resulting equation to express the unknown nodal temperature at the future time frame $T^{p+1}_{m,n}$ and combining the coefficients of $T^p_{m,n}$ together results in:

$$ \begin{aligned} T^{p+1}_{m,n} = {} & (1 - 2\mathrm{Fo_x} - 2\mathrm{Fo_y} - H_\mathrm{d}) T^p_{m,n} + \mathrm{Fo_x}\left(T^p_{m+1,n} + T^p_{m-1,n}\right) \\ & + \mathrm{Fo_y}\left(T^p_{m,n+1} + T^p_{m,n-1}\right) + C_\mathrm{v} {Q_L}^p_{m,n} + K_\mathrm{v}\left(T^p_{m-1,n} - T^p_{m+1,n}\right) v^p + H_\mathrm{d} T_0 \end{aligned} \tag{4.12} $$

where $\mathrm{Fo_x}$ and $\mathrm{Fo_y}$ represent the FD forms of the Fourier number in the x and y directions, respectively:

$$ \mathrm{Fo_x} = \frac{k\Delta t}{c_\mathrm{v}\left(\Delta x\right)^2} \qquad \mathrm{Fo_y} = \frac{k\Delta t}{c_\mathrm{v}\left(\Delta y\right)^2} \tag{4.13} $$

Additionally, C_v, K_v, and H_d are defined as:

$$ C_\mathrm{v} = \frac{\Delta t}{c_\mathrm{v}} \qquad K_\mathrm{v} = \frac{\Delta t}{2\Delta x} \qquad H_\mathrm{d} = \frac{h_\mathrm{c,r}\Delta t}{c_\mathrm{v}\Delta x} \tag{4.14} $$

With the complete FD formulation of the 2D model (4.12), the temperatures of the future time frame p+1 are entirely predicted by the known process inputs and temperatures at the current time frame p. These predictions enable the calculation of various thermal dynamics parameters for the future time frame p+1, such as the peak temperature and the spatial cooling rate.

An undesirable feature of the FD method is that it is not unconditionally stable [183]. This characteristic presents a significant challenge, particularly in transient heat transfer problems, where numerical calculations may result in numerically-induced oscillations. These oscillations may become unstable, resulting in diverging and unreliable solutions. To prevent these instabilities, it is essential to keep the time step size, represented by Δt, below a certain threshold. This ensures that the coefficients of $T^{p}_{m,n}$ in Equation (4.12) remain non-negative [184]. Therefore, the stability criterion is expressed as:

$$1 - 2\mathrm{Fo}_{\mathrm{x}} - 2\mathrm{Fo}_{\mathrm{y}} - H_{\mathrm{d}} \geq 0 \tag{4.15}$$

Utilizing this stability criterion, the minimum allowable value for Δt is calculated after defining the values of Δx, Δy, k, c_{v}, and $h_{\mathrm{c,r}}$.

The accuracy of Equation (4.12) is significantly influenced by the size of the nodes (Δx and Δy) [183]. These dimensions are determined by the number of nodes in the region of interest, which is directly related to the size of the HAZ in the IR image, as illustrated in Figure 4.2. The region of interest must encompass the entire HAZ to accurately capture thermal dynamics. Increasing the number of nodes in both the x and y directions results in smaller individual node sizes and enhanced accuracy. However, this also increases the computational demand. In this research, the thermal model is validated using real-time thermal measurements from an IR camera, which continuously updates the boundary nodes based on thermal pixels captured. Consequently, the node size must be at least as large as each thermal pixel from the IR camera. Additionally, the size of the nodes is influenced by computational requirements and the speed of the camera. The model must operate efficiently enough to make predictions faster than the camera's frame rate. This consideration becomes even more critical when extending the model to include optimization or implementing it in a model-based control environment.

To achieve the optimal balance between accuracy and computational efficiency, the node size is set to cover an area of 3×3 thermal pixels from the camera images. By using pixel binning, the temperatures from each 3×3 pixel area are averaged to create a new pixel that represents the combined area of the original 3×3 thermal pixels. Each

individual pixel covers an area of $0.0288 \times 0.046 \frac{\text{mm}}{\text{pixel}}$, resulting in nodes with dimensions of $\Delta x = 0.0864$ mm and $\Delta y = 0.138$ mm. This node size ensures that the model is computationally efficient enough to handle real-time predictions faster than the camera's frame rate. Additionally, it supports future expansions of the model, such as incorporating optimization or implementing it in a model-based control environment, without compromising performance or exceeding the camera's processing capabilities.

4.1.3 2D Adaptive Thermal Model

In the preceding subsections, a computationally efficient 2D thermal model was developed (4.12) for real-time prediction and control applications. This thermal model consists of three material constants affecting the thermal dynamic predictions: the thermal conductivity k, the volumetric heat capacity c_{v}, and the combined radiation and convection coefficient $h_{\text{c,r}}$. These three material constants depend on the material, temperature, direction of heat transfer, surface roughness, and other environmental conditions. In addition, the thermal model neglects the heat transfer through the material in the z-direction. These model simplifications will affect the prediction accuracy of the 2D thermal model. To enhance the model's performance, this subsection presents a computationally efficient parameter estimation algorithm. This algorithm will update the model parameters more frequently than the rate at which the material properties themselves change. By doing so, it effectively compensates for temperature-dependent variations and maintains the model's accuracy and robustness. The continuous, high-frequency optimization of these parameters allows the model to adapt to evolving thermal conditions, ensuring precise predictions and consistent performance.

The 2D thermal model is developed to accurately predict the real-time thermal dynamics of the LHT process, particularly the peak temperature T_{peak}^{p+1} and the spatial cooling rate $\nabla T^{p+1} = \frac{T_{\text{peak}}^{p+1} - T_{\text{cool}}^{p+1}}{\Delta t^{p+1}}$. To accurately predict these features, precise prediction of the peak temperature T_{peak}^{p+1} and the cooling temperature T_{cool}^{p+1} is required. Therefore, the parameter estimation algorithm aims to minimize the prediction error of these two thermal points compared to the measurements from the LHT process.

Utilizing the model predictions and thermal measurements at time step p, the resulting error vector is formulated as follows:

$$\mathbf{E}^p = \begin{bmatrix} \hat{T}^p_{\text{peak}} \\ \hat{T}^p_{\text{cool}} \end{bmatrix} - \begin{bmatrix} T^p_{\text{peak}} \\ T^p_{\text{cool}} \end{bmatrix} \tag{4.16}$$

where $\hat{T}^p$ represents predicted temperatures for time frame p and T^p represents measured temperatures at time frame p.

To minimize the model's prediction error, the three material constants k, c_{v}, and $h_{\text{c,r}}$ of the 2D thermal model must be optimized. To achieve this, a nonlinear objective function J is formulated as follows [185]:

$$J = \min_{\boldsymbol{\theta}^p} \mathbf{E}^{p\prime} \mathbf{Q} \mathbf{E}^p \tag{4.17}$$

where $\mathbf{Q}$ is a weighting matrix and θ^p is a vector containing the three time-dependent material constants k^p, c^p_{v}, and $h^p_{\text{c,r}}$ at time frame p, given by:

$$\boldsymbol{\theta}^p = \begin{pmatrix} k^p \\ c^p_{\text{v}} \\ h^p_{\text{c,r}} \end{pmatrix} \tag{4.18}$$

Subsequently, integrating the time-dependent material constants into the 2D thermal model from Equation (4.12) yields a 2D adaptive thermal model. This adaptation improves prediction accuracy by accounting for thermal dynamic changes throughout the process. The updated 2D adaptive thermal model, which integrates the three time-dependent material constants, is presented below:

$$\begin{aligned} T^{p+1}_{m,n} = {} & \text{Fo}^p_{\text{x}} \left(T^p_{m+1,n} + T^p_{m-1,n} - 2T^p_{m,n} \right) + \text{Fo}^p_{\text{y}} \left(T^p_{m,n+1} + T^p_{m,n-1} - 2T^p_{m,n} \right) \\ & + C^p_{\text{v}} Q^p_{m,n} + K_{\text{v}} \left(T^p_{m-1,n} - T^p_{m+1,n} \right) v^p + H^p_{\text{d}} \left(T_0 - T^p_{m,n} \right) + T^p_{m,n} \end{aligned} \tag{4.19}$$

Here, $\mathrm{Fo}_{\mathrm{x}}^{p}$ and $\mathrm{Fo}_{\mathrm{y}}^{p}$ represent the FD forms of the time-dependent Fourier number in the x and y directions, respectively:

$$\mathrm{Fo}_{\mathrm{x}}^{p} = \frac{k^{p}\Delta t}{c_{\mathrm{v}}^{p}\left(\Delta x\right)^{2}} \qquad \mathrm{Fo}_{\mathrm{y}}^{p} = \frac{k^{p}\Delta t}{c_{\mathrm{v}}^{p}\left(\Delta y\right)^{2}} \tag{4.20}$$

and where

$$C_{\mathrm{v}}^{p} = \frac{\Delta t}{c_{\mathrm{v}}^{p}} \qquad K_{\mathrm{v}} = \frac{\Delta t}{2\Delta x} \qquad H_{\mathrm{d}}^{p} = \frac{h_{\mathrm{c,r}}^{p}\Delta t}{c_{\mathrm{v}}^{p}\Delta x} \tag{4.21}$$

Similarly, substituting the three time-dependent material constants into the stability criterion outlined in Equation (4.15) yields an adaptive stability criterion:

$$2\frac{k^{p}\Delta t}{c_{\mathrm{v}}^{p}\left(\Delta x\right)^{2}} + 2\frac{k^{p}\Delta t}{c_{\mathrm{v}}^{p}\left(\Delta y\right)^{2}} + \frac{h_{\mathrm{c,r}}^{p}\Delta t}{c_{\mathrm{v}}^{p}\Delta x} - 1 \leq 0 \tag{4.22}$$

Solving the objective function (4.17) will result in material constants that significantly reduce the model prediction error. However, this process may induce rapid and unrealistic changes in these constants, potentially destabilizing the thermal model or yielding undesirable results. To ensure internal model stability, the optimization problem is subjected to the stability criterion from Equation (4.22). Additionally, to prevent rapid and unrealistic changes in these constants, the objective function is expanded to account for the rate of change. This approach helps maintain stability and consistency in the optimization process. The improved objective function is formulated as:

$$J = \min_{\boldsymbol{\theta}^{p}} \mathbf{E}^{p\prime}\mathbf{Q}\mathbf{E}^{p} + \Delta\boldsymbol{\theta}^{p\prime}\mathbf{R}\Delta\boldsymbol{\theta}^{p} \tag{4.23}$$

where $\mathbf{R}$ is a weighting matrix and $\Delta\theta^{p}$ a vector containing the rate at which the three material constants changed compared to the previous time frame $p-1$, formulated as:

$$\Delta\boldsymbol{\theta}^{p} = \boldsymbol{\theta}^{p} - \boldsymbol{\theta}^{p-1} \tag{4.24}$$

In addition, to ensure that the three material constants remain positive and nonzero, they are subjected to the following minimum constraint:

$$\boldsymbol{\theta}^p \geq 10^{-2} \tag{4.25}$$

The resulting 2D adaptive thermal model is implemented within the real-time operating system inside LabVIEW, as described in Section 3.1. In addition, MATLAB [186] is used for most of the real-time numerical calculations. Furthermore, the model parameter estimation algorithm is classified as a constrained nonlinear optimization problem. Therefore, the nonlinear solver *SQP* within the *fmincon* function of MATLAB's Optimization Toolbox [187] is utilized to calculate the optimal model's material constants.

4.1.4 Summary

In this section, a simplified 2D adaptive thermal model was developed for the prediction and control of the peak temperature and spatial cooling rate. Initially, a 2D thermal dynamic model based on PDEs governing conduction, convection, and radiation was formulated to describe the thermal dynamics of the HAZ. Subsequently, the FD method was utilized to discretize these equations for a restricted region around the HAZ, enabling numerical solutions specific to this area and improving computational efficiency. Furthermore, the model's prediction accuracy was improved through the implementation of a model parameter estimation algorithm, which dynamically adjusted the model's material constants in real-time to compensate for model simplifications and minimize prediction errors. The resulting 2D adaptive thermal model is integrated into LabVIEW, enabling real-time prediction and control of peak temperature and spatial cooling rate during the LHT process.

4.2 One-Dimensional Adaptive Thermal Model

Building upon the insights gained from the development of the 2D model discussed in the previous section, this section presents a novel 1D adaptive thermal model for the prediction and control of the thermal dynamics during LDED. Initially, a 1D thermal dynamic model is developed with the PDEs of conduction. Subsequently, the FD method is used to solve these equations, ensuring accurate numerical solutions. Afterwards a computationally efficient optimization algorithm is constructed to optimize the model parameters in real-time, thereby improving the predictive capabilities and suitability for control applications. Finally, the newly developed 1D model is compared to its 2D counterpart and commonly used methods in the literature to highlight the novelty of the proposed model.

4.2.1 1D Dynamic Model

In the development of a model for LDED, special emphasis is placed on the solidified region within the HAZ. This area, situated at the trailing edge of the melt pool, is illustrated in Figure 4.3, where the solidified region is outlined in yellow and the melt pool area is outlined in green. The focus on the solidified region originates from its critical role in influencing the microstructure and mechanical properties of the deposition during manufacturing. By prioritizing this area in modeling, key thermal dynamic features can be captured, such as the position of the trailing edge of the melt pool and the spatial cooling rate. Moreover, focusing on this area enables the development of a simplified 1D model along the direction of movement while considering the critical dynamics that determine the microstructure.

The LDED process encompasses all three main modes of heat transfer, including conduction, convection, and radiation. However, while all three modes contribute to the thermal dynamics of the process, the impact of convection and radiation is relatively minor compared to conduction in the solidified region. Consequently, their effects can be effectively approximated within the conduction mode by adjusting the thermal con-

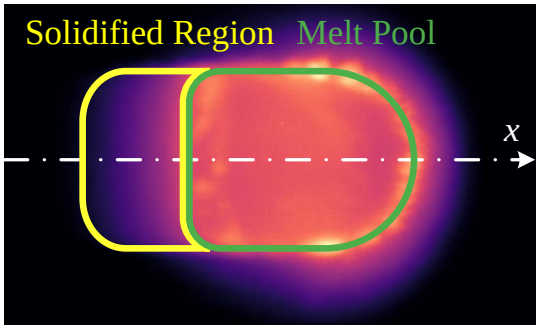


Figure 4.3: Visualization of the HAZ during a typical LDED process. The right border (in green) indicates the region of the melt pool, and the left border (in yellow) indicates the solidified region. The white center line denotes the direction of movement during the process.

ductivity coefficient. This simplification allows for a simplified model that captures the essence of heat transfer in LDED, crucial for real-time control applications. Moreover, research suggests that computational efficiency and robustness are critical for models designed for real-time control applications. Especially pure conduction models have been identified as among the most efficient and robust numerical models for this purpose [98]. Therefore, a 1D pure conduction model is used to describe the thermal dynamics of the LDED process in the solidified region. Consequently, this model not only guarantees computational efficiency and predictive accuracy but also simplifies the representation of heat transfer dynamics in LDED. The equation governing the 1D conduction with a moving heat source is as follows:

$$\frac{\partial}{\partial x}\left(k\left(T\right)\frac{\partial T}{\partial x}\right)+Q_{L}\left(x,t\right)=\frac{\partial\rho\left(T\right)c_{\mathrm{p}}\left(T\right)T}{\partial t}+v\left(t\right)\frac{\partial\rho\left(T\right)c_{\mathrm{p}}\left(T\right)T}{\partial x} \tag{4.26}$$

In contrast to the Gaussian distribution utilized in the 2D model, the 1D model adopts a point heat source to represent energy input. This implies that rather than dispersing energy across an area defined by the laser, the model concentrates energy at a specific point, entering from the edge of the melt pool and conducting into the solidified region. By simplifying the energy input to a point heat source in the 1D model, the essential

dynamics of energy transfer are still captured while improving computational efficiency. This simplification is justified by focusing on the solidified region, which lies beyond the area directly affected by the laser. By concentrating solely on this region, essential heat transfer dynamics can be effectively captured without the computational demands of modeling the entire laser interaction zone. In the 1D model, the heat source $Q_L(x,t)$ is represented as follows:

$$Q_L(x,t) = \zeta(x)P(t) \tag{4.27}$$

with $P(t)$ the effective laser power in $[W]$ at time t, and $\zeta(x)$ a correction factor at the location of the heat input x encompassing all simplifications related to the heat source.

Similarly to the 2D conduction equation, the 1D model conduction equation is highly nonlinear, which makes the model computationally demanding. To improve the computational efficiency of the model, the temperature dependency of the material constants (k, ρ, and c_p) is again removed from the conduction equation. Additionally, the equation is restructured, which results in the following simplified 1D heat conduction equation with a moving heat source in the x-direction:

$$\frac{\partial^2 T}{\partial x^2} + \frac{\zeta(x)}{k}P(t) = \frac{\rho c_\mathrm{p}}{k}\left(\frac{\partial T}{\partial t} + v\,(t)\,\frac{\partial T}{\partial x}\right) \tag{4.28}$$

To address the potential issues arising from the removal of temperature dependency, an optimization algorithm will be incorporated, similar to the approach used for the 2D LHT model. As detailed later in Section 4.2, this algorithm will fine-tune the model parameters at high frequencies, compensating for the inaccuracies introduced by the simplification and ensuring that the model remains both precise and effective.

4.2.2 1D Finite Difference Model

Similar to the approach taken in the 2D model (as discussed in Subsection 4.1.2), the FD method is used to maintain computational efficiency while benefiting from accurate numerical solutions. This method involves calculating temperatures at discrete points,

known as nodes, which collectively form a nodal network. Figure 4.4 illustrates the nodal network utilized to solve the model described by Equation (4.28). In this representation, each node corresponds to a specific region defined by Δx, with T_m denoting the temperature of node m. Additionally, the coordinate system in the 1D model is transformed from the x coordinate system to the m coordinate system. Since these concepts have been previously discussed in Subsection 4.1.2, the focus of this subsection will be on their application to the 1D model.

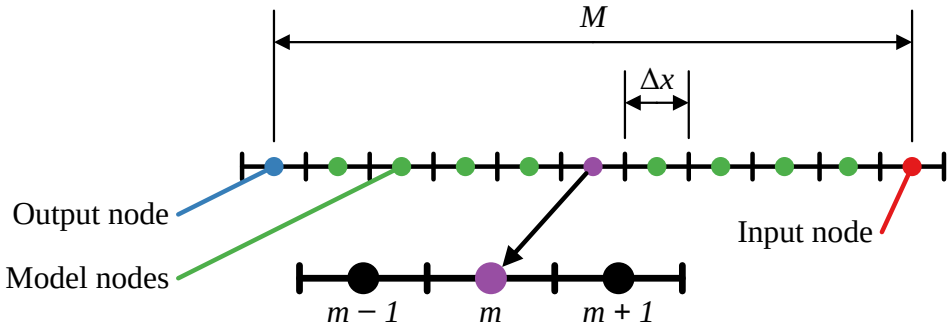


Figure 4.4: Schematic representation of the nodal network for the 1D FD conduction model of the L-DED process.

As explained previously, the 1D model prioritizes the solidified region within the HAZ, as highlighted in Figure 4.3. This region, situated at the trailing edge of the melt pool, is crucial for influencing the microstructure and mechanical properties of the deposition during manufacturing. By concentrating on this area, as shown in Figure 4.5, the 1D model can capture key thermal dynamic features such as the melt pool's trailing edge position and the spatial cooling rate.

As with the 2D model, the governing PDEs in the 1D model are solved by replacing them with difference approximations [183]. Since the model operates within a restricted region, it requires deriving difference approximations for both internal model nodes and boundary nodes.

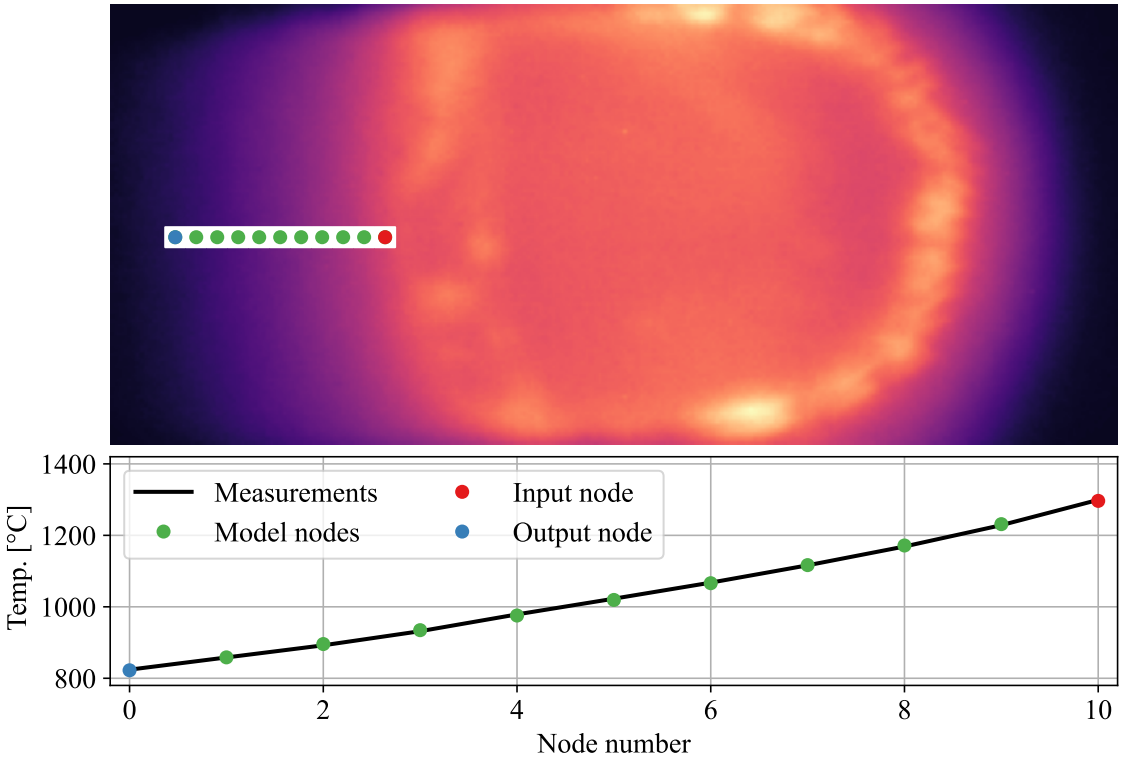


Figure 4.5: Illustration of the LDED process highlighting the melt pool and the nodal network projected onto the solidified region, along with a temperature graph corresponding to the model's temperature predictions.

For the first derivatives in space ∂x, the first-order central-difference approximation is used for the internal model nodes. Meanwhile, for the boundary nodes (output node and input node), the first-order forward-difference and backward-difference approximations, respectively, are utilized. These difference approximations can be expressed as follows:

$$\left.\frac{\partial T}{\partial x}\right|_m^p \approx \begin{cases} \dfrac{T_{m+1}^p - T_{m-1}^p}{2\Delta x}, & \text{if } 0 < m < M \\ \dfrac{2T_{m+1}^p - 2T_m^p}{2\Delta x}, & \text{if } m = 0 \\ \dfrac{2T_m^p - 2T_{m-1}^p}{2\Delta x}, & \text{if } m = M \end{cases} \tag{4.29}$$

For the second derivatives in space ∂x^2, the second-order central-difference approximation is used for the internal model nodes. To account for the rate of temperature change at the boundary nodes, a second-order spatial derivative with the Neumann boundary condition [188] is incorporated. The resulting difference approximations are as follows:

$$\left.\frac{\partial^2 T}{\partial x^2}\right|_m^p \approx \begin{cases} \dfrac{T_{m+1}^p - 2T_m^p + T_{m-1}^p}{\Delta x^2}, & \text{if } 0 < m < M \\ \dfrac{2T_{m+1}^p - 2T_m^p}{\Delta x^2} - \dfrac{2T_L^p}{\Delta x}, & \text{if } m = 0 \\ \dfrac{-2T_m^p + 2T_{m-1}^p}{\Delta x^2} + \dfrac{2T_R^p}{\Delta x}, & \text{if } m = M \end{cases} \tag{4.30}$$

Similarly, the model needs to be discretized in time [183]. Introducing the integer p to indicate the time dependency of T, the time derivative can be approximated using the forward-difference method as follows:

$$\left.\frac{\partial T}{\partial t}\right|_m^p \approx \frac{T_m^{p+1} - T_m^p}{\Delta t}, \quad \forall m \in M \tag{4.31}$$

The FD form of the 1D model is obtained by substituting the FD approximation Equations (4.29), (4.30), and (4.31) into Equation (4.28). This results in three distinct FD form equations, each restricting temperature determination to discrete points in space and time: one equation for the internal model nodes, one for the left boundary node, and one for the right boundary node. Rewriting these equations in terms of the unknown nodal temperature at the future time frame T_m^{p+1} and grouping all coefficients of T_m^p together yields:

$$T_m^{p+1} = \begin{cases} (1 - 2\text{Fo})\, T_m^p + (\text{Fo} + K_v v^p)\, T_{m+1}^p + (\text{Fo} - K_v v^p)\, T_{m-1}^p & \text{if } 0 < m < M \\ (1 - 2\text{Fo} - 2K_v v^p)\, T_m^p + (2\text{Fo} + 2K_v v^p)\, T_{m+1}^p - K_T T_L^p & \text{if } m = 0 \\ (1 - 2\text{Fo} + 2K_v v^p)\, T_m^p + (2\text{Fo} - 2K_v v^p)\, T_{m-1}^p + K_T T_R^p + K_P P^p & \text{if } m = M \end{cases} \tag{4.32}$$

Here, Fo represents the FD form of the Fourier number, defined as:

$$\mathrm{Fo} = \alpha \frac{\Delta \mathrm{t}}{(\Delta \mathrm{x})^2} \tag{4.33}$$

where α denotes the thermal diffusivity of the material [m^2/s].

Additionally, K_T, K_v, and K_P are defined as:

$$K_T = \frac{k}{\rho c_\mathrm{p}} \frac{2\Delta \mathrm{t}}{(\Delta \mathrm{x})} \qquad K_v = \frac{\Delta \mathrm{t}}{2\Delta \mathrm{x}} \qquad K_P = \frac{\zeta}{\rho c_\mathrm{p}} \Delta t \tag{4.34}$$

The current FD model has two unknown temperatures, T_L^p and T_R^p, due to the Neumann boundary condition. These temperatures specify the rate at which the node temperature is allowed to vary at the boundary. For the output node, the term $K_T T_L^p$ is substituted by $K_T T_{m+1}^p$, where $K_T = \beta \frac{2\Delta \mathrm{t}}{(\Delta \mathrm{x})}$, with β representing a new tuning parameter. Similarly, for the input node, the term $K_T T_R^p$ is incorporated into $K_P P^p$, where $K_P = \gamma \Delta t$, with γ being another tuning parameter. These two new tuning parameters, β and γ, provide flexibility in adjusting the boundary conditions of the model. This flexibility is crucial for optimizing the model's prediction accuracy. With these adjustments, the final form of the 1D finite difference model is given by:

$$T_m^{p+1} = \begin{cases} (1 - 2\mathrm{Fo})\, T_m^p + (\mathrm{Fo} + K_v v^p)\, T_{m+1}^p + (\mathrm{Fo} - K_v v^p)\, T_{m-1}^p, & \text{if } 0 < m < M \\ (1 - 2\mathrm{Fo} - 2K_v v^p)\, T_m^p + (2\mathrm{Fo} + 2K_v v^p - K_T)\, T_{m+1}^p, & \text{if } m = 0 \\ (1 - 2\mathrm{Fo} + 2K_v v^p)\, T_m^p + (2\mathrm{Fo} - 2K_v v^p)\, T_{m-1}^p + K_P P^p, & \text{if } m = M \end{cases} \tag{4.35}$$

where

$$\mathrm{Fo} = \alpha \frac{\Delta \mathrm{t}}{(\Delta \mathrm{x})^2} \qquad K_T = \beta \frac{2\Delta \mathrm{t}}{\Delta \mathrm{x}} \qquad K_v = \frac{\Delta \mathrm{t}}{2\Delta \mathrm{x}} \qquad K_P = \gamma \Delta t \tag{4.36}$$

With this final FD form of the 1D thermal dynamic model, the unknown nodal temperatures at the future time frame T_m^{p+1} are entirely calculated by the known nodal temperatures at the current time frame T_m^p and current inputs P^p and v^p. Similar to the 2D FD model, the resulting model is not unconditionally stable. The calculations may

lead to numerically induced oscillations, which may result in unstable diverging solutions. To prevent such instability, the value of Δt should be maintained below a certain limit. This stability criterion is satisfied if "the coefficients of T_m of Equation (4.35) are greater than or equal to zero" [184]. Thus, the stability criterion becomes:

$$\begin{aligned} 1 - 2\text{Fo} &\geq 0 \\ 1 + 2\text{Fo} &\geq 0 \end{aligned} \tag{4.37}$$

Due to the relation $1 - 2\text{Fo} \leq 1 + 2\text{Fo}$, it is evident that the critical stability criterion is $1 - 2\text{Fo} \geq 0$. Upon specifying the values of Δx and α, the minimum value of Δt is derived from the stability criterion.

In addition to temperature predictions, the 1D finite difference model enables the prediction of the spatial cooling rate ∇T^p. This rate is determined by considering the temperatures at the input node T_M^p and output node T_0^p at time p, the total number of nodes between these two points denoted by M, the node size Δx, and the traveling speed of the process v^p. The spatial cooling rate is expressed mathematically as:

$$\nabla T^p = \frac{T_M^p - T_0^p}{M \cdot \Delta x} \cdot v^p \tag{4.38}$$

This equation plays a crucial role in the development of the model predictive control (MPC) algorithm, enabling real-time control of temperature gradients within the material.

Similar to the 2D finite difference model described by Equation (4.12), the accuracy of the 1D model represented by Equation (4.35) is heavily influenced by the length of the nodes (Δx) [183]. To ensure that the 1D model remains efficient when implemented in model-based control, it must operate at a speed that exceeds the camera's frame rate. Therefore, the node size is chosen to balance accuracy and computational efficiency. Specifically, each node must be large enough to handle the frame rate requirements of the IR camera while maintaining computational efficiency. Consequently, the node length is selected to match the length of 5 thermal pixels in the x direction. Additionally, to enhance the accuracy of temperature updates and reduce measurement noise caused by

spatter or smoke, four times as many pixels are considered along the y-direction. Using a 5×20 pixel area helps average measurements over a larger region, thereby improving the reliability of the temperature readings.

Through pixel binning, the temperatures from each 5×20 pixel area are averaged to create a new virtual pixel. Each individual pixel covers an area of 0.035×0.035 mm^2, leading to a new virtual pixel size that represents the combined area of the 5×20 thermal pixels. Consequently, each node in the 1D model effectively represents an area of 0.175×0.7 mm^2. This node size ensures that the model is not only accurate but also computationally efficient, making it suitable for real-time model-based control applications while maintaining efficiency at frame rates slightly higher than the camera's.

4.2.3 1D Adaptive Thermal Model

In the preceding subsections, a computationally efficient 1D thermal model (4.35) was developed for real-time prediction and control applications. This model relies on three key parameters: thermal diffusivity (α) and two boundary tuning parameters (β and γ). These parameters are influenced by factors such as material properties, temperature, and heat transfer direction, which drive the model's predictive accuracy. However, these factors are not explicitly included in the model, and the model simplifies heat transfer to solely the x-direction. While these simplifications enhance computational efficiency, they also impact prediction accuracy.

To address this, a similar optimization algorithm to the 2D adaptive model is introduced to tune the model's parameters in real-time. This algorithm updates the parameters more frequently than the rate at which the material properties change, ensuring that the model adapts quickly to variations in the thermal dynamics. This frequent updating helps to maintain high accuracy and robustness, even with the model's inherent simplifications. The optimization process seeks to minimize the error between thermal model predictions and corresponding process measurements.

This error is represented by the error vector (4.39), which is the difference between the model-predicted temperatures $\bar{\mathbf{T}}^p$ and the actual temperature measurements $\mathbf{T}^p$ at time frame p:

$$\mathbf{E}^p = \bar{\mathbf{T}}^p - \mathbf{T}^p \tag{4.39}$$

where $\mathbf{T}^p$ is a vector with all the model states at time frame p, and $\bar{\mathbf{T}}^p$ is a vector with all corresponding temperature measurements at time frame p.

To optimize the thermal model's predictive capabilities, a nonlinear optimization algorithm is developed [185]. The objective is to minimize the following objective function:

$$J = \min_{\boldsymbol{\theta}^p} \mathbf{E}^{p\prime} \mathbf{Q} \mathbf{E}^p \tag{4.40}$$

Here, $\mathbf{Q}$ represents a weighting matrix, while θ^p denotes a vector containing the three time-dependent model parameters α^p, β^p, and γ^p at time frame p:

$$\boldsymbol{\theta}^p = \begin{pmatrix} \alpha^p \\ \beta^p \\ \gamma^p \end{pmatrix} \tag{4.41}$$

It is worth noting that although the structure of the initial nonlinear optimization problem remains consistent, the vectors involved in the optimization process differ from those of the 2D model. In the 1D model, the error vector $\mathbf{E}^p$ (4.39) encompasses the differences between all model states and their corresponding measurements at time frame p, whereas in the 2D model, the error vector primarily focused on discrepancies in the peak temperature and spatial cooling rate predictions. By optimizing the model based on all states rather than just two states, the 1D model achieves a more accurate optimization process, which in turn improves the overall model dynamics and enhances its predictive capabilities. Additionally, the parameter vector θ^p now encapsulates different model parameters, reflecting the unique characteristics of the 1D thermal model compared to its 2D thermal model. Subsequently, integrating the time-dependent model parameters into the 1D thermal model from Equation (4.35) results in an 1D adaptive thermal

model. This adaptation enhances the model's predictive capabilities by accommodating changes in thermal dynamics over time. The updated 1D adaptive thermal model, which incorporates the three time-dependent model parameters, is presented below:

$$T_m^{p+1} = \begin{cases} \left(1 - 2\mathrm{Fo}^p\right) T_m^p + \left(\mathrm{Fo}^p + K_v v^p\right) T_{m+1}^p + \left(\mathrm{Fo}^p - K_v v^p\right) T_{m-1}^p, & \text{if } 0 < m < M \\ \left(1 - 2\mathrm{Fo}^p - 2K_v v^p\right) T_m^p + \left(2\mathrm{Fo}^p + 2K_v v^p - K_T^p\right) T_{m+1}^p, & \text{if } m = 0 \\ \left(1 - 2\mathrm{Fo}^p + 2K_v v^p\right) T_m^p + \left(2\mathrm{Fo}^p - 2K_v v^p\right) T_{m-1}^p + K_P^p P^p, & \text{if } m = M \end{cases} \tag{4.42}$$

where

$$\mathrm{Fo}^p = \alpha^p \frac{\Delta \mathrm{t}}{(\Delta \mathrm{x})^2} \qquad K_T^p = \beta^p \frac{2\Delta \mathrm{t}}{\Delta \mathrm{x}} \qquad K_v = \frac{\Delta \mathrm{t}}{2\Delta \mathrm{x}} \qquad K_P^p = \gamma^p \Delta t \tag{4.43}$$

Similarly, substituting the three time-dependent model parameters into the stability criterion from Equation (4.37) results in an adaptive stability criterion:

$$2\alpha_p \frac{\Delta \mathrm{t}}{(\Delta \mathrm{x})^2} - 1 \leq 0 \tag{4.44}$$

To ensure stability and prevent rapid changes in the model parameters during optimization, the same approach is taken to expand the objective function as for the 2D adaptive model. The optimization problem for the 1D model is subjected to the stability criterion outlined in Equation (4.44). Additionally, to tune the rate of change of the model parameters, the objective function is expanded to account for the rate of change. This approach helps maintain stability and consistency in the optimization process. The improved objective function is formulated as:

$$J = \min_{\boldsymbol{\theta}^p} \mathbf{E}^{p\prime} \mathbf{Q} \mathbf{E}^p + \Delta \boldsymbol{\theta}^{p\prime} \mathbf{R} \Delta \boldsymbol{\theta}^p \tag{4.45}$$

where $\mathbf{R}$ a weighting matrix and $\Delta\theta^p$ a vector containing the rate at which the three material constants changed compared to the previous time frame $p-1$, formulated as:

$$\Delta \boldsymbol{\theta}^p = \boldsymbol{\theta}^p - \boldsymbol{\theta}^{p-1} \tag{4.46}$$

An improvement over the constraints applied in the 2D adaptive model is implemented in the 1D model optimization process. In the 1D adaptive model, both minimum and maximum constraints are imposed on the model parameters θ^p to ensure they remain within acceptable bounds throughout optimization. These constraints prevent unrealistic parameter values and maintain the stability of the optimization process, and they are given by:

$$\boldsymbol{\theta}_{\min} \leq \boldsymbol{\theta}^p \leq \boldsymbol{\theta}_{\max} \tag{4.47}$$

Additionally, to further enhance the robustness of the optimization algorithm, constraints are imposed on the incremental change in model parameters $\Delta\theta^p$. This improvement signifies a more sophisticated approach to parameter optimization aimed at preventing rapid changes in the model parameters. By enforcing constraints on the incremental changes in parameters, the optimization process maintains stability and prevents erratic fluctuations. Consequently, this refined approach enhances the effectiveness and reliability of the optimization process. The incremental constraints are given by:

$$\Delta\boldsymbol{\theta}^p_{\min} \leq \Delta\boldsymbol{\theta}^p \leq \Delta\boldsymbol{\theta}^p_{\max} \tag{4.48}$$

The resulting 1D adaptive thermal model is integrated into the real-time operating system outlined in Section 3.1. Python 3.9 [189] serves as the primary platform for all numerical computations. Utilizing the efficiency of the NumPy library [190] for array operations and mathematical functions, it handles all real-time numerical calculations. Additionally, the optimization problem is solved using the *SLSQP* solver from the *scipy.optimize* toolbox [191], chosen for its robustness in handling constrained nonlinear optimization problems. This Python-centric approach simplifies the integration of the optimization process into industrial systems, enabling efficient real-time control and optimization of thermal processes.

4.2.4 Advantages of the 1D Adaptive Thermal Model

The developed 1D adaptive thermal model introduces a novel approach to thermal dynamic prediction within LMP, emphasizing the potential advantages of its modeling methodology for real-time applications. Initially, a comparison between the 1D and 2D models highlights the specific advantages of the former in terms of computational efficiency and scalability. Following this, a comparative analysis of the aspects of the model against commonly used methods in the literature is conducted to unveil both similarities and distinctive features, thereby emphasizing the novelty and efficacy of the proposed model.

The 1D adaptive thermal model offers numerous advantages over its 2D counterpart. Firstly, it simplifies the analysis by focusing solely on conduction within the solidified region of the material, where convection and radiation effects are negligible. This targeted approach reduces computational complexity while enhancing precision and relevance for processes that require detailed thermal analysis of the solidified areas. Secondly, by simplifying the energy input as a point heat source, the 1D model is not limited to laser-based applications and can be applied to other processes like arc welding and wire arc additive manufacturing, expanding its versatility and applicability. Moreover, its computational efficiency is notably higher due to the reduced complexity of solving heat transfer equations in one dimension rather than two. This efficiency translates to faster prediction times, making the 1D model much more suitable for real-time control applications where timely decision-making is crucial. The simplification of one-dimensional modeling, combined with the use of simplified model parameters, further streamlines the computational process, allowing for faster model optimization. Additionally, the inclusion of optimization parameters for both the model input and output enhances the model's adaptability and utility in real-world applications. As a result, the 1D model can more quickly adapt to changes in process conditions, ensuring consistent performance and reliability. Overall, these advantages position the 1D adaptive thermal model as a more accurate, more versatile, and more efficient tool for thermal dynamic prediction and control applications compared to its 2D counterpart.

Comparing the 1D adaptive thermal model with traditional analytical solutions like the Rosenthal solution [85] reveals its flexibility and accuracy in representing real-world scenarios. Both models share a mutual objective in modeling thermal conduction dynamics across various dimensions, including 1D systems. While both methods leverage mathematical formulations to describe heat transfer processes, they diverge significantly in methodologies and capabilities. The Rosenthal solution relies on analytical expressions derived from simplified assumptions, often suitable for specific geometries and boundary conditions. However, its rigid framework may struggle to capture intricate thermal dynamics or adapt to diverse scenarios. In contrast, the 1D adaptive thermal model employs numerical techniques, offering greater flexibility and accuracy in representing real-world scenarios. By discretizing the domain and iteratively solving the heat equation, the model accommodates non-linearities, variable boundary conditions, and material properties, enabling an accurate prediction of the thermal dynamic behavior. Its use of a restricted nodal network enables tailoring to the specific requirements of each application or process, optimizing efficiency without sacrificing prediction accuracy. Furthermore, the model's adaptive nature enables it to dynamically adjust to varying systems and conditions, positioning it as a superior tool for studying and predicting thermal conduction in real-time across various practical applications. By leveraging numerical techniques and a restricted nodal network, the model offers greater flexibility and accuracy in representing real-world scenarios compared to traditional analytical solutions like the Rosenthal model. This flexibility is anticipated to enable a more comprehensive analysis of thermal behavior, particularly in dynamic or non-linear systems.

The 1D adaptive thermal model utilizes the finite difference model (FDM) method, chosen primarily to accommodate real-time thermal data captured from an IR camera. This selection aligns with the square nodes and square image pixels typically utilized in IR imaging, facilitating seamless integration between the model and the thermal data. While the model is built upon the numerical FDM method as its foundation, it distinguishes itself from conventional FDM and finite element model (FEM) methods through its innovative combination of a restricted nodal network and an advanced optimization algorithm. This unique approach enables the dynamic adjustment of model parameters

in real-time. Moreover, the size and location of the restricted nodal network can be precisely tailored based on the specific requirements of each application or process, thanks to the optimization algorithm. By strategically optimizing computational resources and predictive accuracy, this synergy empowers the 1D adaptive thermal model to surpass traditional FDM and FEM approaches in terms of flexibility, computational efficiency, and prediction accuracy, making it ideal for various real-time thermal prediction and control applications.

Compared to traditional optimization methods such as Kalman filtering [192] or gradient-based techniques [193], the optimization algorithm used in this research offers several advantages, particularly for real-time thermal prediction and control applications. The algorithm's adaptability and flexibility align closely with the dynamic nature of thermal systems, allowing it to accommodate a broad spectrum of system behaviors and uncertainties. Kalman filtering, by contrast, is suited for linear, Gaussian systems and may struggle with the nonlinearities and complexities inherent in the thermal dynamics of LMP processes. Furthermore, traditional gradient-based methods often require explicit knowledge of the system's mathematical model and face challenges with computational complexity or convergence in real-time scenarios. In contrast, the employed algorithm uses a cost function with constraints similar to MPC algorithms, iteratively adjusting parameters based on system behavior and predictive performance. This process improves model prediction accuracy over time without relying on explicit models or restrictive assumptions, offering a robust, adaptive, and efficient solution for parameter estimation and optimization in dynamic thermal systems.

In summary, the developed 1D adaptive thermal model offers a comprehensive solution for real-time thermal dynamic prediction and control, surpassing the 2D and conventional methods in terms of flexibility, efficiency, and accuracy. By leveraging numerical techniques, a restricted nodal network, and an advanced optimization algorithm, the model can accommodate complex thermal dynamics and diverse system conditions. Its ability to dynamically adjust parameters in real-time makes it an invaluable tool for thermal dynamic prediction and control during various applications and processes.

4.2.5 Summary

In this section, a novel 1D adaptive thermal model was developed for accurate and efficient prediction and control of the thermal dynamics during LDED processes. Initially, a 1D thermal dynamic model based on PDEs governing conduction was formulated to describe the thermal behavior within the solidified region of the HAZ. Subsequently, the FD method was utilized to discretize these equations for a restricted region within the solidified region of the HAZ, enabling numerical solutions specific to this area and improving computational efficiency. Furthermore, the model's prediction accuracy was improved through the implementation of a model parameter estimation algorithm, dynamically adjusting the model parameters in real-time to compensate for model simplifications and minimize prediction errors. The resulting 1D adaptive thermal model is integrated into the real-time operating system, enabling real-time prediction and control of the temperatures and spatial cooling rate during LDED processes. Finally, the comparative analysis highlighted that the developed 1D adaptive thermal model surpasses the 2D and conventional methods in terms of flexibility, efficiency, and accuracy, thereby offering a comprehensive solution for real-time thermal dynamic prediction and control.

4.3 Chapter Summary

This chapter presents the development of two adaptive thermal models tailored for predicting and controlling thermal dynamics in LMP. Initially, a 2D model focusing on LHT is developed, wherein PDEs governing the heat transfer are formulated, and numerical solutions are obtained using the FD method. Additionally, a model parameter estimation algorithm is incorporated to dynamically adjust material constants, thereby enhancing prediction accuracy. Subsequently, a 1D model optimized for LDED processes is developed. Similarly to its 2D counterpart, the 1D model utilizes PDEs, the FD method, and a model parameter estimation algorithm. However, the 1D model represents a significant advancement over the 2D model, prioritizing efficiency, accuracy, and suitability for control applications. Furthermore, the subsequent chapter will present the integration of the 2D thermal model into an MPCs algorithm and the integration of the 1D adaptive thermal model into an adaptive model predictive controls algorithm.

Chapter 5

Model Predictive Control for Laser Material Processing

Model predictive control (MPC) is an advanced process control method designed to operate within a set of constraints. Its key advantage over traditional error-based controllers, such as proportional-integral-derivative controllers, is its ability to anticipate future process behavior. This is achieved by solving an optimization problem using a dynamic model of the process—in this case, the thermal model of the laser material processing (LMP) process developed in the previous chapter. By iteratively solving these optimization problems based on dynamic models, MPC determines optimal process inputs that consider both current and future states, optimizing not only the present conditions but also preparing for future changes.

An important aspect of these control strategies is the use of a thermal model to effectively manage the thermal dynamics of the process. By leveraging MPC to control these dynamics, the system can precisely regulate the temperature and cooling rates in real time. This level of precision is crucial because thermal dynamics directly influence how the material's microstructure evolves during processing. Therefore, by optimizing thermal dynamics through MPC and employing an accurate thermal model, it is possible to indirectly influence and refine the material's microstructure. This approach not only

ensures optimal control of temperature and cooling rates but also achieves the desired microstructure characteristics, leading to enhanced material properties and improved process stability.

The chapter begins with the development of an MPC algorithm for single-input single-output (SISO) peak temperature control during laser heat treatment (LHT), utilizing the two-dimensional (2D) thermal model presented in the preceding chapter (4.12). Subsequently, the chapter delves into the development of a multi-input multi-output (MIMO) adaptive model predictive control (AMPC) algorithm for simultaneous temperature and spatial cooling rate control, leveraging the improved one-dimensional (1D) adaptive thermal model presented in the preceding chapter (4.42). This controller represents a significant step forward from the previous SISO MPC version, as it leverages the advantages of the 1D adaptive model. This model not only enhances computational efficiency, increases prediction accuracy, and improves adaptability to varying dynamics during the process, but also introduces MIMO control capability. This allows the controller to address complex, varying dynamics during the process by simultaneously controlling multiple process parameters, resulting in improved overall performance and stability of the process, which is critical to achieving consistent and repeatable material characteristics.

5.1 SISO Model Predictive Control for LHT

This section presents the development of a MPC algorithm utilizing the 2D thermal model (4.12) for real-time prediction and control of the peak temperature during LHT. Before delving into the linear MPC algorithm, it is important to explore other types of MPC algorithms, such as nonlinear model predictive control (NMPC), robust model predictive control (RMPC), and explicit model predictive control (EMPC). NMPC is a method of MPC where predictions are made using nonlinear models compared to linear models with linear MPC. Although these issues are convex in linear MPC, they may no longer be convex in nonlinear MPC. This presents difficulties for the numerical solution and NMPC stability theory and results in higher computational requirements. RMPC is a set of MPC algorithms that account for set bounded disturbances while still ensuring state constraints are met. This addition to account for set-bounded disturbances will increase the computational requirement. The higher the complexity of the model, the higher the computational requirement to add robustness to MPC. With EMPC, the control solutions to the MPC problem are pre-computed offline. This requires significantly less real-time computation. However, the pre-computation of the control variables scales badly with the increasing complexity of the problem and model. In addition, each new process requires the pre-computation of the control variables, which makes it less suitable for process control during manufacturing.

Given the computational challenges with NMPC, RMPC, and EMPC, linear MPC is selected for the control algorithm to enable real-time prediction and control of the peak temperature during LHT. First, the 2D thermal model is transformed into a state-space model, enabling the prediction of future temperatures by process input increments. Subsequently, an objective function is constructed to minimize the deviation between the actual and reference peak temperatures, as well as the change in the process control input increments for optimal control response. Furthermore, the cost function is transformed into a quadratic optimization problem, and inequality constraints are defined to improve computational efficiency and assure a stable process within acceptable and viable parameters. Finally, the implementation of this MPC algorithm is presented.

5.1.1 SISO State-Space Model Formulation

To formulate the optimization problem for MPC, the 2D thermal model represented by Equation (4.12) is transformed into a standard state-space model. This state-space model, as depicted in Equation (5.1), consists of two equations: one governing the evolution of the state vector $\mathbf{x}(p)$ over time, and another relating the output $\mathbf{y}(p+1)$ to the state vector.

$$\begin{cases} \mathbf{x}(p+1) &= \mathbf{A}\mathbf{x}(p) + \mathbf{B}\mathbf{u}(p) \\ \mathbf{y}(p+1) &= \mathbf{C}\mathbf{x}(p+1) \end{cases} \tag{5.1}$$

where $\mathbf{x}(p)$ represents the state vector, $\mathbf{A}$, $\mathbf{B}$, and $\mathbf{C}$ are the state-space matrices, and $\mathbf{u}(p)$ is the input vector at time frame p. Furthermore, the output $\mathbf{y}(p+1)$ represents the output vector with the temperature of a specific node at the average location of the peak temperature within the LHT process.

The states $\mathbf{x}(p)$ of the state-space model encompass all nodal temperatures $T^p_{j,i}$ of the nodal network depicted in Figure 4.2. Each element $T^p_{j,i}$ represents the temperature at a specific node within the nodal network. These temperatures are organized into the following state matrix of size $N+1 \times M+2$:

$$\mathbf{T}^p = \begin{bmatrix} T^p_{1,1} & \cdots & T^p_{1,M+2} \\ \vdots & \ddots & \vdots \\ T^p_{N+1,1} & \cdots & T^p_{N+1,M+2} \end{bmatrix} \tag{5.2}$$

By rearranging $\mathbf{T}^p$ into a state vector $\mathbf{x}(p)$, each element $x_i(p)$ of $\mathbf{x}(p)$ corresponds to the temperature at a particular node. This state vector is given by:

$$\mathbf{x}(p) = \begin{bmatrix} x_1(p) \\ x_2(p) \\ \vdots \\ x_{N\times M}(p) \end{bmatrix} = \begin{bmatrix} T^p_{2,2} \\ T^p_{2,3} \\ \vdots \\ T^p_{N+1,M+1} \end{bmatrix} \tag{5.3}$$

Furthermore, the input vector $\mathbf{u}(p)$ of the state-space model contains laser power P^p and the traveling speed v^p as the process inputs, as given by:

$$\mathbf{u}(p) = \begin{bmatrix} P^p \\ v^p \end{bmatrix} \tag{5.4}$$

The current input vector includes two process inputs, but since the laser power P^p remains constant during the process, only the traveling speed v^p varies. As a result, the controller is reduced to a SISO system with one varying input and a single output. This reduction simplifies the control algorithm and improves computational efficiency.

While the standard state-space formulation offers a detailed view of process dynamics, it often struggles with capturing incremental changes, leading to suboptimal control performance and reduced stability, especially when dealing with complex process dynamics and model uncertainties. To address this, an alternative state-space formulation focused on incremental changes is implemented, improving the controller's ability to changing process dynamics and mitigate the effects of modeling inaccuracies. The incremental state-space formulation involves expressing the model states and inputs in terms of their changes from one time step to the next. This incremental representation, denoted as $\Delta\mathbf{x}(p) = \mathbf{x}(p) - \mathbf{x}(p-1)$ and $\Delta\mathbf{u}(p) = \mathbf{u}(p) - \mathbf{u}(p-1)$, captures the variations occurring between consecutive time steps. While the state variables are represented incrementally, it is important to note that the controller still requires the total value of the output for control purposes. To obtain the total output value at the future time step, $\mathbf{y}(p+1)$ is expressed as $\mathbf{y}(p+1) = \mathbf{y}(p) + \Delta\mathbf{x}(p+1)$. Integrating these incremental variables into the state-space model results in:

$$\begin{aligned} \overbrace{\begin{bmatrix} \Delta\mathbf{x}(p+1) \\ \mathbf{y}(p+1) \end{bmatrix}}^{\tilde{\mathbf{x}}(p+1)} &= \overbrace{\begin{bmatrix} \mathbf{A} & \mathbf{0} \\ \mathbf{CA} & \mathbf{I} \end{bmatrix}}^{\tilde{\mathbf{A}}} \overbrace{\begin{bmatrix} \Delta\mathbf{x}(p) \\ \mathbf{y}(p) \end{bmatrix}}^{\tilde{\mathbf{x}}(p)} + \overbrace{\begin{bmatrix} \mathbf{B} \\ \mathbf{CB} \end{bmatrix}}^{\tilde{\mathbf{B}}} \Delta\mathbf{u}(p) \\ \mathbf{y}(p+1) &= \overbrace{\begin{bmatrix} \mathbf{0} & \mathbf{I} \end{bmatrix}}^{\tilde{\mathbf{C}}} \overbrace{\begin{bmatrix} \Delta\mathbf{x}(p+1) \\ \mathbf{y}(p+1) \end{bmatrix}}^{\tilde{\mathbf{x}}(p+1)} \end{aligned} \tag{5.5}$$

5.1.2 SISO Optimization Problem Formulation

After defining the state-space model, a standard objective function J is constructed to minimize deviations from the reference state and penalize changes in control inputs. This optimization problem aims to find the optimal control input increments $\Delta\mathbf{u}(p)$ that minimizes J. Specifically, the objective function minimizes the deviation of predicted outputs from their references over the prediction horizon N_p while penalizing changes in control inputs over the control horizon N_c. Additionally, a terminal penalty is included at the end of the prediction horizon to ensure a smooth transition. The objective function is expressed as follows:

$$\begin{aligned} J = \min_{\Delta\mathbf{U}(p)} & \sum_{i=p}^{p+N_p-1} \left[\mathbf{y}(i+1) - \mathbf{y}_{\mathrm{ref}}(i+1)\right]^T \mathbf{Q} \left[\mathbf{y}(i+1) - \mathbf{y}_{\mathrm{ref}}(i+1)\right]. \\ & + \sum_{i=p}^{p+N_c-1} \left[\Delta\mathbf{u}(i)^T \mathbf{R} \Delta\mathbf{u}(i)\right] + \left[\mathbf{y}(N_p) - \mathbf{y}_{\mathrm{ref}}(N_p)\right]^T \mathbf{P} \left[\mathbf{y}(N_p) - \mathbf{y}_{\mathrm{ref}}(N_p)\right] \end{aligned} \tag{5.6}$$

where $\Delta\mathbf{U}(p) = [\Delta\mathbf{u}(p), \Delta\mathbf{u}(p+1), \ldots, \Delta\mathbf{u}(p+N_c-1)]$ is the vector with the predicted change in the process inputs from time step p till $p+N_c-1$; $\mathbf{R}$ are the weighting matrices for the process inputs increments $\Delta\mathbf{u}$ from time step p till $p+N_c-1$; $\mathbf{Q}$ are the weighting matrices for the reference tracking errors from time steps p till $p+N_p-1$, with the reference tracking error denoted as the difference between the predicted outputs $\mathbf{y}$ and the reference process setpoints $\mathbf{y}_{\mathrm{ref}}$; and $\mathbf{P}$ is the terminal weighting matrix for the reference tracking error at the final time step of the prediction horizon N_p.

Determining the prediction horizon N_p and the control horizon N_c are essential steps in tuning the MPC algorithm. The prediction horizon dictates the number of future time steps over which the controller predicts outputs, while the control horizon determines the number of future time steps over which the controller adjusts control inputs. A longer prediction horizon, characterized by a larger N_p, enables the controller to anticipate future changes in the process with greater accuracy. This extended horizon allows for more robust planning and adaptation to anticipated changes in the process dynamics.

However, a larger prediction horizon also leads to increased computational complexity since the controller needs to analyze and optimize predictions over a more extended time span. Conversely, a shorter prediction horizon with a smaller prediction horizon reduces the computational burden but may result in less accurate predictions. A shorter horizon may limit the controller's ability to predict and adapt to future changes in the process effectively, particularly in scenarios with dynamic or unpredictable changes.

Similarly, the control horizon N_c determines the duration over which the controller adjusts control inputs to achieve the desired behavior of the process. A longer control horizon, characterized by a larger N_c, allows the controller to plan control actions over an extended period. This longer horizon facilitates more comprehensive optimization of the process performance over time, potentially leading to smoother transitions and improved overall performance. However, a larger control horizon also increases computational demands since the controller must analyze and optimize control inputs over a longer time frame. In contrast, a smaller control horizon reduces computational complexity but may limit the controller's ability to react to changes during the process effectively, particularly in scenarios requiring rapid or precise adjustments. Therefore, selecting appropriate values for N_p and N_c involves striking a balance between predictive accuracy, computational efficiency, and responsiveness to changes during the process.

To efficiently solve the objective function, it needs to be rewritten as a quadratic objective function. This involves expressing the cost function in terms of the prediction matrices and weighting matrices, followed by transforming it into a quadratic form. Beginning with the objective function, it is rewritten in terms of the prediction matrices as follows:

$$J = \min_{\Delta\mathbf{U}(p)} \left[\mathbf{Y}(p) - \mathbf{Y}_{\mathrm{ref}}(p)\right]^T \mathbf{Q} \left[\mathbf{Y}(p) - \mathbf{Y}_{\mathrm{ref}}(p)\right] + \Delta\mathbf{U}(p)^T \mathbf{R} \Delta\mathbf{U}(p) \tag{5.7}$$

Here, $\mathbf{Y}(p)$ represents the predicted output vector over the prediction horizon, while $\mathbf{Y}_{\mathrm{ref}}(p)$ denotes the reference output vector over the same horizon. The term $\Delta\mathbf{U}(p)$ refers to the process input increment vector over the control horizon. Additionally, $\mathbf{Q}$ represents the full prediction weighting matrix applied over the prediction horizon to

address reference tracking errors, while $\mathbf{R}$ serves as the full weighting matrix utilized over the control horizon to manage process input increments.

To create a concise formulation of the prediction model, the predicted output vector $\mathbf{Y}(p)$ and the process input increment vector $\Delta\mathbf{U}(p)$ expressed in terms of the state and input matrices yields:

$$\mathbf{Y}(p) = \mathbf{\Phi}\tilde{\mathbf{x}}(p) + \mathbf{\Gamma}\Delta\mathbf{U}(p) \tag{5.8}$$

where $\mathbf{\Phi}$ is the prediction matrix, representing the relationship between the state vector and the predicted output, while $\mathbf{\Gamma}$ is the control matrix, governing the influence of process inputs on the predicted outputs. Moreover, $\tilde{\mathbf{x}}(p)$ refers to the state vector at time p.

Substituting this concise prediction model into the objective function results in:

$$\begin{aligned} J = \min_{\Delta\mathbf{U}(p)} & \left[\mathbf{\Phi}\tilde{\mathbf{x}}(p) + \mathbf{\Gamma}\Delta\mathbf{U}(p) - \mathbf{Y}_{\text{ref}}(p)\right]^T \mathbf{Q}\left[\mathbf{\Phi}\tilde{\mathbf{x}}(p) + \mathbf{\Gamma}\Delta\mathbf{U}(p) - \mathbf{Y}_{\text{ref}}(p)\right] \\ & + \Delta\mathbf{U}(p)^T\mathbf{R}\Delta\mathbf{U}(p) \end{aligned} \tag{5.9}$$

To transform the objective function into a quadratic form, it is essential to expand and simplify the expression. This involves multiplying out the terms, collecting similar terms, and eliminating constant values that do not affect the optimization problem. Following these steps, the resulting quadratic expression in terms of $\Delta\mathbf{U}(p)$ is given by:

$$J = \min_{\Delta\mathbf{U}(p)} \frac{1}{2}\Delta\mathbf{U}(p)^T\mathbf{G}\Delta\mathbf{U}(p) + \Delta\mathbf{U}(p)^T\mathbf{F}\tilde{\mathbf{x}}(p) \tag{5.10}$$

where $\mathbf{G}$ is defined as $2(\mathbf{R} + \mathbf{\Gamma}^T\mathbf{Q}\mathbf{\Gamma})$ and serves as the quadratic term matrix, and $\mathbf{F}$ is characterized by $-2\mathbf{\Gamma}^T\mathbf{Q}\mathbf{\Phi}$ and acts as the linear term matrix. These matrices are fundamental in transforming the cost function into a quadratic form, facilitating efficient optimization procedures for the predictive control problem.

With the resulting quadratic objective function, the optimal process input increments $\Delta\mathbf{U}^*(p)$ can be found by solving:

$$\Delta\mathbf{U}^*(p) = -\mathbf{G}^{-1}\mathbf{F}\left(\mathbf{\Phi}\tilde{\mathbf{X}}(p) - \mathbf{Y}_{\text{ref}}(p)\right) \tag{5.11}$$

The optimal process input at time step p is then obtained by adding the optimal process input increment to the previous process input at time step $p-1$:

$$\mathbf{u}(p) = \mathbf{u}(p-1) + \Delta\mathbf{u}(p) \tag{5.12}$$

Since the MPC algorithm will be implemented on a real LMP system shown in Figure 3.1, the MPC optimization problem will be subjected to process input constraints and process input increment constraints. These constraints can be written as:

$$\mathbf{U}_{\min} \leq \mathbf{U}(p) \leq \mathbf{U}_{\max} \qquad \Delta\mathbf{U}_{\min} \leq \Delta\mathbf{U}(p) \leq \Delta\mathbf{U}_{\max} \tag{5.13}$$

To integrate the constraints from Equation (5.13) into the quadratic objective function, they must first be redefined in a quadratic form. By leveraging Equation (5.12), all input constraints can be expressed in terms of $\Delta\mathbf{U}(p)$. This yields the following quadratic formulation:

$$\mathbf{W}\Delta\mathbf{U}(p) \leq \mathbf{d} \tag{5.14}$$

where $\mathbf{W}$ is the coefficient matrix and $\mathbf{d}$ is the constraint vector.

By integrating the quadratic objective function (5.10) with the quadratic constraints (5.14), the resultant quadratic optimization problem is expressed as follows:

$$\text{minimize} \quad \frac{1}{2}\Delta\mathbf{U}(p)^T\mathbf{G}\Delta\mathbf{U}(p) + \Delta\mathbf{U}(p)^T\mathbf{F}\tilde{\mathbf{x}}(p) \tag{5.15}$$

$$\text{subject to} \quad \mathbf{W}\Delta\mathbf{U}(p) \leq \mathbf{d} \tag{5.16}$$

5.1.3 SISO MPC Implementation

The MPC algorithm involves solving a quadratic optimization problem with input increment constraints, as defined by Equation (5.15). To efficiently address this optimization problem, a quadratic programming (QP) solver is used. Specifically, the *quadprog* solver from the *Optimization Toolbox* [187] in *MATLAB R2021a* [186] is used. QP solvers are tailored to handle quadratic optimization problems by utilizing specialized algorithms that efficiently find optimal solutions while satisfying the constraints. Using the *quadprog* solver for the MPC algorithm enhances computational efficiency, providing a versatile and robust method of solving the quadratic optimization problem associated with adjusting the process inputs to achieve the desired process behavior. The MPC algorithm is integrated into the real-time operating system described in Section 3.1. Here, temperature measurements from an infrared camera update the MPC model states. Subsequently, the optimal traveling speed is determined by solving Equation (5.15), comparing the measured peak temperature with the reference peak temperature. Afterwards, the optimal traveling speed is sent to the LHT process to control the process to the desired peak temperature. A block diagram illustrating this closed-loop process is presented in Figure 5.1.

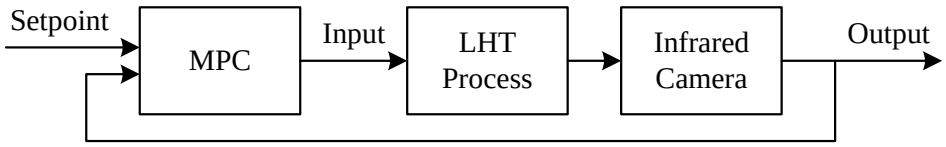


Figure 5.1: MPC block diagram used to control the peak temperature during LHT.

5.2 MIMO Adaptive Model Predictive Control for LDED

Building upon the insights gained from the development of the MPC algorithm for SISO control discussed in the previous section, which utilizes the 2D thermal dynamic model, this section presents a novel AMPC algorithm tailored for MIMO control. The AMPC algorithm leverages the adaptability and efficiency of the 1D thermal dynamic model to extend the capabilities of the control system.

First, the equations of both the 1D thermal model and the spatial cooling rate calculation are transformed into state-space matrices. Subsequently, the individual state-space matrices are combined into a single MIMO state-space model, enabling the prediction of future temperatures and spatial cooling rates by process input increments. Secondly, an objective function is formulated to minimize the deviation between the actual and reference temperatures, as well as the spatial cooling rate, while also aiming to minimize variations in the increments of process control inputs to optimize control response. Moreover, the cost function is transformed into a quadratic optimization problem, and inequality constraints are defined to improve computational efficiency and assure a stable process within acceptable and viable parameters. Finally, the implementation of this MPC algorithm is presented.

5.2.1 MIMO State-Space Model Formulation

Similar to the MPC algorithm presented in Section 5.1, to construct an optimization problem for the AMPC algorithm, the model equations must first be transformed into a state-space model. This subsection first presents the design of two SISO state-space models from the one-dimensional adaptive thermal model (4.42) and the spatial cooling rate (4.38), respectively. Afterwards, these two SISO state-space models are combined into a single MIMO state-space model.

First SISO Adaptive State-Space Model

Utilizing the adaptive thermal model (4.42), a novel adaptive SISO state-space formulation is introduced, tailored to dynamically respond to the evolving dynamics of the system. Unlike conventional static state-space models, this adaptive model enables the controller to continually adapt its parameters based on real-time feedback from thermal measurements, improving prediction accuracy and robustness during the process. The adaptive SISO state-space formulation is constructed as follows:

$$\begin{cases} \mathbf{T}^{p+1} & = \mathbf{A_1}^p \mathbf{T}^p + \mathbf{B_1}^p P^p \\ \mathbf{y}_1^{p+1} & = \mathbf{C_1} \mathbf{T}^{p+1} \end{cases} \tag{5.17}$$

where $\mathbf{T}^p$ is the state vector; $\mathbf{A_1}^p$ is the adaptive state matrix; $\mathbf{B_1}^p$ is the adaptive input vector; $\mathbf{C_1}$ is the output vector; P^p is the laser power; and p is the current time-frame. Furthermore, the output $y_1(p+1)$ represents the temperature of the input node, which is located in the solidified region at the edge of the melt pool during the laser-directed energy deposition (LDED) process.

The state vector $\mathbf{T}^p$ of the state-space model is a vector representation of all nodal temperatures T_m^p of the nodal network depicted in Figure 4.4. It is structured as follows:

$$\mathbf{T}^p = \begin{bmatrix} T_0^p \\ T_1^p \\ \vdots \\ T_{M-1}^p \\ T_M^p \end{bmatrix} \tag{5.18}$$

In the formulation of the first adaptive state-space model regarding the temperature distribution of the solidified region behind the melt pool, the model includes the multiplication of the traveling speed v^p with the nodal temperatures T_m^p due to the incorporation of a moving heat source. Here, an assumption is made that the traveling speed remains relatively constant throughout the prediction horizon N_p. This implies that once v^p is

set to its initial value at time step p, it maintains a consistent value across the entire horizon. This assumption effectively linearizes the influence of v^p, simplifying the control problem by removing its time-varying behavior and nonlinearity from the state-space equations. This assumption is based on the fact that the traveling speed in the LDED process significantly impacts material characteristics. Rapid changes in the traveling speed can introduce undesired variations in the process, thereby greatly affecting the quality of the end product. Consequently, the traveling speed typically changes gradually during the process. The laser power P^p directly influences the temperatures of the heat-affected zone in the LDED process, making it critical for achieving and maintaining desired temperatures. By reducing the state-space formulation to include only the laser power as the single process input and having a single output, the controller is simplified to a SISO system. This reduction significantly enhances the computational efficiency of the control algorithm, enabling real-time optimization and control of the laser power to maintain a consistent temperature at the edge of the melt pool. With this approach, the adaptive state-space matrices A_1, $\mathrm{B}_1{}^p$, and C_1 are defined as follows:

$$\mathbf{A_1}^p = \begin{bmatrix} 1-2\mathrm{Fo}^p-2K_v v^p & 2\mathrm{Fo}^p+2K_v v^p-K_T^p & & & & \\ \mathrm{Fo}^p-K_v v^p & 1-2\mathrm{Fo}^p & \mathrm{Fo}^p+K_v v^p & & & \\ & \ddots & \ddots & \ddots & & \\ & & \mathrm{Fo}^p-K_v v^p & 1-2\mathrm{Fo}^p & \mathrm{Fo}^p+K_v v^p & \\ & & & -2\mathrm{Fo}^p-2K_v v^p & 1-2\mathrm{Fo}^p+2K_v v^p & \end{bmatrix} \tag{5.19}$$

$$\mathbf{B_1}^p = \begin{bmatrix} 0 \\ 0 \\ \vdots \\ 0 \\ K_P^p \end{bmatrix} \tag{5.20}$$

$$\mathbf{C_1} = \begin{bmatrix} 0 & 0 & \cdots & 0 & 1 \end{bmatrix} \tag{5.21}$$

This first SISO adaptive state-space formulation enables the AMPC algorithm to continually optimize the laser power P to maintain a consistent temperature at the edge of the melt pool T_M, utilizing the known nodal temperatures T_m^p, laser power P^p, and traveling speed v^p.

Second SISO Adaptive State-Space Model

Utilizing the spatial cooling rate calculation (4.38), a second novel adaptive SISO state-space formulation is introduced and is constructed as follows:

$$\begin{cases} \nabla \mathrm{T}^{p+1} & = \mathrm{A}_2 \nabla \mathrm{T}^p + \mathrm{B}_2{}^p v^p \\ \mathbf{y}_2^{p+1} & = \mathrm{C}_2 \nabla \mathrm{T}^{p+1} \end{cases} \tag{5.22}$$

where $\nabla \mathrm{T}^p$ is the single state; A_2 is the zero state matrix; $\mathrm{B}_2{}^p$ is the adaptive input vector; C_2 is the output vector; v^p is the traveling speed; and p is the current time-frame.

In the formulation of the second adaptive state-space model regarding the spatial cooling rate $\nabla \mathrm{T}^p$, the model includes the multiplication of the spatial temperature gradient $\frac{T_M^p - T_0^p}{M \cdot \Delta x}$ with the traveling speed v^p. Here, an assumption is made that the nodal temperatures T_M^p and T_0^p remain relatively constant throughout the prediction horizon N_p. This implies that once the initial values of T_M^p and T_0^p are set at time step p, they maintain a consistent value across the entire horizon. This assumption effectively linearizes the influence of T_M^p and T_0^p, simplifying the control problem by removing its time-varying behavior and nonlinearity from the state-space equations. This simplification is based on the fact that small variations in the traveling speed do not significantly affect these temperatures over the prediction horizon. Instead, the traveling speed itself predominantly impacts the spatial cooling rate. Therefore, to appropriately capture this dynamic relationship, the focus during the optimization of process inputs within the MPC framework centers on the speed rather than the gradient of temperature states. Furthermore, by reducing the state-space formulation to include only the traveling speed as the single process input and having a single output, the controller complexity is reduced to a SISO system. This reduction in complexity simplifies the control algorithm

and enhances its computational efficiency. This approach enables the optimization and control of the traveling speed to maintain a consistent spatial cooling rate. With this assumption, the adaptive state-space matrices A_2, ${\mathrm{B}_2}^p$, and C_2 are defined as follows:

$$\mathrm{A}_2 = \begin{bmatrix} 0 \end{bmatrix} \tag{5.23}$$

$${\mathrm{B}_2}^p = \begin{bmatrix} \frac{T_M^p - T_0^p}{M \cdot \Delta x} \end{bmatrix} \tag{5.24}$$

$$\mathrm{C}_2 = \begin{bmatrix} 1 \end{bmatrix} \tag{5.25}$$

This second SISO adaptive state-space formulation enables the AMPC algorithm to continually optimize the traveling speed v to maintain a consistent spatial cooling rate ∇T, utilizing the known nodal temperatures T_m^p and traveling speed v^p.

MIMO Adaptive State-Space Model

The MIMO adaptive state-space model integrates the two SISO adaptive state-space models introduced earlier. While each model individually addresses different aspects of the thermal dynamics, the glsmimo framework combines these aspects to manage multiple inputs and outputs simultaneously. This integration allows for a more comprehensive control approach, accommodating interactions between temperature distribution and spatial cooling rate within the overall system.

The MIMO adaptive state-space model is given by:

$$\begin{cases} \mathbf{x}(p+1) & = \mathbf{A}^p \mathbf{x}(p) + \mathbf{B}^p \mathbf{u}(p) \\ \mathbf{y}(p+1) & = \mathbf{C}\mathbf{x}(p+1) \end{cases} \tag{5.26}$$

where $\mathbf{x}(p)$ is the state vector; $\mathbf{A}^p$ is the adaptive state matrix; $\mathbf{B}^p$ is the adaptive input matrix; $\mathbf{C}$ is the output matrix; $\mathbf{u}(p)$ is the input vector; and p is the current time-frame.

The MIMO state vector $\mathbf{x}(p)$ encompasses the state variables from both SISO models, representing the nodal temperatures $\mathbf{T}^p$ and the spatial cooling rate $\nabla \mathrm{T}^p$, and is given by:

$$\mathbf{x}(p) = \begin{bmatrix} \mathbf{T}^p \\ \nabla \mathrm{T}^p \end{bmatrix} \tag{5.27}$$

The MIMO input vector $\mathbf{u}(p)$ incorporates the process inputs from both SISO models, including the laser power $\mathbf{P}^p$ and the traveling speed v^p, and is expressed as:

$$\mathbf{u}(p) = \begin{bmatrix} P^p \\ v^p \end{bmatrix} \tag{5.28}$$

The MIMO adaptive state-space matrices $\mathbf{A}^p$, $\mathbf{B}^p$, and $\mathbf{C}$ include the adaptive state-space matrices of both SISO models, positioned diagonally within the MIMO formulation:

$$\mathbf{A}^p = \begin{bmatrix} \mathbf{A_1}^p & 0 \\ 0 & \mathrm{A}_2 \end{bmatrix} \tag{5.29}$$

$$\mathbf{B}^p = \begin{bmatrix} \mathbf{B_1}^p & 0 \\ 0 & \mathrm{B}_2{}^p \end{bmatrix} \tag{5.30}$$

$$\mathbf{C} = \begin{bmatrix} \mathbf{C_1} & 0 \\ 0 & \mathrm{C}_2 \end{bmatrix} \tag{5.31}$$

This combined MIMO adaptive state-space formulation enables the AMPC algorithm to continually and simultaneously optimize the laser power P and traveling speed v to maintain a consistent temperature at the edge of the melt pool T_M and a consistent spatial cooling rate $\nabla \mathrm{T}$ by utilizing only the known nodal temperatures T_m^p, laser power P^p, and traveling speed v^p.

MIMO Incremental Adaptive State-Space Model

Similar to the SISO MPC algorithm utilizing the 2D thermal model in Section 5.1, the developed MIMO state-space model is reformulated as a MIMO incremental state-space model. This reformulation expresses the model states and inputs in terms of their changes from one time step to the next, improving the controller's ability to adapt to changing process dynamics and mitigate the effects of modeling inaccuracies. The MIMO incremental adaptive state-space model is defined as follows:

$$\begin{aligned} \overbrace{\begin{bmatrix} \Delta\mathbf{x}(p+1) \\ \mathbf{y}(p+1) \end{bmatrix}}^{\tilde{\mathbf{x}}(p+1)} &= \overbrace{\begin{bmatrix} \mathbf{A}^p & \mathbf{0} \\ \mathbf{C}\mathbf{A}^p & \mathbf{I} \end{bmatrix}}^{\tilde{\mathbf{A}^p}} \overbrace{\begin{bmatrix} \Delta\mathbf{x}(p) \\ \mathbf{y}(p) \end{bmatrix}}^{\tilde{\mathbf{x}}(p)} + \overbrace{\begin{bmatrix} \mathbf{B}^p \\ \mathbf{C}\mathbf{B}^p \end{bmatrix}}^{\tilde{\mathbf{B}^p}} \Delta\mathbf{u}(p) \\ \mathbf{y}(p+1) &= \overbrace{\begin{bmatrix} \mathbf{0} & \mathbf{I} \end{bmatrix}}^{\tilde{\mathbf{C}}} \overbrace{\begin{bmatrix} \Delta\mathbf{x}(p+1) \\ \mathbf{y}(p+1) \end{bmatrix}}^{\tilde{\mathbf{x}}(p+1)} \end{aligned} \tag{5.32}$$

5.2.2 MIMO Optimization Problem Formulation

After establishing the MIMO state-space model, an objective function J is formulated to optimize the control inputs while minimizing deviations from the reference states. Similar to the SISO case in Section 5.1, the objective is to find the optimal control input $\mathbf{u}(p)$ that minimizes J. However, in the MIMO setting, the objective function now considers multiple output states $\mathbf{y}(p)$ compared to the single output state $y(p)$ in the SISO model. Similarly to the SISO case, the objective function aims to minimize the deviations of predicted outputs $\mathbf{Y}(p)$ from their respective references $\mathbf{Y}_{\text{ref}}(p)$ over the prediction horizon N_{p}, while also penalizing changes in control inputs $\Delta\mathbf{U}(p)$ over the control horizon N_{c}. Additionally, a terminal penalty is applied at the end of the prediction horizon to ensure a smooth transition.

The MIMO objective function is expressed as follows:

$$\begin{aligned} J = \min_{\Delta \mathbf{U}(p)} & \sum_{i=p}^{p+N_p-1} \left[\mathbf{y}(i+1) - \mathbf{y}_{\text{ref}}(i+1)\right]^T \mathbf{Q} \left[\mathbf{y}(i+1) - \mathbf{y}_{\text{ref}}(i+1)\right]. \\ & + \sum_{i=p}^{p+N_c-1} \left[\Delta \mathbf{u}(i)^T \mathbf{R} \Delta \mathbf{u}(i)\right] + \left[\mathbf{y}(N_p) - \mathbf{y}_{\text{ref}}(N_p)\right]^T \mathbf{P} \left[\mathbf{y}(N_p) - \mathbf{y}_{\text{ref}}(N_p)\right] \end{aligned} \tag{5.33}$$

To efficiently solve the objective function, it needs to be rewritten as a quadratic objective function. Much like the SISO case in Section 5.1, this involves expressing the cost function in terms of the prediction matrices and weighting matrices, followed by transforming it into a quadratic form. This enables a more compact representation of the objective function and simplifies the optimization process, making it computationally more efficient. Beginning with the objective function, it is rewritten in terms of the prediction matrices as follows:

$$J = \min_{\Delta \mathbf{U}(p)} \left[\mathbf{Y}(p) - \mathbf{Y}_{\text{ref}}(p)\right]^T \mathbf{Q} \left[\mathbf{Y}(p) - \mathbf{Y}_{\text{ref}}(p)\right] + \Delta \mathbf{U}(p)^T \mathbf{R} \Delta \mathbf{U}(p) \tag{5.34}$$

To efficiently solve this objective function as well, it is crucial to create a concise formulation of the MIMO prediction model. Expressing the predicted output vector $\mathbf{Y}(p)$ and the process input increment vector $\Delta \mathbf{U}(p)$ in terms of the adaptive state and adaptive input matrices yields:

$$\mathbf{Y}(p) = \mathbf{\Phi}^p \tilde{\mathbf{x}}(p) + \mathbf{\Gamma}^p \Delta \mathbf{U}(p) \tag{5.35}$$

where matrix $\mathbf{\Phi}^p$ represents the dynamic relationship between the state vector and the predicted output, adapting over time to capture the dynamic behavior of the process. Similarly, $\mathbf{\Gamma}^p$ is the adaptive control matrix, dictating how changes in process inputs influence the predicted outputs. Together, these matrices enables dynamic adjustments in the prediction during the process, ensuring prediction accuracy during the varying process. Additionally, $\tilde{\mathbf{x}}(p)$ denotes the current state vector at time p.

Substituting this expression into the objective function results in:

$$J = \min_{\Delta \mathbf{U}(p)} \left[\mathbf{\Phi}^p \tilde{\mathbf{x}}(p) + \mathbf{\Gamma}^p \Delta \mathbf{U}(p) - \mathbf{Y}_{\text{ref}}(p)\right]^T \mathbf{Q} \left[\mathbf{\Phi}^p \tilde{\mathbf{x}}(p) + \mathbf{\Gamma}^p \Delta \mathbf{U}(p) - \mathbf{Y}_{\text{ref}}(p)\right] + \Delta \mathbf{U}(p)^T \mathbf{R} \Delta \mathbf{U}(p) \tag{5.36}$$

To convert the MIMO objective function into a quadratic form for the MIMO controller, it is necessary to expand and simplify the expression. This process entails multiplying out the terms, grouping similar terms, and eliminating constant values that do not impact the optimization problem. The resulting quadratic expression, in terms of $\Delta \mathbf{U}(p)$, is as follows:

$$J = \min_{\Delta \mathbf{U}(p)} \frac{1}{2} \Delta \mathbf{U}(p)^T \mathbf{G}^p \Delta \mathbf{U}(p) + \Delta \mathbf{U}(p)^T \mathbf{F}^p \tilde{\mathbf{x}}(p) \tag{5.37}$$

where $\mathbf{G}^p$ is defined as $2(\mathbf{R} + \mathbf{\Gamma}^{pT} \mathbf{Q} \mathbf{\Gamma}^p)$ and serves as the adaptive quadratic term matrix, and $\mathbf{F}^p$ is characterized by $-2\mathbf{\Gamma}^{pT} \mathbf{Q} \mathbf{\Phi}^p$ and acts as the adaptive linear term matrix. These matrices are fundamental in transforming the cost function into a quadratic form, facilitating efficient optimization procedures for the predictive control problem.

The optimal process input increments $\Delta \mathbf{U}^*(p)$ can then be found by solving:

$$\Delta \mathbf{U}^*(p) = -\mathbf{G}^{p-1} \mathbf{F}^p \left(\mathbf{\Phi}^p \tilde{\mathbf{x}}(p) - \mathbf{Y}_{\text{ref}}(p)\right) \tag{5.38}$$

Identical to the SISO case in Section 5.1, the optimal process inputs at time step p are then obtained by adding the optimal process inputs increment $\Delta \mathbf{u}$ to the previous process inputs $\mathbf{u}$ at time step $p-1$:

$$\mathbf{u}(p) = \mathbf{u}(p-1) + \Delta \mathbf{u}(p) \tag{5.39}$$

Similarly, the AMPC algorithm will be implemented on a real LMP system shown in Figure 3.1 and is therefore also subjected to process input constraints and process input increment constraints, which are expressed as:

$$\mathbf{U}_{\min} \leq \mathbf{U}(p) \leq \mathbf{U}_{\max} \qquad \Delta\mathbf{U}_{\min} \leq \Delta\mathbf{U}(p) \leq \Delta\mathbf{U}_{\max} \tag{5.40}$$

Also, the constraints from Equation (5.40) are redefined in quadratic form. By leveraging Equation (5.39), all input constraints can be expressed as:

$$\mathbf{W}\Delta\mathbf{U}(p) \leq \mathbf{d} \tag{5.41}$$

where $\mathbf{W}$ is the coefficient matrix and $\mathbf{d}$ is the constraint vector.

By integrating the quadratic objective function (5.37) with the quadratic constraints (5.41), the resulting quadratic optimization problem is expressed as follows:

$$\text{minimize} \quad \frac{1}{2}\Delta\mathbf{U}(p)^T\mathbf{G}^p\Delta\mathbf{U}(p) + \Delta\mathbf{U}(p)^T\mathbf{F}^p\tilde{\mathbf{x}}(p) \tag{5.42}$$

$$\text{subject to} \quad \mathbf{W}\Delta\mathbf{U}(p) \leq \mathbf{d} \tag{5.43}$$

5.2.3 MIMO AMPC Implementation

Similar to the implementation of the SISO MPC algorithm for LHT in Section 5.1, the implementation of the MIMO AMPC algorithm for LDED involves addressing a quadratic optimization problem and enforcing quadratic constraints as defined by Equation (5.42). Therefore, a QP solver is employed to find the optimal control inputs. While the MATLAB environment was utilized for the SISO MPC algorithm, Python 3.9 [189] was chosen for the implementation of the MIMO AMPC algorithm. This choice leverages powerful numerical computing libraries such as NumPy [190] and SciPy [191] for numerical calculations. Additionally, the *quadprog* solver from the *qpsolvers* library [194] is utilized to solve the quadratic optimization problem defined by Equation (5.42).

Furthermore, the AMPC algorithm is integrated into the real-time operating system outlined in Section 3.1. In this setup, temperature measurements of the process are obtained from an infrared camera to update the 1D adaptive thermal model and subsequently adjust the matrices within the quadratic optimization problem of Equation (5.42). Afterwards, the optimal process inputs are determined by solving Equation (5.42), which compares the measured states with the reference states. Once the quadratic optimization problem with constraints is solved, the optimal traveling speed and laser power are sent to the LDED process to control the process to the preferred temperature and spatial cooling rate. A block diagram illustrating this closed-loop process is presented in Figure 5.2.

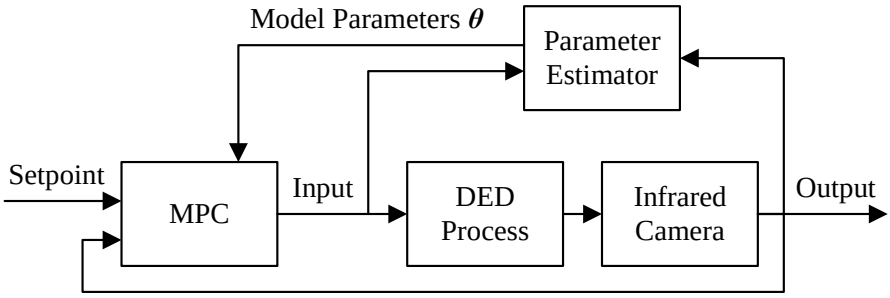


Figure 5.2: AMPC block diagram used to control the process inputs during LDED.

5.3 Chapter Summary

This chapter introduces the development of two MPC algorithms designed to control the thermal dynamics in LMP processes with the aim of indirectly optimizing the material's microstructure. Initially, an MPC algorithm is constructed for SISO peak temperature control during LHT. Here, the 2D thermal model, as defined by Equation (4.12), is used to formulate a SISO state-space model. Subsequently, this model is used for constructing a quadratic optimization problem with constraints for the MPC algorithm. Following this, an AMPC algorithm is designed for MIMO temperature and spatial cooling rate control during LDED. Utilizing the 1D adaptive thermal model (4.42), a MIMO state-space model is constructed. Leveraging this model, an adaptive quadratic optimization problem with constraints is formulated for the AMPC algorithm. The MIMO AMPC algorithm signifies a notable advancement beyond its SISO MPC counterpart. Notably, this algorithm harnesses the computational efficiency and adaptability of the 1D adaptive model. Moreover, compared to the single process parameter control in the SISO MPC algorithm, the AMPC algorithm enables precise control of multiple process parameters simultaneously. These advancements significantly enhance process stability, which is crucial for achieving consistent and repeatable material characteristics.

Chapter 6

Experiments

This chapter presents the experiments to validate the thermal dynamic models introduced in Chapter 4 and the model predictive control (MPC) algorithms developed in Chapter 5. The overarching objective of these experiments is to achieve real-time accurate prediction and precise control of thermal dynamics in laser material processing (LMP) processes, thereby ensuring consistent material characteristics with the focus on the microstructure. To achieve this goal, the experimental setup and thermal dynamic monitoring methodology detailed in Chapter 3 are utilized.

The chapter is structured as follows: First, a series of experiments are designed to validate the real-time thermal dynamic prediction capabilities of the developed thermal dynamic models. Then, experiments are designed to validate the real-time control capabilities of the MPC algorithms.

6.1 Real-Time Thermal Dynamic Prediction Experiments

This section presents a wide range of experiments designed to assess and validate the real-time thermal dynamic prediction capabilities of the developed thermal models. With a focus on both laser heat treatment (LHT) and laser-directed energy deposition (LDED) processes, the experiments aim to systematically evaluate the performance and accuracy of the thermal models under varying conditions. The following subsections delve into the specifics of the experimental designs, starting with LHT experiments followed by LDED experiments. Additionally, the evaluation criteria utilized to assess the performance of these models are explained in the subsequent section.

6.1.1 2D Adaptive Thermal Model Predictions in LHT

The objective of the two-dimensional (2D) adaptive thermal model is to accurately predict the thermal dynamics of the LHT process in real-time, including peak temperature and spatial cooling rate. To accomplish this, a series of LHT experiments are designed to assess and validate the predictive capabilities of the 2D adaptive thermal model. These experiments exclusively consist of single-track LHT experiments, where the substrates are heat-treated in single straight lines, as shown in Figure 6.1.

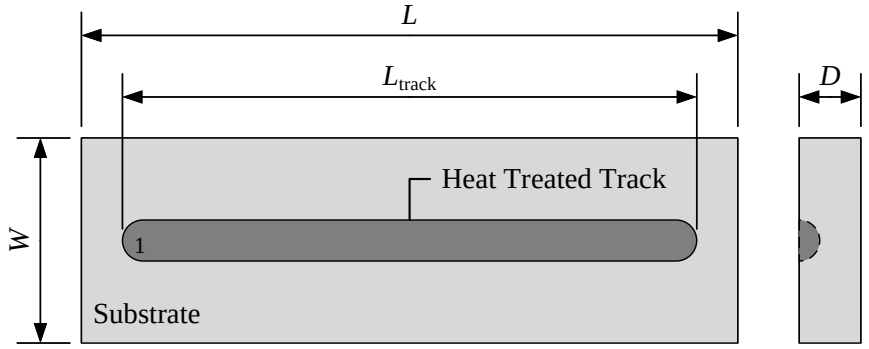


Figure 6.1: Single-track LHT experimental case and substrate dimensions.

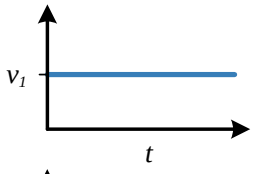
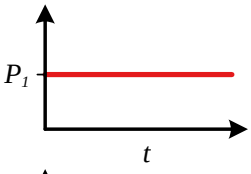
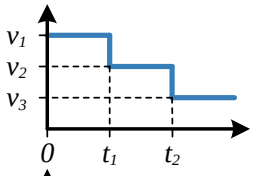
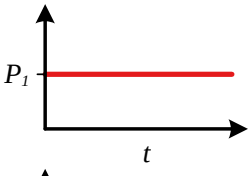
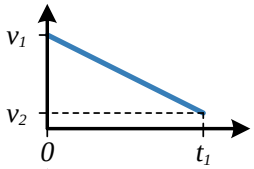
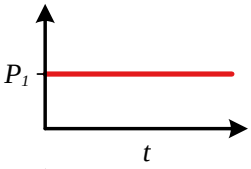
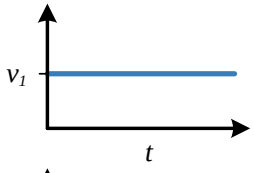
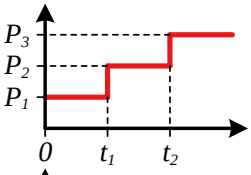
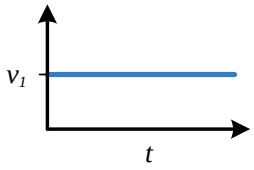
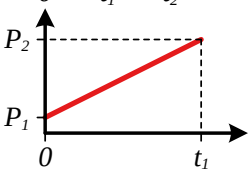
In Figure 6.1, L, W, and D represent the length, width, and thickness of the substrate, respectively, while L_{track} denotes the length of the heat-treated track. The experiments are carried out using two distinct substrate materials, with specifications outlined in Table 6.1. To improve laser absorption, the substrates will undergo sandblasting and ethanol rinsing to eliminate any contamination prior to conducting the experiments.

Table 6.1: LHT substrate material specifications.

Material	**Standard**	**Dimensions** ($L \times W \times D$)	**Track Length** (L_{track})
Carbon Steel	AISI 1018	$150 \times 38 \times 6$ mm	135 mm
Stainless Steel	AISI 304L	$150 \times 25 \times 6$ mm	135 mm

The LHT process is controlled by two primary parameters: laser power and traveling speed. Moreover, these two parameters serve as the sole inputs for the 2D adaptive thermal model. Therefore, it is vital to validate the 2D adaptive thermal model across variations in these process inputs. To achieve this, five distinct experiment cases are designed, each involving different laser power and traveling speed signals during the LHT process, as outlined in Table 6.2. Each experiment case incorporates a variety of input signal profiles, including constant, step, and ramp profiles. These input signals are carefully selected to excite a diverse range of modes within the LHT process to ensure a thorough evaluation of the 2D adaptive thermal model. Furthermore, the heat-treated track length (L_{track}) for each experiment is 135 mm. All five experiment cases are conducted for both substrate materials detailed in Table 6.1. The complete set of process parameters for these experiments can be found in Appendix A.1.

Table 6.2: The five distinct LHT experiment cases conducted for both substrate materials, each with a track length (L_{track}) of 135 mm.

LHT Exp. Case	**Traveling Speed**	**Laser Power**
1. *Const*		
2. v_{step}		
3. v_{ramp}		
4. P_{step}		
5. P_{ramp}		

Before conducting these experiments, the optimal size for the region of interest of the 2D nodal network shown in Figure 4.2 is determined experimentally, resulting in $M = 25$, $m_1 = 13$, and $N = 8$. Additionally, the coefficients for the laser radius and the order of the Gaussian profile of the laser heat source (4.11) are determined experimentally, resulting in $r = 1.5$ mm and $\eta = 0.15$, respectively. The laser absorption coefficient from Equation (4.11) is adopted from previous research [50], where $\mu = 3$.

6.1.2 1D Adaptive Thermal Model Predictions in LDED

Similar to the 2D model, the objective of the one-dimensional (1D) adaptive thermal model is to predict the thermal dynamics of the LDED process in real-time, including temperatures and the spatial cooling rate of the solidified region. To accomplish this, a series of LDED experiments are designed to assess and validate the predictive capabilities of the 1D adaptive thermal model. These experiments exclusively consist of single-track LDED experiments, where material is deposited onto the substrate in a single straight line, as shown in Figure 6.2.

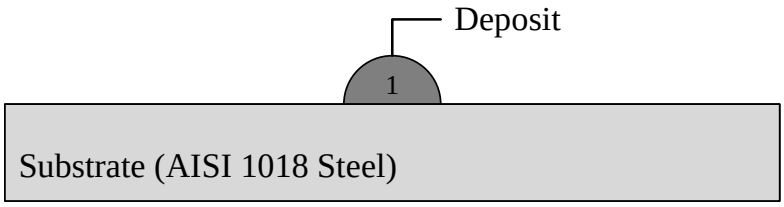


Figure 6.2: Single-track LDED experimental case.

The specifications of this substrate are detailed in Table 6.3, with corresponding dimensions visually depicted in Figure 6.1. Similar to the LHT experiments, for LDED, the substrates will also undergo sandblasting and ethanol rinsing to improve laser absorption and eliminate any contamination prior to conducting the experiments.

Table 6.3: LDED substrate material specifications.

Material	**Standard**	**Dimensions** ($L \times W \times D$)	**Track Length** ($L_{\mathbf{track}}$)
Carbon Steel	AISI 1018	$200 \times 50 \times 6$ mm	180 mm

The LDED process is mainly controlled by three primary parameters: laser power, traveling speed, and powder feed rate. While the current experimental setup, shown in Figure 3.1, lacks the capability to adjust the feed rate in real-time, the laser power

and traveling speed can be controlled. Moreover, these two parameters serve as the sole inputs for the 1D adaptive thermal model. Therefore, it is vital to validate the 1D adaptive thermal model across variations in these process inputs. To achieve this, a comprehensive signal profile was designed for both the laser power and traveling speed, as illustrated in Figure 6.3. Unlike the simpler input signals utilized for validating the 2D model during LHT experiments, the comprehensive signal profile designed for the LDED process incorporates a more intricate combination of ramp and step profiles for both laser power and traveling speed. This approach allows for the effective excitation of a more diverse range of modes within the LDED process during a single experiment, aiming to cover as many modes as possible. By capturing a broader range of modes within the LDED process in a single experiment, the efficiency of validation efforts is improved while reducing the need for multiple experiments and maximizing the insights gained.

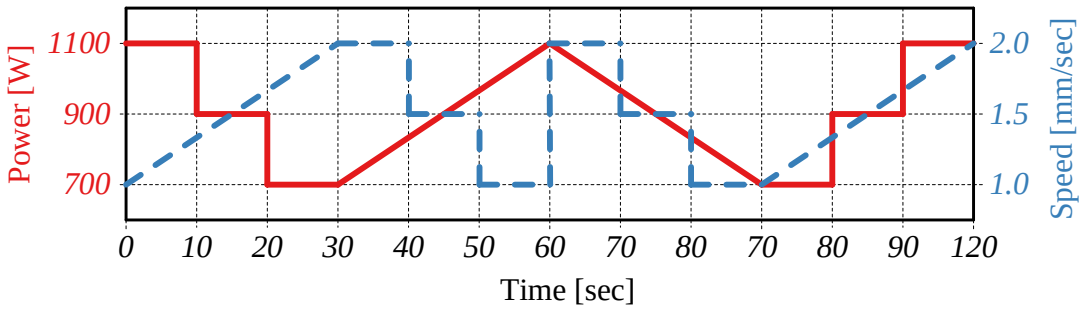


Figure 6.3: The LDED process inputs used for the adaptive 1D thermal model validation. The solid red line represents laser power, and the dashed blue line represents traveling speed.

In total, four experiments will be conducted using the substrate materials specified in Table 6.3 and with the process inputs described in Figure 6.3. Each experiment uses a distinct material, and the specifications of all four different materials are shown in Table 6.4. This approach allows for a comprehensive assessment of the 1D adaptive thermal model's sensitivity to varying material properties and enhances its generalizability across different materials.

Table 6.4: LDED deposition powder specifications.

LDED Exp. Case	Material	Size [µm]	Flow Rate [g/min]
1. IN 635	Inconel 625	∼100	2.63
2. STLT 6	Stellite® 6	∼100	2.61
3. H13 TS	H13 Tool Steel	∼100	2.43
4. SS 431	Stainless Steel 431	∼100	2.40

Furthermore, the deposition track length L_{track} for each experiment is 180mm. Before conducting these experiments, the optimal length of the 1D nodal network shown in Figure 4.4 is determined experimentally, resulting in $M = 10$.

6.1.3 Model Performance Evaluation

In order to evaluate the performance of the developed models quantitatively, the mean absolute percentage error (MAPE) between the measured and predicted parameters will be calculated. The MAPE is a measure of the average error between the process measurements and model predictions. In addition, the MAPE is easy to understand because the error is calculated in terms of percentages. On top of that, the MAPE is more natural compared to the root mean square error and is commonly used in the literature [195, 196]. The formula for MAPE is expressed as:

$$\text{MAPE} = \frac{1}{p}\sum_{i=1}^{p}\left|\frac{y_i - \hat{y}_i}{y_i}\right| \times 100\% \tag{6.1}$$

where p is the number of time frames, y_i represents the measured value, and $\hat{y}_i$ represents the predicted value.

6.2 Real-Time Microstructure Control Experiments

In this section, a wide range of experiments for both LHT and LDED processes are designed to assess and validate the real-time thermal dynamic control capabilities of the developed MPC algorithms. These experiments aim to evaluate the performance of the MPC algorithms in controlling the thermal dynamics, which in turn indirectly influences and optimizes the microstructure of the material. The experiments are structured to systematically test how well the MPC algorithms maintain consistent microstructure under varying process conditions by controlling thermal dynamics precisely.

The subsequent subsections will delve into the specific experimental designs, starting with closed-loop controlled LHT experiments and progressing to closed-loop controlled LDED experiments. By controlling thermal dynamics effectively, these experiments demonstrate the capability of the MPC algorithms to achieve desired microstructure characteristics through indirect control mechanisms.

6.2.1 Closed-Loop LHT Process with MPC

The primary objective of the LHT process is to modify the surface properties of materials, particularly enhancing the local hardness at a specific hardening depth. However, achieving consistent and reproducible surface properties of the heat-treated area remains one of the most significant challenges with LHT. Therefore, three LHT experiments are designed to assess the consistency of the hardness and hardening depth when controlling the peak temperature during the LHT process with the MPC algorithm. The first experiment case is a single-track LHT experiment, as shown in Figure 6.1 of the previous Subsection 6.1.1. This experiment case is designed to assess the controller's ability to control the peak temperature during the LHT process. The second experiment case is a multi-track LHT experiment, as shown in Figure 6.4. This experiment case is designed to include the effects of heat buildup in the material. The third experiment case is a single-track LHT experiment with variable thickness, as depicted in Figure 6.5. This experiment case is designed to incorporate the impacts of thermal dynamic changes on

different material thicknesses. The second and third experiment cases are thus selected to analyze the controller's capabilities and limitations when confronted with the introduced process disturbances. Additionally, open-loop experiments are performed for the second and third experiment cases to evaluate the differences between the open-loop and closed-loop experiments.

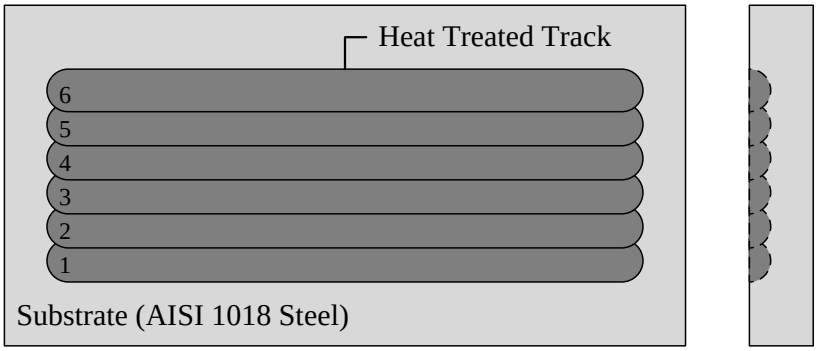


Figure 6.4: Multi-track LHT experimental case with adjacent tracks, top view (left), side view (right).

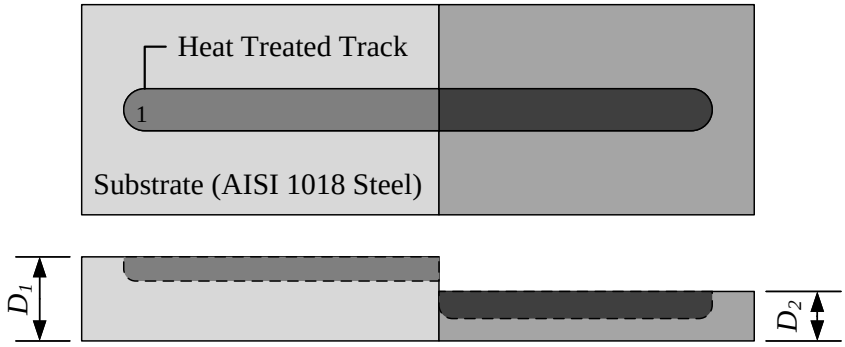


Figure 6.5: Single-track LHT experimental case on a substrate with variable thickness, top view (top), front view (bottom).

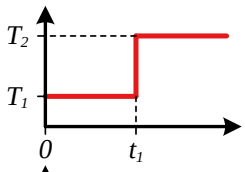
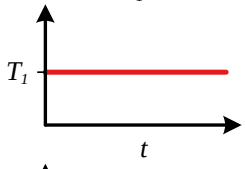
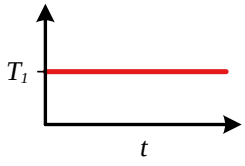
All three LHT experiment cases use a carbon steel (AISI 1018) substrate, with corresponding specifications provided in Table 6.5.

Table 6.5: Substrate specifications of the three experiment cases.

LHT Exp. Case	**Dimensions** ($L \times W \times D$)	**Track Length** ($L_{\mathbf{track}}$)
Single-track	$200 \times 25 \times 6$ mm	150 mm
Multi-track	$100 \times 38 \times 3$ mm	90 mm
Single-track	$100 \times 25 \times$ (6 and 3) mm	150 mm

With the three closed-loop LHT experiments, the process will be controlled to a certain setpoint, as illustrated in Table 6.6. In the first experiment case, the single-track will be controlled to a stepped temperature setpoint. In the second experiment case, all six tracks will be controlled to a single temperature setpoint. Finally, in the third experiment case, the single-track will be controlled to a single temperature setpoint while adapting to two different substrate thicknesses.

Table 6.6: Controller setpoints for the three LHT experiment cases with constant laser power.

LHT Exp. Case	**MPC Setpoints**		**Temp. Profile**	**Process Input**
	$\boldsymbol{T_1}$	$\boldsymbol{T_2}$		$\boldsymbol{P}$
1. Single-track	1100 °C	1300 °C		300 W
2. Multi-track	1200 °C	-		300 W
3. Single-track	1200 °C	-		300 W

The model used in the MPC algorithm relies on parameters that must be established prior to the experiments. The dimensions of the nodal network, illustrated in Figure 4.2, are configured to correspond with the size of the heat-affected zone and the relative position of the laser, yielding $M = 10$, $m_1 = 6$, and $N = 4$. The laser absorption coefficient is $\mu = 0.3$ [10], and the laser radius, determined experimentally, is $r = 1.5$ mm. Furthermore, selecting an appropriate prediction and control horizon for the MPC algorithm is crucial. A longer prediction horizon provides better insights into system dynamics and constraints, while an extended control horizon optimizes actions and responds proactively to future changes. However, longer horizons significantly increase the computational demand. Hence, finding the right balance between complexity and performance is essential. The horizon should be long enough to predict how changes in process inputs and temperature measurements on one side of the model impact the temperatures on the other side of the model. Consequently, the minimum horizon required to capture these dynamics is the model length M, which is ten. Conversely, a larger horizon substantially increases computational demands due to model complexity and state count. To constrain computational requirements while capturing essential dynamics, both prediction and control horizons are set to ten, denoted as $N_\mathrm{p} = N_\mathrm{c} = 10$.

6.2.2 Closed-Loop LDED Process with AMPC

The primary objective of the LDED process is to add material to a substrate in a controlled manner to build or repair parts. However, achieving consistent and reproducible material characteristics remains one of the most significant challenges. To address this, multiple LDED wall experiments are designed to evaluate the adaptive model predictive control (AMPC) algorithm's performance. Each experiment involves five layers with single-track depositions, as shown in 6.6. These experiments aim to assess various control strategies—open-loop, speed control, power control, and combined speed and power control—on material characteristics and evaluate the potential of multi-input multi-output (MIMO) control to significantly enhance the consistency and reproducibility of material characteristics during the LDED process.

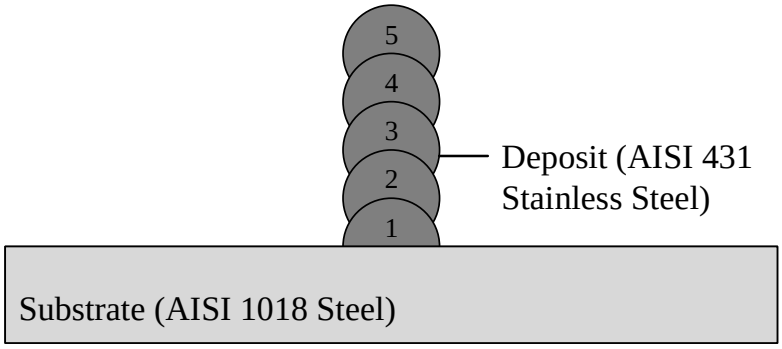


Figure 6.6: Five-layer LDED wall experimental case.

In total, four experiments will be conducted to evaluate the performance of the AMPC algorithm. The controller setpoints and open-loop process inputs for these experiments are shown in Table 6.7. The experiments are described as follows:

1. The first experiment establishes a baseline understanding of the LDED process behavior without feedback control. This open-loop setup provides critical insights into the inherent variability of thermal dynamics and their effects on the microstructure and material characteristics.
2. The second experiment focuses on laser power control while maintaining a constant traveling speed. The aim is to maintain a consistent temperature at the edge of the melt pool, effectively controlling the position of the trailing edge and preventing heat accumulation. This allows for analysis of how a constant trailing edge position affects the resulting microstructure and material characteristics.
3. The third experiment evaluates the control of traveling speed while maintaining constant laser power. This experiment aims to achieve a consistent spatial cooling rate in the solidified region. By isolating variations in cooling rate, it examines their effects on the microstructure and material characteristics.
4. The fourth experiment integrates both single-input single-output (SISO) controllers to simultaneously maintain a consistent temperature and spatial cooling rate. This experiment aims to proof how MIMO control can improve the microstructure and material characteristics compared to SISO control.

Table 6.7: Controller setpoints and open-loop process inputs for the four LDED wall experiment cases.

LDED Exp. Case	**AMPC Setpoints**		**OL Process Inputs**	
	Temp.	**∇Temp.**	$\boldsymbol{v}$	$\boldsymbol{P}$
1. Open-loop	-	-	1 mm/sec	1100 W
2. SISO power control	1200 °C	-	1 mm/sec	-
3. SISO speed control	-	150 °C/sec	-	1100 W
4. MIMO power & speed control	1200 °C	150 °C/sec	-	-

All LDED experiments are conducted using a carbon steel substrate, and the specifications of this substrate are depicted in Table 6.8, with corresponding dimensions visually depicted in Figure 6.1. Similar to the previous experiments, the substrates for these experiments will also undergo sandblasting and ethanol rinsing to improve laser absorption and eliminate any contamination prior to conducting the experiments.

Table 6.8: LDED substrate material specifications.

Material	**Standard**	**Dimensions** ($L \times W \times D$)	**Track Length** ($L_{\mathbf{track}}$)
Carbon Steel	AISI 1018	$75 \times 25 \times 6$ mm	60 mm

Additionally, stainless steel 431 powder is used as the deposition material for all LDED experiments, with its specifications shown in Table 6.9. Furthermore, it has been experimentally determined that the deposition tracks have an average layer thickness of 0.9 mm. This means that the LMP system moves up by 0.9 mm after each layer.

Table 6.9: LDED deposition powder specifications.

Material	**Standard**	**Size [µm]**	**Flow Rate [g/min]**
Stainless Steel	AISI 431	∼100	3.6

The model utilized in the AMPC algorithm is the same model that will be validated with the LDED experiments discussed in Subsection 6.1.2. Therefore, this model uses identical model parameters as used during the model validation. Furthermore, this model has ten states in the travel direction, which is identical to the model used in the MPC algorithm for LHT. Therefore, the prediction horizon N_p is selected to be ten as well, e.g., $N_\mathrm{p} = 10$. Furthermore, the control horizon N_c is chosen to be half of the prediction horizon, e.g., $N_\mathrm{c} = 5$. The control horizon has been reduced to improve computational efficiency while maintaining satisfactory control performance. This decision allows the controller to focus on a shorter time frame for determining optimal control actions, reducing the computational burden without significantly compromising control quality.

6.2.3 Controller Performance Evaluation

In order to comprehensively assess the effectiveness of the developed MPC algorithms, a thorough evaluation of their performance is essential. One key aspect of this evaluation involves conducting hardness measurements on the produced parts. Hardness serves as a crucial indicator of material properties, reflecting its resistance to plastic deformation, penetration, and scratching, among other factors. By measuring hardness at multiple cross-sections using Vickers microhardness testing with indentation forces of 0.5 and 1 kg, valuable insights can be gained into how the process conditions affect the resulting material properties. Hence, by contrasting the hardness measurements obtained from experiments conducted under different process conditions, the effectiveness of the MPC algorithms in improving the consistency of the material properties can be analyzed.

6.3 Chapter Summary

at validating the real-time thermal dynamic prediction capabilities of the developed thermal models, as well as the effectiveness of the control algorithms in controlling the thermal dynamics during LMP processes to indirectly achieve consistent microstructure. First, experiments have been designed to validate the 2D adaptive thermal dynamic model and the MPC algorithm for the LHT process. Afterwards, experiments have been designed to validate the 1D adaptive thermal model and AMPC algorithm for the LDED process. The results of these experiments are presented in the subsequent chapter.

Chapter 7

Results and Discussions

This chapter presents and discusses the results of the experiments outlined in Chapter 6, which were designed to validate the thermal dynamic models introduced in Chapter 4 and the model predictive control (MPC) algorithms developed in Chapter 5. By examining the results of these experiments, this chapter aims to provide insights into the effectiveness and reliability of the developed models and control algorithms, as well as their practical applicability and potential for improving process stability and achieving consistent material characteristics. It begins by analyzing the real-time thermal prediction capabilities of the thermal dynamic models. Subsequently, it explores the ability of the MPC algorithms to control the thermal dynamics in real time, aiming to achieve consistent microstructure.

7.1 Real-Time Thermal Dynamic Prediction Experiments Results

This section delves into the results and discussions of a wide range of both laser heat treatment (LHT) and laser-directed energy deposition (LDED) experiments designed to assess and validate the real-time thermal dynamic prediction capabilities of the developed thermal models. Initially, the results of the LHT experiments are analyzed, focusing on the prediction accuracy of both the peak temperature and spatial cooling rate. Furthermore, the predictive capabilities of the two-dimensional (2D) non-adaptive thermal dynamic model are compared to those of the adaptive model with the model parameter estimation algorithm, aiming to assess the improvements and adaptability achieved through real-time model parameter estimation. Subsequently, the LDED experiments are examined, with the main focus on assessing the temperature and spatial cooling rate predictions of the one-dimensional (1D) adaptive thermal model, as well as its adaptability across various materials.

7.1.1 2D Adaptive Thermal Model Predictions in LHT

In total, ten LHT experiments were carried out: five experiments with a carbon steel substrate and five experiments with a stainless steel substrate, which are shown in Figure 7.1 and Figure 7.2, respectively.

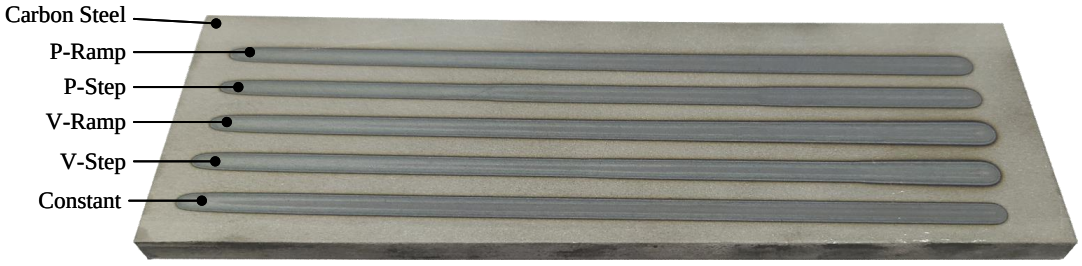


Figure 7.1: Carbon steel substrate featuring all five single LHT tracks.

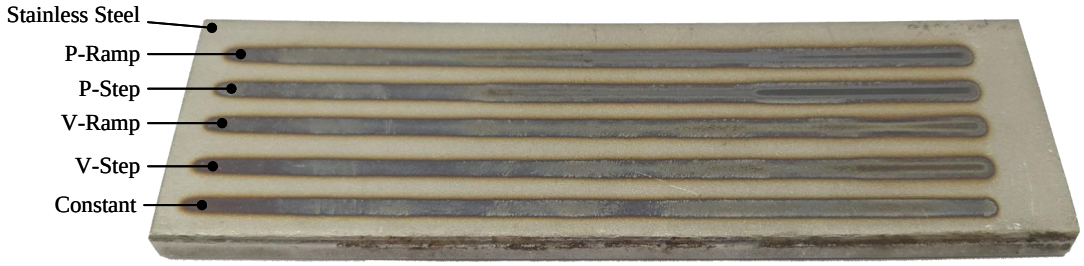


Figure 7.2: Stainless steel substrate featuring all five single LHT tracks.

In these experiments, the real-time peak temperature and spatial cooling rate predictions are compared with the real-time peak temperature and spatial cooling rate measurements. First, the results related to the 2D non-adaptive thermal model are analyzed, and then the results related to the 2D adaptive thermal model are examined.

Thermal Dynamic Predictions with the 2D non-adaptive Thermal Model

The result of the v_{ramp} experiment with a carbon steel substrate is shown in Figure 7.3. As can clearly be seen from Figure 7.3, the change in CNC traveling speed has a clear influence on the peak temperature and spatial cooling rate of the 2D non-adaptive thermal model and the LHT process. Lower travel speeds result in a higher peak temperature and a lower spatial cooling rate. The peak temperature and spatial cooling rate predictions, around the experiment time of 40 sec, are almost identical to the measurements of the LHT process. However, at the start of the experiment, the peak temperature prediction was much higher compared to the measurements of the LHT process. Furthermore, melting occurs at the end of the experiment, resulting in a deviation of the peak temperature and spatial cooling rate predictions compared to the measurements. In general, comparable results are observed with the other four experiments with a carbon steel substrate, which are shown in Appendix B.1. At the start of these experiments, the peak temperature prediction is higher compared to the measurements of the LHT process, and melting occurs at the end of these experiments. In some cases, the process reacts differently to input changes compared to the 2D non-adaptive thermal model, resulting in peak temperature and spatial cooling rate deviations.

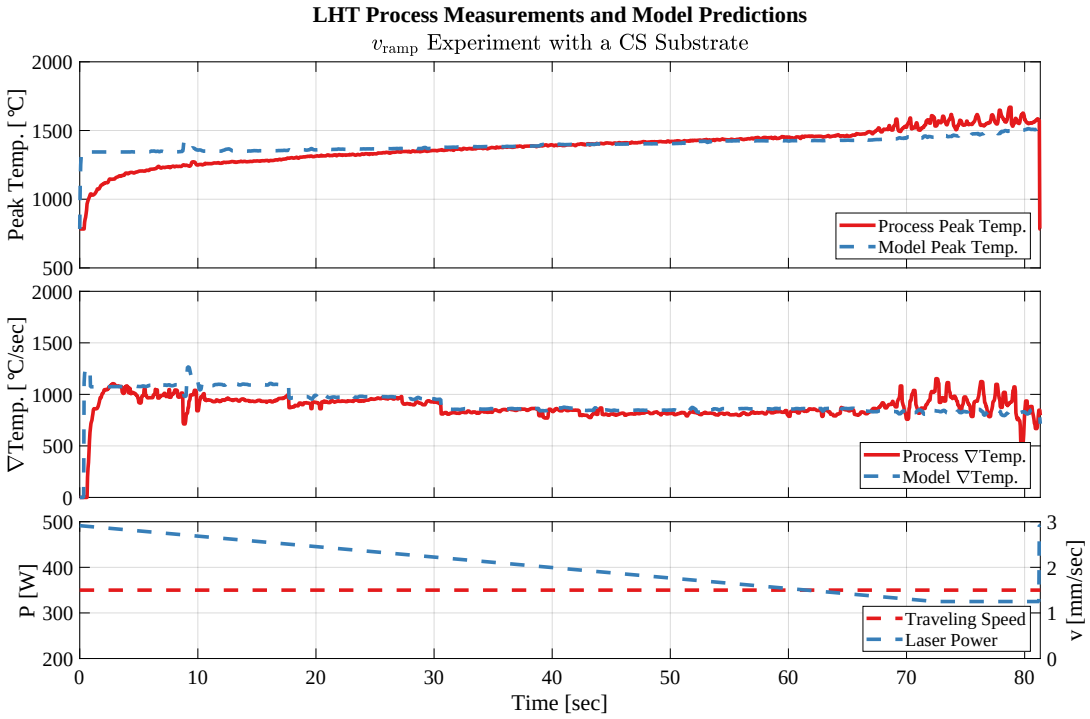


Figure 7.3: Real-time peak temperature and spatial cooling rate comparison between the 2D non-adaptive thermal model predictions and the LHT process measurements of the v_{ramp} experiment with a carbon steel substrate.

The mean absolute percentage errors (MAPEs) between the model predictions and the process measurements of all five experiments with a carbon steel substrate are provided in Table 7.1. As can be observed from this table, the average MAPE of the peak temperature prediction T_{peak} is 3.9 %, and the average MAPE of the spatial cooling rate prediction ∇T is 13.1 %.

Table 7.1: MAPE of the 2D non-adaptive thermal model with respect to the LHT process after the experiments with a carbon steel substrate.

	Experiment Case					
MAPE	*Const*	v_{step}	v_{ramp}	P_{step}	P_{ramp}	**Units**
T_{peak}	3.0	6.1	4.7	3.1	2.6	%
∇T	9.3	9.1	7.4	27.1	12.8	%

The results of the P_{step} experiment with a stainless steel substrate are shown in Figure 7.4. As can be seen from Figure 7.4, the change in laser power has a clear influence on the peak temperature and spatial cooling rate of the 2D non-adaptive thermal model. Higher laser power results in a higher peak temperature and a higher spatial cooling rate. The same holds true for the process with a change in laser power from 300 W to 350 W. However, the change in laser power from 350 W to 400 W results in almost the same peak temperature and a slightly lower spatial cooling rate with the LHT process. In other words, the process reacts differently to this change in laser power compared to the model. This discrepancy occurs because the increased laser power causes the substrate metal to melt, and the thermal measurements from the infrared camera are inaccurate for liquid metal, leading to inaccurate measurements compared to the model's predictions. Furthermore, at the beginning of these experiments, the peak temperature prediction of the 2D non-adaptive thermal model was higher compared to the LHT process. In general, comparable results are observed with the other four experiments with a stainless steel substrate, which are shown in Appendix B.2. At the start of these experiments, the peak temperature prediction was slightly higher compared to the measurements of the LHT process. In some cases, the process reacts differently compared to the 2D non-adaptive thermal model, resulting in a small peak temperature and spatial cooling rate deviation.

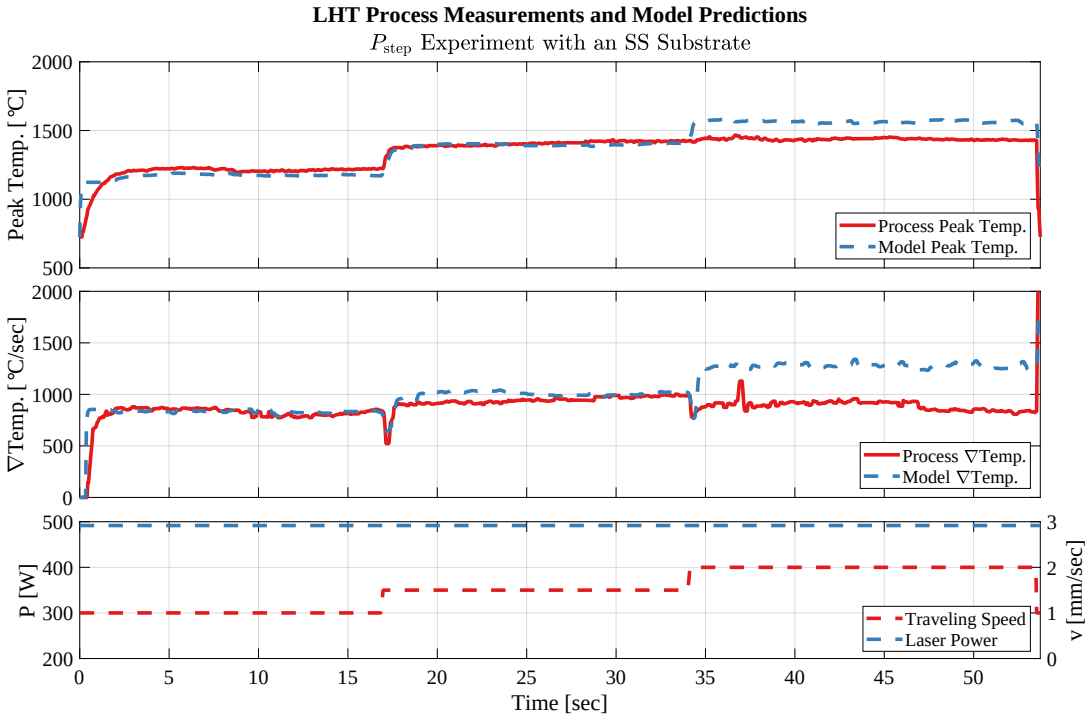


Figure 7.4: Real-time peak temperature and spatial cooling rate comparison between the 2D non-adaptive thermal model predictions and the LHT process measurements of the P_{step} experiment with a stainless steel substrate.

The MAPE of the peak temperature and spatial cooling rate prediction between the 2D non-adaptive thermal model and the LHT process of all five experiments with a stainless steel substrate are provided in Table 7.2. As can be observed from this table, the average MAPE of the peak temperature prediction T_{peak} is 2.2 %, and the average MAPE of the spatial cooling rate prediction ∇T is 9.5 %.

Table 7.2: MAPE of the 2D non-adaptive thermal model with respect to the LHT process after the experiments with a stainless steel substrate.

	Experiment Case					
MAPE	*Const*	v_{step}	v_{ramp}	P_{step}	P_{ramp}	**Units**
T_{peak}	1.3	1.2	1.2	5.1	2.1	%
∇T	4.5	12.3	5.9	18.9	5.9	%

These results show that the 2D non-adaptive thermal model can accurately predict the peak temperature, with prediction accuracy between 1.2 % and 6.1 %. Other researchers report their thermal models predict the peak temperature of the LHT process with an accuracy between 3.5 % and 7.0 % [197, 198, 91, 50]. Thus, the 2D non-adaptive thermal model demonstrates better prediction accuracy even without adaptation. Additionally, the spatial cooling rate prediction accuracy ranges from 4.4 % to 27.1 %, being quite accurate in some experiments but less so in others. These large prediction errors are mainly caused by two factors. First, inaccurate thermal measurements from the infrared (IR) camera resulted in prediction errors because the IR camera cannot accurately measure the temperatures of liquid metal. Second, heat accumulation in the substrate caused prediction errors because it significantly altered the thermal dynamic behavior of the process. The 2D non-adaptive thermal model cannot handle these changes because it has temperature-independent parameters and it does not account for phase changes. Moreover, prediction errors due to heat accumulation are common in the literature [199] and are also significant in other additive processes such as wire arc additive manufacturing [173]. Heat accumulation not only affects the size and temperature of the heat-affected zone and material properties during a closed-loop controlled process [154], but it is also the primary reason why the substrate started to melt. Therefore, it is crucial for the model to adapt to heat accumulation in real-time before being implemented in a real-time model-based control system. Nonetheless, the developed 2D non-adaptive thermal model is more accurate in most cases compared to the 2D non-adaptive thermal models in the literature and therefore serves as a good basis for the 2D adaptive thermal model.

Thermal Dynamic Predictions with the 2D adaptive Thermal Model

The result of the v_{ramp} experiment with a carbon steel substrate is shown in Figure 7.5, and the corresponding estimation of the material constants is shown in Figure 7.6. For easy comparison, the predictions by the 2D non-adaptive thermal model presented in the previous section are included in Figure 7.5. As can clearly be seen from Figures 7.5 and 7.6, real-time estimation of the material constants resulted in similar peak temperature and spatial cooling rate predictions of the 2D adaptive thermal model compared to the measurements of the LHT process. Also, the peak temperature and spatial cooling rate deviation problems due to melting are solved. However, at the beginning of the experiment, the spatial cooling rate prediction of the 2D adaptive thermal model was much lower compared to the LHT process. This deviation is caused by inaccurate temperature measurements. The measurement is hitting the lower temperature limit of the IR camera, resulting in inaccurate measurement data. In general, similar results are observed with the other four experiments with a carbon steel substrate, which are shown in Appendix B.1. However, the amount of time it takes for the temperatures to be above the lower temperature limit of the IR camera is different for each experiment.

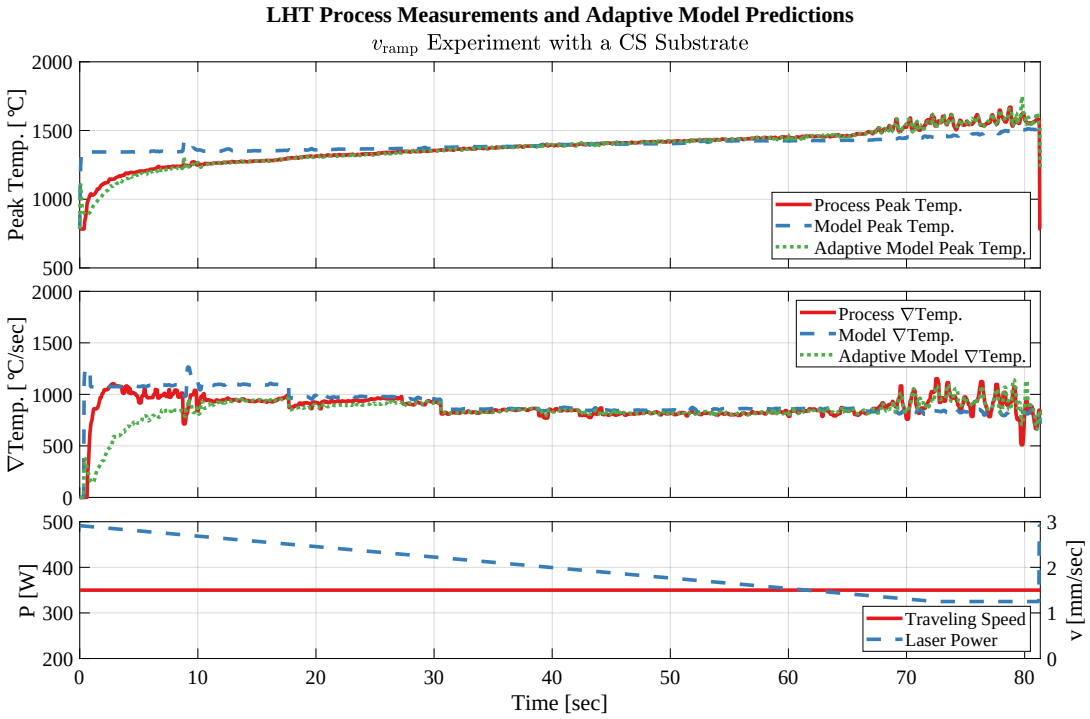


Figure 7.5: Real-time peak temperature and spatial cooling rate comparison between the 2D adaptive thermal model predictions and the LHT process measurements of the v_{ramp} experiment with a carbon steel substrate.

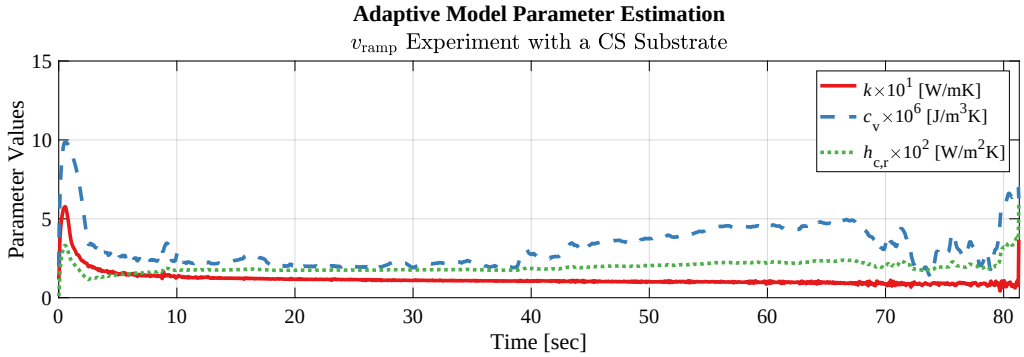


Figure 7.6: Real-time parameter estimation of the v_{ramp} experiment with a carbon steel substrate.

The MAPEs between the adaptive model predictions and the process measurements of all five experiments with a carbon steel substrate are provided in Table 7.3. As can be observed from this table, the average MAPE of the peak temperature prediction T_{peak} is 1.1 %, and the average MAPE of the spatial cooling rate prediction ∇T is 8.4 %. To analyze the performance of the 2D adaptive thermal model without the inaccurate measurement data, the inaccurate measurement data at the start of all five experiments was removed from the MAPE calculations. As shown in Table 7.3, the new average MAPE of the peak temperature prediction T_{peak} is 0.6 %, and the new average MAPE of the spatial cooling rate prediction ∇T is 4.4 %.

Table 7.3: MAPE of the 2D adaptive thermal model with respect to the LHT process after the experiments with a carbon steel substrate.

	Experiment Case					
MAPE	*Const*	v_{step}	v_{ramp}	P_{step}	P_{ramp}	**Units**
T_{peak}	0.7	1.1	0.9	1.7	1.0	%
∇T	3.0	10.5	6.0	15.0	7.7	%
Time	> 3	> 24	> 12	> 17	> 10	sec
T_{peak}	0.4	0.7	0.5	1.0	0.5	%
∇T	1.8	4.6	2.6	10.5	2.4	%

The results of the P_{step} experiment with a stainless steel substrate are shown in Figure 7.7, and the corresponding estimation of the material constants is shown in Figure 7.8. Again, for easy comparison, the predictions by the 2D non-adaptive thermal model presented in the previous section are included in Figure 7.7.

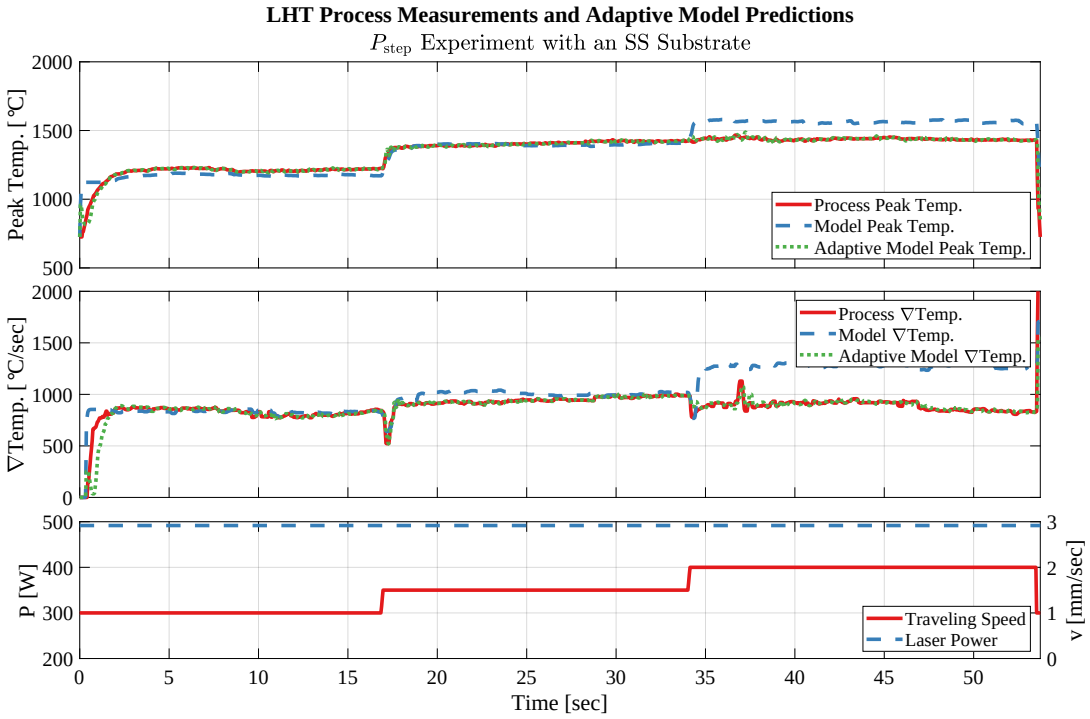


Figure 7.7: Real-time peak temperature and spatial cooling rate comparison between the 2D adaptive thermal model predictions and the LHT process measurements of the P_{step} experiment with a stainless steel substrate.

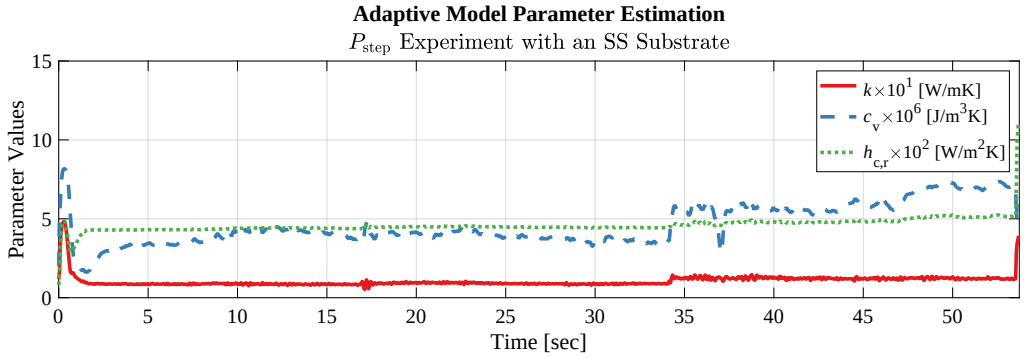


Figure 7.8: Real-time parameter estimation of the P_{step} experiment with a stainless steel substrate.

As can clearly be seen from Figures 7.7 and 7.8, the peak temperature and spatial cooling rate predictions of the 2D adaptive thermal model are almost identical to the measurements of the LHT process. The deviations that occurred with the 2D non-adaptive thermal model are solved by real-time estimation of the material constants. However, at the start of the experiment, a prediction deviation occurred due to the startup phase of the parameter estimation. In general, comparable results are observed with the other four experiments with a stainless steel substrate, which are shown in Appendix B.2. In addition, the time of the startup phase is equal for all five experiments.

The MAPE of the peak temperature and spatial cooling rate prediction between the 2D non-adaptive thermal model and the LHT process of all five experiments with a stainless steel substrate is provided in Table 7.4. As can be observed from this table, the average MAPE of the peak temperature prediction T_{peak} is 0.4 %, and the average MAPE of the spatial cooling rate prediction ∇T is 1.9 %. To analyze the performance of the 2D adaptive thermal model after the startup phase, the first two seconds of MAPE data are removed. As shown in Table 7.4, the new average MAPE of the peak temperature prediction T_{peak} is 0.3 %, and the new average MAPE of the spatial cooling rate prediction ∇T is 1.4 %.

Table 7.4: MAPE of the 2D adaptive thermal model with respect to the LHT process after the experiments with a stainless steel substrate.

	Experiment Case					
MAPE	*Const*	v_{step}	v_{ramp}	P_{step}	P_{ramp}	**Units**
T_{peak}	0.4	0.4	0.4	0.5	0.4	%
∇T	1.4	2.0	2.2	2.4	1.7	%
Time	> 2	> 2	> 2	> 2	> 2	sec
T_{peak}	0.3	0.3	0.3	0.4	0.3	%
∇T	0.9	1.6	1.6	1.8	1.1	%

The LHT experiments show that the 2D adaptive thermal model is much more accurate compared to the 2D non-adaptive thermal model. The 2D adaptive thermal model can accurately deal with heat accumulation in real-time, which significantly improved the peak temperature and spatial cooling rate prediction accuracy compared to the 2D non-adaptive thermal model. The peak temperature prediction accuracy of the 2D adaptive thermal model is between 0.4 % and 1.7 %. In addition, the prediction accuracy, with most experiments, is within the IR camera accuracy of 1 %. This prediction accuracy is a significant improvement compared to the peak temperature prediction accuracy between 3.5 % and 7.0 % found in the literature [197, 198, 91, 50]. Furthermore, the spatial cooling rate prediction accuracy of the 2D adaptive thermal model is between 1.4 % and 15.0 %.

This prediction accuracy is also a huge improvement compared to the 2D non-adaptive thermal model. In addition, most experiments show a huge improvement in spatial cooling rate prediction accuracy compared to the prediction accuracy between 6.5 % and 9.2 % found in previous research [50]. However, in some cases, the spatial cooling rate prediction error is much higher compared to previous research. Furthermore, the startup phase of the optimization algorithm within the 2D adaptive thermal model introduces prediction errors at the start of all ten LHT experiments. The high spatial cooling rate prediction error values are the result of significant prediction errors at the beginning of the LHT experiments, which particularly manifest themselves with the experiments with a carbon steel substrate. At the beginning of the LHT experiments, the IR camera is hitting the lower temperature limit that the camera is able to measure. This lower limit is 783 °C for thermal measurements with a carbon steel substrate and 725 °C for thermal measurements with a stainless steel substrate. If the IR camera had a lower temperature limit, these significant prediction errors would not have occurred, resulting in lower peak temperature and spatial cooling rate prediction error values.

The prediction error caused by the startup phase of the optimization algorithm can be clearly seen in Figure 7.7 together with Figure 7.8. At the start of the experiment, the 2D non-adaptive thermal model increases much faster in temperature compared to the LHT process because of the wrong initial values for the three material constants. As a result,

the 2D adaptive thermal model tunes all three material constants to reduce the prediction error. After a short period, all three material constants are tuned in such a way that the predicted peak temperature and spatial cooling rate are almost identical to the measured peak temperature and spatial cooling rate of the LHT experiment. After the startup phase, the 2D adaptive thermal model can accurately predict the peak temperature and spatial cooling rate throughout the experiment. Removing the prediction errors caused by inaccurate measurements due too the lower camera limit during the startup phase significantly reduces the MAPE values, as can be seen in Tables 7.3 and 7.4. The peak temperature prediction accuracy of the 2D adaptive thermal model, without startup phase data and inaccurate measurement data, is between 0.3 % and 1.0 %. This prediction accuracy is within the IR camera accuracy of 1 %. In addition, the spatial cooling rate prediction accuracy, with most experiments, is also within the IR camera accuracy of 1 %. As a result, the 2D adaptive thermal model is highly suitable for real-time prediction and control applications. Combining this model with a model-based controller in a real-time feedback control system can significantly improve the consistency of the material and mechanical properties during LHT.

The most commonly used model-based control approaches in the literature use a second-order state-space model that is identified using general system identification methods or complex FEM models [200, 169, 201, 202]. These second-order models are more computationally efficient than the adaptive model developed in this research. However, the accuracy of these models is comparable to the dynamic model without the parameter estimation algorithm, which means that they can have prediction errors larger than 100 °C. In addition, these models are limited to specific process settings and need to be optimized for each experiment. The developed model does not have this drawback because it automatically adapts to process changes in real-time. As a result, the 2D adaptive thermal model has a prediction accuracy that is comparable to complex modeling methods found in the literature [98, 37, 39, 203, 180, 204]. Moreover, the developed adaptive thermal model is computationally efficient enough for real-time prediction and control applications. In contrast, these complex modeling methods found in the literature are too computationally intensive for real-time applications and can only be used offline.

Concluding Remarks

While the 2D adaptive thermal model demonstrates impressive prediction accuracy in single-track LHT experiments with two different substrate materials of the same thickness, its validation is limited. To fully understand its potential and limitations, the model should undergo validation across a broader range of LHT experiments, materials, and thicknesses. It is crucial to recognize that the 2D adaptive thermal model is tailored specifically for the LHT process. Given the simplicity of LHT compared to more complex laser material processing (LMP) processes, such as LDED, there is uncertainty about its applicability to those processes. Hence, it is imperative to develop and validate advanced models tailored specifically for LMP processes, ensuring not only their effectiveness and accuracy but also their generalizability across a broader spectrum of conditions. These models must possess the flexibility and adaptability to accommodate the diverse variables and complexities inherent in various LMP processes, thereby enhancing their applicability and robustness in real-world industrial settings. Additionally, while the nonadaptive model has been implemented in a MPC algorithm, an adaptive model should be similarly implemented with MPC to enhance its control capabilities.

7.1.2 1D Adaptive Thermal Model Predictions in LDED

This subsection delves into the results obtained from the validation experiments of the 1D adaptive thermal model. In total, four LDED experiments were conducted, each depositing a single track onto a carbon steel substrate with a different deposition material. The substrate with the four different depositions is shown in Figure 7.9. In the subsequent analysis, the real-time temperature and spatial cooling rate predictions from the 1D adaptive thermal model are examined and compared with the corresponding real-time measurements obtained from the four LDED experiments.



Figure 7.9: Carbon steel substrate showing the four LDED experiments, each depositing a single track with a different deposited material.

The result of the LDED experiment with the Stellite® 6 powder is shown in Figure 7.10, and the corresponding estimation of the model parameters is depicted in Figure 7.11. As can be observed from these figures, the trend of the temperature and spatial cooling rate data diverges from the anticipated patterns based on the process inputs. This discrepancy underscores the complexity of thermal dynamics within the LDED process, where the intricate interactions between various process parameters significantly influence the resulting thermal dynamic behavior.

The process parameters, such as laser power, traveling speed, and powder feed rate, among others, each contribute to the complex thermal dynamics observed during the process. These complex dynamics, which include heat accumulation and energy density fluctuations, are not explicitly accounted for in the model. However, by integrating a parameter estimation algorithm that automatically adjusts the model parameters based on real-time measurements, as depicted in Figure 7.11, the model can effectively adapt to and track the observed thermal dynamic changes during the process. As a result, the temperature and spatial cooling rate predictions of the 1D adaptive thermal model, illustrated in Figure 7.10, closely match the process measurements. Overall, equivalent results are observed in the other three LDED experiments, each involving a distinct deposition material, as depicted in Appendix C.1.

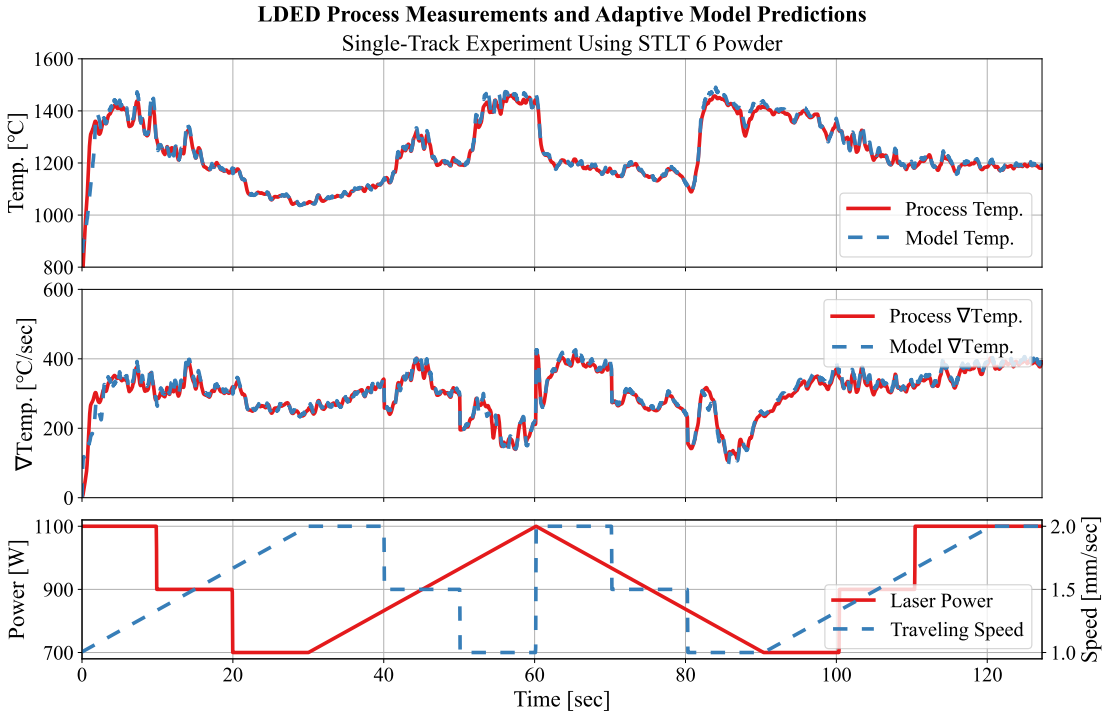


Figure 7.10: Real-time temperature and spatial cooling rate comparison between the adaptive 1D thermal model predictions and the LDED process measurements of the experiment with Stellite® 6 powder.

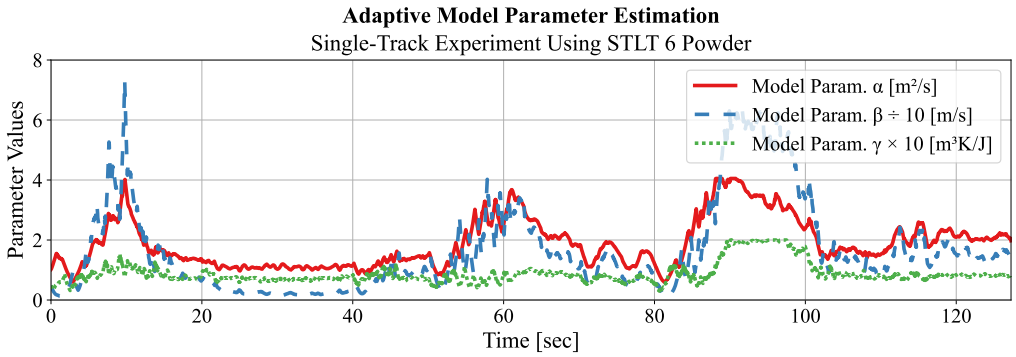


Figure 7.11: Real-time parameter estimation of the experiment with Stellite® 6 powder.

The MAPEs between the model predictions and the process measurements of all four LDED experiments are provided in Table 7.5. As can be observed from this table, the average MAPE of the temperature prediction T is around 0.44 %, and the average MAPE of the spatial cooling rate prediction ∇T is around 2.09 %. These findings underscore the precision of the 1D adaptive thermal model in predicting both temperature and spatial cooling rate. Across all four experiments, the temperature predictions fall within the ± 1 % accuracy range of the IR camera measurements. Additionally, the spatial cooling rate predictions demonstrate exceptional alignment with the thermal measurements, with the maximum MAPE reaching just 2.78%. This remarkable accuracy showcases the model's adaptability to the complex thermal dynamics inherent in the LDED process. Moreover, the extensive validation across four distinct deposition materials highlights the versatility and robustness of the 1D model, affirming its suitability for a diverse array of manufacturing applications.

Table 7.5: MAPE of the adaptive 1D thermal model with respect to the LDED process after the LDED experiments with all four powders.

	Deposition Material				
MAPE	IN 625	STLT 6	H13 TS	SS 431	
Temp.	0.31	0.58	0.44	0.44	[%]
∇Temp.	1.43	2.78	1.91	2.25	[%]

Concluding Remarks

The transition from the 2D to the 1D thermal model marks a significant advancement in predictive capabilities within LMP processes. Unlike its 2D counterpart, the 1D model offers a more comprehensive validation process, covering a more complex process and incorporating a diverse set of four materials. Despite this expanded scope, the 1D model demonstrated improved prediction accuracy relative to the 2D model. This improvement underscores the versatility and robustness of the 1D model, highlighting its adeptness in accurately capturing the intricate thermal dynamics inherent to LMP processes. Another notable improvement of the 1D model over its 2D counterpart is its prediction accuracy and adaptability during the startup phase of the process.

While the 2D model struggled to quickly adapt to the thermal dynamic changes at the start of the process, the 1D model can rapidly adjust to these changes, resulting in accurate predictions from the start. By circumventing these startup phase issues, the 1D model ensures more consistent and reliable predictions throughout the entire manufacturing process. Furthermore, the transition to a 1D framework significantly enhances the computational efficiency of the model, making it well-suited for real-time prediction and control applications, including MPC algorithms. This efficiency not only facilitates optimized process control but also conserves computational resources, ultimately improving overall process efficiency.

In summary, the advancements offered by the 1D model over its 2D counterpart result in higher prediction accuracy, improved robustness, enhanced computational efficiency, and broader applicability, including its suitability for model-based control applications such as MPC. These improvements position it as a valuable tool for optimizing LMP processes, with significant implications for enhanced product quality, manufacturing efficiency, and control precision.

7.2 Real-Time Microstructure Control Experiments Results

This section delves into the results and discussions of a wide range of both LHT and LDED experiments designed to assess and validate the real-time thermal dynamic control capabilities of the developed MPC algorithms. Initially, the results of the LHT experiments are analyzed, focusing on the peak temperature control capabilities aimed at achieving consistent microstructure under varying conditions. Subsequently, the LDED experiments are examined, with the main focus on assessing different control strategies and analyzing multi-input multi-output (MIMO) control capabilities to achieve consistent microstructure throughout the manufactured part.

7.2.1 Closed-Loop LHT Process with MPC

Three LHT experiments were carried out to assess the consistency of the hardness and hardening depth when controlling the peak temperature during the LHT process with the MPC algorithm. These experiments include a single-track LHT experiment with a step setpoint temperature, a multi-track LHT experiment involving six tracks, and a single-track LHT experiment with variations in substrate thickness.

Single-track LHT with a step setpoint temperature.

With the single-track LHT experiment with a step setpoint temperature, a straight track is laser heat-treated and controlled to a peak temperature with a stepped profile. The first part of the track is controlled to 1100 °C, and the second part of the track is controlled to 1300 °C. This experiment has been conducted to analyze the influence of different peak temperatures on hardness and hardening depth and to validate the ability of the controller to control different setpoints. The substrate of the closed-loop experiment is shown in Figure 7.12.

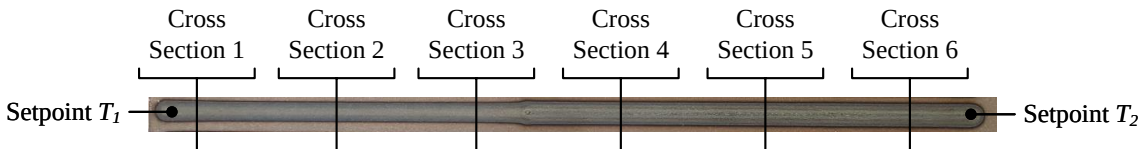


Figure 7.12: Carbon steel substrate featuring a single LHT track, processed with a closed-loop controlled temperature using a step setpoint.

The resulting peak temperature and traveling speed of the closed-loop single-track experiment with a step setpoint temperature are shown in Figure 7.13. As shown in the figure, the controller accurately maintains the peak temperature at 1100 °C and 1300 °C during the LHT process, with measured temperatures closely matching the setpoints. Additionally, the controller begins adjusting the traveling speed before the temperature setpoint changes, showcasing the predictive capabilities of the MPC algorithm. However, at the start of each temperature setpoint, the controller overshoots before stabilizing at the setpoint temperature. These overshoots are likely due to non-optimal weighting matrix values in the MPC algorithm and the slower response of the real system compared to the model predictions.

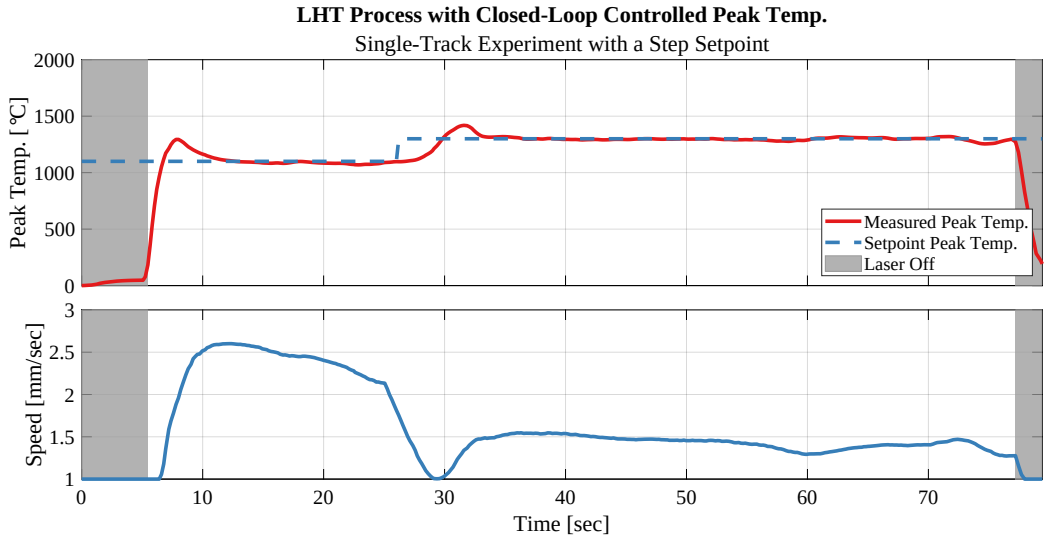
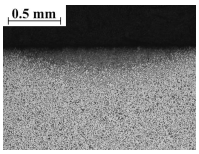
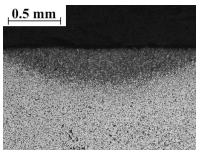


Figure 7.13: Peak temperature and traveling speed results of the closed-loop single-track experiment with a step setpoint temperature and a constant laser power of 300 W.

To inspect the microstructure and hardness values between the two different peak temperatures, the substrate was cut at six locations, as shown in Figure 7.12. Microscopic images were taken at the second and fifth cross sections, and the results are shown in Table 7.6. As can be observed from these cross sections, these cross sections clearly show that a higher peak temperature setpoint results in an increased hardening depth.

Table 7.6: Microscopic images at cross section 2 and 5 of the closed-loop single-track experiment with a step setpoint temperature.

Case	$T_P = 1100$°C	$T_P = 1300$°C
Closed-loop		

Each cross section had its hardness measured, and Table 7.7 shows the results of those measurements. From this table, it can be concluded that the hardness values of three sections with the same setpoint are very consistent. The maximum hardness deviation is only 4 HV. This clearly shows that consistent hardness can be achieved when controlling the peak temperature to a constant setpoint. This table also shows that when increasing the setpoint temperature, a higher average hardness is achieved. This indicates that it is possible to produce a part with different local hardness when controlling the peak temperature at different setpoints in different regions.

Table 7.7: Hardness measurements of the closed-loop single-track experiment with a step setpoint temperature.

Average Hardness ± [Standard Deviation] (HV1.00)	
$T_P = 1100$°C, Section 1 to 3	351±[4]
$T_P = 1300$°C, Section 4 to 6	402±[3]

Multi-track LHT with six adjacent tracks

With the multi-track LHT experiments, six straight adjacent tracks are laser heat-treated, and each track is controlled to the same peak temperature setpoint of 1200 °C. The substrate of the closed-loop experiment is shown in Figure 7.14. With each added track, the internal substrate temperature increases, which changes the thermal dynamics of the process and can be seen as a process disturbance. To observe the influence of this disturbance on the thermal output of a heat-treated surface, an open-loop experiment was also conducted. This open-loop experiment consists of six LHT tracks next to each other with constant process inputs, and the substrate of this experiments is shown in Figure 7.15.

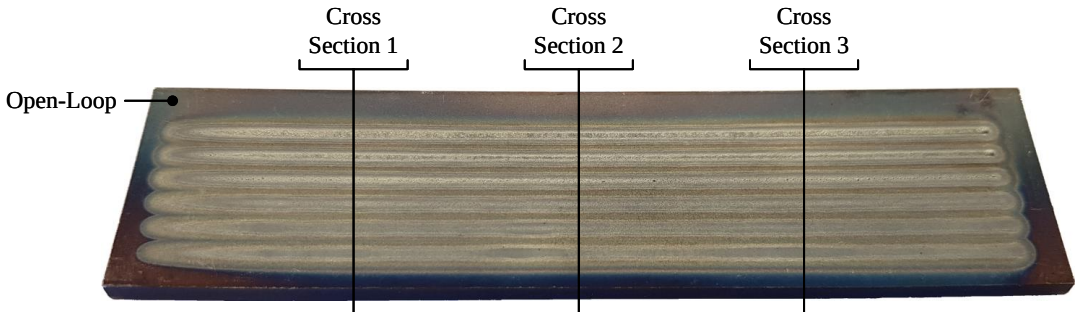


Figure 7.14: Carbon steel substrate featuring six adjacent LHT tracks, processed with closed-loop controlled peak temperature.

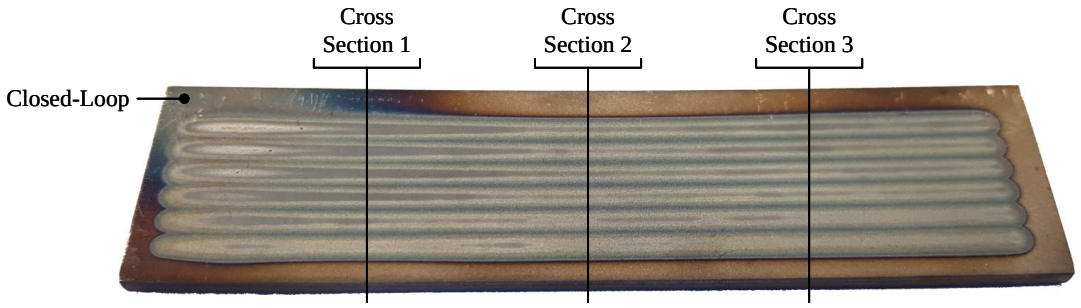


Figure 7.15: Carbon steel substrate featuring six adjacent LHT tracks, processed in open-loop.

The resulting peak temperature and traveling speed of the open-loop and closed-loop multi-track experiments are shown in Figures 7.16 and 7.17, respectively. The shaded region in these figures indicates when the laser is turned off because the substrate is moved to the right location for the next track. As illustrated in Figure 7.16, the peak temperature in the six open-loop LHT tracks increases with each track because the substrate is heating up. For the closed-loop process, shown in Figure 7.17, the controller is increasing the traveling speed to reduce the peak temperature during the process. As a result, the measured process peak temperature in the six LHT tracks is following the setpoint without a steady-state error. However, the peak temperature overshoots at the beginning of each track, and after each track, the initial temperature of the substrate is higher, resulting in a larger overshoot and a higher controlled traveling speed.

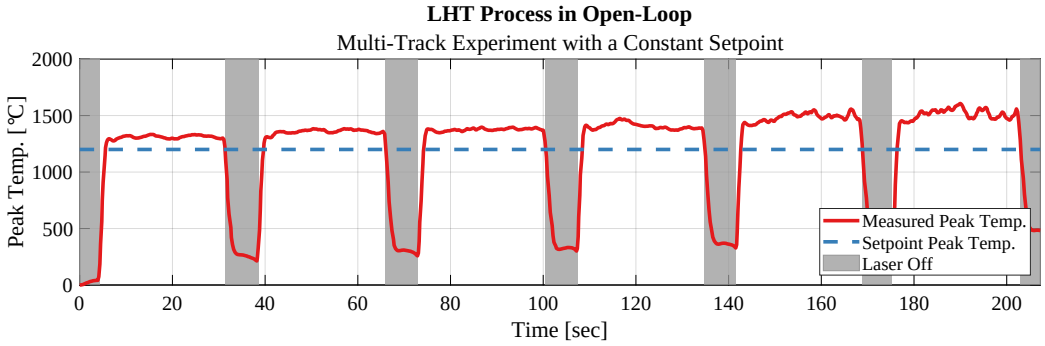


Figure 7.16: Peak temperature and traveling speed results of the open-loop multi-track experiment with constant laser power of 300 W and a constant traveling speed of 3.33 mm/sec

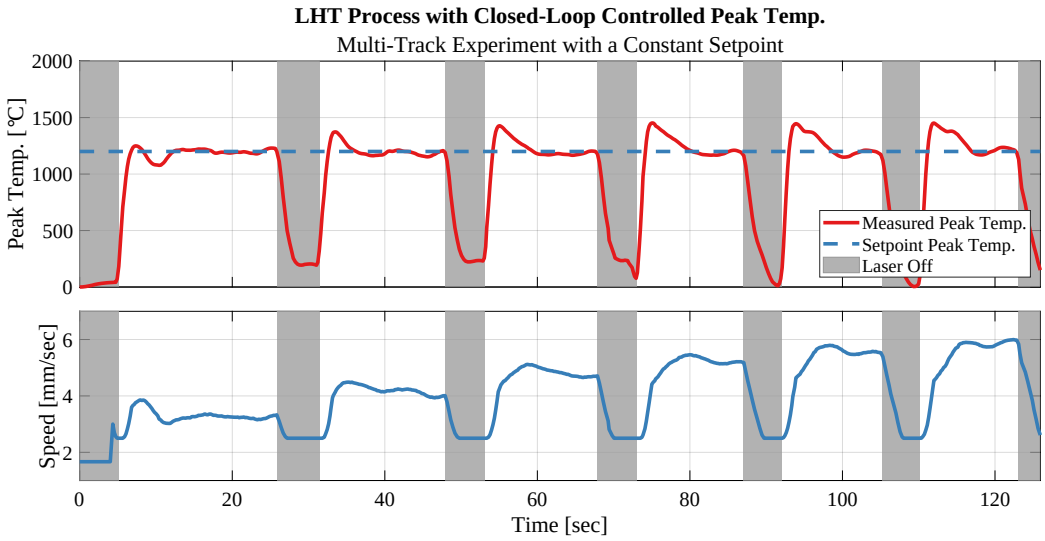
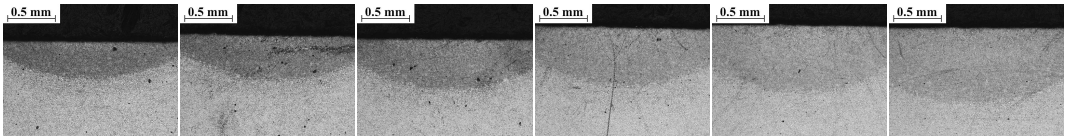
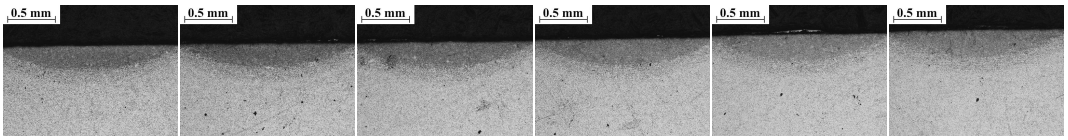


Figure 7.17: Peak temperature and traveling speed results of the closed-loop multi-track experiment with constant laser power of 300 W.

Each open-loop and closed-loop substrate was cut at three locations, as shown in Figures 7.14 and 7.15, to evaluate and compare the microstructure and hardness values. Microscopic images were taken at the second cross section from both substrates at all six tracks, and the results are shown in Table 7.8. It can be observed that the open-loop multi-track experiment substrate has an increased hardening depth for each subsequent track. On the other hand, the closed-loop multi-track experiment has a constant hardening depth for all six tracks. Therefore, a constant hardening depth can be obtained when using MPC to control the peak temperature.

Table 7.8: Microscopic images at cross section 2 of all six tracks from the open-loop and closed-loop multi-track experiment.

Case	Track 1	Track 2	Track 3	Track 4	Track 5	Track 6
Open-loop						
Closed-loop						

Hardness measurements for each cross-section and track are provided in Table 7.9. The open-loop hardness values demonstrate a clear correlation with increased temperatures at each track, showing a progressive increase in hardness due to the varying peak temperatures. In contrast, the closed-loop experiment achieved a consistent peak temperature across all six tracks, resulting in uniform hardness with tight tolerance. These results show that maintaining a constant peak temperature with MPC ensures consistent hardness throughout the LHT process. The closed-loop MPC algorithm effectively eliminated the effects of disturbances due to heat accumulation in real-time.

Table 7.9: Hardness measurements of both LHT multi-track experiments.

Average Hardness ± [Standard Deviation] (HV1.00)		
	Open-loop	**Closed-loop**
Track 1, Section 1 to 3	238±[6]	293±[10]
Track 2, Section 1 to 3	244±[4]	293±[3]
Track 3, Section 1 to 3	254±[5]	296±[8]
Track 4, Section 1 to 3	259±[5]	288±[2]
Track 5, Section 1 to 3	275±[5]	302±[4]
Track 6, Section 1 to 3	301±[3]	297±[10]

Single-track LHT with a variable substrate thickness

With the single-track LHT experiment with a variable substrate thickness, a straight track is laser heat-treated and controlled to a single peak temperature setpoint of 1200 °C. The introduction of a variable substrate thickness will result in a rapid change in the thermal dynamics during the process. This change in thermal dynamics can be seen as a process disturbance. To observe the influence of this disturbance on the peak temperature and microstructure of a heat-treated track, an open-loop experiment was also conducted. This open-loop experiment consists of a single LHT track with constant process inputs. The substrate from both the open-loop and closed-loop experiments is shown in Figure 7.18.

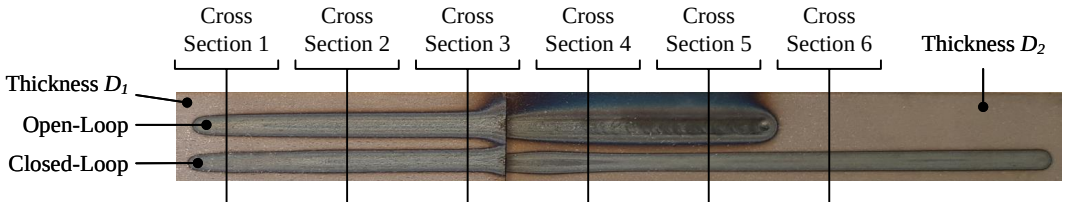


Figure 7.18: Carbon steel substrate featuring two single LHT tracks: one processed in open-loop and the other with closed-loop controlled temperature.

The resulting peak temperature and traveling speed of the open-loop and closed-loop single-track experiments with a variable substrate thickness are shown in Figure 7.19 and Figure 7.20, respectively. As shown in Figure 7.19, the peak temperature in the open-loop experiment increases rapidly when the substrate thickness changes from 0.25 in to 0.125 in. This is caused by the difference in the ability to conduct heat away from the HAZ between a thick and thin substrate. A thick substrate can transfer more heat away than a thin substrate. For the closed-loop process shown in Figure 7.20, the controller is adjusting the real-time traveling speed to compensate for this change in heat transfer. As a result, the peak temperature quickly settles back at 1200 °C after the substrate changes in thickness.

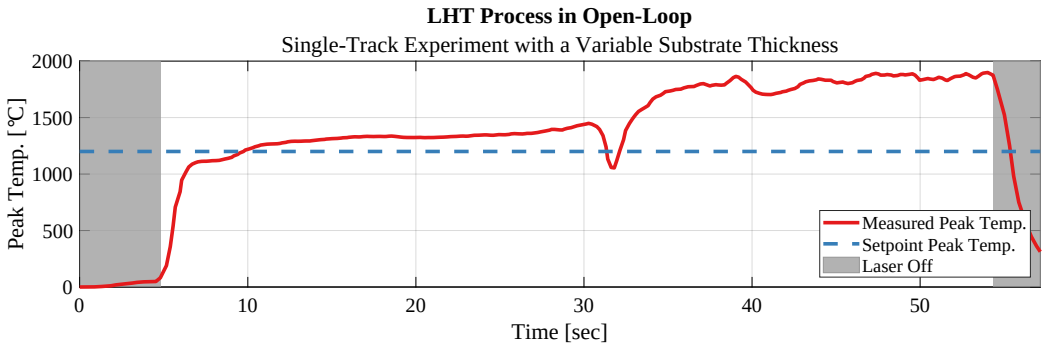


Figure 7.19: Peak temperature and traveling speed results of the open-loop single-track experiment with a variable substrate thickness, a constant laser power of 300 W, and a constant traveling speed of 3.33 mm/sec.

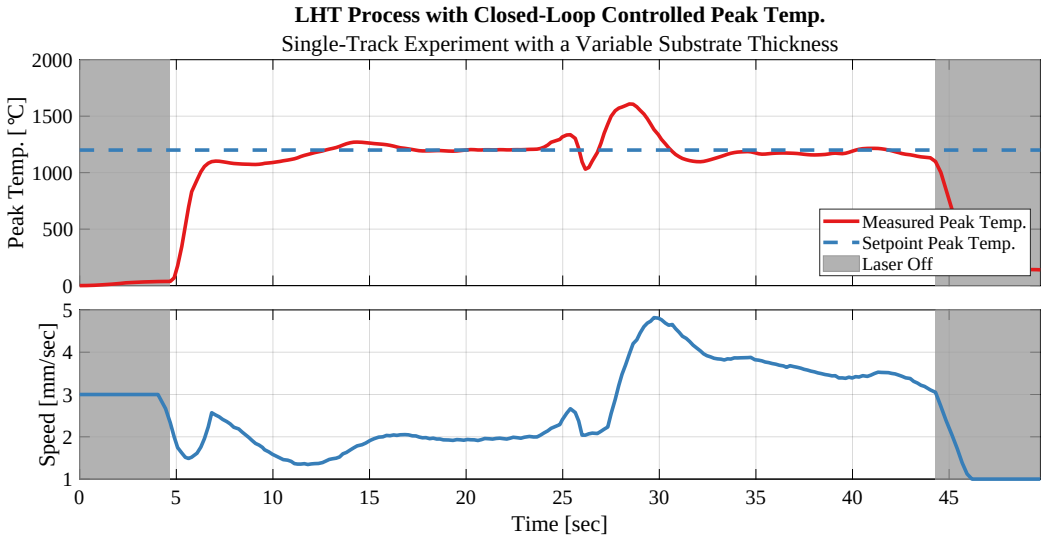
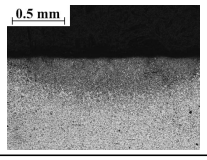
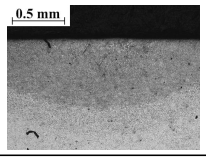
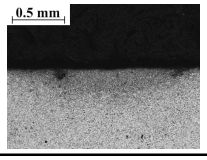
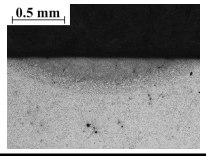


Figure 7.20: Peak temperature and traveling speed results of the closed-loop single-track experiment with a variable substrate thickness and a constant laser power of 300 W.

The substrate with the two different material thicknesses was cut at six locations, as shown in Figure 7.18, to evaluate and compare the microstructure and hardness values between the thick and thin substrate and between the open-loop and closed-loop conditions. Microscopic images were taken at the second and fifth cross sections, and the

results are shown in Table 7.10. It can be clearly observed with the open-loop experiment that a thin substrate resulted in a significantly increased hardening depth. On the other hand, the closed-loop experiment has a constant hardening depth for the thick and thin substrates. Therefore, a constant hardening depth can be obtained with different material thicknesses by controlling the peak temperature.

Table 7.10: Microscopic images at cross section 2 and 5 of the open-loop and closed-loop single-track experiment with a variable substrate thickness.

Case	**Thick Substrate**	**Thin Substrate**
Open-loop		
Closed-loop		

Each cross section had its hardness measured, and Table 7.11 shows the results of those measurements. For the open-loop case, no hardness measurements were taken at the sixth cross section in Figure 7.18. Looking at the hardness values of the open-loop experiment, one can clearly see the consequences of the effect of the change in substrate thickness. The hardness value decreased significantly with a thinner substrate, which is the result of the change in peak temperature and the change in heat transfer through the material. The hardness between the thick and thin substrates in the closed-loop experiment is much more similar. However, there is still a significant difference in hardness compared to the multi-track experiment. The reason for the difference in hardness is that the thicker substrate has a greater thermal mass, allowing it to dissipate heat more efficiently than the thinner substrate. This efficient heat dissipation leads to faster cooling rates in the localized LHT area, which can promote the formation of harder microstructures, such as martensite, in carbon steels, as shown in literature [38, 39, 40, 50]. One possible

solution is to both control the traveling speed and laser power to achieve a constant peak temperature and spatial cooling rate. By controlling multiple process parameters, constant hardness and hardening depths for different material thicknesses can be achieved simultaneously.

Table 7.11: Hardness measurements of the single-track open-loop and closed-loop experiment with a variable substrate thickness.

Average Hardness ± [Standard Deviation] (HV1.00)		
	Open-loop	**Closed-loop**
Thick substrate, Section 1 to 3	396±[4]	362±[4]
Thin substrate, Section 4 to 6	224±[4]	300±[3]

Concluding Remarks

The integration of the 2D thermal dynamic model with MPC represents a unique approach in the literature, showcasing the potential of combining predictive numerical modeling with advanced control techniques for LMP processes. Utilizing MPC, real-time control of process parameters based on model predictions enables precise control over key variables such as the peak temperature. Experimental results demonstrate that an MPC algorithm using the 2D thermal dynamic model for real-time peak temperature control is highly effective in achieving consistent hardness during the LHT process. Moreover, the MPC significantly increases the consistency of microstructure and quality of processed substrates by eliminating process disturbances and accurately following the reference trajectory for all experiments. Most experiments resulted in a constant hardening depth and hardness value, showcasing the robust performance of the developed MPC algorithm.

However, it is important to acknowledge that the simplicity of the 2D model may lead to prediction errors, particularly in complex and dynamic manufacturing scenarios. These errors can significantly impact control performance, potentially leading to deviations from desired microstructural outcomes. Therefore, while the 2D model pro-

vides a valuable foundation for control strategies, its limitations highlight the necessity of implementing adaptive models within the MPC framework. By incorporating adaptive models, MPC can dynamically adjust to changing process conditions, mitigating the impact of prediction errors and enhancing control accuracy. This adaptive approach ensures robust performance across a broader range of manufacturing scenarios, addressing the uncertainties inherent in LMP processes.

Furthermore, the experiment with a variable substrate thickness resulted in different hardness values for each material thickness while achieving a similar hardening depth. This reduced performance is attributed to different effective cooling rates at different material thicknesses. To address this issue, the MPC algorithm will be improved by incorporating spatial cooling rate control. This advancement will result in a new MIMO algorithm that simultaneously controls both the temperatures and cooling rate by adjusting laser power and traveling speed, improving process stability and achieving more consistent material characteristics of parts manufactured with LMP processes.

In summary, integrating the 2D thermal model with MPC provides a promising approach for real-time control of thermal dynamics to achieve consistent microstructure during LMP processes. However, to fully harness its potential, the implementation of adaptive models within the MPC framework, particularly through MIMO control, is essential. This adaptive approach ensures robust performance during manufacturing, addressing the complexities and uncertainties inherent in LMP processes and enabling consistent material characteristics of parts manufactured with LMP processes.

7.2.2 Closed-Loop LDED Process with AMPC

In total, four five-layer LDED wall experiments were conducted to assess the performance of the adaptive model predictive control (AMPC) algorithm and explore the impact of various control strategies. Additionally, the potential of MIMO control in achieving consistent material characteristics during the LDED process has been evaluated. The first two experiments, depicted in Figure 7.21, consist of an open-loop experiment and a closed-loop temperature control experiment. The subsequent two experiments, shown in Figure 7.22, include a closed-loop spatial cooling rate control experiment and a simultaneous closed-loop temperature and spatial cooling rate control experiment. Both substrates have been cut at three locations each, as shown in Figure 7.21 and Figure 7.22, to analyze the microstructure and hardness values across all four experiments.

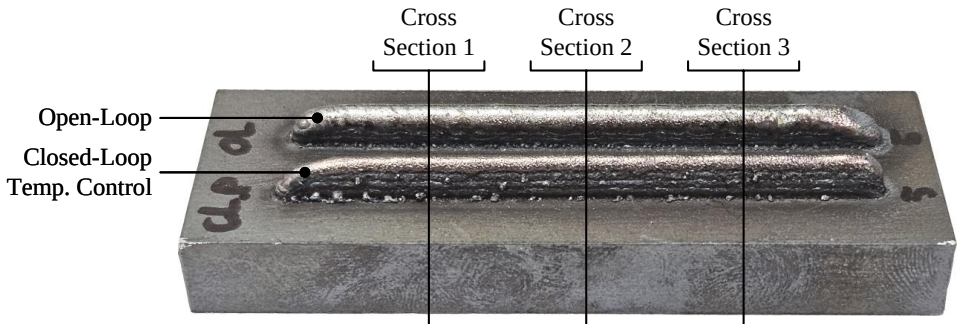


Figure 7.21: Carbon steel substrate with two five-layer LDED wall experiments: one in open-loop and the other with closed-loop temperature control.

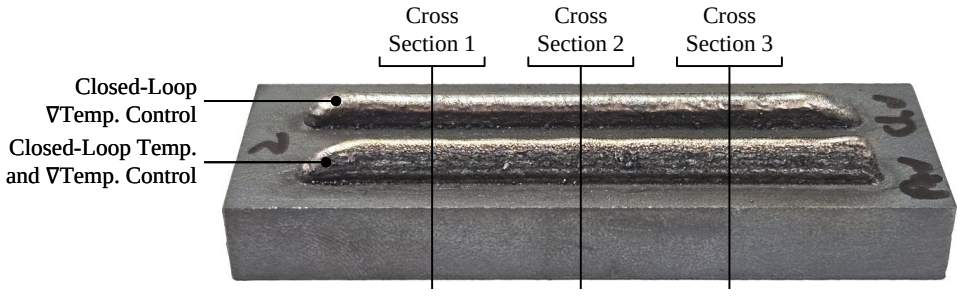


Figure 7.22: Carbon steel substrate with two five-layer LDED wall experiments: one with closed-loop controlled spatial cooling rate and the other with simultaneous closed-loop controlled temperature and spatial cooling rate.

LDED in open-loop.

In the open-loop experiment, a baseline understanding of the LDED process behavior without the influence of feedback control is established. This provides important insights into the inherent variability of thermal dynamics and their effects on the microstructure and material characteristics. The temperature and spatial cooling rate results of the LDED wall experiment in open-loop are depicted in Figure 7.23.

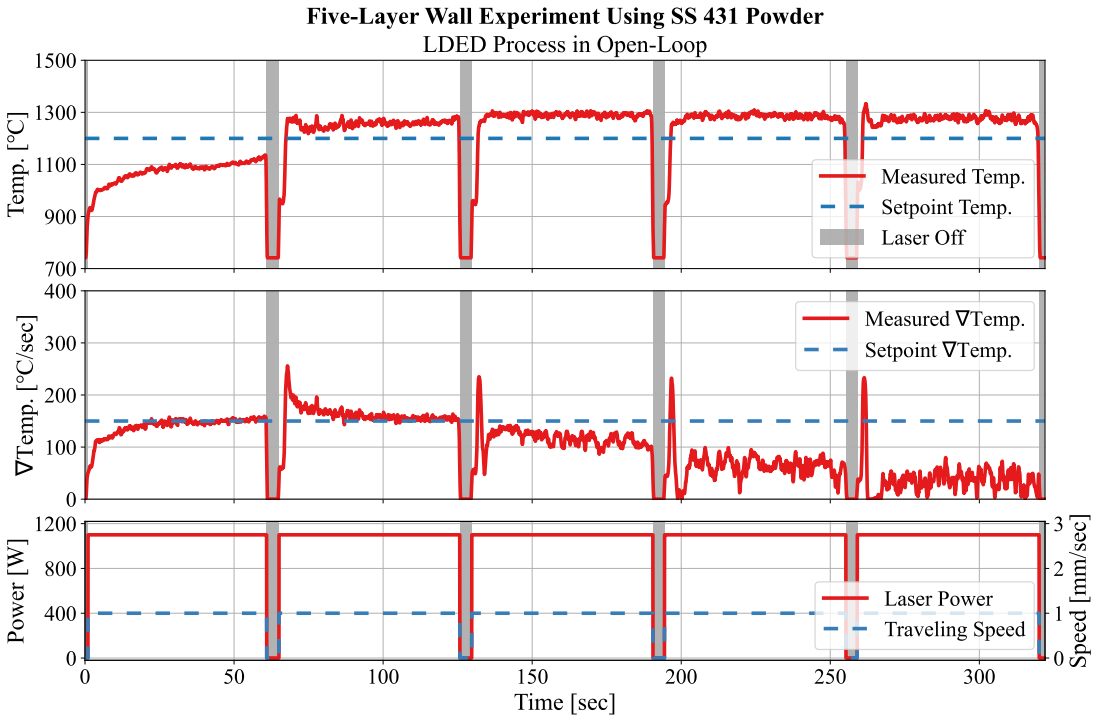


Figure 7.23: Temperature and spatial cooling rate results of the five-layer LDED wall experiment in open-loop.

As depicted in Figure 7.23, the temperature initially increases steadily with each layer throughout the experiment until the metal melts. This observed increase is attributed to the nature of the IR camera, which can accurately measure the solidified temperature but faces limitations when the melt pool expands, leading to a constant value in the measured temperature as it enters the molten region. Meanwhile, the spatial cooling

rate shows a slight increase for the first two layers. However, with each subsequent layer, the spatial cooling rate experiences a notable decrease. This decline can be attributed to heat accumulation within the deposition, leading to reduced cooling efficiency. The accumulation of heat alters the thermal dynamics, creating a feedback loop where increased temperature leads to decreased cooling rates, further exacerbating heat accumulation.

The size and shape of the melt pool, as depicted by its edge position, can reveal intricate details about the thermal behavior and material deposition dynamics that may not be fully captured by temperature and spatial cooling rate measurements alone. In Figure 7.24, the position of the melt pool edge at 1200 °C during the corresponding open-loop experiment is illustrated. As shown in this figure, the melt pool trailing edge position moves to the left with each subsequent layer, as indicated by the decrease in horizontal pixel location in the IR image. This observation indicates an expansion of the melt pool size due to the rapid accumulation of heat during the wall experiment, which can cause the remelting of previously solidified layers.

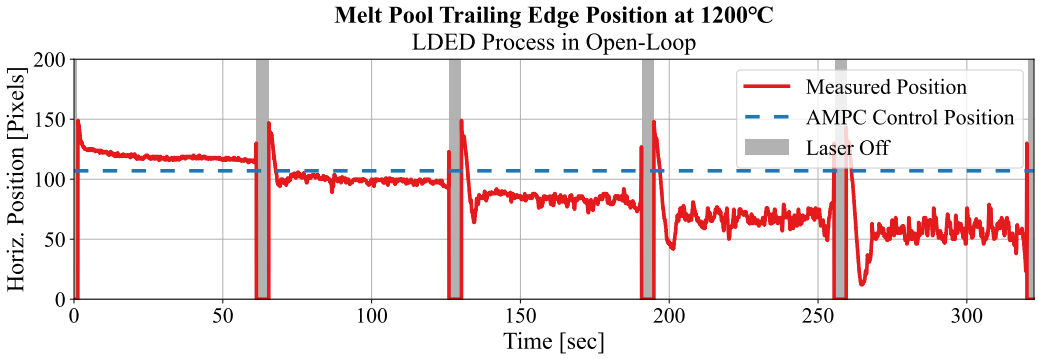


Figure 7.24: Melt pool edge position at 1200 °C during the five-layer LDED wall experiment in open-loop.

The observation of heat accumulation could promote the formation of larger grains or dendritic structures due to prolonged exposure to elevated temperatures. Additionally, the remelting of previously solidified layers between deposition passes can significantly affect the microstructure of the final part. Remelting introduces thermal cycling and variations in cooling rates, which can lead to heterogeneous microstructural features such as

grain boundaries, phase transformations, and residual stresses. Moreover, microstructural variations induced by remelting can significantly influence material properties, including hardness. To gain insights into the effects of remelting on material characteristics, hardness measurements are taken from the three cross sections and are presented in Figure 7.25. Additionally, corresponding boxplots of the hardness measurements across deposition heights can be found in Figure C.7 of Appendix C.1.

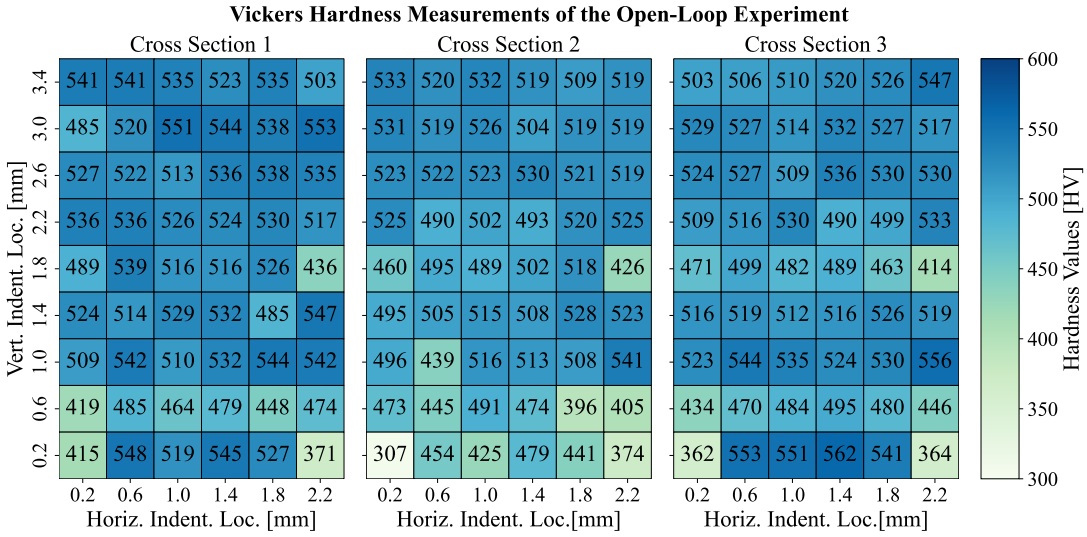


Figure 7.25: Hardness measurements from the three cross sections of the five-layer LDED wall experiment in open-loop.

The hardness measurements reveal notable differences between the first and subsequent layers. The average hardness of the first layer is approximately 465 HV, while the subsequent layers exhibit an average hardness of around 525 HV. This increase in hardness coincides with a significant decrease in the spatial cooling rate. Therefore, the heat accumulation became a significant issue by the third layer, indicating remelting of the second layer and contributed to the hardness disparity. This increase in hardness in the subsequent layers can thus be attributed to the effects of remelting on the microstructure. Effective mechanisms for controlling thermal dynamics are therefore crucial to mitigating these challenges and ensuring consistent material properties.

LDED with closed-loop controlled temperature.

In the closed-loop temperature control experiment, the laser power is adjusted in real-time to maintain a consistent temperature at the edge of the melt pool. This approach allows for an analysis of how temperature control affects the position of the trailing melt pool edge, as well as heat buildup and its impact on microstructure and material characteristics. Figure 7.26 presents the temperature and spatial cooling rate results from the LDED wall experiment with closed-loop temperature control.

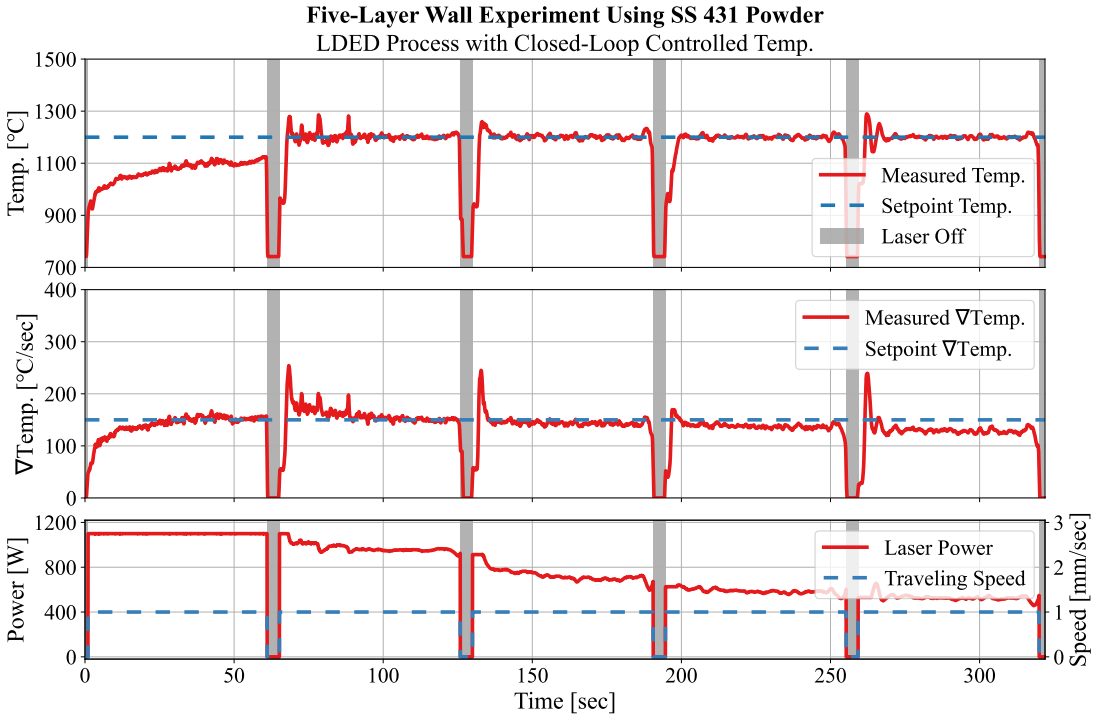


Figure 7.26: Temperature and spatial cooling rate results of the five-layer LDED wall experiment with closed-loop controlled temperature.

Figure 7.26 shows that during the first layer, the controller maximizes the laser power to reach the desired temperature setpoint but fails to achieve it due to rapid heat dissipation from the cold substrate. However, as additional layers are deposited, the controller effectively maintains the temperature setpoint by continuously adjusting the laser power.

The spatial cooling rate analysis indicates relatively consistent cooling rates throughout the process, with a modest decrease observed from the second layer to the final layer. Despite this minor variation, the overall stability and consistency of the spatial cooling rate highlight the effectiveness of the temperature control strategy.

In Figure 7.27, the real-time parameter estimation process of the 1D adaptive thermal model during the experiment is depicted. This figure illustrates how the model parameters are continually adjusted to align with the evolving thermal dynamics of the process. Notably, as the thermal conditions fluctuate, the model parameters adapt accordingly, ensuring an accurate representation of the system's behavior. Moreover, during periods of process stability, the model parameters exhibit relative steadiness, indicating the effectiveness of the parameter estimation approach in optimizing the model performance. This adaptive capability underscores the robustness and versatility of the parameter estimation technique in facilitating precise control of the LDED process. Comparatively, the nonadaptive MPC algorithm utilized in the LHT experiments lacks the capability to dynamically adjust model parameters based on real-time process conditions. While the nonadaptive approach may provide satisfactory control under stable operating conditions, it will lack performance due to evolving process dynamics or disturbances. In contrast, the adaptive parameter estimation technique used in the AMPC experiments enables the control system to continuously update its internal model to reflect the current state of the system, thereby enhancing adaptability and robustness in controlling the LDED process. Given the inherently complex nature of the LDED process, characterized by variable material compositions, intricate deposition geometries, and dynamic heat transfer phenomena, the ability to adaptively adjust the model parameters becomes critical. This adaptive capability allows the control system to respond accurately to changing process conditions, ensuring optimal performance and consistent part quality across varying operating scenarios. Therefore, the adaptive nature of the parameter estimation approach represents a significant advancement in control strategy, offering improved stability and performance over traditional nonadaptive methods.

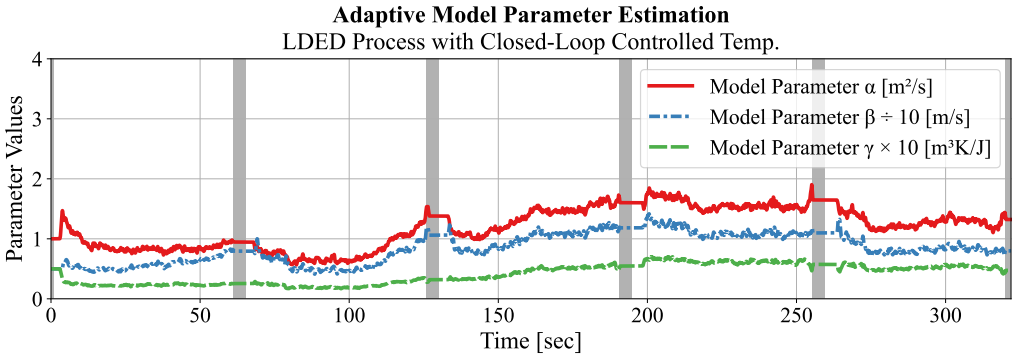


Figure 7.27: Real-time parameter estimation of the five-layer LDED wall experiment with closed-loop controlled temperature.

After analyzing the temperature and spatial cooling rate dynamics along with the real-time parameter estimation process, the next step is to explore the melt pool edge position at 1200 °C as depicted in Figure 7.28. In this figure, it is evident that for the first layer, the position of the melt pool edge is notably shifted towards the right in the IR image. This shift suggests that the melt pool size is relatively smaller compared to the preferred melt pool size. This observation is consistent with the lower melt pool temperature observed in Figure 7.26, indicating that the maximum laser power set by the controller during the first layer is not sufficient to achieve the preferred melt pool size. As subsequent layers are deposited, the position of the melt pool edge at 1200 °C aligns precisely with the AMPC control position. This alignment underscores the effectiveness of laser power control in regulating the temperature at the edge of the melt pool, resulting in a consistent location of the melt pool edge throughout the deposition process. This consistency in melt pool edge position signifies the stability and precision achieved through closed-loop temperature control, further highlighting the robustness of the control strategy in maintaining the desired melt pool trailing edge position.

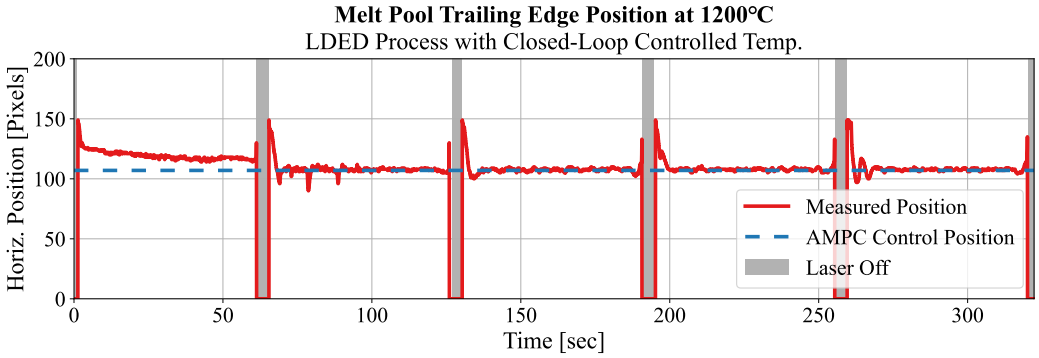


Figure 7.28: Melt pool edge position at 1200 °C during the five-layer LDED wall experiment with closed-loop controlled temperature.

Figure 7.29 visualizes the hardness measurements from all three cross-sections of the five-layer LDED wall experiment conducted under closed-loop controlled temperature conditions. For a more comprehensive view of hardness distribution within each layer, corresponding boxplots of hardness measurements across deposition heights are provided in Figure C.8 of Appendix C.1. The figures reveal that the average hardness of the first layer is approximately 450 HV, gradually decreasing to around 420 HV in the final layers. Subtle reductions in hardness are also observed at the boundaries between layers, likely due to thermal effects associated with the deposition process. When a new layer is deposited, the heat from the molten material can penetrate into the underlying layers, causing localized reheating of the previous layer's surface. This reheating can induce annealing, leading to reduced hardness. Furthermore, it is important to note that a sample from the first cross-section was accidentally flipped during preparation, resulting in hardness measurements closer to the start of the wall, which may explain the slightly higher hardness values observed in the first cross-section due to higher cooling rates. Overall, a consistent trend of slight reduction in hardness for subsequent layers is observed, aligning with the decrease in spatial cooling rate shown in Figure 7.26. This trend is consistent with existing literature, which indicates that a reduction in cooling rate leads to decreased hardness [48, 107, 17, 18, 50]. Additionally, the observed reduction in spatial cooling rate and hardness suggests that incorporating spatial cooling rate control into the controller could further improve material characteristics and hardness.

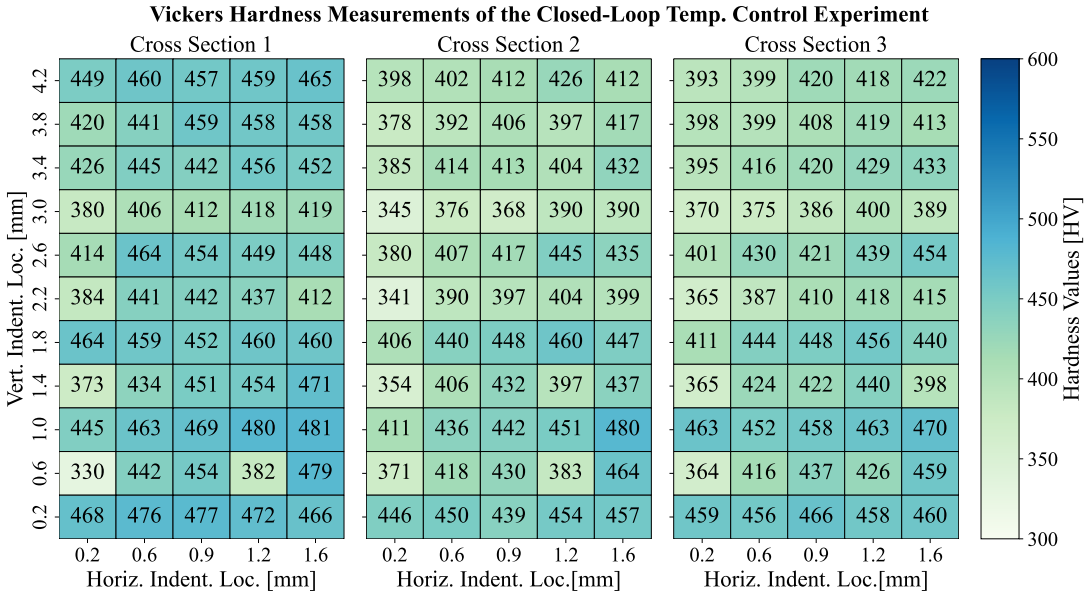


Figure 7.29: Hardness measurements from the three cross sections of the five-layer LDED wall experiment with closed-loop controlled temperature.

LDED with closed-loop controlled spatial cooling rate.

In the closed-loop spatial cooling rate control experiment, the traveling speed is controlled in real-time to maintain a consistent spatial cooling rate in the solidified deposition region. This setup allows for a detailed analysis of how variations in the spatial cooling rate affect the microstructure and material characteristics. Figure 7.30 displays the temperature and spatial cooling rate results from this LDED wall experiment. The figure reveals similar trends to those observed in the open-loop experiment. During the first layer, the temperature is below the setpoint, while subsequent layers show temperatures above the setpoint, suggesting rapid heat buildup within the deposition layers, a pattern also seen in the open-loop experiment. The similarity in temperature trends can be attributed to the consistent amount of energy added per second in both experiments. In LDED, the total energy added per second is determined by the energy deposition rate, which is influenced by the laser power and feed rate, as well as heat dissipation. In both the closed-loop spatial cooling rate control experiment and the open-loop experiment, laser

power and feed rate are kept constant throughout the process, meaning the same amount of energy is deposited per second, regardless of traveling speed. As a result, the heat buildup within the part remains consistent. Interestingly, the initial layers show effective control of the spatial cooling rate, achieved by adjusting the traveling speed to meet the setpoint. However, as the experiment progresses, rapid heat accumulation leads to a significant decline in the spatial cooling rate, necessitating a substantial increase in traveling speed to compensate. Consequently, towards the end of the experiment, the traveling speed becomes nearly three times higher than its initial value. Despite this, the controller's ability to adapt the traveling speed quickly is constrained by predefined limits on its maximum adjustment rate. These constraints are intentionally set to avoid sudden, large changes in traveling speed that could adversely affect material characteristics, such as deposition geometry, potentially leading to porosity and defects.

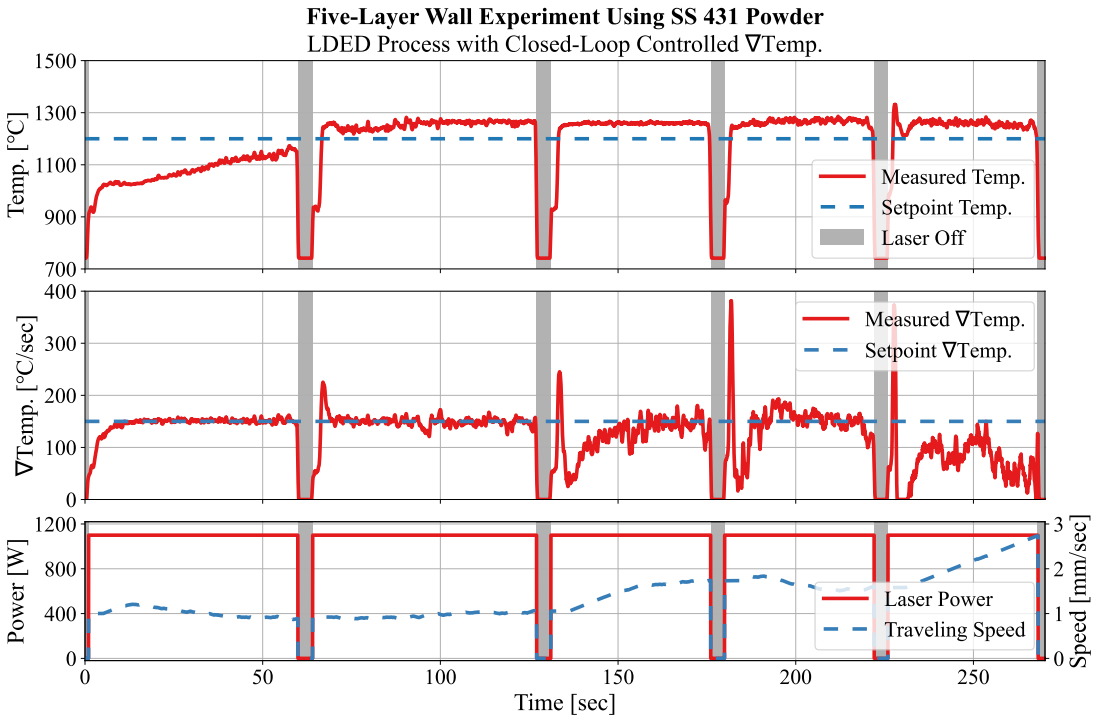


Figure 7.30: Temperature and spatial cooling rate results of the five-layer LDED wall experiment with closed-loop controlled spatial cooling rate.

Similar to the open-loop experiment, comparable trends in the melt pool edge position at 1200 °C are observable in the closed-loop controlled spatial cooling rate experiment, as depicted in Figure 7.31. With each deposited layer, the melt pool trailing edge position gradually shifts to the left, again indicative of rapid heat accumulation. However, in comparison to the open-loop experiment, the melt pool edge position exhibits slightly greater consistency between the second and fourth layers due to the controller actions. Nevertheless, this consistency does not deviate from the overarching trend of increasing melt pool size, attributed to the constant energy deposition throughout the experiment, as observed in the open-loop scenario. Consequently, this suggests that solely controlling the cooling rate without addressing the underlying heat buildup may not be sufficient for effectively maintaining a constant spatial cooling rate.

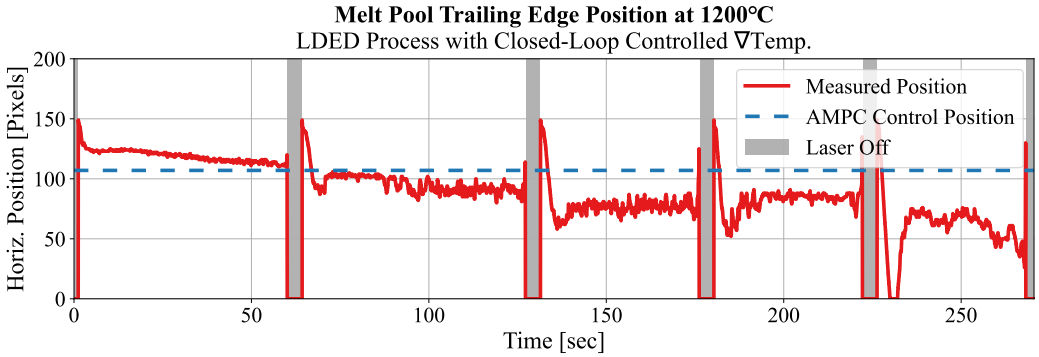


Figure 7.31: Melt pool edge position at 1200 °C during the five-layer LDED wall experiment with closed-loop controlled spatial cooling rate.

In Figure 7.32, the hardness measurements from the three cross sections of the five-layer LDED wall experiment with closed-loop controlled spatial cooling rate are displayed. Additionally, corresponding boxplots of the hardness measurements across deposition heights can be found in Figure C.9 of Appendix C.1. Initially, a hardness of around 500 HV is observed, gradually increasing to approximately 560 HV in the final layers. The initial hardness is lower compared to the open-loop experiment, whereas the final hardness exceeds that of the open-loop experiment. The lower values observed at the initial layers compared to the open-loop experiment may be attributed to a reduction in

remelting, likely due to the higher speeds resulting in less time available for remelting. Additionally, the higher cooling rates observed in the final layers compared to the open-loop experiment could be due to a combination of remelting and higher cooling rates resulting from the higher traveling speeds. These observations further highlight that solely controlling the cooling rate without addressing the underlying heat buildup is not sufficient to effectively maintain a constant spatial cooling rate during the process.

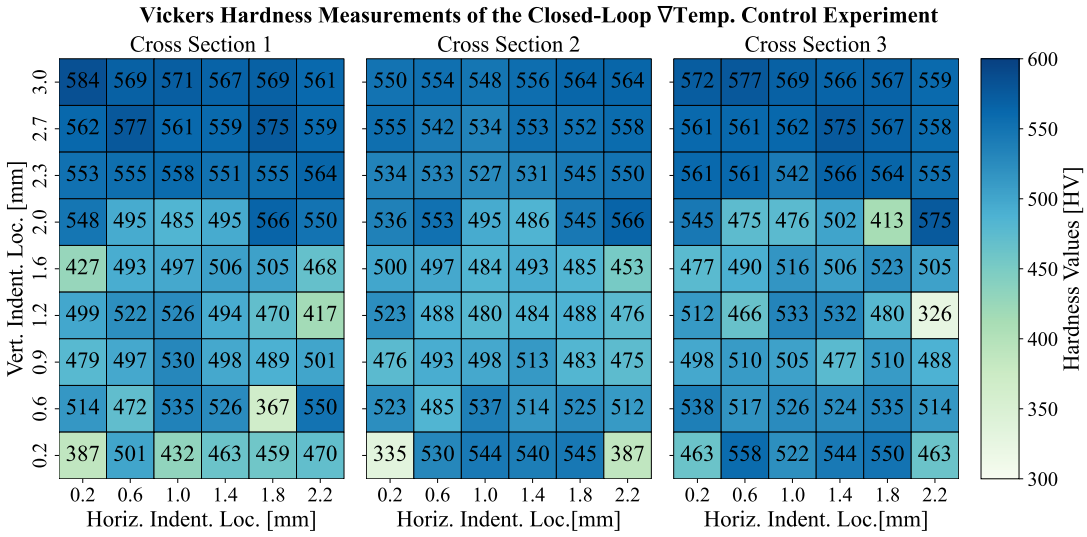


Figure 7.32: Hardness measurements from the three cross sections of the five-layer LDED wall experiment with closed-loop controlled spatial cooling rate.

In this closed-loop spatial cooling rate control experiment for LDED, the traveling speed is adjusted in real-time to maintain a consistent spatial cooling rate in the solidified region of the deposition. This approach shares similarities with the method employed in LHT experiments, where controlling the traveling speed ensures precise regulation of the surface temperature and thermal dynamics during LHT. However, the rapid accumulation of heat within the deposition layers presents a notable challenge unique to LDED, despite similarities in the control method. While the LHT experiments demonstrated the effectiveness of speed control in achieving uniform hardness, the dynamic nature of heat transfer and accumulation in LDED processes introduces complexities that demand

a more comprehensive control strategy. Therefore, addressing underlying heat buildup necessitates a MIMO control framework. By integrating simultaneous temperature and cooling rate control, as also mentioned with the LHT experiments, the LDED process can achieve enhanced thermal stability, ensuring consistent material characteristics across various process conditions.

LDED with closed-loop controlled temperature and spatial cooling rate.

In the closed-loop controlled temperature and spatial cooling experiment, both laser power and traveling speed are controlled in real-time to simultaneously maintain a consistent temperature at the edge of the melt pool and a consistent spatial cooling rate in the solidified region of the deposition. This approach allows for a comprehensive investigation of their combined effect on the microstructure and material characteristics. Moreover, it offers insights into how MIMO control can potentially enhance the microstructure and material characteristics compared to single-input single-output (SISO) control strategies. The temperature and spatial cooling rate results of the LDED wall experiment with simultaneous closed-loop controlled temperature and spatial cooling rate are shown in Figure 7.33. In this figure, the controller initially struggles to reach the temperature setpoint during the first layer due to heat dissipation from the cold substrate, which is similar to the SISO closed-loop temperature control experiment. However, due to the slower traveling speed during the first layer, the temperature is closer to the setpoint compared to the SISO temperature control experiment. Furthermore, the controller demonstrates accurate control over the spatial cooling rate for the first layer. As subsequent layers are deposited, the controller showcases its advanced capabilities by effectively maintaining both the temperature and spatial cooling rate at the required setpoints through simultaneous control of both the laser power and traveling speed. Notably, the changes in traveling speed to compensate for spatial cooling rate variations are minimal, indicating the added benefit of temperature control in reducing heat accumulation. This underscores the importance and advantage of employing MIMO control strategies, which offer enhanced control over the LDED process compared to SISO strategies.

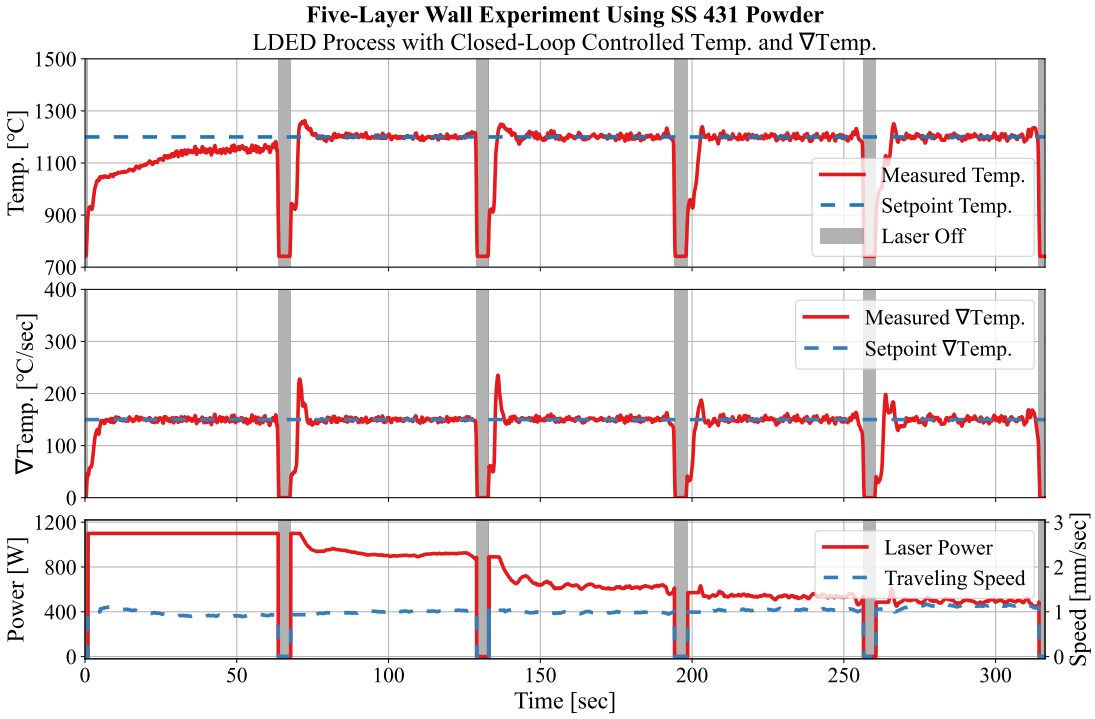


Figure 7.33: Temperature and spatial cooling rate results of the five-layer LDED wall experiment with closed-loop controlled temperature and spatial cooling rate.

In Figure 7.34, the real-time parameter estimation process of the 1D adaptive thermal model during the MIMO experiment is depicted. The figure shows the continuous adjustments made to the model parameters to accurately reflect the evolving thermal dynamics, ensuring precise control of the LDED process. These results reaffirm the effectiveness of the parameter estimation approach in optimizing model performance and underscore its robustness and versatility in facilitating accurate control. Notably, in MIMO control scenarios, where multiple inputs and outputs are interconnected, the adaptability of the model becomes even more crucial. Without an adaptive model, the dynamics between different process variables may change over time, leading to inaccuracies and instability in the model predictions and control output. However, with an adaptive model, as demonstrated here, the control system can adapt to these changing dynamics, ensuring stability and optimal performance even in complex MIMO control scenarios.

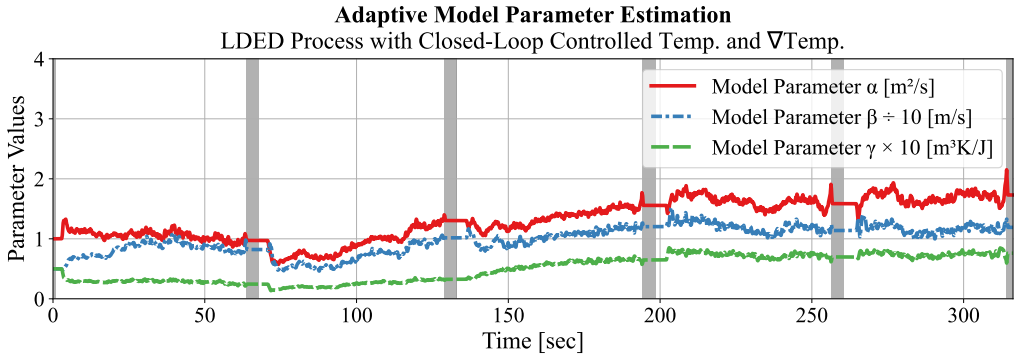


Figure 7.34: Real-time parameter estimation of the five-layer LDED wall experiment with simultaneous closed-loop controlled temperature and spatial cooling rate.

Similar to the SISO closed-loop temperature control experiment, comparable trends in the melt pool edge position at 1200 °C are observable in the MIMO control experiment, as depicted in Figure 7.35. The melt pool is slightly shifted to the right in the IR image. Nonetheless, this shift is less compared to the SISO closed-loop temperature control experiment. Moreover, the position of the melt pool edge at 1200 °C during the subsequent layers aligns precisely with the AMPC control position. This again underscores the effectiveness of controlling the temperature at the edge of the melt pool, resulting in a consistent location of the melt pool edge throughout the deposition process.

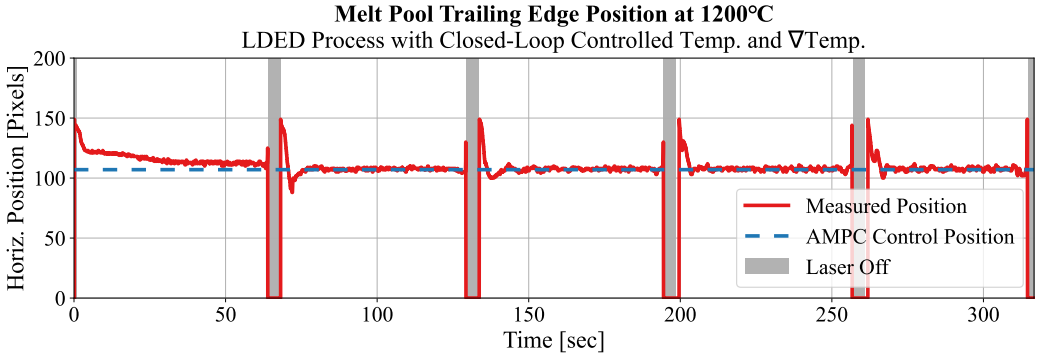


Figure 7.35: Melt pool edge position at 1200 °C during the five-layer LDED wall experiment with simultaneous closed-loop controlled temperature and spatial cooling rate.

The figures presented in Figure 7.36 showcase hardness measurements obtained from three cross sections of the five-layer LDED wall experiment conducted under closed-loop controlled temperature and spatial cooling rate conditions. Corresponding boxplots detailing hardness measurements across deposition heights can be found in Figure C.10 of Appendix C.1. Examination of these figures reveals a remarkable consistency in hardness values, averaging around 460 HV across all three cross sections and deposition layers. Additionally, slight reductions in hardness at layer boundaries, similar to those in the SISO closed-loop temperature control experiment, are observed. This is likely caused by localized reheating of the previous layer's surface, which induces annealing. Nonetheless, the consistency in hardness throughout the manufactured wall highlights the importance of maintaining a consistent temperature and spatial cooling rate throughout the process via real-time control of laser power and traveling speed. Moreover, the stability and uniformity achieved during the process, enabled by the MIMO control capabilities and the adaptive nature of the AMPC algorithm, underscore the unique advantages of this control technique over traditional methods.

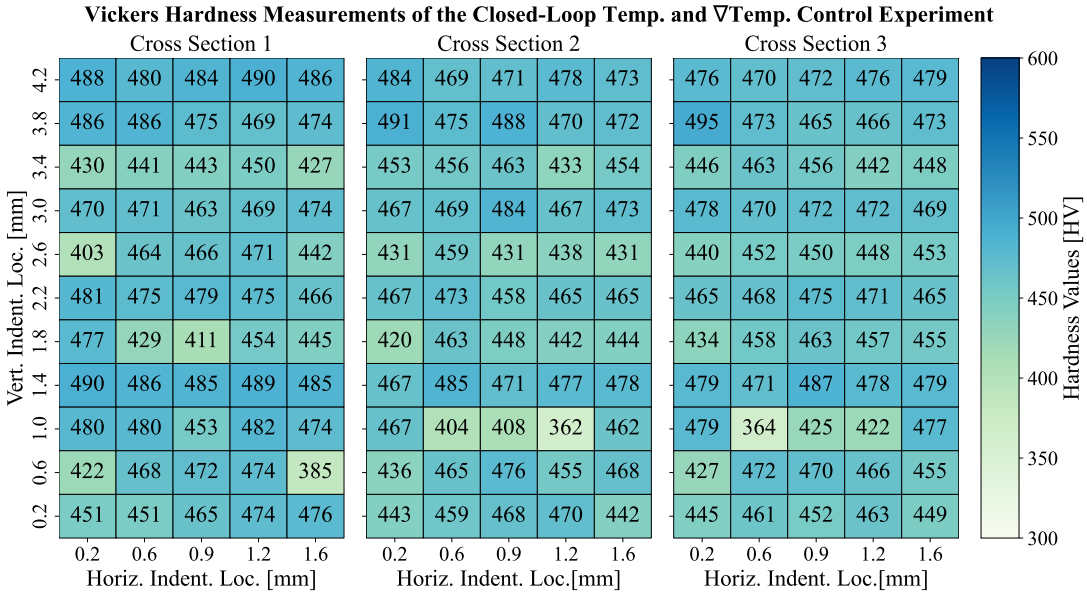


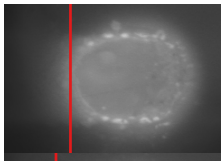
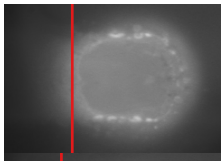
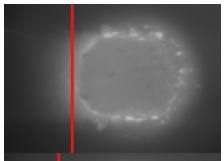
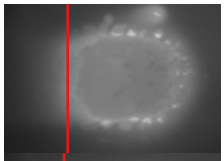
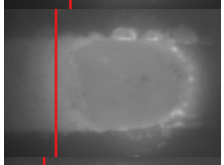
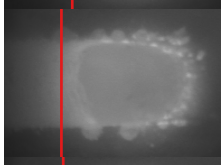
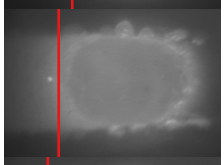
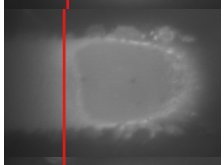
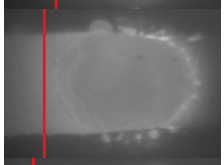
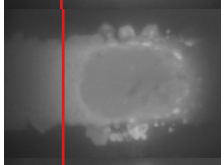
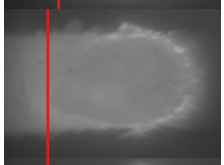
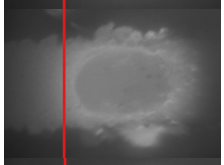
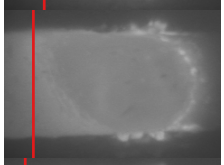
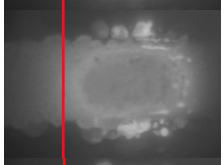
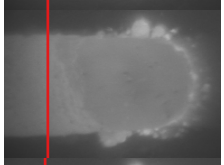
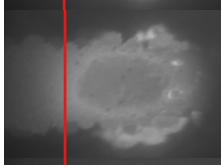
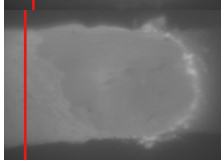
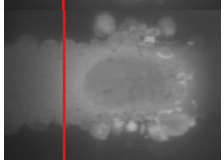
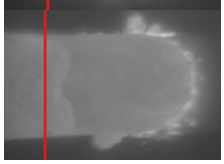
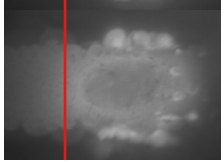
Figure 7.36: Hardness measurements from the three cross sections of the five-layer LDED wall experiment with closed-loop controlled temperature and spatial cooling rate.

Comparative analysis of all four LDED experiments

In this subsubsection, a comparative analysis of the four LDED wall experiments is conducted. The analysis focuses on several key aspects: analyzing melt pool images from each layer to understand the melt pool dynamics; evaluating height measurements to assess the influence of process parameters on the final part; and examining the mean hardness across deposition height to provide a comprehensive comparison of the four experiments.

A detailed comparison of melt pool evolution across deposition layers for all four LDED experiments is provided in Table 7.12. The table presents cropped images from the IR camera, showcasing the melt pool of each layer for the four LDED wall experiments. Moreover, each image includes a vertical red line indicating the melt pool trailing edge position at 1200 °C, corresponding to the same position presented in the previous figures. Upon analyzing these red lines across the four experiments, a consistent trend emerges, mirroring the observations from the images displaying the melt pool position in previous subsections. Notably, in the open-loop experiment, the trailing edge position shifts progressively to the left with each layer, indicating a significant heat buildup over time. Similarly, this trend is observed, though to a lesser extent, in the spatial cooling rate control experiment, suggesting again a high degree of heat accumulation. In contrast, both the closed-loop temperature control and MIMO temperature and spatial cooling rate control experiments exhibit a stable melt pool trailing edge position after the first layer. This consistency shows a successful mitigation of heat accumulation, resulting in minimal variation in the melt pool position throughout subsequent layers.

Table 7.12: Comparison of melt pool evolution across deposition layers for all four LDED Experiments.

	Open-Loop	**T Control**	**∇T Control**	**T+∇T Control**
Layer 1				
Layer 2				
Layer 3				
Layer 4				
Layer 5				

Upon comparing the brightness of the melt pool trailing edge across the experiments, a notable observation emerges. Experiments conducted with constant laser power exhibit a significantly brighter trailing edge, signifying significant heat accumulation within the deposition and also a reduction in cooling rate. Moreover, alongside the increase in brightness, the whole melt pool size increased as well. This expansion in melt pool size could have implications for the height of each layer deposited. A wider melt pool in LDED can cause the layer height to be reduced. When the heat causes the melt pool to widen, the same amount of material is spread over a larger horizontal area. As a result, there is less material available to build up the height of the deposited layer. Therefore,

the height of each layer may decrease due to the widening of the melt pool. Moreover, the increased melt pool size also causes previous layers to remelt, affecting their material properties. This has been observed in experiments with excessive heat buildup from constant laser power, as shown in the hardness measurements discussed earlier. This underscores the critical relationship between process parameters, heat management, and resulting material properties. The excessive heat accumulation not only influences the geometry of the deposited layers but also has tangible effects on material characteristics, such as hardness. Therefore, addressing issues related to heat buildup is essential for achieving desired material properties and ensuring the overall quality of the additive manufacturing process.

While the melt pool widens in experiments where temperature is not controlled, leading to heat buildup and subsequent issues such as reduced layer height and material remelting, experiments with temperature control exhibit a contrasting effect. In these controlled experiments, the melt pool width tends to narrow with each subsequent deposition layer, while the position of the melt pool trailing edge remains consistent across deposition layers. This narrowing is most likely attributed to the characteristics of the Gaussian laser beam of the LMP setup used in the experiments. Gaussian beams typically have a higher energy density at the center, gradually tapering off towards the edges. Therefore, reducing the laser power effectively diminishes the energy at the sides of the deposition, resulting in a narrower melt pool width. This phenomenon indicates that the observed narrowing of the melt pool width in experiments with temperature control is most likely attributed to the inherent characteristics of the Gaussian laser beam rather than solely to temperature control. Moreover, the use of a lateral nozzle in the LMP setup further amplifies this effect. With reduced energy at the sides of the deposition, the powder may not be effectively melted at the edges, contributing to the observed narrowing of the melt pool width. The lack of melting of the powder is evident in the images by the bright spots alongside both sides of the deposition, which are not visible in the experiment without laser power control. These bright spots indicate areas where the powder has not fully melted, further highlighting the impact of laser power control on the melt pool width and deposition quality.

Height measurements have been taken from the four experiments utilizing digital image correlation (DIC), a non-contact optical technique for measuring surface deformations and displacements. With DIC, precise measurements of the deposition height at various locations along the deposition length are achieved, boasting an accuracy of approximately 0.01 mm. Figure 7.37 illustrates the deposition height measurements across the deposition length for all four five-layer LDED wall experiments. In comparison, the open-loop experiment exhibits an average layer height of 4.9 mm, while the temperature control experiment achieves a slightly higher average layer height of 5.4 mm. Conversely, the experiment with only spatial cooling rate control demonstrates the lowest layer height, averaging 4.2 mm. This reduction in layer height compared to the open-loop experiment is mainly attributed to a substantial increase in traveling speed, leading to reduced material deposition per unit length. Significantly, the MIMO control experiment achieved the highest average height of 4.8 mm, outperforming the others and showing the achievement of effective controlling the temperature and spatial cooling rate simultaneously. Furthermore, it is intriguing that despite the smaller melt pool associated with the Gaussian beam characteristics, both experiments with temperature control still achieved a higher average layer height compared to the experiments with a constant later power. This indicates that factors beyond just melt pool size, such as precise control over temperature gradients and deposition parameters, play crucial roles in determining the final layer height.

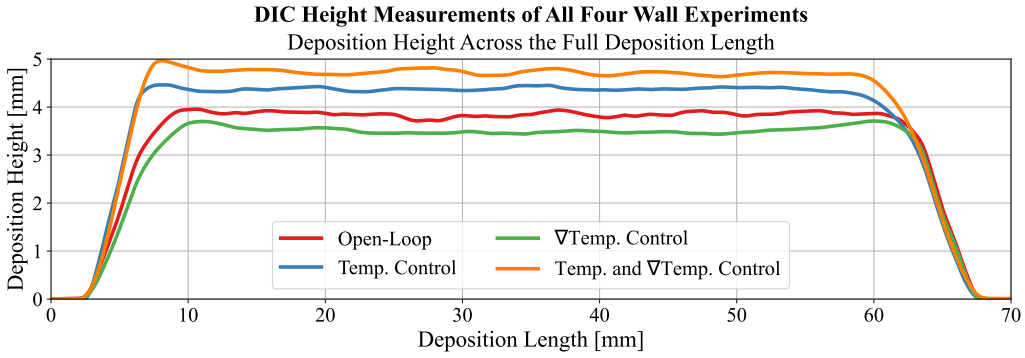


Figure 7.37: DIC deposition height measurements across deposition length for of all four five-layer LDED wall experiments.

In Figure 7.38, the mean hardness measurements across the deposition height for all four five-layer LDED wall experiments are depicted. This figure provides a comprehensive overview of the material properties throughout the deposition process. Observing the lines in the figure, it can be noted that the initial hardness of the open-loop experiment is similar to that of both experiments with temperature control. However, after the first layer, there is a significant increase in mean hardness, consistent with previous observations. This increase aligns with the lower layer heights and extreme heat accumulation observed, which can lead to remelting, which can significantly alter the material properties and increase the hardness. Therefore, it can be concluded that remelting is indeed the cause of the increase in hardness observed in subsequent layers. Similar reasoning can be applied to the spatial cooling rate control experiment. The mean hardness of this experiment also shows a significant increase compared to the two experiments with temperature control. Additionally, similar heat accumulation was observed, indicating an increase in hardness due to the presence of remelting. In contrast, the mean hardness of the temperature control experiments gradually reduces at higher depositions. This reduction coincides with a slow decrease in cooling rate previously observed in each layer, which reduces the hardness. On the other hand, the mean hardness remains relatively constant throughout the deposition height in the MIMO control experiment. This consistency highlights the effectiveness of MIMO control in maintaining uniform material properties, further underscoring its significance.

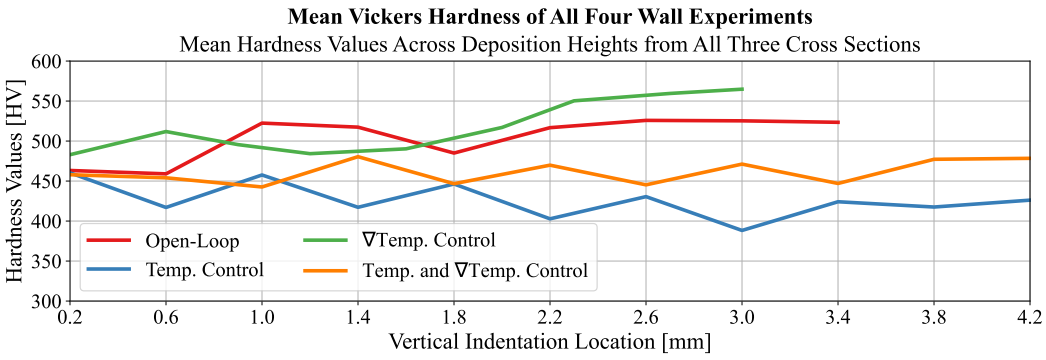


Figure 7.38: Mean hardness measurements from the three cross sections of all four five-layer LDED wall experiments.

Concluding Remarks

The comparative analysis of the four LDED experiments provides crucial insights into how process parameters affect melt pool dynamics, layer height, and material properties. The trends observed underscore the importance of controlling the thermal dynamics to prevent issues such as heat accumulation and remelting, which can significantly influence final material characteristics. Additionally, the superiority of MIMO control in maintaining uniform material properties throughout the deposition process is evident, highlighting its role in ensuring consistent part quality in LDED. This research not only deepens the understanding of the LDED process but also emphasizes the critical role of advanced control strategies, like MIMO, in improving process stability and product reliability.

The advancements demonstrated in this study, especially in MIMO model-based control, represent a significant improvement over traditional SISO and error-based control methodologies. While non-adaptive approaches may falter in maintaining stability during evolving process dynamics, the adaptive nature of MIMO control facilitates real-time adjustments in response to changing conditions, thereby ensuring robustness and reliability in controlling intricate LDED processes. Furthermore, MIMO control offers a holistic solution compared to SISO methods by considering multiple inputs and outputs simultaneously. Thereby, enabling real-time control of multiple process features ensures improved consistency in material characteristics within LMP processes. Moreover, the integration of numerical models further enhances the efficacy of MIMO control by providing a more accurate depiction of the dynamic behavior of the LDED process. This adaptive numerical approach enables precise correlation and adjustment of multiple process variables, leading to notable improvements in control performance and part quality.

However, despite these advancements, several limitations and areas for future research emerge. The observed inconsistencies in material characteristics, particularly regarding the reduced deposition width with each layer due to the reduction in laser power, underscore the need for further investigations using alternative laser setups. Additionally, while height measurements were taken, deviations in height were observed, indicating the need for direct height control. In addition, it is important to acknowledge that adjusting

the process traveling speed directly affects the layer height, a factor that has not been thoroughly investigated. To ensure a uniform layer height, direct control of other process parameters, such as powder feed rate, is required. Consequently, controlling additional process parameters beyond temperature and spatial cooling rate becomes necessary.

Furthermore, while the 1D adaptive model has been validated for multiple feedstock materials, the current AMPC algorithm has only been validated for one feedstock material. Moreover, the AMPC algorithm is only validated for one LMP process with a single deposition geometry, Therefore, the AMPC algorithm requires further validation across various systems, processes, materials, and deposition geometries to comprehensively assess the potential and limitations of this process control methodology. Moreover, the current research focuses on simultaneous control of two process parameters, yet numerous other factors such as powder feed rate, layer thickness, layer spacing, travel direction, and material composition significantly impact final material characteristics. Integrating more process parameters and models into the MIMO AMPC algorithm is essential to further improving the consistency of the material characteristics.

Importantly, addressing these limitations and executing the outlined future research steps are crucial to unlocking the full potential of MIMO AMPC in advanced manufacturing processes and achieving complete consistency and repeatability in the material characteristics. Furthermore, while this research focuses on laser-based processes, similar methodologies can be applied to other processes with a concentrated energy source, such as electron beam processes, electric arc processes, and plasma arc processes. By conducting further investigations into alternative setups, validating the AMPC algorithm across diverse systems and deposition geometries, integrating additional models and process parameters into the control algorithm, and extending the methodology to a broader range of manufacturing techniques, including welding, cladding, additive manufacturing, and other processes, the full capabilities of the MIMO AMPC for enhancing the quality and reliability of advanced manufacturing processes can be achieved. Moreover, the development and implementation of MIMO AMPC algorithms will not only contribute to advancing the field of advanced manufacturing but also pave the way for the widespread adoption of advanced manufacturing across various industries.

7.3 Chapter Summary

This chapter presents the results of experiments conducted to validate the thermal dynamic models and MPC algorithms developed in the preceding chapters. The aim is to assess their effectiveness, reliability, and practical utility in improving process stability and ensuring consistent material properties. Initially, the results and discussions of experiments assessing the real-time thermal dynamic prediction capabilities of developed thermal models in both LHT and LDED processes are presented. First, the predictive accuracy of non-adaptive and adaptive 2D thermal models in LHT are compared, revealing that while the non-adaptive model demonstrates improved accuracy compared to existing models in literature, the adaptive model significantly improves accuracy by dynamically adjusting parameters in real-time, particularly mitigating errors caused by heat accumulation. Second, the 1D adaptive thermal model is evaluated across four experiments with different deposition materials. Despite the complexity of the thermal dynamics in LDED, the adaptive model is able to effectively track real-time thermal dynamic changes, closely matching process measurements. Overall, these findings underscore the potential of adaptive thermal models for enhancing prediction accuracy in LMP processes and broader applicability, including their suitability for model-based control applications such as MPC.

Subsequently, the results and discussions of experiments assessing real-time thermal dynamic control in both LHT and LDED processes using MPC algorithms. With the LHT experiments, the peak temperature control for consistent microstructure under various conditions is analyzed. These experiments include single-track experiments with stepped setpoint temperatures and variations in substrate thickness, as well as multi-track experiments. The MPC algorithm effectively controls peak temperatures, achieving consistent hardness and hardening depth, as validated through microscopy and hardness measurements. With the LDED experiments, four experiments were conducted, including open-loop and closed-loop temperature control, closed-loop spatial cooling rate control, and simultaneous closed-loop temperature and spatial cooling rate control. Comparative analysis of these experiments revealed insights into melt pool dynamics, layer height, and

material properties. Observations indicate that the experiments that included temperature control exhibit stable melt pool dynamics and consistent layer heights compared to a reduced layer height with the experiments using constant laser power. However, the experiments that included temperature control showed a narrowing of the melt pool width due to the Gaussian laser beam characteristics, leading to a reduced melt pool width. In contrast, using constant laser power results in wider melt pools, reducing layer heights and material remelting, which increases hardness. Moreover, SISO temperature control is not enough to achieve uniform material properties. Whereas the MIMO control experiment demonstrated superior performance in maintaining uniform material properties.

This MIMO AMPC approach marks a significant improvement over traditional non-adaptive, SISO, and error-based control methodologies by enabling real-time control of multiple process features, facilitating real-time adjustments in response to changing conditions, and improving the efficacy of MIMO control due to the integration of numerical models. Therefore, the implementation of MIMO AMPC is critical in ensuring consistent material characteristics in parts manufactured with LMP processes. Nonetheless, limitations and areas for future research are identified. These include the need for further investigation into alternative laser setups, direct control of process parameters affecting layer height, validation of the AMPC algorithm across different materials and process geometries, and integration of additional process parameters into the control algorithm. Addressing these will enhance the consistency and repeatability of material characteristics in LMP processes and pave the way for widespread adoption of advanced manufacturing processes in various industries.

Chapter 8

Conclusions and Future Work

8.1 Conclusions

The primary objective of this research was to develop an adaptive model predictive control (AMPC) algorithm designed for real-time control of thermal dynamics in laser material processing (LMP) processes. This approach aims to indirectly control the microstructure through real-time monitoring, prediction, and control of the thermal dynamics. Through systematic development and integration of adaptive thermal models and model predictive control (MPC) algorithms, this study has successfully developed and implemented an AMPC algorithm, demonstrating its effectiveness, including multi-input multi-output control, in enabling consistent microstructure throughout the manufactured part in LMP processes. The conclusions and contributions of this work are summarized as follows:

- A two-dimensional (2D) adaptive thermal model was developed for real-time prediction of peak temperature and spatial cooling rate during the laser heat treatment (LHT) process. This model, which is based on a numerical approach, surpasses the accuracy and adaptability of models found in existing literature, thereby marking a significant advancement in the field. Experimental results using two different materials demonstrate the model's impressive prediction accuracy, with average peak temperature and spatial cooling rate prediction errors of only ± 0.8 % and ± 5.2 %,

respectively. Notably, the average peak temperature prediction error is within the thermal camera's accuracy of ±1 %, underscoring the model's reliability. Moreover, the average spatial cooling rate prediction error falls within an acceptable range that has negligible effects on material properties. The developed adaptive thermal model showcases both exceptional accuracy and computational efficiency, rendering it highly suitable for real-time AMPC applications. Furthermore, its ability to effectively address thermal dynamic changes in real-time enhances its utility in ensuring consistent and high-quality parts in LMP processes. This model, therefore, stands as a testament to the potential of numerical models in revolutionizing real-time prediction and control in advanced manufacturing processes.

- Building on the success of the prior 2D model, a novel one-dimensional (1D) adaptive thermal model was developed to precisely predict and control thermal dynamics during laser-directed energy deposition (LDED) processes. Leveraging insights gleaned from the prior 2D model, this innovative approach represents a significant leap forward in precision, adaptability, and computational efficiency. Experimental results across four distinct deposition materials demonstrated remarkable precision in predicting temperature and spatial cooling rate, with temperature predictions consistently falling within the ±1 % accuracy range of infrared camera measurements across all four experiments. Moreover, spatial cooling rate predictions demonstrate exceptional alignment with thermal measurements, with a maximum prediction error of just 2.78%. This level of precision is a testament to the model's superior predictive capabilities. These advancements position the 1D adaptive thermal model as a valuable tool for optimizing LDED processes, offering enhanced predictive capabilities, computational efficiency, and suitability for real-time control applications such as AMPC. This model, therefore, stands as a significant contribution to the field of numerical models for real-time prediction and control applications.

- An MPC algorithm, utilizing a 2D numerical model, has been developed for real-time peak temperature control in LHT. This algorithm is designed to achieve consistent hardness during the LHT process, thereby enhancing the quality and reliability of the final product. The MPC algorithm was able to eliminate process disturbances and accurately follow the reference trajectory for all experiments. As a result, most experiments resulted in a constant hardening depth and hardness value. In addition, experiments showed that controlling the peak temperature at specific setpoints results in specific local hardness and hardening depth, underscoring the precision and adaptability of the developed MPC algorithm. Therefore, the developed MPC algorithm has been found to be extremely effective and, at the same time, computationally efficient for real-time peak temperature control during LHT. Moreover, the integration of computationally efficient numerical models with advanced control strategies represents a revolutionary approach for optimizing the material characteristics LMP processes, paving the way for more reliable and efficient production of high-quality components.
- An AMPC algorithm, which incorporates an 1D numerical model, has been developed for real-time simultaneous control of temperature and spatial cooling rate in LDED to achieve consistent material characteristics in the manufactured part. By building upon the insights gained from previous models and control strategies developed for LHT, this innovative method allows for the precise control of several process parameters simultaneously. Experimental validation confirms the AMPC algorithm's efficacy in maintaining stable melt pool dynamics, consistent layer heights, and uniform material properties during the deposition process. The integration of the 1D adaptive thermal model further enhances its predictive accuracy and enables dynamic adjustments to evolving process conditions. These advancements signify a major shift in process control methodologies for LMP processes, offering unprecedented levels of process stability and reliability in producing high-quality parts. Consequently, the AMPC algorithm has the potential to revolutionize the advanced manufacturing industry, given its unique capability to guarantee uniformity and consistency in the material characteristics of LMP processes.

In summary, this research has achieved significant advancements in the field of process control in LMP. The development and integration of adaptive thermal models and MPC algorithms have enabled precise control over thermal dynamics, resulting in consistent material characteristics in LMP processes. Specifically, a 2D adaptive thermal model was developed for real-time prediction of peak temperature and spatial cooling rate during the LHT process, showcasing exceptional accuracy and computational efficiency. Subsequently, a novel 1D adaptive thermal model was introduced for precise prediction and control of thermal dynamics in LDED processes, demonstrating remarkable precision and enhancing predictive capabilities. Moreover, an MPC algorithm utilizing a 2D numerical model was developed for real-time peak temperature control during LHT, significantly improving the consistency of microstructure and quality of processed samples. Notably, an AMPC algorithm employing a 1D numerical model was developed for simultaneous control of temperature and spatial cooling rate in LDED, revolutionizing process control methodologies by offering unprecedented levels of control, stability, and reliability. Moreover, the versatility and simplicity of the AMPC methodology extend its applicability beyond LMP processes, facilitating adoption in various advanced manufacturing processes utilizing concentrated energy sources such as electron beam, electric arc, and plasma arc processes. The scalability of the AMPC methodology underscores its potential to revolutionize advanced manufacturing by ensuring consistent and reproducible material characteristics in manufactured parts across the entire industry.

8.2 Future Work

To advance this work and further enhance the performance, versatility, and scalability of the AMPC methodology outlined in this study, the following recommendations are proposed:

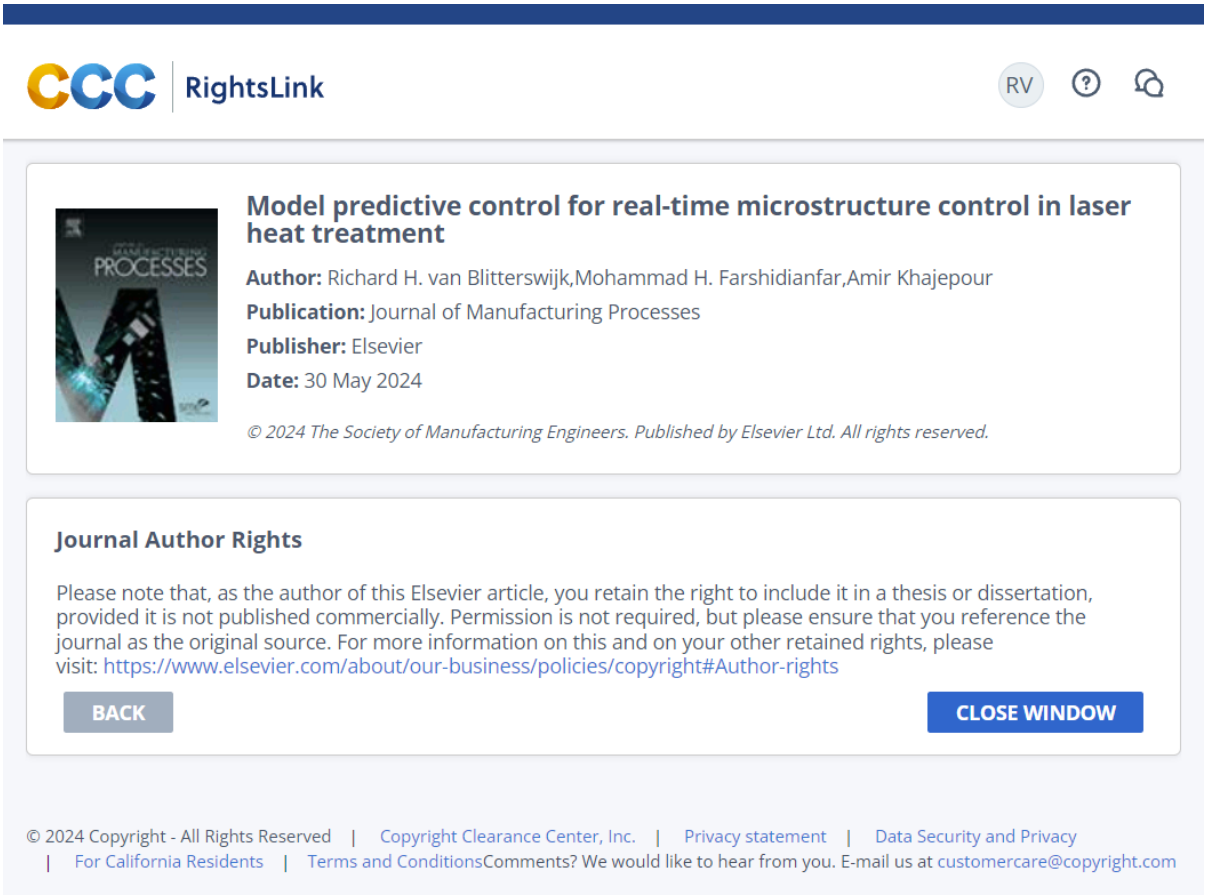
- **Broader Validation Across Systems:** The current validation of the AMPC algorithm has been limited to a single material and process configuration. However, to comprehensively evaluate its robustness and generalizability, it is essential to extend validation efforts beyond these constraints. This includes validating the algorithm across a broader range of systems, processes, materials, and deposition geometries representative of diverse advanced manufacturing scenarios. Conducting a much wider validation study enables a deeper understanding of the algorithm's performance under various operating conditions. This comprehensive validation approach is crucial for ensuring that the AMPC algorithm remains effective and reliable across a wide spectrum of real-world manufacturing environments, thereby enhancing its practical utility and applicability in the advanced manufacturing industry.
- **Enhance Predictive Models:** Continuously refining and expanding the predictive models underlying the AMPC algorithm is crucial for enhancing its accuracy, adaptability, and predictive capabilities across diverse process conditions and materials. While refining the existing 1D numerical model to better capture the intricate thermal dynamics of LMP processes remains essential, expanding the model to incorporate additional process variables can provide deeper insights into the complex relationships between various process parameters. This holistic approach to model refinement and expansion will not only improve the algorithm's predictive capability and accuracy but also open the door to the simultaneous control of multiple parameters in advanced manufacturing processes, improving process stability and thereby enhancing the consistency of the material characteristics of parts manufactured with advanced manufacturing processes.

- **Expand Control Capabilities:** While the AMPC algorithm demonstrates effective simultaneous control of temperature and spatial cooling rate, there is potential to enhance its capabilities further by integrating additional process parameters into the control framework. Examples of such parameters include material feed rate, layer spacing, layer thickness, and travel direction, among others. Incorporating a wider range of process variables into the AMPC algorithm would not only optimize the complete set of material characteristics but also improve overall process stability and repeatability. Moreover, the possibility of accommodating a broader range of process variables distinguishes the AMPC methodology from traditional control methods, underscoring its adaptability and effectiveness in optimizing advanced manufacturing processes.

Letter of Copyright Permission



Permission for the reuse of published content from [205]



Permission for the reuse of published content from [49]

References

[1] J. D. Majumdar, I. Manna, Laser material processing, International Materials Reviews 56 (5-6) (2011) 341–388. doi:10.1179/1743280411Y.0000000003.

[2] M. Keskitalo, J. Sundqvist, K. Mäntyjärvi, J. Powell, A. Kaplan, The influence of shielding gas and heat input on the mechanical properties of laser welds in ferritic stainless steel, Physics Procedia 78 (2015) 222–229. doi:10.1016/j.phpro.2015.11.032.

[3] D. Thomas, Costs, benefits, and adoption of additive manufacturing: a supply chain perspective, The International Journal of Advanced Manufacturing Technology 85 (2016) 1857–1876. doi:10.1007/s00170-015-7973-6.

[4] L. Nickels, Inside out 3d printing, Metal Powder Report 73. doi:10.1016/j.mprp.2018.03.050.

[5] G. Bi, C.-N. Sun, A. Gasser, Study on influential factors for process monitoring and control in laser aided additive manufacturing, Journal of Materials Processing Technology 213 (2013) 463–468. doi:10.1016/j.jmatprotec.2012.10.006.

[6] A. B. J. Sullivan, P. F. Houldcroft, Gas-jet laser cutting, British Welding Journal 46 (1967) 443.

[7] A. Sharma, V. Yadava, Experimental analysis of nd-yag laser cutting of sheet materials – a review, Optics & Laser Technology 98 (2018) 264–280. doi:10.1016/j.optlastec.2017.08.002.

[8] A. C. Tam, W. P. Leung, W. Zapka, Wernerand Ziemlich, Laser-cleaning techniques for removal of surface particulates, Journal of Applied Physics 71 (7) (1992) 3515–3523. doi:10.1063/1.350906.

[9] J. Rohde, A. Jeppsson, Literature review of heat treatment simulations with respect to phase transformation, residual stresses and distortion, Scandinavian Journal of Metallurgy 29 (2) (2000) 47–62. doi:10.1034/j.1600-0692.2000.d01-6.x.

[10] S. Katayama, Handbook of Laser Welding Technologies, Woodhead Publishing Series in Electronic and Optical Materials, Elsevier Science, 2013.
URL: https://books.google.ca/books?id=wWZEAgAAQBAJ

[11] W. M. Steen, J. Mazumder, Laser material processing, 3rd Edition, springer science & business media, 2010. doi:10.1007/978-1-84996-062-5.

[12] K. Moeinfar, F. Khodabakhshi, S. Kashani-bozorg, M. Mohammadi, A. Gerlich, A review on metallurgical aspects of laser additive manufacturing (lam): Stainless steels, nickel superalloys, and titanium alloys, Journal of Materials Research and Technology 16 (2022) 1029–1068. doi:10.1016/j.jmrt.2021.12.039.

[13] Y. Cai, J. Xiong, H. Chen, G. Zhang, A review of in-situ monitoring and process control system in metal-based laser additive manufacturing, Journal of Manufacturing Systems 70 (2023) 309–326. doi:10.1016/j.jmsy.2023.07.018.

[14] R. Nandhakumar, K. Venkatesan, A process parameters review on selective laser melting-based additive manufacturing of single and multi-material: Microstructure, physical properties, tribological, and surface roughness, Materials Today Communications 35 (2023) 105538. doi:10.1016/j.mtcomm.2023.105538.

[15] M. Liu, A. Kumar, S. Bukkapatnam, M. Kuttolamadom, A review of the anomalies in directed energy deposition (ded) processes & potential solutions - part quality & defects, Procedia Manufacturing 53 (2021) 507–518, 49th SME North American Manufacturing Research Conference (NAMRC 49, 2021). doi:10.1016/j.promfg.2021.06.093.

[16] J. Bi, L. Wu, S. Li, Z. Yang, X. Jia, M. D. Starostenkov, G. Dong, Beam shaping technology and its application in metal laser additive manufacturing: A review, Journal of Materials Research and Technology 26 (2023) 4606–4628. doi:10.1016/j.jmrt.2023.08.037.

[17] M. H. Farshidianfar, F. Khodabakhshi, A. Khajepour, A. P. Gerlich, Closed-loop control of microstructure and mechanical properties in additive manufacturing by directed energy deposition, Materials Science and Engineering: A 803 (2021) 140483. doi:10.1016/j.msea.2020.140483.

[18] M. Farshidianfar, F. Khodabakhshi, A. Khajepour, A. Gerlich, Closed-loop deposition of martensitic stainless steel during laser additive manufacturing to control microstructure and mechanical properties, Optics and Lasers in Engineering 145 (2021) 106680. doi:10.1016/j.optlaseng.2021.106680.

[19] M. Ansari, M. Khamooshi, E. Toyserkani, Adaptive model-based optimization for fusion-based metal additive manufacturing (directed energy deposition), Journal of Manufacturing Processes 108 (2023) 588–595. doi:10.1016/j.jmapro.2023.11.026.

[20] Z. Wang, C. Wang, C. Li, Y. Qin, L. Zhong, B. Chen, Z. Li, H. Liu, F. Chang, J. Wang, Analysis of factors influencing bone ingrowth into three-dimensional printed porous metal scaffolds: A review, Journal of Alloys and Compounds 717 (2017) 271–285. doi:10.1016/j.jallcom.2017.05.079.

[21] J. Zhang, B. Song, Q. Wei, D. Bourell, Y. Shi, A review of selective laser melting of aluminum alloys: Processing, microstructure, property and developing trends, Journal of Materials Science & Technology 35 (2) (2019) 270–284, recent Advances in Additive Manufacturing of Metals and Alloys. doi:10.1016/j.jmst.2018.09.004.

[22] D. Han, H. Lee, Recent advances in multi-material additive manufacturing: methods and applications, Current Opinion in Chemical Engineering 28 (2020) 158–166. doi:10.1016/j.coche.2020.03.004.

[23] S. Cooke, K. Ahmadi, S. Willerth, R. Herring, Metal additive manufacturing: Technology, metallurgy and modelling, Journal of Manufacturing Processes 57 (2020) 978–1003. doi:10.1016/j.jmapro.2020.07.025.

[24] P. Patil, D. Singh, S. J. Raykar, J. Bhamu, Multi-objective optimization of process parameters of fused deposition modeling (fdm) for printing polylactic acid (pla) polymer components, Materials Today: Proceedings 45 (2021) 4880–4885, second International Conference on Aspects of Materials Science and Engineering (ICAMSE 2021). doi:10.1016/j.matpr.2021.01.353.

[25] A. Majeed, Y. Zhang, J. Lv, T. Peng, Z. Atta, A. Ahmed, Investigation of t4 and t6 heat treatment influences on relative density and porosity of alsi10mg alloy components manufactured by slm, Computers & Industrial Engineering 139 (2020) 106194. doi:10.1016/j.cie.2019.106194.

[26] L. Tonelli, A. Fortunato, L. Ceschini, Cocr alloy processed by selective laser melting (slm): effect of laser energy density on microstructure, surface morphology, and hardness, Journal of Manufacturing Processes 52 (2020) 106–119. doi:10.1016/j.jmapro.2020.01.052.

[27] Y. Karabulut, E. Tascioglu, Y. Kaynak, Heat treatment temperature-induced microstructure, microhardness and wear resistance of inconel 718 produced by selective laser melting additive manufacturing, Optik 227 (2021) 163907. doi:10.1016/j.ijleo.2019.163907.

[28] N. Rahulan, S. S. Sharma, N. Rakesh, R. Sambhu, Withdrawn: A short review on mechanical properties of slm titanium alloys based on recent research works, Materials Today: Proceedings 54 (2022) 451–456, 5th International Conference on Advanced Research in Mechanical, Materials and Manufacturing Engineering-2021. doi:10.1016/j.matpr.2021.10.184.

[29] B. B. Babamiri, J. Indeck, G. Demeneghi, J. Cuadra, K. Hazeli, Quantification of porosity and microstructure and their effect on quasi-static and dynamic behavior

of additively manufactured inconel 718, Additive Manufacturing 34 (2020) 101380. doi:10.1016/j.addma.2020.101380.

[30] A. Khorasani, I. Gibson, U. S. Awan, A. Ghaderi, The effect of slm process parameters on density, hardness, tensile strength and surface quality of ti-6al-4v, Additive Manufacturing 25 (2019) 176–186. doi:10.1016/j.addma.2018.09.002.

[31] M. Al-Amin, A. M. Abdul-Rani, T. Rao, M. Danish, S. Rubaiee, A. bin Mahfouz, R. Parameswari, M. Wani, Investigation of machining and modified surface features of 316l steel through novel hybrid of ha/cnt added-edm process, Materials Chemistry and Physics 276 (2022) 125320. doi:10.1016/j.matchemphys.2021.125320.

[32] T. DebRoy, H. Wei, J. Zuback, T. Mukherjee, J. Elmer, J. Milewski, A. Beese, A. Wilson-Heid, A. De, W. Zhang, Additive manufacturing of metallic components – process, structure and properties, Progress in Materials Science 92 (2018) 112 – 224. doi:10.1016/j.pmatsci.2017.10.001.

[33] Y. Chen, S. J. Clark, Y. Huang, L. Sinclair, C. Lun Alex Leung, S. Marussi, T. Connolley, O. V. Magdysyuk, R. C. Atwood, G. J. Baxter, M. A. Jones, I. Todd, P. D. Lee, In situ x-ray quantification of melt pool behaviour during directed energy deposition additive manufacturing of stainless steel, Materials Letters 286 (2021) 129205. doi:10.1016/j.matlet.2020.129205.

[34] A. Jaisingh Sheoran, H. Kumar, Fused deposition modeling process parameters optimization and effect on mechanical properties and part quality: Review and reflection on present research, Materials Today: Proceedings 21 (2020) 1659–1672, international Conference on Mechanical and Energy Technologies. doi:10.1016/j.matpr.2019.11.296.

[35] T. H. Becker, P. Kumar, U. Ramamurty, Fracture and fatigue in additively manufactured metals, Acta Materialia 219 (2021) 117240. doi:10.1016/j.actamat.2021.117240.

[36] X. Wang, K. Chou, The effects of stress relieving heat treatment on the microstructure and residual stress of inconel 718 fabricated by laser metal powder bed fusion additive manufacturing process, Journal of Manufacturing Processes 48 (2019) 154–163. doi:10.1016/j.jmapro.2019.10.027.

[37] C. Luo, J. Qiu, Y. Yan, J. Yang, C. Uher, X. Tang, Finite element analysis of temperature and stress fields during the selective laser melting process of thermoelectric snte, Journal of Materials Processing Technology 261 (2018) 74 – 85. doi:10.1016/j.jmatprotec.2018.06.001.

[38] H. Lhachemi, A. Malik, R. Shorten, Augmented reality, cyber-physical systems, and feedback control for additive manufacturing: A review, IEEE Access 7 (2019) 50119 – 50135. doi:10.1109/ACCESS.2019.2907287.

[39] Z. Zhang, R. Kovacevic, A thermo-mechanical model for simulating the temperature and stress distribution during laser cladding process, The International Journal of Advanced Manufacturing Technology 102 (2019) 457–472. doi:10.1007/s00170-018-3127-y.

[40] H. Liu, X. Qin, M. Wu, M. Ni, S. Huang, Numerical simulation of thermal and stress field of single track cladding in wide-beam laser cladding, The International Journal of Advanced Manufacturing Technology 104 (2019) 3959–3976. doi:10.1007/s00170-019-04056-8.

[41] Y. Choi, D.-G. Lee, Correlation between surface tension and fatigue properties of ti-6al-4v alloy fabricated by ebm additive manufacturing, Applied Surface Science 481 (2019) 741–746. doi:10.1016/j.apsusc.2019.03.099.

[42] H. Shipley, D. McDonnell, M. Culleton, R. Coull, R. Lupoi, G. O'Donnell, D. Trimble, Optimisation of process parameters to address fundamental challenges during selective laser melting of ti-6al-4v: A review, International Journal of Machine Tools and Manufacture 128 (2018) 1–20. doi:10.1016/j.ijmachtools.2018.01.003.

[43] A. Takaichi, Y. Kajima, N. Kittikundecha, H. L. Htat, H. H. Wai Cho, T. Hanawa, T. Yoneyama, N. Wakabayashi, Effect of heat treatment on the anisotropic microstructural and mechanical properties of co–cr–mo alloys produced by selective laser melting, Journal of the Mechanical Behavior of Biomedical Materials 102 (2020) 103496. doi:10.1016/j.jmbbm.2019.103496.

[44] Y. Kajima, A. Takaichi, N. Kittikundecha, T. Nakamoto, T. Kimura, N. Nomura, A. Kawasaki, T. Hanawa, H. Takahashi, N. Wakabayashi, Effect of heat-treatment temperature on microstructures and mechanical properties of co–cr–mo alloys fabricated by selective laser melting, Materials Science and Engineering: A 726 (2018) 21–31. doi:10.1016/j.msea.2018.04.048.

[45] N. Tamanna, R. Crouch, S. Naher, Progress in numerical simulation of the laser cladding process, Optics and Lasers in Engineering 122 (2019) 151 – 163. doi:10.1016/j.optlaseng.2019.05.026.

[46] J. Zuback, T. DebRoy, The hardness of additively manufactured alloys, Materials 11 (11). doi:10.3390/ma11112070.

[47] Y. Kok, X. Tan, P. Wang, M. Nai, N. Loh, E. Liu, S. Tor, Anisotropy and heterogeneity of microstructure and mechanical properties in metal additive manufacturing: A critical review, Materials & Design 139 (2018) 565 – 586. doi:10.1016/j.matdes.2017.11.021.

[48] B. Qian, K. Saeidi, L. Kvetková, F. Lofaj, C. Xiao, Z. Shen, Defects-tolerant co-cr-mo dental alloys prepared by selective laser melting, Dental Materials 31 (12) (2015) 1435–1444. doi:10.1016/j.dental.2015.09.003.

[49] R. H. van Blitterswijk, M. H. Farshidianfar, A. Khajepour, Model predictive control for real-time microstructure control in laser heat treatment, Journal of Manufacturing Processes 118 (2024) 116–127. doi:10.1016/j.jmapro.2024.03.038.

[50] M. H. Farshidianfar, Real-time closed-loop control of microstructure and geometry in laser materials processing, Ph.D. thesis, Waterloo University, Canada (2017). URL: http://hdl.handle.net/10012/12735

[51] X. Dong, Y. Zhou, Q. Sun, Y. Qu, H. Shi, W. Liu, H. Peng, B. Zhang, S. Xu, J. Yan, N. Li, Fatigue behavior of biomedical co–cr–mo–w alloy fabricated by selective laser melting, Materials Science and Engineering: A 795 (2020) 140000. doi:10.1016/j.msea.2020.140000.

[52] M. Ahmed Obeidi, S. M. Uí Mhurchadha, R. Raghavendra, A. Conway, C. Souto, D. Tormey, I. U. Ahad, D. Brabazon, Comparison of the porosity and mechanical performance of 316l stainless steel manufactured on different laser powder bed fusion metal additive manufacturing machines, Journal of Materials Research and Technology 13 (2021) 2361–2374. doi:10.1016/j.jmrt.2021.06.027.

[53] Q. Chao, S. Thomas, N. Birbilis, P. Cizek, P. D. Hodgson, D. Fabijanic, The effect of post-processing heat treatment on the microstructure, residual stress and mechanical properties of selective laser melted 316l stainless steel, Materials Science and Engineering: A 821 (2021) 141611. doi:10.1016/j.msea.2021.141611.

[54] D. Dong, C. Chang, H. Wang, X. Yan, W. Ma, M. Liu, S. Deng, J. Gardan, R. Bolot, H. Liao, Selective laser melting (slm) of cx stainless steel: Theoretical calculation, process optimization and strengthening mechanism, Journal of Materials Science & Technology 73 (2021) 151–164. doi:10.1016/j.jmst.2020.09.031.

[55] F. Caiazzo, V. Alfieri, G. Bolelli, Residual stress in laser-based directed energy deposition of aluminum alloy 2024: simulation and validation, The International Journal of Advanced Manufacturing Technology 118 (3) (2022) 1197–1211. doi:10.1007/s00170-021-07988-2.

[56] T. R. Smith, J. D. Sugar, J. M. Schoenung, C. San Marchi, Relationship between manufacturing defects and fatigue properties of additive manufactured austenitic stainless steel, Materials Science and Engineering: A 765 (2019) 138268. doi:10.1016/j.msea.2019.138268.

[57] C. M. Smudde, C. R. D'Elia, C. W. San Marchi, M. R. Hill, J. C. Gibeling, The influence of residual stress on fatigue crack growth rates of additively manufactured type 304l stainless steel, International Journal of Fatigue 162 (2022) 106954. doi:https://doi.org/10.1016/j.ijfatigue.2022.106954.

[58] C. M. Smudde, C. C. San Marchi, M. R. Hill, J. C. Gibeling, The influence of residual stress on fatigue crack growth rates in stainless steel processed by different additive manufacturing methods, Journal of Materials Engineering and Performancedoi:10.1007/s11665-024-09558-5.

[59] L. Bhandari, V. Gaur, Different post-processing methods to improve fatigue properties of additively built ti-6al-4v alloy, International Journal of Fatigue 176 (2023) 107850. doi:https://doi.org/10.1016/j.ijfatigue.2023.107850.

[60] Z. Chen, S. Cao, X. Wu, C. H. Davies, 13 - surface roughness and fatigue properties of selective laser melted ti–6al–4v alloy, in: F. Froes, R. Boyer (Eds.), Additive Manufacturing for the Aerospace Industry, Elsevier, 2019, pp. 283–299. doi:https://doi.org/10.1016/B978-0-12-814062-8.00015-7.

[61] H. Zhang, M. Xu, Z. Liu, C. Li, P. Kumar, Z. Liu, Y. Zhang, Microstructure, surface quality, residual stress, fatigue behavior and damage mechanisms of selective laser melted 304l stainless steel considering building direction, Additive Manufacturing 46 (2021) 102147. doi:10.1016/j.addma.2021.102147.

[62] J. Gockel, L. Sheridan, B. Koerper, B. Whip, The influence of additive manufacturing processing parameters on surface roughness and fatigue life, International Journal of Fatigue 124 (2019) 380–388. doi:10.1016/j.ijfatigue.2019.03.025.

[63] J. Pegues, M. Roach, R. Scott Williamson, N. Shamsaei, Surface roughness effects on the fatigue strength of additively manufactured ti-6al-4v, International Journal of Fatigue 116 (2018) 543–552. doi:10.1016/j.ijfatigue.2018.07.013.

[64] A. A. A. Aliyu, C. Puncreobutr, S. Kuimalee, T. Phetrattanarangsi, T. Boonchuduang, P. Taweekitikul, C. Panwisawas, J. Shinjo, B. Lohwongwatana, Laser-

inherent porosity defects in additively manufactured ti–6al–4v implant: Formation, distribution, and effect on fatigue performance, Journal of Materials Research and Technology 30 (2024) 5121–5132. doi:https://doi.org/10.1016/j.jmrt.2024.04.225.

[65] Y. R. Choi, S. D. Sun, Q. Liu, M. Brandt, M. Qian, Influence of deposition strategy on the microstructure and fatigue properties of laser metal deposited ti-6al-4v powder on ti-6al-4v substrate, International Journal of Fatigue 130 (2020) 105236. doi:https://doi.org/10.1016/j.ijfatigue.2019.105236.

[66] M. S. Yasin, A. Soltani-Tehrani, S. Shao, M. Haghshenas, N. Shamsaei, A comparative study on fatigue performance of various additively manufactured titanium alloys, Procedia Structural Integrity 38 (2022) 519–525, fatigue Design 2021, International Conference Proceedings, 9th Edition. doi:https://doi.org/10.1016/j.prostr.2022.03.052.

[67] W.-S. Shin, B. Son, W. Song, H. Sohn, H. Jang, Y.-J. Kim, C. Park, Heat treatment effect on the microstructure, mechanical properties, and wear behaviors of stainless steel 316l prepared via selective laser melting, Materials Science and Engineering: A 806 (2021) 140805. doi:10.1016/j.msea.2021.140805.

[68] H. C. Aksa, İlyas Hacısalihoğlu, F. Yıldız, T. Varol, O. Güler, G. Kaya, S. B. Akçay, Effects of fabrication parameters and post-processing treatments on the mechanical and tribological behavior of surface-enhanced copper based materials by selective laser melting, Journal of Materials Processing Technology 304 (2022) 117564. doi:10.1016/j.jmatprotec.2022.117564.

[69] C. Chang, X. Yan, Z. Deng, Q. Chu, S. Deng, R. Bolot, M. Chemkhi, M. Liu, H. Liao, J. Gardan, Effect of heat treatment on residual stress and wear resistance of cx stainless steel manufactured by selective laser melting, Procedia CIRP 104 (2021) 738–743, 54th CIRP CMS 2021 - Towards Digitalized Manufacturing 4.0. doi:10.1016/j.procir.2021.11.124.

[70] B. Chen, Y. Su, Z. Xie, C. Tan, J. Feng, Development and characterization of 316l/inconel625 functionally graded material fabricated by laser direct metal deposition, Optics & Laser Technology 123 (2020) 105916. doi:10.1016/j.optlastec.2019.105916.

[71] R. Weber, T. Graf, P. Berger, V. Onuseit, M. Wiedenmann, C. Freitag, A. Feuer, Heat accumulation during pulsed laser materials processing, Opt. Express 22 (9) (2014) 11312–11324. doi:10.1364/OE.22.011312.

[72] W. Xi, B. Song, Y. Zhao, T. Yu, J. Wang, Geometry and dilution rate analysis and prediction of laser cladding, The International Journal of Advanced Manufacturing Technology 103 (9) (2019) 4695–4702. doi:10.1007/s00170-019-03932-7.

[73] V. Gunenthiram, P. Peyre, M. Schneider, M. Dal, F. Coste, I. Koutiri, R. Fabbro, Experimental analysis of spatter generation and melt-pool behavior during the powder bed laser beam melting process, Journal of Materials Processing Technology 251 (2018) 376–386. doi:10.1016/j.jmatprotec.2017.08.012.

[74] M. Boutaous, X. Liu, D. A. Siginer, S. Xin, Balling phenomenon in metallic laser based 3d printing process, International Journal of Thermal Sciences 167 (2021) 107011. doi:10.1016/j.ijthermalsci.2021.107011.

[75] H. Wei, T. Mukherjee, W. Zhang, J. Zuback, G. Knapp, A. De, T. DebRoy, Mechanistic models for additive manufacturing of metallic components, Progress in Materials Science 116 (2021) 100703. doi:10.1016/j.pmatsci.2020.100703.

[76] V. Vukkum, R. Gupta, Review on corrosion performance of laser powder-bed fusion printed 316l stainless steel: Effect of processing parameters, manufacturing defects, post-processing, feedstock, and microstructure, Materials & Design 221 (2022) 110874. doi:10.1016/j.matdes.2022.110874.

[77] D. Svetlizky, M. Das, B. Zheng, A. L. Vyatskikh, S. Bose, A. Bandyopadhyay, J. M. Schoenung, E. J. Lavernia, N. Eliaz, Directed energy deposition (ded) addi-

tive manufacturing: Physical characteristics, defects, challenges and applications, Materials Today 49 (2021) 271–295. doi:10.1016/j.mattod.2021.03.020.

[78] Z. Li, S. Sui, X. Ma, H. Tan, C. Zhong, G. Bi, A. T. Clare, A. Gasser, J. Chen, High deposition rate powder- and wire-based laser directed energy deposition of metallic materials: A review, International Journal of Machine Tools and Manufacture 181 (2022) 103942. doi:10.1016/j.ijmachtools.2022.103942.

[79] C. Vundru, R. Singh, W. Yan, S. Karagadde, A comprehensive analytical-computational model of laser directed energy deposition to predict deposition geometry and integrity for sustainable repair, International Journal of Mechanical Sciences 211 (2021) 106790. doi:https://doi.org/10.1016/j.ijmecsci.2021.106790.

[80] M. Ansari, A. Martinez-Marchese, M. Khamooshi, A. Keshavarzkermani, R. Esmaeilizadeh, E. Toyserkani, Analytical modeling of multi-track powder-fed laser directed energy deposition: On the relationships among process, deposition dimensions, and solidification microstructure in additively manufactured near-beta titanium alloy, Journal of Materials Processing Technology 306 (2022) 117643. doi:https://doi.org/10.1016/j.jmatprotec.2022.117643.

[81] C. Hagenlocher, P. O'Toole, W. Xu, M. Brandt, M. Easton, A. Molotnikov, Analytical modelling of heat accumulation in laser based additive manufacturing processes of metals, Additive Manufacturing 60 (2022) 103263. doi:https://doi.org/10.1016/j.addma.2022.103263.

[82] Z. Liu, M. Grandhi, I. Z. Era, H.-C. Zhang, Analytical modeling and experimental investigation of the particle scale energy absorption mechanism in laser-based directed energy deposition, Journal of Manufacturing Processes 88 (2023) 157–166. doi:https://doi.org/10.1016/j.jmapro.2023.01.030.

[83] S. Webster, J. Jeong, S. Liao, J. Cao, Machine-agnostic energy density model for laser, powder-blown directed energy deposition, Journal of Manufacturing Pro-

cesses 100 (2023) 11–19. doi:https://doi.org/10.1016/j.jmapro.2023.05.013.

[84] A. Zapata, A. Benda, M. Spreitler, X. F. Zhao, C. Bernauer, H. Yoshioka, M. F. Zaeh, A model-based approach to reduce kinematics-related overfill in robot-guided laser directed energy deposition, CIRP Journal of Manufacturing Science and Technology 45 (2023) 200–209. doi:https://doi.org/10.1016/j.cirpj.2023.06.014.

[85] D. Rosenthal, Mathematical theory of heat distribution during welding and cutting, Welding Journal 20 (1941) 220–234.
URL: https://api.semanticscholar.org/CorpusID:210757123

[86] P. J. DePond, G. Guss, S. Ly, N. P. Calta, D. Deane, S. Khairallah, M. J. Matthews, In situ measurements of layer roughness during laser powder bed fusion additive manufacturing using low coherence scanning interferometry, Materials & Design 154 (2018) 347–359. doi:https://doi.org/10.1016/j.matdes.2018.05.050.

[87] S. A. Khairallah, A. T. Anderson, A. Rubenchik, W. E. King, Laser powder-bed fusion additive manufacturing: Physics of complex melt flow and formation mechanisms of pores, spatter, and denudation zones, Acta Materialia 108 (2016) 36–45. doi:https://doi.org/10.1016/j.actamat.2016.02.014.
URL: https://www.sciencedirect.com/science/article/pii/S135964541630088X

[88] M. Moda, A. Chiocca, G. Macoretta, B. D. Monelli, L. Bertini, Technological implications of the rosenthal solution for a moving point heat source in steady state on a semi-infinite solid, Materials & Design 223 (2022) 110991. doi:https://doi.org/10.1016/j.matdes.2022.110991.

[89] Y. Huang, M. B. Khamesee, E. Toyserkani, A new physics-based model for laser directed energy deposition (powder-fed additive manufacturing): From single-track to multi-track and multi-layer, Optics and Laser Technology 109 (2019) 584 – 599. doi:10.1016/j.optlastec.2018.08.015.

[90] T.-P. Hung, H.-E. Shi, J.-H. Kuang, Temperature modeling of aisi 1045 steel during surface hardening processes, Materials 11 (2018) 1815. doi:10.3390/ma11101815.

[91] T.-P. Hung, C.-M. Hsu, H.-A. Tsai, S.-C. Chen, Z.-R. Liu, Temperature field numerical analysis mode and verification of quenching heat treatment using carbon steel in rotating laser scanning, Materials 12 (2019) 534. doi:10.3390/ma12030534.

[92] V. E. Alexopoulou, E. L. Papazoglou, P. Karmiris-Obratański, A. P. Markopoulos, 3d finite element modeling of selective laser melting for conduction, transition and keyhole modes, Journal of Manufacturing Processes 75 (2022) 877–894. doi:10.1016/j.jmapro.2022.01.054.

[93] Z. Liao, Y. Zhang, J. Chen, J. Ouyang, H. Chen, Finite element simulation of selective laser melting based on the layer thickness-dependent shrinkage ratio model, Optics & Laser Technology 174 (2024) 110565. doi:https://doi.org/10.1016/j.optlastec.2024.110565.

[94] K. Dortkasli, M. Isik, E. Demir, A thermal finite element model with efficient computation of surface heat fluxes for directed-energy deposition process and application to laser metal deposition of in718, Journal of Manufacturing Processes 79 (2022) 369–382. doi:https://doi.org/10.1016/j.jmapro.2022.04.049.

[95] Y. Chang, F. Zhao, J. Ran, L. Gan, F. Zhao, Numerical simulation of thermal behavior and analysis of microstructure evolution during laser melting deposition of m2 high-speed steel powder, Vacuum 224 (2024) 113188. doi:https://doi.org/10.1016/j.vacuum.2024.113188.

[96] Y. C. Shin, N. Bailey, C. Katinas, W. Tan, Predictive modeling capabilities from incident powder and laser to mechanical properties for laser directed energy deposition, Computational Mechanics 61 (5) (2018) 617–636. doi:10.1007/s00466-018-1545-1.

[97] J. G. Michopoulos, A. P. Iliopoulos, J. C. Steuben, A. J. Birnbaum, S. G. Lambrakos, On the multiphysics modeling challenges for metal additive manufacturing processes, Additive Manufacturing 22 (2018) 784 – 799. doi:10.1016/j.addma.2018.06.019.

[98] M. Bayat, W. Dong, J. Thorborg, A. C. To, J. H. Hattel, A review of multi-scale and multi-physics simulations of metal additive manufacturing processes with focus on modeling strategies, Additive Manufacturing 47 (2021) 102278. doi:10.1016/j.addma.2021.102278.

[99] T. Lehmann, D. Rose, E. Ranjbar, M. Ghasri-Khouzani, M. Tavakoli, H. Henein, T. Wolfe, A. J. Qureshi, Large-scale metal additive manufacturing: a holistic review of the state of the art and challenges, International Materials Reviews 67 (4) (2022) 410–459. doi:10.1080/09506608.2021.1971427.

[100] F. Hajializadeh, A. Ince, Integration of artificial neural network with finite element analysis for residual stress prediction of direct metal deposition process, Materials Today Communications 27 (2021) 102197. doi:https://doi.org/10.1016/j.mtcomm.2021.102197.

[101] F. Hajializadeh, A. Ince, Residual stress computation in direct metal deposition using integrated artificial neural networks and finite element analysis, Materials Today Communications 38 (2024) 108471. doi:https://doi.org/10.1016/j.mtcomm.2024.108471.

[102] X. Cao, C. Duan, X. Luo, S. Zheng, X. Hao, D. Shang, Z. Zhang, Physics-informed machine learning approach for molten pool morphology prediction and process evaluation in directed energy deposition of 12crni2 alloy steel, Journal of Manufacturing Processes 119 (2024) 806–826. doi:https://doi.org/10.1016/j.jmapro.2024.04.023.

[103] R. Fakir, N. Barka, J. Brousseau, Case study of laser hardening process applied to 4340 steel cylindrical specimens using simulation and experimental validation,

Case Studies in Thermal Engineering 11 (2017) 15–25. doi:10.1016/j.csite.2017.12.002.

[104] R. Fakir, N. Barka, J. Brousseau, G. C.-Guillemette, Numerical investigation by the finite difference method of the laser hardening process applied to aisi-4340, Journal of Applied Mathematics and Physics 06 (2018) 2087–2106. doi:10.4236/jamp.2018.610176.

[105] Y. Ren, Q. Wang, A finite difference method for fast prediction and control of part-scale temperature evolution in laser powder bed fusion, Journal of Manufacturing Processes 93 (2023) 299–314. doi:10.1016/j.jmapro.2023.03.020.

[106] X. Yu, X. Lin, F. Liu, L. Wang, Y. Tang, J. Li, S. Zhang, W. Huang, Influence of post-heat-treatment on the microstructure and fracture toughness properties of inconel 718 fabricated with laser directed energy deposition additive manufacturing, Materials Science and Engineering: A 798 (2020) 140092. doi:https://doi.org/10.1016/j.msea.2020.140092.

[107] O. Mehrabi, S. Hossein Seyedkashi, M. Moradi, Experimental and response surface study on additive manufacturing of functionally graded steel-inconel wall using direct laser metal deposition, Optics & Laser Technology 167 (2023) 109707. doi:https://doi.org/10.1016/j.optlastec.2023.109707.

[108] E. Awannegbe, Y. Zhao, Z. Qiu, H. Li, Influence of heat treatment on the tensile properties of ti–15mo additively manufactured by laser metal deposition, Materials Science and Engineering: A 892 (2024) 146062. doi:https://doi.org/10.1016/j.msea.2023.146062.

[109] L. Zhang, W. Zhai, K. Zhao, G. Bi, X. Chen, W. Zhou, Oxidation behavior and resultant deposition efficiency and material properties of laser aided additively manufactured stainless steel 316 l, Journal of Manufacturing Processes 115 (2024) 352–364. doi:https://doi.org/10.1016/j.jmapro.2024.02.032.

[110] G. Su, Y. Shi, G. Li, G. Zhang, Y. Xu, Highly-efficient additive manufacturing of inconel 625 thin wall using hot-wire laser metal deposition: Process optimization, microstructure, and mechanical properties, Optics & Laser Technology 175 (2024) 110763. doi:https://doi.org/10.1016/j.optlastec.2024.110763.

[111] M. M. Bakhshayesh, F. Khodabakhshi, M. Farshidianfar, S. Nagy, M. Mohammadi, G. Wilde, Additive manufacturing of stellite 6 alloy by laser-directed energy deposition: Engineering the crystallographic texture, Materials Characterization 207 (2024) 113511. doi:https://doi.org/10.1016/j.matchar.2023.113511.

[112] Z. Wang, L. Zeng, X. Lin, J. Wang, Z. Feng, C. Dang, H. Li, Y. Wang, W. Huang, Microstructural evolution and strengthening mechanisms of additively-manufactured al-mg-sc-zr alloys: Laser directed energy deposition versus laser powder bed fusion, Journal of Alloys and Compounds 985 (2024) 173946. doi:https://doi.org/10.1016/j.jallcom.2024.173946.

[113] X. Qi, G. Chen, Y. Li, X. Cheng, C. Li, Applying neural-network-based machine learning to additive manufacturing: Current applications, challenges, and future perspectives, Engineering 5 (4) (2019) 721 – 729. doi:https://doi.org/10.1016/j.eng.2019.04.012.

[114] L. Meng, B. McWilliams, W. Jarosinski, H.-Y. Park, Y.-G. Jung, J. Lee, J. Zhang, Machine learning in additive manufacturing: A review, JOM 72. doi:10.1007/s11837-020-04155-y.

[115] H. Liu, X. Qin, S. Huang, L. Jin, Y. Wang, K. Lei, Geometry characteristics prediction of single track cladding deposited by high power diode laser based on genetic algorithm and neural network, International Journal of Precision Engineering and Manufacturing 19 (2018) 1061–1070. doi:10.1007/s12541-018-0126-8.

[116] P. Pant, D. Chatterjee, Prediction of clad characteristics using ann and combined pso-ann algorithms in laser metal deposition process, Surfaces and Interfaces 21 (2020) 100699. doi:https://doi.org/10.1016/j.surfin.2020.100699.

[117] D. Knüttel, S. Baraldo, A. Valente, E. Carpanzano, K. Wegener, Height prediction in directed metal deposition with artificial neural networks, Procedia CIRP 113 (2022) 312–317, 21st CIRP CONFERENCE ON ELECTRO PHYSICAL AND CHEMICAL MACHINING, ISEM XXIJune, 14 to 17, 2022 in Zurich. doi:https://doi.org/10.1016/j.procir.2022.09.108.

[118] L. Zhenglong, J. Shen, Q. Wang, Y. Chen, Real-time weld geometry prediction based on multi-information using neural network optimized by pca and ga during thin-plate laser welding, Journal of Manufacturing Processes 43 (2019) 207–217. doi:10.1016/j.jmapro.2019.05.013.

[119] C. Gonzalez Val, A. Pallas, V. Panadeiro, A. Rodriguez, A convolutional approach to quality monitoring for laser manufacturing, Journal of Intelligent Manufacturingdoi:10.1007/s10845-019-01495-8.

[120] D. Gonçalves, M. Stemmer, M. Pereira, A convolutional neural network approach on bead geometry estimation for a laser cladding system, The International Journal of Advanced Manufacturing Technology 106 (2020) 1–11. doi:10.1007/s00170-019-04669-z.

[121] L. A. Botelho, Real-time monitoring of thermal processes, Ph.D. thesis, Waterloo University, Canada (2023).
URL: http://hdl.handle.net/10012/19968

[122] Z. Zhang, Z. Liu, D. Wu, Prediction of melt pool temperature in directed energy deposition using machine learning, Additive Manufacturing 37 (2021) 101692. doi:https://doi.org/10.1016/j.addma.2020.101692.

[123] Q. Zhu, Z. Liu, J. Yan, Machine learning for metal additive manufacturing: Predicting temperature and melt pool fluid dynamics using physics-informed neural networks, Computational Mechanics (2021) 619–635doi:https://doi.org/10.1007/s00466-020-01952-9.

[124] L. Zheng, Q. Zhang, H. Cao, W. Wu, H. Ma, X. Ding, J. Yang, X. Duan, S. Fan, Melt pool boundary extraction and its width prediction from infrared images in selective laser melting, Materials & Design 183 (2019) 108110. doi:10.1016/j.matdes.2019.108110.

[125] A. Da Silva, J. Frostevarg, A. F. Kaplan, Melt pool monitoring and process optimisation of directed energy deposition via coaxial thermal imaging, Journal of Manufacturing Processes 107 (2023) 126–133. doi:10.1016/j.jmapro.2023.10.021.

[126] M. H. Farshidianfar, A. Khajepour, A. P. Gerlich, Real-time control of microstructure in laser additive manufacturing, Advanced Manufacturing Technology 82 (2015) 1173–1186. doi:10.1007/s00170-015-7423-5.

[127] M. H. Farshidianfar, A. Khajepour, A. P. Gerlich, Effect of real-time cooling rate on microstructure in laser additive manufacturing, Journal of Materials Processing Technology 231 (2016) 468 – 478. doi:10.1016/j.jmatprotec.2016.01.017.

[128] A. M. Nair, G. Muvvala, S. Sarkar, A. K. Nath, Real-time detection of cooling rate using pyrometers in tandem in laser material processing and directed energy deposition, Materials Letters 277 (2020) 128330. doi:10.1016/j.matlet.2020.128330.

[129] C. K. P. Vallabh, X. Zhao, Melt pool temperature measurement and monitoring during laser powder bed fusion based additive manufacturing via single-camera two-wavelength imaging pyrometry (stwip), Journal of Manufacturing Processes 79 (2022) 486–500. doi:10.1016/j.jmapro.2022.04.058.

[130] A. Gökhan Demir, C. De Giorgi, B. Previtali, Design and Implementation of a Multisensor Coaxial Monitoring System With Correction Strategies for Selective Laser Melting of a Maraging Steel, Journal of Manufacturing Science and Engineering 140 (4) (2018) 041003. doi:10.1115/1.4038568.

[131] J. A. Mitchell, T. A. Ivanoff, D. Dagel, J. D. Madison, B. Jared, Linking pyrometry to porosity in additively manufactured metals, Additive Manufacturing 31 (2020) 100946. doi:10.1016/j.addma.2019.100946.

[132] W. Devesse, D. De Baere, P. Guillaume, High resolution temperature measurement of liquid stainless steel using hyperspectral imaging, Sensors (Basel) 17 (1) (2017) 91. doi:10.3390/s17010091.

[133] Y. Liu, L. Guo, H. Gao, Z. You, Y. Ye, B. Zhang, Machine vision based condition monitoring and fault diagnosis of machine tools using information from machined surface texture: A review, Mechanical Systems and Signal Processing 164 (2022) 108068. doi:10.1016/j.ymssp.2021.108068.

[134] Y. Fu, A. R. Downey, L. Yuan, T. Zhang, A. Pratt, Y. Balogun, Machine learning algorithms for defect detection in metal laser-based additive manufacturing: A review, Journal of Manufacturing Processes 75 (2022) 693–710. doi:10.1016/j.jmapro.2021.12.061.

[135] R. Liu, H. Yang, Multimodal probabilistic modeling of melt pool geometry variations in additive manufacturing, Additive Manufacturing 61 (2023) 103375. doi:10.1016/j.addma.2022.103375.

[136] T.-N. Le, M.-H. Lee, Z.-H. Lin, H.-C. Tran, Y.-L. Lo, Vision-based in-situ monitoring system for melt-pool detection in laser powder bed fusion process, Journal of Manufacturing Processes 68 (2021) 1735–1745. doi:10.1016/j.jmapro.2021.07.007.

[137] A. S. Hsu, C. Chen, E. Greenberger, Parental warmth moderates the association between bmi trajectories and academic achievement, The Journal of Early Adolescence 39 (3) (2018) 371–394. doi:10.1177/0272431618757677.

[138] M. Iravani-Tabrizipour, E. Toyserkani, An image-based feature tracking algorithm for real-time measurement of clad height, Machine Vision and Applications 18 (2007) 343–354. doi:10.1007/s00138-006-0066-7.

[139] M. A. Naiel, D. S. Ertay, M. Vlasea, P. Fieguth, Adaptive vision-based detection of laser-material interaction for directed energy deposition, Additive Manufacturing 36 (2020) 101468. doi:10.1016/j.addma.2020.101468.

[140] J. R. Tempelman, A. J. Wachtor, E. B. Flynn, P. J. Depond, J.-B. Forien, G. M. Guss, N. P. Calta, M. J. Matthews, Detection of keyhole pore formations in laser powder-bed fusion using acoustic process monitoring measurements, Additive Manufacturing 55 (2022) 102735. doi:10.1016/j.addma.2022.102735.

[141] J. R. Tempelman, A. J. Wachtor, E. B. Flynn, P. J. Depond, J.-B. Forien, G. M. Guss, N. P. Calta, M. J. Matthews, Sensor fusion of pyrometry and acoustic measurements for localized keyhole pore identification in laser powder bed fusion, Journal of Materials Processing Technology 308 (2022) 117656. doi:10.1016/j.jmatprotec.2022.117656.

[142] Y. Plotnikov, D. Henkel, J. Burdick, A. French, J. Sions, K. Bourne, Infrared-assisted acoustic emission process monitoring for additive manufacturing, AIP Conference Proceedings 2102 (1) (2019) 020006. doi:10.1063/1.5099710.

[143] K. Gutknecht, M. Cloots, R. Sommerhuber, K. Wegener, Mutual comparison of acoustic, pyrometric and thermographic laser powder bed fusion monitoring, Materials & Design 210 (2021) 110036. doi:10.1016/j.matdes.2021.110036.

[144] L. Chen, X. Yao, C. Tan, W. He, J. Su, F. Weng, Y. Chew, N. P. H. Ng, S. K. Moon, In-situ crack and keyhole pore detection in laser directed energy deposition through acoustic signal and deep learning, Additive Manufacturing 69 (2023) 103547. doi:10.1016/j.addma.2023.103547.

[145] S. Nallusamy, K. Sujatha, Experimental analysis of nanoparticles with cobalt oxide synthesized by coprecipitation method on electrochemical biosensor using ftir and tem, Materials Today: Proceedings 37 (2021) 728–732, international Conference on Newer Trends and Innovation in Mechanical Engineering: Materials Science. doi:10.1016/j.matpr.2020.05.735.

[146] Y. Huang, F. Zhang, J. Yuan, C. Jia, X. Ren, L. Yang, Investigation on surface morphology and microstructure of double-wire+arc additive manufactured aluminum alloys based on spectral analysis, Journal of Manufacturing Processes 84 (2022) 639–651. doi:10.1016/j.jmapro.2022.10.043.

[147] Y. Shi, N. Zhao, Y. Chen, J. Liu, J. Li, Z. Hou, G. Zhou, Spectroscopic analysis of nd/al co-doped silica glass fabricated by laser additive manufacturing, Journal of Non-Crystalline Solids 604 (2023) 122139. doi:10.1016/j.jnoncrysol.2023.122139.

[148] C. S. Lough, L. I. Escano, M. Qu, C. C. Smith, R. G. Landers, D. A. Bristow, L. Chen, E. C. Kinzel, In-situ optical emission spectroscopy of selective laser melting, Journal of Manufacturing Processes 53 (2020) 336–341. doi:10.1016/j.jmapro.2020.02.016.

[149] S. Liu, W. Liu, M. Harooni, J. Ma, R. Kovacevic, Real-time monitoring of laser hot-wire cladding of inconel 625, Optics & Laser Technology 62 (2014) 124–134. doi:10.1016/j.optlastec.2014.03.007.

[150] A. J. D. Mohammad Montazeri, Abdalla R. Nassar, P. Rao, In-process monitoring of porosity in additive manufacturing using optical emission spectroscopy, IISE Transactions 52 (5) (2020) 500–515. doi:10.1080/24725854.2019.1659525.

[151] A.-W. Saif, A frame work for the integration of statistical process control and engineering process control, 2019 Industrial & Systems Engineering Conference (ISEC) (2019) 1–4doi:10.1109/IASEC.2019.8686557.

[152] D. Homberg, W. Weiss, Pid control of laser surface hardening of steel, IEEE Transactions on Control Systems Technology 14 (5) (2006) 896–904. doi:10.1109/TCST.2006.879978.

[153] M. H. Farshidianfar, A. Khajepour, A. P. Gerlich, Real-time monitoring and prediction of martensite formation and hardening depth during laser heat treatment,

Surface and Coatings Technology 315 (2017) 326–334. doi:10.1016/j.surfcoat.2017.02.055.

[154] Y. Su, Z. Wang, H. Lu, K. Luo, J. Lu, Improved wear resistance of directed energy deposited fe-ni-cr alloy via closed-loop controlling laser power, Journal of Manufacturing Processes 75 (2022) 802–813. doi:10.1016/j.jmapro.2022.01.047.

[155] Y. Su, Z. Wang, X. Xu, K. Luo, J. Lu, Effect of closed-loop controlled melt pool width on microstructure and tensile property for fe-ni-cr alloy in directed energy deposition, Journal of Manufacturing Processes 82 (2022) 708–721. doi:https://doi.org/10.1016/j.jmapro.2022.08.049.

[156] R. Wang, B. Standfield, C. Dou, A. C. Law, Z. J. Kong, Real-time process monitoring and closed-loop control on laser power via a customized laser powder bed fusion platform, Additive Manufacturing 66 (2023) 103449. doi:https://doi.org/10.1016/j.addma.2023.103449.

[157] H. Rezaeifar, M. A. Elbestawi, On-line melt pool temperature control in l-pbf additive manufacturing, The International Journal of Advanced Manufacturing Technology 112 (9) (2021) 2789–2804. doi:10.1007/s00170-020-06441-0.

[158] Z. Smoqi, B. D. Bevans, A. Gaikwad, J. Craig, A. Abul-Haj, B. Roeder, B. Macy, J. E. Shield, P. Rao, Closed-loop control of meltpool temperature in directed energy deposition, Materials & Design 215 (2022) 110508. doi:10.1016/j.matdes.2022.110508.

[159] J. Hofman, B. Pathiraj, J. van Dijk, D. de Lange, J. Meijer, A camera based feedback control strategy for the laser cladding process, Journal of Materials Processing Technology 212 (11) (2012) 2455–2462. doi:https://doi.org/10.1016/j.jmatprotec.2012.06.027.

[160] T. G. Fleming, S. G. Nestor, T. R. Allen, M. A. Boukhaled, N. J. Smith, J. M. Fraser, Tracking and controlling the morphology evolution of 3d powder-bed fusion

in situ using inline coherent imaging, Additive Manufacturing 32 (2020) 100978. doi:https://doi.org/10.1016/j.addma.2019.100978.

[161] M. Zeinali, A. Khajepour, Height Control in Laser Cladding Using Adaptive Sliding Mode Technique: Theory and Experiment, Journal of Manufacturing Science and Engineering 132 (4) (2010) 041016. doi:10.1115/1.4002023.

[162] H. Wang, W. Liu, Z. Tang, Y. Wang, X. Mei, K. M. Saleheen, Z. Wang, H. Zhang, Review on adaptive control of laser-directed energy deposition, Optical Engineering 59 (7) (2020) 070901. doi:10.1117/1.OE.59.7.070901.

[163] G. Singer, Y. Cohen, A framework for smart control using machine-learning modeling for processes with closed-loop control in industry 4.0, Engineering Applications of Artificial Intelligence 102 (2021) 104236. doi:https://doi.org/10.1016/j.engappai.2021.104236.

[164] Closed-Loop Simulation Integrating Finite Element Modeling With Feedback Controls in Powder Bed Fusion Additive Manufacturing, Vol. 2020 International Symposium on Flexible Automation of International Symposium on Flexible Automation. doi:10.1115/ISFA2020-9611.

[165] Q. Wang, P. P. Michaleris, A. R. Nassar, J. E. Irwin, Y. Ren, C. B. Stutzman, Model-based feedforward control of laser powder bed fusion additive manufacturing, Additive Manufacturing 31 (2020) 100985. doi:https://doi.org/10.1016/j.addma.2019.100985.

[166] S. Z. Hussain, Z. Kausar, Z. U. Koreshi, S. R. Sheikh, H. Z. U. Rehman, H. Yaqoob, M. F. Shah, A. Abdullah, F. Sher, Feedback control of melt pool area in selective laser melting additive manufacturing process, Processes 9 (9). doi:10.3390/pr9091547.

[167] D. Tyralla, H. Köhler, T. Seefeld, C. Thomy, R. Narita, A multi-parameter control of track geometry and melt pool size for laser metal deposition, Procedia CIRP

94 (2020) 430–435, 11th CIRP Conference on Photonic Technologies [LANE 2020]. doi:https://doi.org/10.1016/j.procir.2020.09.159.

[168] Z.-Q. Guo, G. Bi, J. Wei, Design of a novel control strategy for laser-aided additive manufacturing processes, in: IECON 2016 - 42nd Annual Conference of the IEEE Industrial Electronics Society, 2016, pp. 6091–6096. doi:10.1109/IECON.2016.7793430.

[169] X. Cao, B. Ayalew, Robust multivariable predictive control for laser-aided powder deposition processes, Journal of the Franklin Institute 356 (5) (2019) 2505 – 2529. doi:10.1016/j.jfranklin.2018.12.015.

[170] F. Ogoke, A. B. Farimani, Thermal control of laser powder bed fusion using deep reinforcement learning, Additive Manufacturing 46 (2021) 102033. doi:https://doi.org/10.1016/j.addma.2021.102033.

[171] Q. Zhong, X. Tian, X. Huang, C. Huo, D. Li, Using feedback control of thermal history to improve quality consistency of parts fabricated via large-scale powder bed fusion, Additive Manufacturing 42 (2021) 101986. doi:https://doi.org/10.1016/j.addma.2021.101986.

[172] M. Akbari, R. Kovacevic, Closed loop control of melt pool width in robotized laser powder–directed energy deposition process, The International Journal of Advanced Manufacturing Technology 104 (5) (2019) 2887–2898. doi:10.1007/s00170-019-04195-y.

[173] C. Xia, Z. Pan, J. Polden, H. Li, Y. Xu, S. Chen, Y. Zhang, A review on wire arc additive manufacturing: Monitoring, control and a framework of automated system, Journal of Manufacturing Systems 57 (2020) 31–45. doi:10.1016/j.jmsy.2020.08.008.

[174] M. H. Farshidianfar, Control of microstructure in laser additive manufacturing, Master's thesis, Waterloo University, Canada (2014).
URL: http://hdl.handle.net/10012/8841

[175] Optris, Optris PI 08M Infrared Camera, Retrieved from https://www.optris.com/thermalimager-pi-08m (2015).

[176] M. N. Özışık, Heat Conduction, 2nd Edition, A Wiley-Interscience Publication, John Wiley & Sons, Inc., 1993.
URL: https://books.google.ca/books?id=LkGis_1erIIC

[177] E. Toyserkani, A. Khajepour, S. Corbin, Laser Cladding, Mechanical engineering, Taylor & Francis, 2004. doi:10.1201/9781420039177.

[178] J. Goldak, M. Bibby, J. Moore, R. House, B. Patel, Computer modeling of heat flow in welds, Metallurgical Transactions B 17 (3) (1986) 587–600. doi:10.1007/BF02670226.

[179] L. Yang, X. Peng, B. Wang, Numerical modeling and experimental investigation on the characteristics of molten pool during laser processing, International Journal of Heat and Mass Transfer 44 (23) (2001) 4465 – 4473. doi:10.1016/S0017-9310(01)00086-2.

[180] J. Gao, C. Wu, Y. Hao, X. Xu, L. Guo, Numerical simulation and experimental investigation on three-dimensional modelling of single-track geometry and temperature evolution by laser cladding, Optics & Laser Technology 129 (2020) 106287. doi:10.1016/j.optlastec.2020.106287.

[181] K. Dai, L. Shaw, Finite element analysis of the effect of volume shrinkage during laser densification, Acta Materialia 53 (18) (2005) 4743–4754. doi:https://doi.org/10.1016/j.actamat.2005.06.014.

[182] Z. Wang, Y. Chen, Data-driven modeling of building thermal dynamics: Methodology and state of the art, Energy and Buildings 203 (2019) 109405. doi:10.1016/j.enbuild.2019.109405.

[183] T. Bergman, A. Lavine, F. Incropera, Fundamentals of Heat and Mass Transfer, 7th Edition, John Wiley & Sons, Inc., 2011.
URL: https://books.google.ca/books?id=5cgbAAAAQBAJ

[184] A. Ghajar, D. Yunus A. Cengel, Heat and Mass Transfer: Fundamentals and Applications, 5th Edition, McGraw-Hill Education, 2014.
URL: https://books.google.ca/books?id=B89MnwEACAAJ

[185] S. Bradley, A. Hax, T. Magnanti, Applied Mathematical Programming, Addison-Wesley Publishing Company, 1977.
URL: https://books.google.nl/books?id=MSWdWv3Gn5cC

[186] MATLAB, version 9.7 (R2019b), The MathWorks Inc., Natick, MA, 2019.
URL: https://www.mathworks.com

[187] MATLAB, Optimization toolbox version: 9.4 (r2022b), natick, MA: The MathWorks Inc., 2019 (2019).
URL: https://www.mathworks.com/products/optimization.html

[188] A. Tveito, H. P. Langtangen, B. F. Nielsen, X.-C. Cai, Elements of Scientific Computing, 1st Edition, Springer, Berlin, Heidelberg, 2007.

[189] G. Van Rossum, F. L. Drake, Python 3 Reference Manual, CreateSpace, Scotts Valley, CA, 2009.
URL: https://www.python.org/

[190] C. R. Harris, K. J. Millman, S. J. van der Walt, R. Gommers, P. Virtanen, D. Cournapeau, E. Wieser, J. Taylor, S. Berg, N. J. Smith, R. Kern, M. Picus, S. Hoyer, M. H. van Kerkwijk, M. Brett, A. Haldane, J. F. del Río, M. Wiebe, P. Peterson, P. Gérard-Marchant, K. Sheppard, T. Reddy, W. Weckesser, H. Abbasi, C. Gohlke, T. E. Oliphant, Array programming with NumPy, Nature 585 (7825) (2020) 357–362. doi:10.1038/s41586-020-2649-2.

[191] P. Virtanen, R. Gommers, T. E. Oliphant, M. Haberland, T. Reddy, D. Cournapeau, E. Burovski, P. Peterson, W. Weckesser, J. Bright, S. J. van der Walt, M. Brett, J. Wilson, K. J. Millman, N. Mayorov, A. R. J. Nelson, E. Jones, R. Kern, E. Larson, C. J. Carey, I. Polat, Y. Feng, E. W. Moore, J. VanderPlas, D. Laxalde, J. Perktold, R. Cimrman, I. Henriksen, E. A. Quintero, C. R. Harris, A. M.

Archibald, A. H. Ribeiro, F. Pedregosa, P. van Mulbregt, SciPy 1.0 Contributors, Scipy 1.0: Fundamental algorithms for scientific computing in python, Nature Methods 17 (2020) 261–272. doi:10.1038/s41592-019-0686-2.

[192] R. E. Kalman, A New Approach to Linear Filtering and Prediction Problems, Journal of Basic Engineering 82 (1) (1960) 35–45. doi:10.1115/1.3662552.

[193] J. Nocedal, S. J. Wright., Numerical Optimization, 2nd Edition, Springer, 2006. doi:10.1007/978-0-387-40065-5.

[194] P. J. Goulart, M. F. Anjos, qpsolvers: Quadratic programming solvers for python (2020).
URL: https://github.com/stephane-caron/qpsolvers

[195] C. Willmott, K. Matsuura, Advantages of the mean absolute error (mae) over the root mean square error (rmse) in assessing average model performance, Climate Research 30 (2005) 79–82. doi:10.3354/cr030079.

[196] B. L. Bowerman, R. T. O'Connell, A. B. Koehler, Forecasting, time series, and regression: an applied approach, 3rd Edition, Thomson Brooks/Cole, Belmont, CA, 2005.
URL: http://www.loc.gov/catdir/toc/fy051/2003115455.html

[197] S. Santhanakrishnan, F. Kong, R. Kovacevic, A thermo-kinetic phase transformation model for multi-pass laser heat treatment by using high power direct diode laser, International Congress on Applications of Lasers & Electro-Optics (2010) 573–582doi:10.2351/1.5062083.

[198] S. Guarino, G. S. Ponticelli, High power diode laser (hpdl) for fatigue life improvement of steel: Numerical modelling, Metals 7 (10). doi:10.3390/met7100447.

[199] D. Svetlizky, B. Zheng, A. Vyatskikh, M. Das, S. Bose, A. Bandyopadhyay, J. M. Schoenung, E. J. Lavernia, N. Eliaz, Laser-based directed energy deposition (ded-lb) of advanced materials, Materials Science and Engineering: A 840 (2022) 142967. doi:10.1016/j.msea.2022.142967.

[200] L. Song, V. Bagavath-Singh, B. Dutta, J. Mazumder, Control of melt pool temperature and deposition height during direct metal deposition process, The International Journal of Advanced Manufacturing Technology 8. doi:10.1007/s00170-011-3395-2.

[201] Prediction of Thermal Conditions of DED With FEA Metal Additive Simulation, Vol. Volume 1: Additive Manufacturing; Advanced Materials Manufacturing; Biomanufacturing; Life Cycle Engineering; Manufacturing Equipment and Automation of International Manufacturing Science and Engineering Conference, v001T01A022. doi:10.1115/MSEC2021-63841.

[202] W. Chen, L. Xu, Y. Han, L. Zhao, H. Jing, Control of residual stress in metal additive manufacturing by low-temperature solid-state phase transformation: An experimental and numerical study, Additive Manufacturing 42 (2021) 102016. doi:10.1016/j.addma.2021.102016.

[203] Z. Gan, H. Liu, S. Li, X. He, G. Yu, Modeling of thermal behavior and mass transport in multi-layer laser additive manufacturing of ni-based alloy on cast iron, International Journal of Heat and Mass Transfer 111 (2017) 709 – 722. doi:10.1016/j.ijheatmasstransfer.2017.04.055.

[204] D.-G. Ahn, Directed energy deposition (ded) process: State of the art, International Journal of Precision Engineering and Manufacturing-Green Technology 8. doi:10.1007/s40684-020-00302-7.

[205] R. H. van Blitterswijk, L. A. Botelho, M. H. Farshidianfar, P. Etman, A. Khajepour, Adaptive thermal model for real-time peak temperature and cooling rate prediction in laser material processing, Journal of Manufacturing Processes 101 (2023) 1301–1317. doi:10.1016/j.jmapro.2023.06.037.

APPENDICES

Appendix A

Laser Heat Treatment Process Parameters

A.1 Thermal Dynamic Predictions in LHT with a 2D Adaptive Thermal Model

Table A.1: The process parameters of the five different LHT experiment cases conducted with the carbon steel substrate.

Expt Case	**Speed [mm/s]**			**Power [W]**			**Time [s]**	
CS	$\mathbf{v_1}$	$\mathbf{v_2}$	$\mathbf{v_3}$	$\mathbf{P_1}$	$\mathbf{P_2}$	$\mathbf{P_3}$	$\mathbf{t_1}$	$\mathbf{t_2}$
Const	2.92			400				
v_{step}	2.92	2.08	1.25	350			25	50
v_{ramp}	2.92	1.25		350			72	
P_{step}	2.92			300	350	400	17	34
P_{ramp}	2.92			300	400		35	

Table A.2: The process parameters of the five different LHT experiment cases conducted with the stainless steel substrate.

Expt Case	**Speed [mm/s]**			**Power [W]**			**Time [s]**	
SS	$\mathbf{v_1}$	$\mathbf{v_2}$	$\mathbf{v_3}$	$\mathbf{P_1}$	$\mathbf{P_2}$	$\mathbf{P_3}$	$\mathbf{t_1}$	$\mathbf{t_2}$
Const	2.92			300				
v_{step}	2.92	2.08	1.25	300			25	50
v_{ramp}	2.92	1.25		300			80	
P_{step}	2.92			300	350	400	17	34
P_{ramp}	2.92			300	400		35	

Appendix B

Laser Heat Treatment Experiments Results

B.1 Real-Time Thermal Dynamic Prediction Experiments Results with a CS Substrate

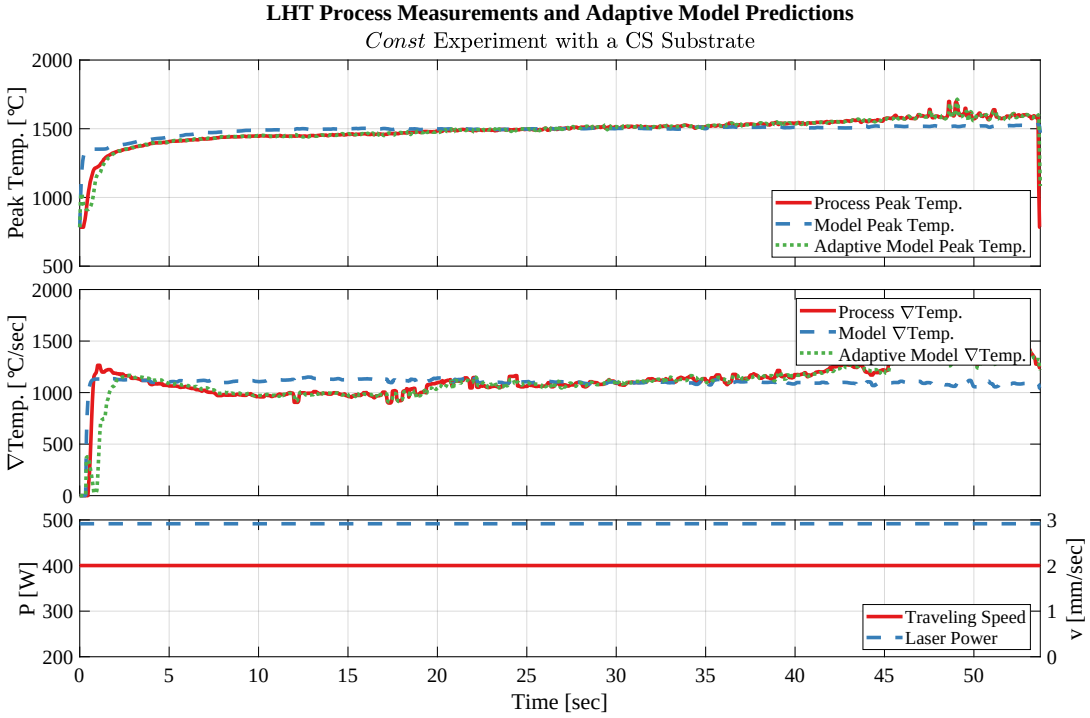


Figure B.1: Real-time peak temperature and cooling rate comparison between the 2D adaptive thermal model predictions and the LHT process measurements during the *Const* experiment with a carbon steel substrate.

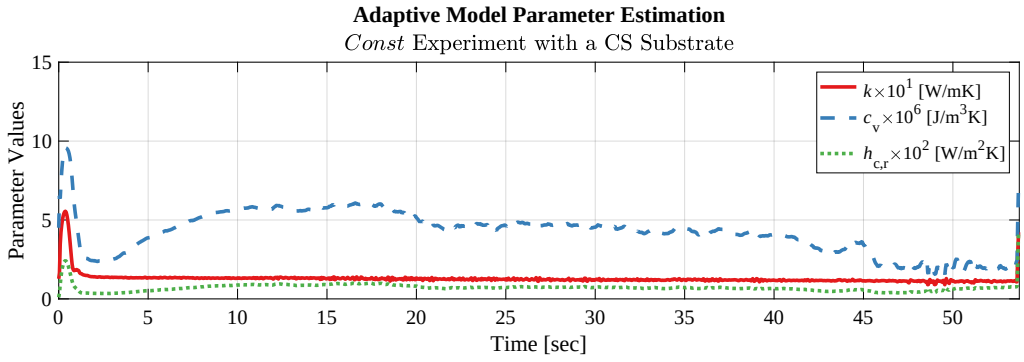


Figure B.2: Real-time parameter estimation during the *Const* experiment with a carbon steel substrate.

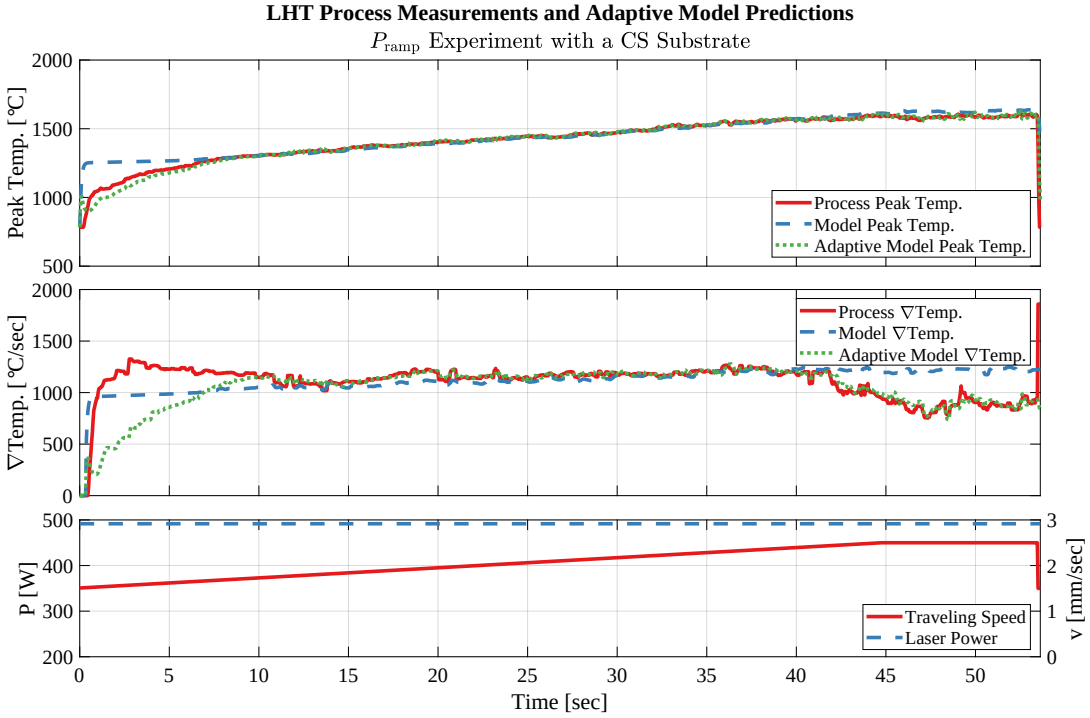


Figure B.3: Real-time peak temperature and cooling rate comparison between the 2D adaptive thermal model predictions and the LHT process measurements during the P_{ramp} experiment with a carbon steel substrate.

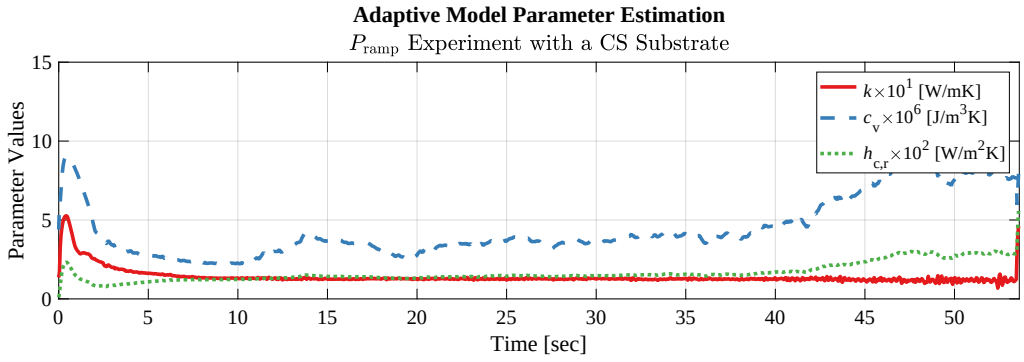


Figure B.4: Real-time parameter estimation during the P_{ramp} experiment with a carbon steel substrate.

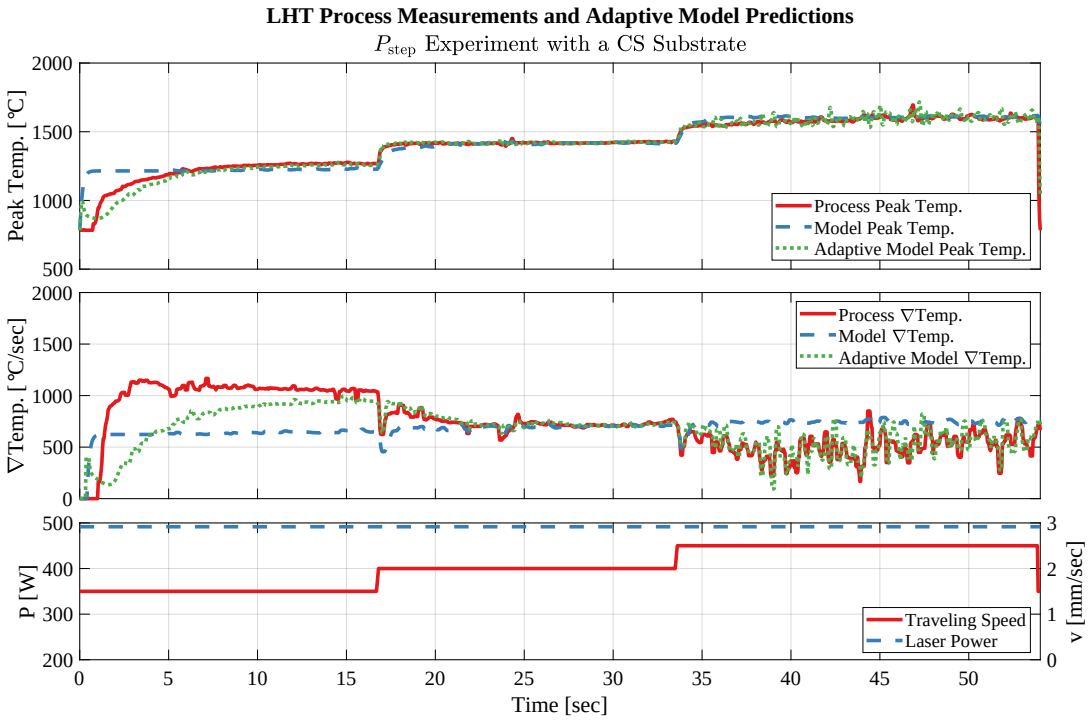


Figure B.5: Real-time peak temperature and cooling rate comparison between the 2D adaptive thermal model predictions and the LHT process measurements during the P_{step} experiment with a carbon steel substrate.

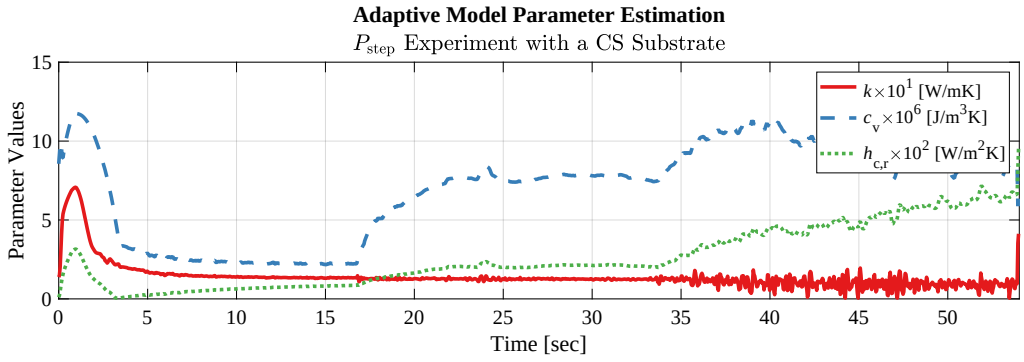


Figure B.6: Real-time parameter estimation during the P_{step} experiment with a carbon steel substrate.

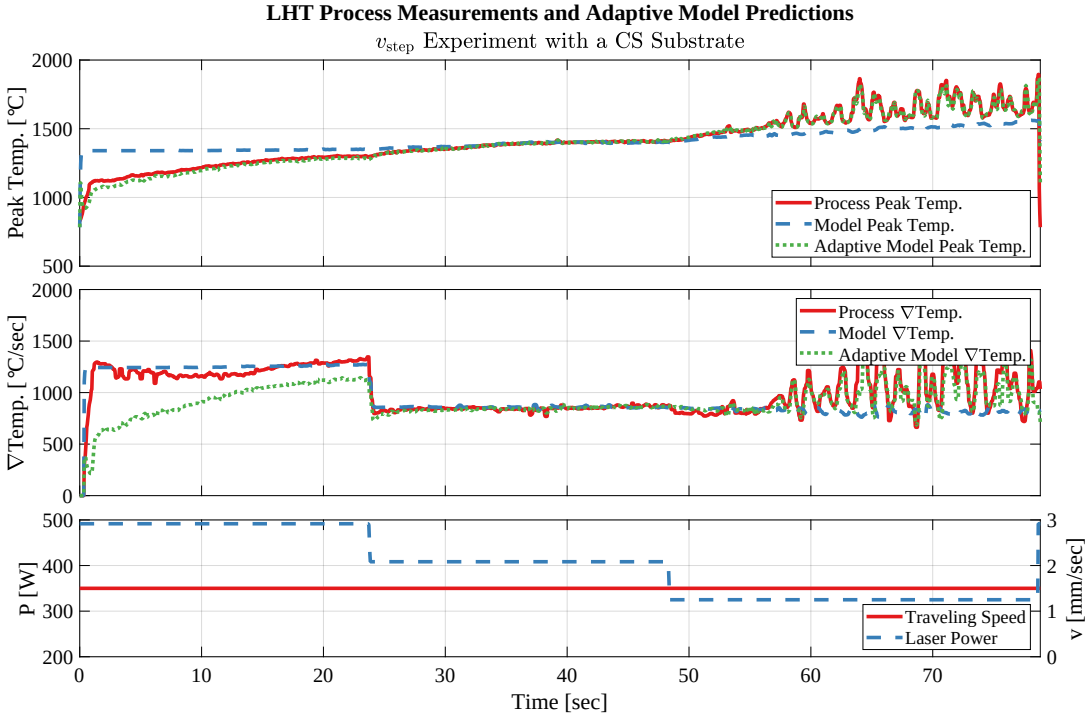


Figure B.7: Real-time peak temperature and cooling rate comparison between the 2D adaptive thermal model predictions and the LHT process measurements during the v_{step} experiment with a carbon steel substrate.

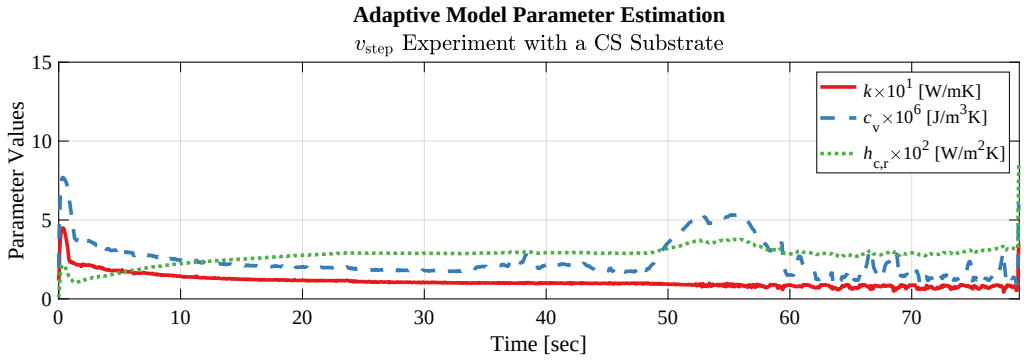


Figure B.8: Real-time parameter estimation during the v_{step} experiment with a carbon steel substrate.

B.2 Real-Time Thermal Dynamic Prediction Experiments Results with an SS Substrate

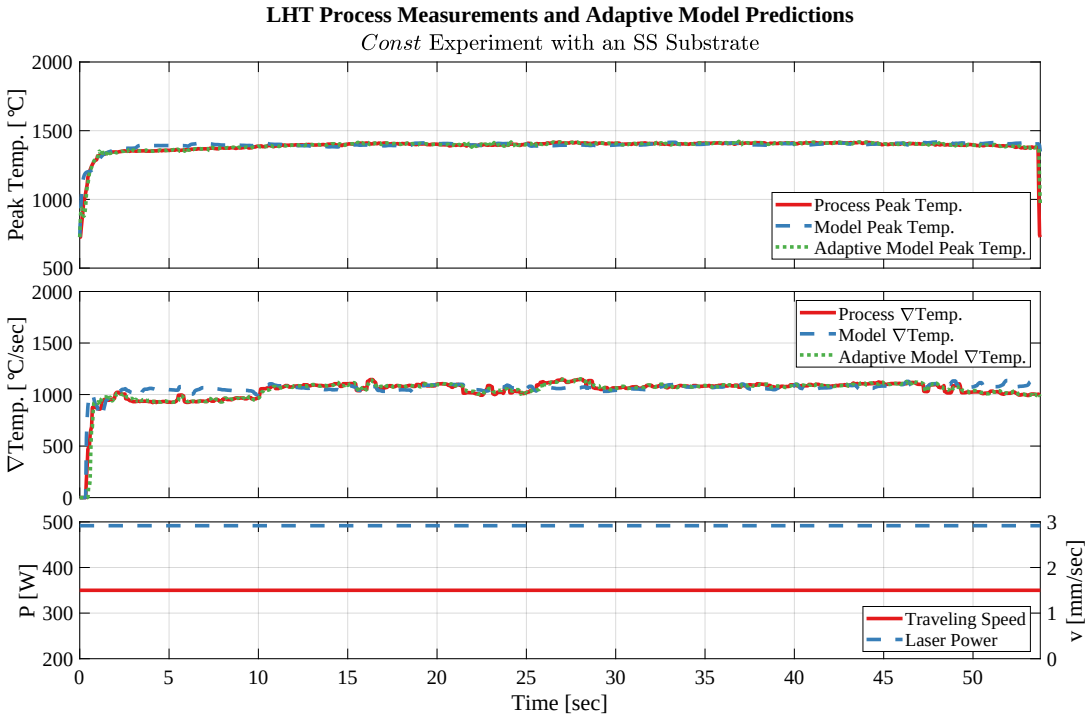


Figure B.9: Real-time peak temperature and cooling rate comparison between the 2D adaptive thermal model predictions and the LHT process measurements during the *Const* experiment with a stainless steel substrate.

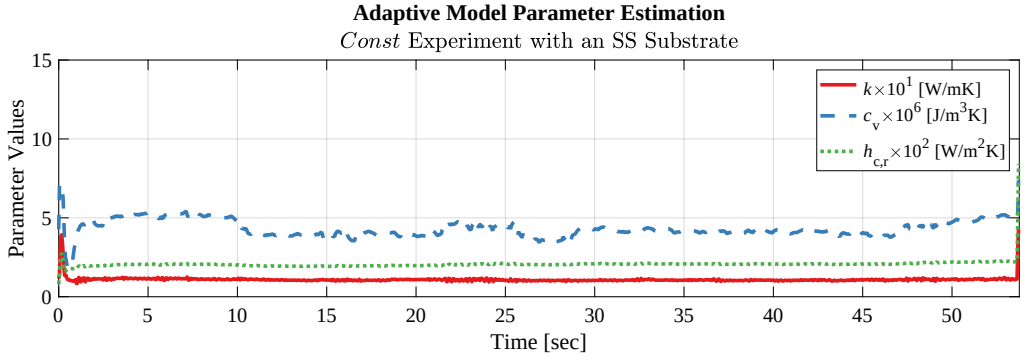


Figure B.10: Real-time parameter estimation during the *Const* experiment with a stainless steel substrate.

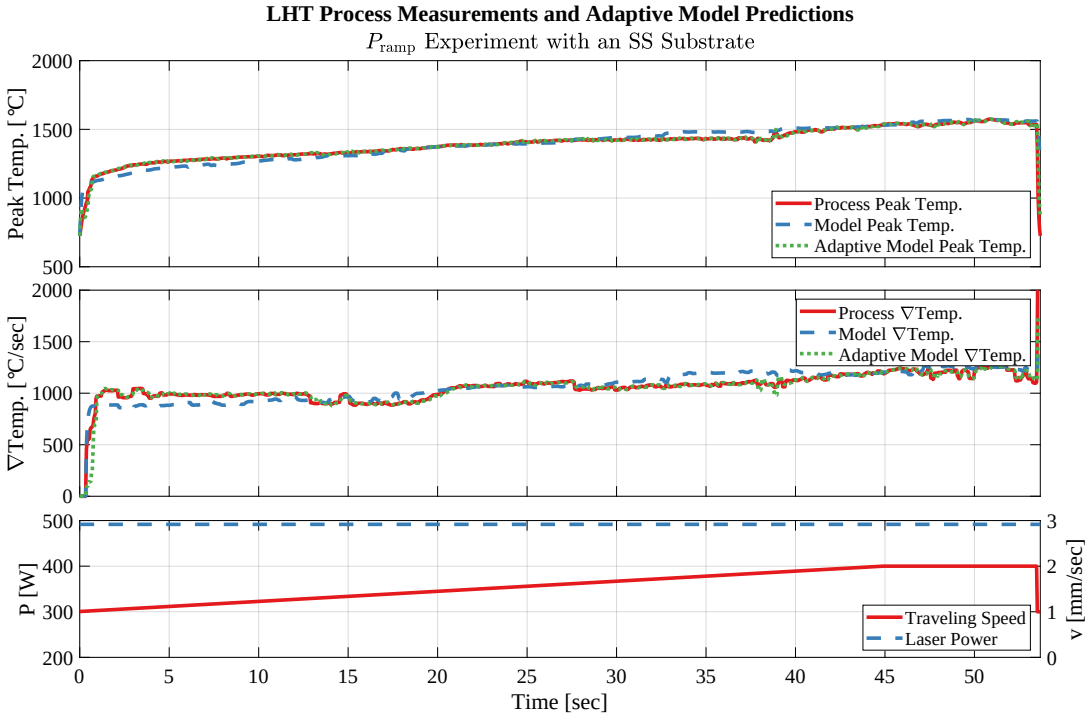


Figure B.11: Real-time peak temperature and cooling rate comparison between the 2D adaptive thermal model predictions and the LHT process measurements during the P_{ramp} experiment with a stainless steel substrate.

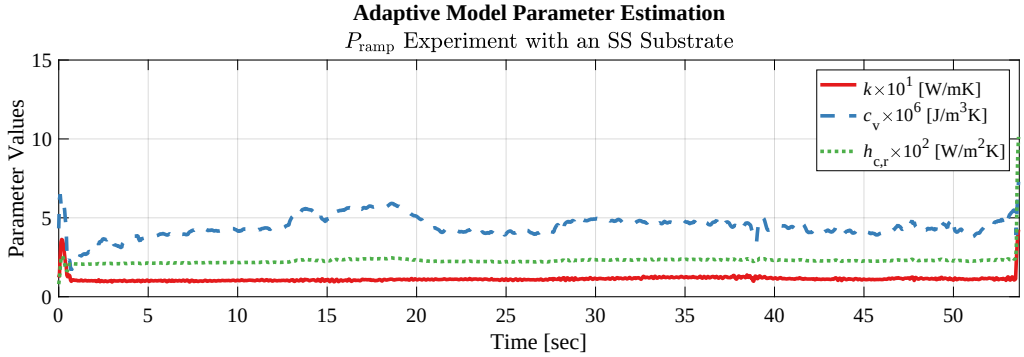


Figure B.12: Real-time parameter estimation during the P_{ramp} experiment with a stainless steel substrate.

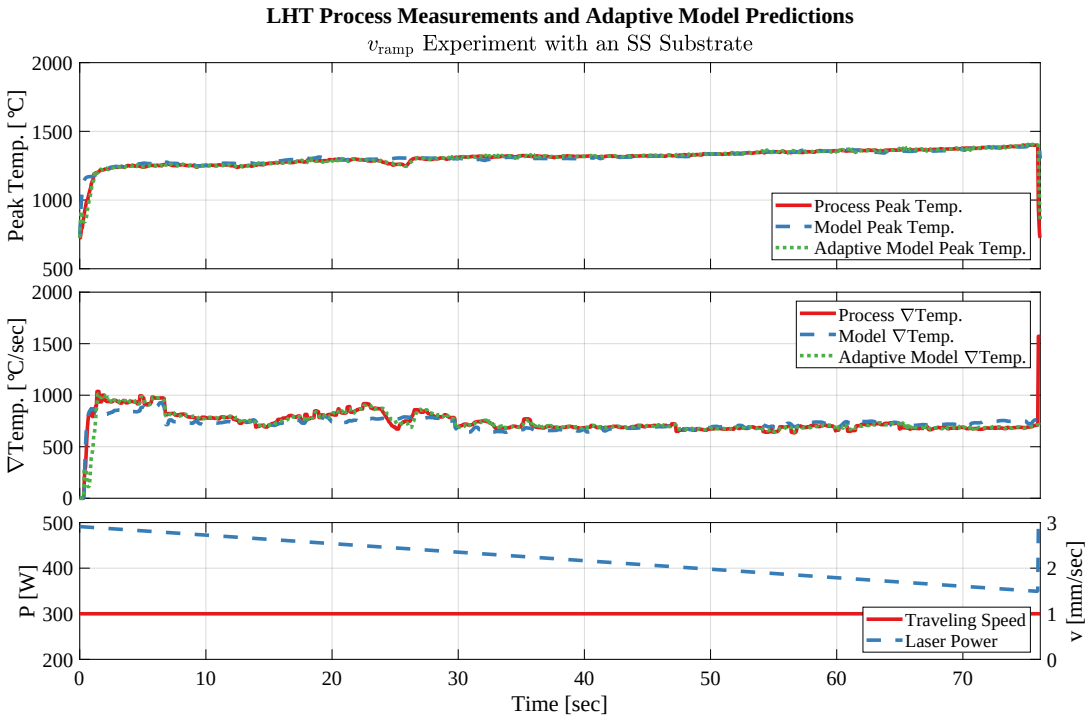


Figure B.13: Real-time peak temperature and cooling rate comparison between the 2D adaptive thermal model predictions and the LHT process measurements during the v_{ramp} experiment with a stainless steel substrate.

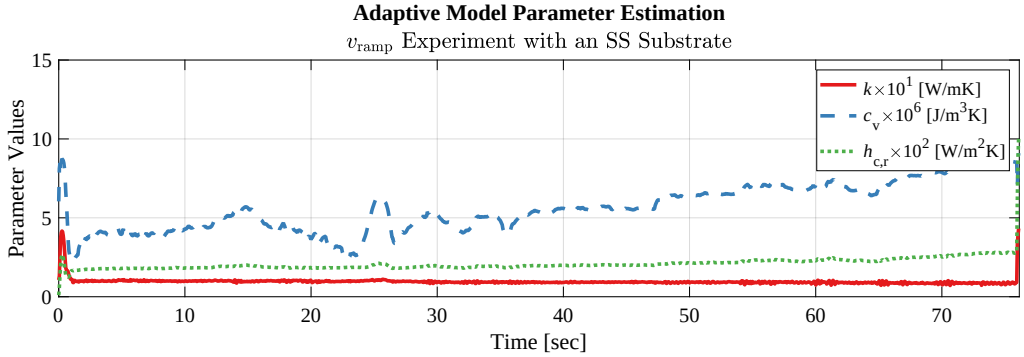


Figure B.14: Real-time parameter estimation during the v_{ramp} experiment with a stainless steel substrate.

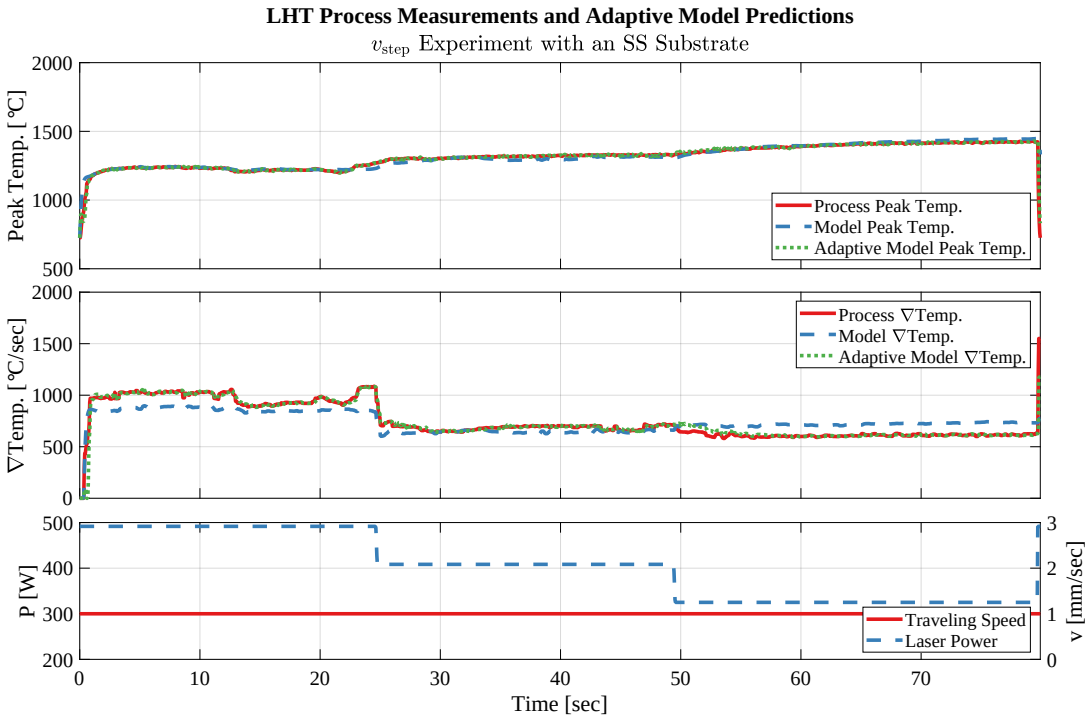


Figure B.15: Real-time peak temperature and cooling rate comparison between the 2D adaptive thermal model predictions and the LHT process measurements during the v_{step} experiment with a stainless steel substrate.

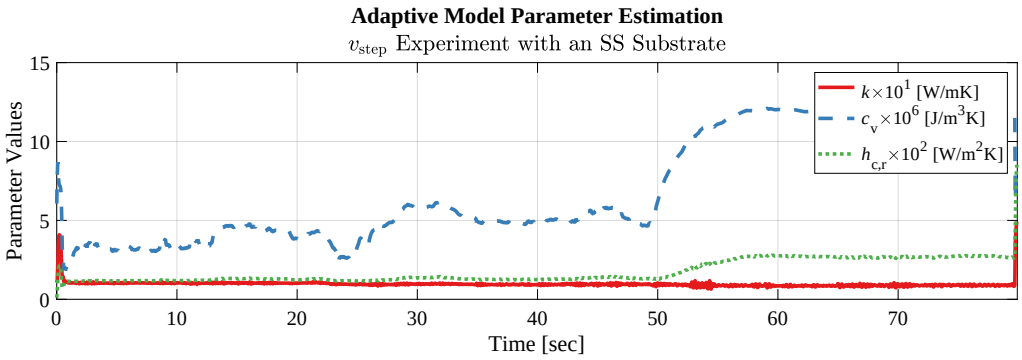


Figure B.16: Real-time parameter estimation during the v_{step} experiment with a stainless steel substrate.

Appendix C

Directed Energy Deposition Experiments Results

C.1 Real-Time Thermal Dynamic Prediction Experiments Results

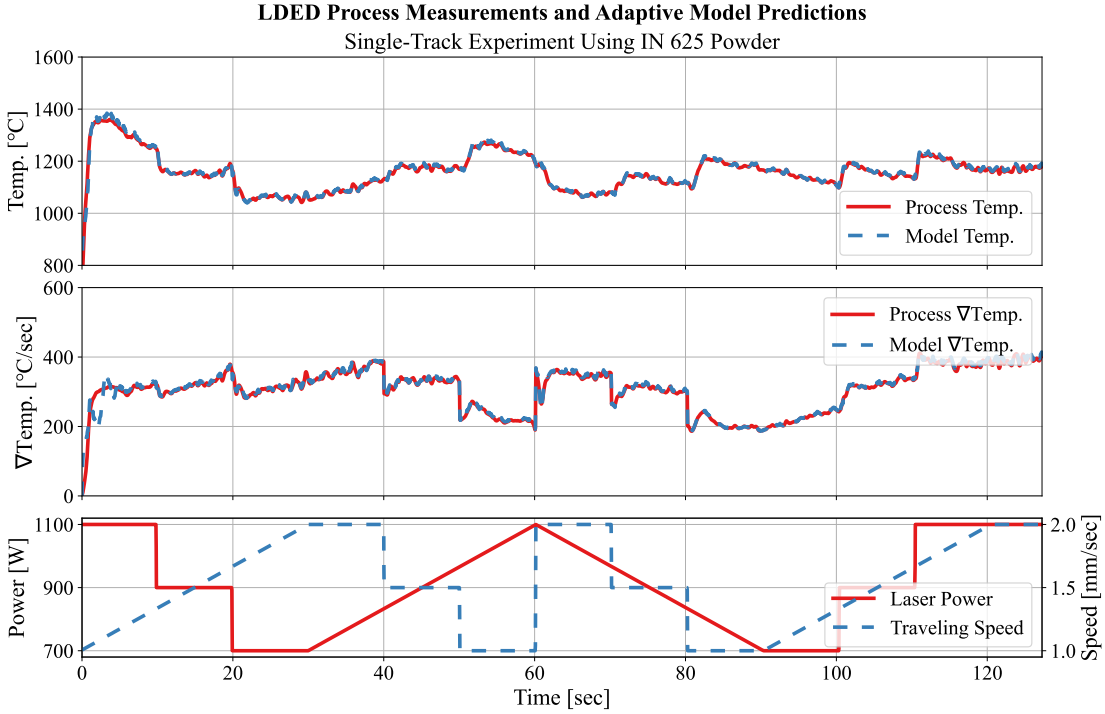


Figure C.1: Real-time temperature and spatial cooling rate comparison between the 1D adaptive thermal model predictions and the L-DED process measurements during the experiment with Inconel 625 powder.

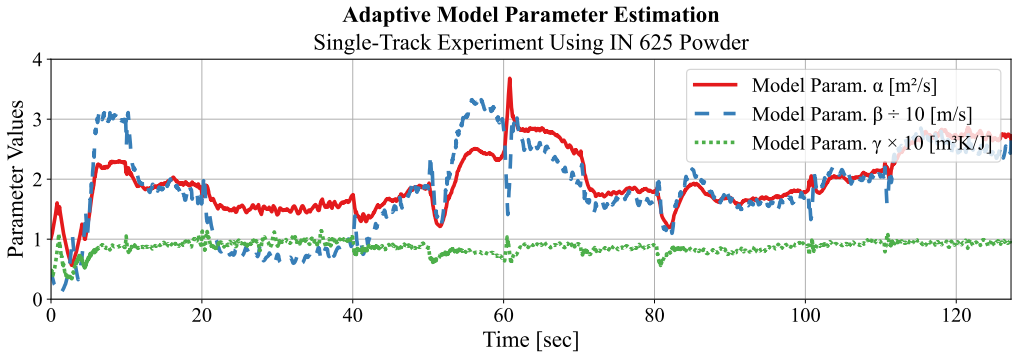


Figure C.2: Real-time parameter estimation during the experiment with Inconel 625 powder.

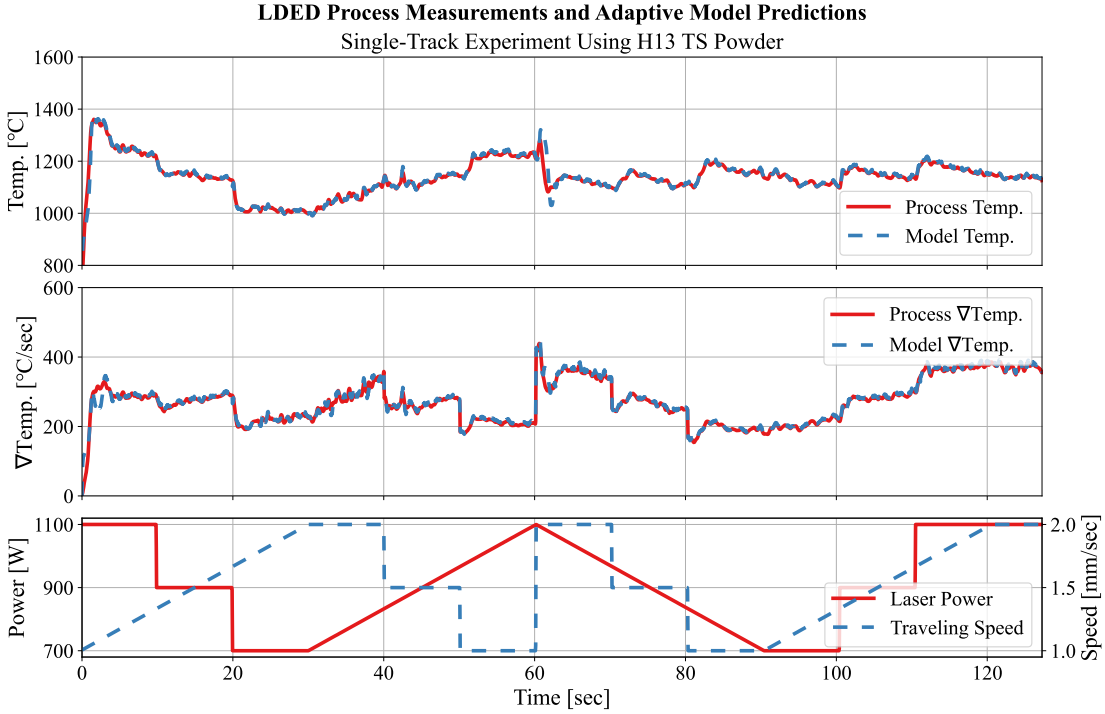


Figure C.3: Real-time temperature and spatial cooling rate comparison between the 1D adaptive thermal model predictions and the L-DED process measurements during the experiment with H13 Tool Steel powder.

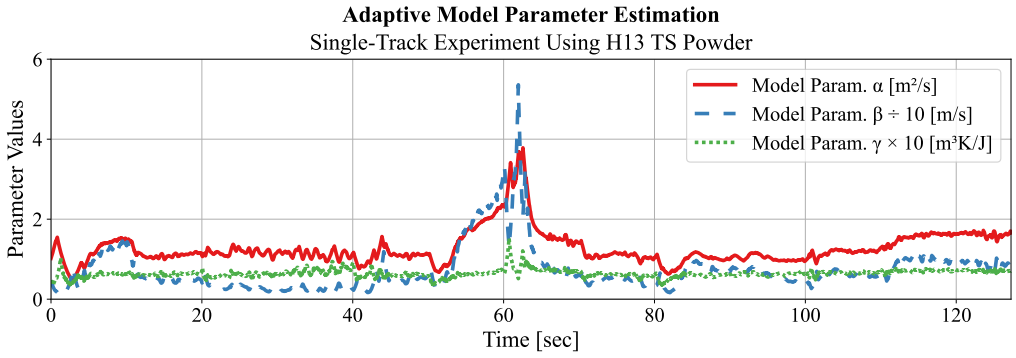


Figure C.4: Real-time parameter estimation during the experiment with H13 Tool Steel powder.

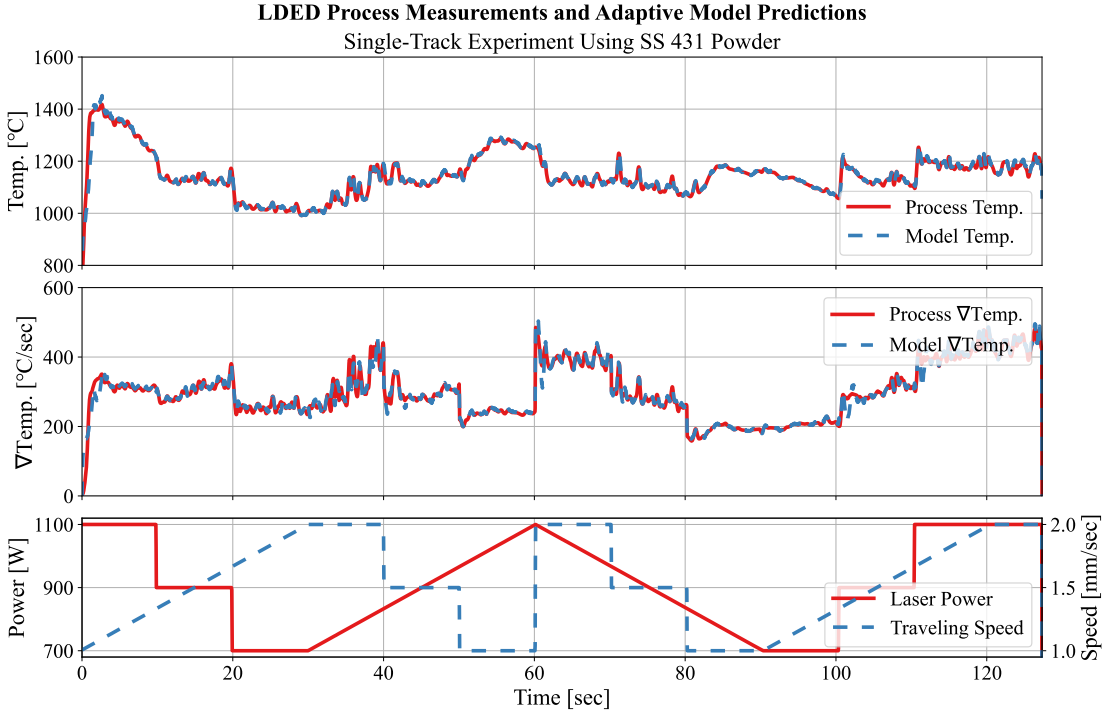


Figure C.5: Real-time temperature and spatial cooling rate comparison between the 1D adaptive thermal model predictions and the L-DED process measurements during the experiment with Stainless Steel 431 powder.

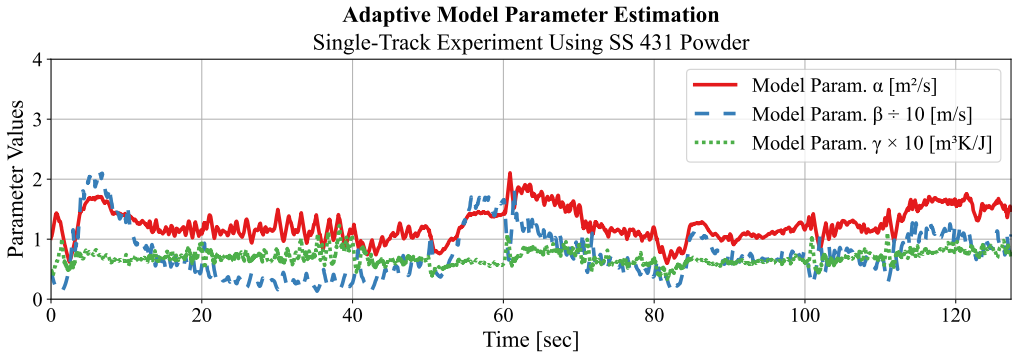


Figure C.6: Real-time parameter estimation during the experiment with Stainless Steel 431 powder.

C.2 Vickers Hardness Measurements of the LDED Wall Experiments

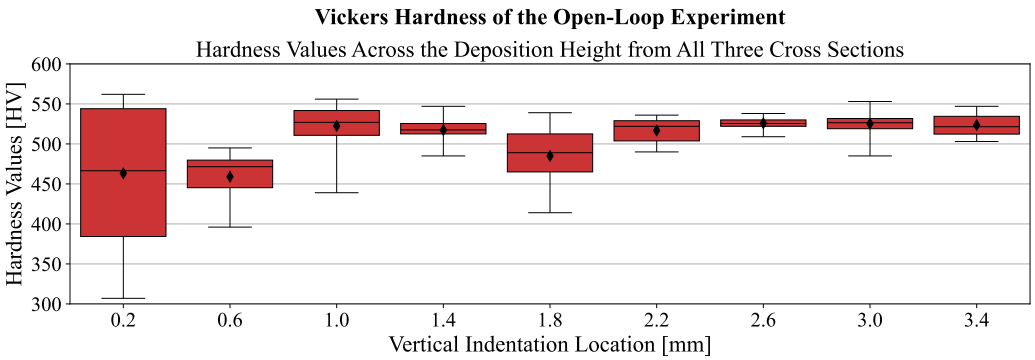


Figure C.7: Boxplot with the Hardness measurements across deposition heights from the three cross sections of the five-layer L-DED wall experiment in open-loop.

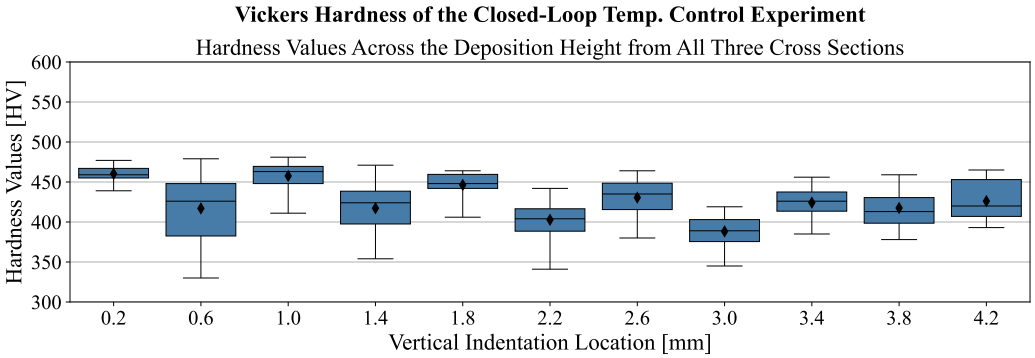


Figure C.8: Boxplot with the Hardness measurements across deposition heights from the three cross sections of the five-layer L-DED wall experiment with closed-loop controlled temperature.

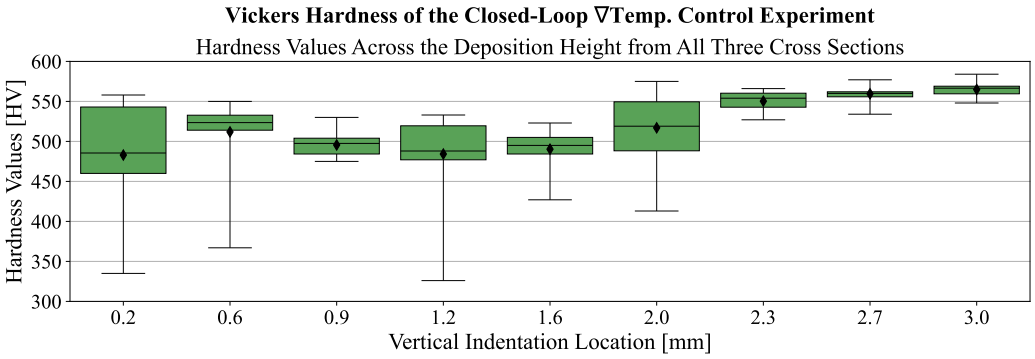


Figure C.9: Boxplot with the Hardness measurements across deposition heights from the three cross sections of the five-layer L-DED wall experiment with closed-loop controlled spatial cooling rate.

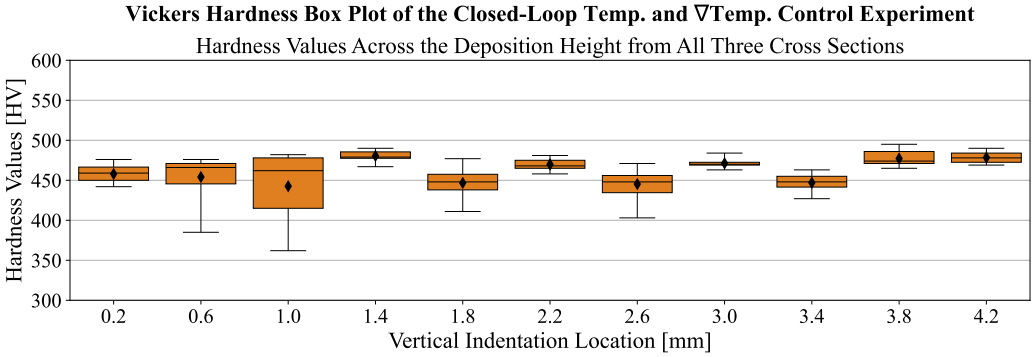


Figure C.10: Boxplot with the Hardness measurements across deposition heights from the three cross sections of the five-layer L-DED wall experiment with closed-loop controlled temperature and spatial cooling rate.